

ABSTRACT

LOU, YI. Nano-Assembled Plasmonic Crystals Devices for Sensing Applications. (Under the direction of Dr. John F. Muth).

The ability of plasmonic nano-structures to concentrate light into sub-wavelength volumes offers the potential for developing new devices and applications. Surface plasmons are electron oscillations that propagate on a metal surface. The interaction of light with surface plasmons can be tailored by periodic nano-structures on a surface, thus allowing miniaturized photonic devices with length scales much smaller than those currently achieved. The purpose of this dissertation is to develop a low cost self-assembly method to fabricate large area plasmonic crystals and study the physical properties of surface plasmons. Several plasmonic devices are designed using the self-assembled gold nanobump arrays.

A polystyrene sphere self-assembly technique was developed for fabricating holes or bumps as small as 150 nm with spacing controlled by the sphere diameter (typically 500 -700 nm). Several applications were developed, which were based on the sensitivity of the photon-plasmons coupling to 1) the surface dielectric and 2) the incident angle. A sensitivity to refractive index changes of about 100 nm per refractive index units was demonstrated by varying the surrounding dielectric environment with several chemicals for sensing applications. An increasing variation in the color of a vanadium oxides thermochromic device was observed by using surface plasmons to enhance the variation in reflection. Surface plasmons were also used in an optical modulator, where excitation by one wavelength was used to changes the transmission at a different wavelength.

Using the angular sensitivity of the nano-structured plasmonic thin films, an angle of arrival sensor was fabricated. This sensor can be used to track the position of the sun or other collimated light sources like lasers. The polarization dependency of the device was studied and its behavior was explained by the lattice momentum matching mechanism. Inspired by the novel concept of this angle of arrival sensor, a wavefront sensor was theoretically examined. It measured the incident angles of the incoming wavefront on a pixel array and reconstructed the wavefront with a least-squares fitting algorithm.

Nano-Assembled Plasmonic Crystals Devices for Sensing Applications

by
Yi Lou

A dissertation submitted to the Graduate Faculty of
North Carolina State University
in partial fulfillment of the
requirements for the Degree of
Doctor of Philosophy

Electrical Engineering

Raleigh, North Carolina
2011

APPROVED BY:

Dr. John F. Muth
Committee Chair

Dr. Leda M. Lunardi

Dr. Robert M. Kolbas

Dr. David Aspnes

BIOGRAPHY

Yi Lou was born in Tianjin, which is a beautiful city located in north China. He spent 18 years there, and then he went to Peking University in Beijing to pursue his Bachelor's degree in Physics. He developed his interests in photonics and did some research work on organic luminescent devices during the undergraduate study. In 2006, he came to U.S. and become a graduate student at North Carolina State University. He joined Dr. John Muth's research group in 2007 and started a four year's journey to his PhD in Electrical Engineering. He had a great experience conducting world class research at the frontier of nano-photonics. He worked on studying the physical properties of surface plasmons and developing plasmonic devices for sensing applications.

ACKNOWLEDGEMENTS

I would like to thank all my professors, colleagues and friends that I have met and worked with during the four years at North Carolina State University:

Jiang Li & Meng'ao Lou Support and encourage from my family, mom and dad, are always the most important part in my life. Their love and understanding is so clear although I have travelled far-off from home.

Dr. John F. Muth For the guidance in my study and the professional research environment he built up. He gave me not only the knowledge but also the courage to explore. As an old Chinese proverb, a teacher for a day is a father for a lifetime.

Dr. Leda Lunardi For acting as my committee members. The support they provided when Dr. Muth was serving in Iraq provide me the momentum to accelerate my research progress in the early stage.
Dr. Robert M. Kolbas
Dr. David Aspnes

Joe Matthews For all the technical support in the labs and the training to let me work independently.

All the members in our group and the people in MRC 112 For discussion and collaboration in every day's work. They inspired me to explore novel ideas and catch up with the frontier of the field. Their support in the labs and in office provided great help.

Jing Xie & Jianchen Hu For the time we spent together to discuss those interesting topic.

TABLE OF CONTENTS

LIST OF TABLES	vii
LIST OF FIGURES.....	viii
CHAPTER 1 INTRODUCTION.....	1
1.1 Overview	1
1.2 Dissertation Organization.....	4
CHAPTER 2 PHYSICS OF SURFACE PLASMONS	6
2.1 Maxwell’s Equation and Boundary Conditions.....	6
2.2 Dielectric Constant of Metal	10
2.3 Surface Plasmon Excitation.....	14
2.3.1 Dispersion Relation	15
2.3.2 Plasmon Decay Length.....	19
2.3.3 Skin Depth	20
2.4 Periodic Array for Surface Plasmon Coupling.....	22
2.4.1 Metal Grating	23
2.4.2 Dielectric Grating	25
2.5 Localized Surface Plasmon	28
CHAPTER 3 REVIEW OF RECENT PLASMONIC CRYSTAL RESEARCH.....	32
3.1 Extraordinary Transmission	33
3.1.1 Metallic Nanohole Array Enhanced Transmission	33
3.1.2 Enhanced Transmission with Different Structures	38
3.2 Plasmonic Crystal Dispersion Relation	41
3.3 FDTD EM Field Simulation.....	45
3.4 Surface Plasmon Dielectric Sensing.....	49
3.4.1 Bio-chemical Sensing	49
3.4.2 Microarrays for Bio-sensing	51
3.5 Surface Plasmon Enhanced Fluorescence	52

3.6 Plasmonic Devices for Novel Applications.....	54
3.6.1 Plasmonic Switch.....	54
3.6.2 Plasmonic Laser	56
3.6.3 Plasmon Enhanced Solar Energy Harvesting	58
3.6.4 Plasmonic Filters for Spectral Imaging	59
CHAPTER 4 PLASMONIC CRYSTAL FABRICATION AND CHARACTERIZATION.....	61
4.1 Plasmonic Crystal Fabrication.....	61
4.1.1 Nanosphere Self-Assembly	61
4.1.2 Reactive Ion Etching (RIE).....	65
4.1.3 E-beam Deposition	66
4.1.4 Annealing.....	67
4.1.5 Photolithography.....	69
4.1.6 Focused Ion Beam (FIB) Milling	71
4.1.7 Nano-stamp Imprint.....	72
4.1.8 Summary of the Fabrication Methods	74
4.2 Device Characterization	76
4.2.1 Scanning Electron Microscope (SEM) Imaging.....	76
4.2.2 Atomic Force Microscopy and Optical Microscope.....	80
4.2.3 Optical Spectrum.....	83
CHAPTER 5 PLASMONIC CRYSTALS WITH DIFFERENT SURFACE DIELECTRIC MATERIALS	88
5.1 Introduction	89
5.2 Chemical Sensing using Plasmonic Crystals.....	90
5.3 Vanadium Oxide Reflectivity Modulation	95
5.4 All Optical Modulation Device with Organic Photovoltaic Material.....	106
5.5 Cell Migration on Large Periodicity Nanohole Array.....	111
CHAPTER 6 PLASMONIC CRYSTAL SUN SENSOR	117
6.1 Introduction	117
6.2 Device Structure and Optical Properties	120

6.3 Device Response for the Sun Light	126
6.4 Angle Resolved Spectrum for Polarized Light.....	129
6.5 Device Response for Collimated Laser Beam	132
6.6 Hexagonal and Rectangular Symmetry	137
CHAPTER 7 PLASMONIC CRYSTAL WAVEFRONT SENSOR	140
7.1 Wavefront Sensor Pixel Array Design	140
7.2 System Model for the Sensor	147
7.3 Imaging Processing Algorithm.....	149
CHAPTER 8 CONCLUSIONS AND SUGGESTIONS FOR FUTURE WORK.....	155
8.1 Conclusions	155
8.2 Suggestions for Future Work.....	156
REFERENCES.....	160

LIST OF TABLES

Table 2-1 Plasmon frequency of several commonly used noble metals.	13
Table 7-1 Comparison of several wavefront sensors.	152

LIST OF FIGURES

Figure 1-1 The number of publications on the topic of plasmonic each year.....	2
Figure 1-2 The journals that contain plasmonic related topics.....	3
Figure 2-1 Reflectance of a glass/silver/air interface for different incident angles.....	9
Figure 2-2 Dielectric constant for gold as a function of photon energy.....	13
Figure 2-3 Physics principles of surface plasmon.....	15
Figure 2-4 Surface plasmon dispersion $\omega(k_x)$ on a gold surface.....	18
Figure 2-5 SPP propagation length measured by CL imaging spectroscopy for 400 nm thick gold and silver films.....	20
Figure 2-6 The Kretschmann Configuration (left) and its surface momentum matching mechanism (right) for exciting SPR on a flat metal film.....	23
Figure 2-7 Near field image of surface plasmon on a 1D gold grating.....	23
Figure 2-8 SEM image of a Focused Ion Beam prepared 2D holes array in a polycrystalline silver film.....	24
Figure 2-9 Enhanced transmission effect on a 2D dielectric grating.....	26
Figure 2-10 Devices structures for R6D /PMMA grating.....	27
Figure 2-11 The intensity comparison of R6D/PMMA gratings.....	27
Figure 2-12 Near-field optical images with normal incident light on an isolated nano-hole in a gold film.....	29
Figure 2-13 Impact of the LSP on the 2D array enhanced transmission spectra.....	30
Figure 2-14 Effect of size and shape on LSP excitation for silver nano-particles formed by nanosphere lithography.....	31

Figure 3-1 Traditional optical configurations to excite SPR on a flat metal film.....	33
Figure 3-2 Zero-order transmission of a 2D array patterned silver film.....	34
Figure 3-3 Transmission spectra as a function of incident angle for a square Ag array.....	35
Figure 3-4 Energy dispersion of surface plasmons and loci of Wood's anomaly	37
Figure 3-5 Device structure of a 1D grating plasmonic structure.....	38
Figure 3-6 Transmission spectra of the 1D grating structure on ITO waveguide.....	39
Figure 3-7 Enhanced transmission effect on a concentric circle structure.	41
Figure 3-8 Dispersion diagram of a 2D plasmonic crystal.	42
Figure 3-9 The sample geometry and reflection spectra collecting optical setup.....	43
Figure 3-10 The reciprocal lattice of the rectangular 2D array and its dispersion relation measured by optical spectra.....	44
Figure 3-11 Dispersion relation of an Au nano-pyramidal array collected from p-polarized reflection spectra measurement with different dielectric materials above the surface.	45
Figure 3-12 FDTD field simulation of a 2D gold array.....	46
Figure 3-13 FDTD simulation for the ridge-enhanced transmission effect.	47
Figure 3-14 Dependencies of the peak transmittance and the resonant wavelength on the width of the ridge.....	48
Figure 3-15 Dependencies of the peak transmittance and the resonant wavelength on the height of the ridge.	49
Figure 3-16 Nanopost array for surface plasmon excitation.....	50
Figure 3-17 PEG solution concentration sensing uses the nanopost array.	51
Figure 3-18 Microarray uses in sensing glucose solutions with different refractive indexes.	52
Figure 3-19 Enhancing fluorescence dye emission with 2D nanohole array gold film.	53

Figure 3-20 Structure and dispersion relation of the plasmon transistor device.....	55
Figure 3-21 FDTD simulation of the plasmostor shows the transmitted power distribution for a 2 μm long optical source-drain separation. The device was illuminated with a Gaussian beam of wavelength $\lambda=1.55 \mu\text{m}$	56
Figure 3-22 Device structure and field distribution of the plasmonic laser.....	57
Figure 3-23 Three structures that utilize surface plasmons to enhance solar conversion efficiency.....	58
Figure 3-24 A single concentric ring structure that has plasmon enhanced transmission effect depending on its periodicity.....	59
Figure 3-25 Triple rings structure prepared with the same parameter as one ring structure for color separating measurement.....	60
Figure 4-1 The process flow and tools for nanosphere directed self-assembly.....	62
Figure 4-2 The tools for patterning large area nanosphere array on a glass substrate.....	64
Figure 4-3 RIE and metal deposition tools in the lab.	67
Figure 4-4 SEM images of RIE etched nanospheres.	68
Figure 4-5 Annealing the gold film improves surface smoothness.	69
Figure 4-6 Photolithography tools in the lab.	70
Figure 4-7 1D and 2D arrays fabricated by FIB milling.....	72
Figure 4-8 Hexagonal arrays fabricated by nano-imprinting technique.	73
Figure 4-9 Summary of the nanosphere lithography process flow.	75
Figure 4-10 SEM picture for a 600 nm periodicity nanobump array plasmonic crystal..	77
Figure 4-11 SEM micro-image of a 600 nm period nanobump array.....	78
Figure 4-12 A cross section SEM image of the nanobump array surface.....	79

Figure 4-13 Nanohole arrays with different RIE time.....	79
Figure 4-14 A large area (~80 μm x 50 μm) hexagonal nanohole plasmonic crystal with a 90 nm gold layer.....	80
Figure 4-15 AFM images of a 600 nm period nanobump array patterned gold film.....	81
Figure 4-16 Surface geometry of a nanohole array.....	82
Figure 4-17 Height profile analysis of the AFM image of a nanobump array.....	82
Figure 4-18 The optical configuration to collect the transmission spectra of a 20 μm diameter spot on the sample.....	83
Figure 4-19 OceanOptics USB 4000 spectrometer.....	84
Figure 4-20 The rotation stage for collecting the angle resolved transmission spectra of a large area plasmonic crystal.....	84
Figure 4-21 Transmission spectrum of a 90 nm flat gold film.	85
Figure 4-22 Spectra of a collimated white light beam for several patterned film structures.	86
Figure 5-1 The SEM image of a 600 nm periodicity nanobump array patterned gold surface.....	91
Figure 5-2 Spectra response of a plasmonic crystal with several kinds of chemicals on its surface.....	92
Figure 5-3 Transmission spectra response of a 500 nm periodicity plasmonic crystal with air and water on top of its surface.....	94
Figure 5-4 Schematics and optical configurations of the three devices for VO ₂ film thermochromic effect study.....	96
Figure 5-5 Spectra of the VO ₂ /ITO/Glass structure at different temperature.....	98
Figure 5-6 Reflection spectra at 30 °C and 80 °C for a flat gold (180 nm) /VO ₂ (120 nm)/ITO (130 nm)/glass structure.....	99

Figure 5-7 Spectra of the gold nanobump array/VO ₂ /ITO/Glass structure at different temperature..	99
Figure 5-8 The SPR peak shifting scheme for the air/plasmonic crystal/VO ₂ /ITO structure.	101
Figure 5-9 Color changing traces on CIE 1931 color space during VO ₂ phase transitions..	102
Figure 5-10 Light intensity traces at 675 nm wavelength showed hysteresis effect during the phase transition..	103
Figure 5-11 Color changing trace for the Gold/VO ₂ and Al/VO ₂ devices during the semiconducting-metallic phase transition.....	104
Figure 5-12 Reflectivity for a multilayer thin film structure with different conductivities.	105
Figure 5-13 The P3HT coated plasmonic crystal thin film structures for light modulation applications..	107
Figure 5-14 Spectra response of the light modulation device and the input light source....	108
Figure 5-15 The schematic of the all optical modulation device.....	109
Figure 5-16 Transmission intensities of the signal light respond to a switching input.....	110
Figure 5-17 Strategy to generate patterned hybrid nanohole SAM surfaces for studies of cell adhesion and cell migration..	112
Figure 5-18 ESEM images of the hybrid nanohole surfaces..	114
Figure 5-19 Representative micrographs of fibroblast cells adhered to various hybrid nanohole surfaces.....	115
Figure 6-1 Conventional methods of sensing the incident angle of light that rely on shadowing a sensor or measuring the position of a spot determined by an aperture or lens...	119

Figure 6-2 The schematic shows the hexagonal nano-bump array used in conjunction with a silicon photodiode, with the angle θ determining the angle of incidence of the wavefront..	121
Figure 6-3 An SEM image of the 600 nm periodicity self-assembled gold nanobump array with the inset showing the cross section of one nano-bump.....	122
Figure 6-4 The reciprocal lattice of a hexagonal array..	123
Figure 6-5 The angle resolved transmission spectra of the sensor in response to an unpolarized light from a collimated tungsten white light source.....	125
Figure 6-6 The optical setup for outdoor data collection.....	127
Figure 6-7 The schematic for the device response testing setup under the sunlight.....	127
Figure 6-8 Experimental data for the device response to the sunlight shows strong angular dependence when the nanobump array is installed.....	128
Figure 6-9 The p-polarized light transmission spectra for 0-10 degree incident angles.....	130
Figure 6-10 The s-polarized light transmission spectra for 0-10 degree incident angles. ...	130
Figure 6-11 The p-polarized light provides additional momentum at the direction parallel to the incident plane.	131
Figure 6-12 Optical setup for collimated laser beam transmission intensity collection..	133
Figure 6-13 Photocurrent response to a 780 nm collimated laser beam with both s and p polarizations.	134
Figure 6-14 Device response for p-polarized laser with different wavelength (775-790 nm)..	135
Figure 6-15 Device response curve for a 633 nm He-Ne laser with both s and p polarized light.	136
Figure 6-16 The primitive vectors for rectangular and hexagonal arrays.....	138

Figure 7-1 The principles of operation of the Shack-Hartmann wavefront sensor.....	141
Figure 7-2 The cross section schematic of the plasmonic crystal (PC) wavefront sensor...	142
Figure 7-3 Layout of a $\sim 4 \text{ mm}^2$ PC wavefront sensor that is constructed by an array of pixels. One pixel is a photodiode with a protection border.....	144
Figure 7-4 The layout for a pixel with multiple PC sensors. One pixel contents two gratings, one flat gold surface and one hexagonal nanobump array.....	145
Figure 7-5 The wavevector model for measuring the polar and azimuthal angle of the incident wavefront with the four photodiode in one pixel structure.	146
Figure 7-6 Block diagram of the data collection and processing system.....	148
Figure 7-7 Schematic of the analog part of the system, which contents an op-amp and an ADC.	149
Figure 7-8 The surface fitting result of a curving input wavefront using Matlab simulation.	152
Figure 8-1 Hexagonal array pattern with regular defects for lithography mask design.	157

CHAPTER 1

INTRODUCTION

1.1 Overview

The interaction of light with matter is of great interest in scientific research and everyday life. It has found wide spread application in devices used for communications, medical treatment, displays and solar energy. For example, the invention of the Charge-Coupled Device (CCD) provides a convenient tool to capture high quality imaging and has been widely applied since its invention. Another example is solar energy which is becoming an important alternate energy source for our society. Technology advances that convert the sun's radiation into electricity with high efficiency will make it possible to replace fossil or nuclear energy with the clean and renewable energy. Since about 2000, strong interest in nano-scale material and physics research has led to many new applications and devices that are built using novel nano-structures. Part of the interest in nano-optical science is in plasmonic, photonic and meta-materials. These fields focus on the interaction of visible-NIR light with metal or semiconductor materials that have structures with their sizes similar to the incident light wavelength.

Plasmonic crystals are constructed by fabricating periodic metal structures with length scales comparable to the wavelength of optical waves.[1,2,3,4] Surface Plasmon Resonance (SPR) occurs when the periodic metal structure provides the momentum matching conditions for light incident on a plasmonic crystal. The electric field of the photon results in an oscillation of the electron gas that travels along the plane of the surface at the incoming photon's frequency. The excited surface plasmon polariton changes the metal's dielectric properties at the resonant frequency, thus it modifies the optical properties of the plasmonic crystals. The nano-pattern structures allow the SPR characteristics to be controlled.

Studies on SPR were mainly focused on flat metal thin film or nano-particles before the observation of extraordinary transmission effect on nanohole array patterned silver film.[5] This effect was explained by surface plasmon enhanced transmission, where the noble metal

film was an active element in this light propagation path rather than just a passive light blocking structure. Since then, there has been interest in structuring plasmonic crystal such that plasmon resonance can be engineered to occur at specific wavelengths or engineered to be suitable for novel device applications. Adopting plasmonic crystals for surface plasmon excitation greatly simplified the optical setups that previously used, which include Kretschmann and Otto configurations.[6] It provides a new way to satisfy the momentum matching requirement.

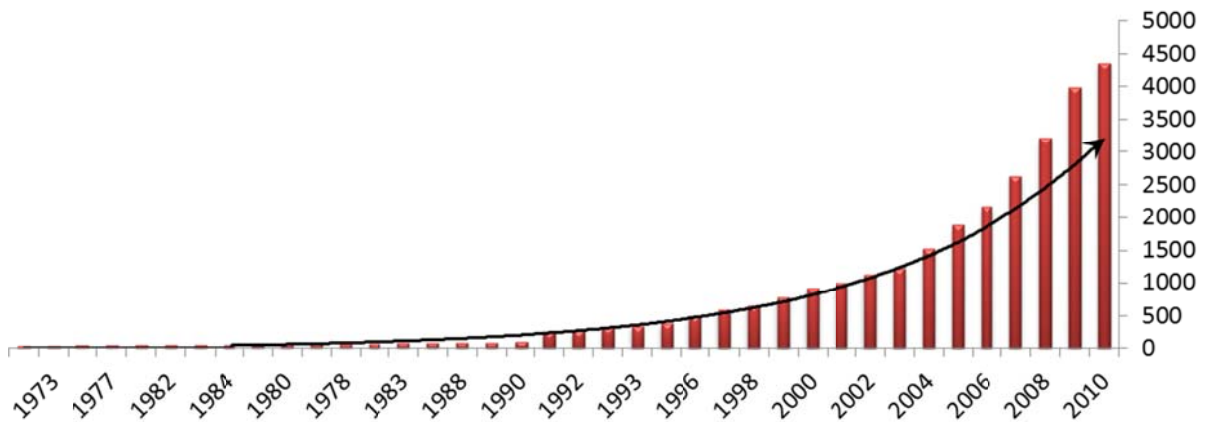


Figure 1-1 The number of publications on the topic of plasmonic each year. The black curve is the exponential trend curve of the data points. (Obtained from Web of Science, Thomson Reuters on June 16, 2011. [7])

The research on plasmonic related materials and structures were enabled by the development of nano-scale processing tools. The microelectronic industry entered sub-micron scale in the 1990's and has provided numerous fabrication and observation methods that have now been applied in plasmonic crystal research, such as FIB milling and E-beam lithography. The numbers of research publications on the topic of plasmonic devices and applications are exponentially increasing since 1990, which is presented in Figure 1-1. In the past 5 years, this number is growing even faster than the exponential trend line. These publications are multidisciplinary, but can be sorted into the fields of chemistry (46.7%), physics (40%), biochemistry & molecular biology (30.6%) and materials science (23.6%).

The multidisciplinary nature of the publications lead to a total of more than 100% since some of them are listed in more than one category. The major journals to publish plasmonic research works are Physical Review B (5.6%), Applied Physics Letters (3.6%), Optics Express (3.5%), Journal of Biological Chemistry (3.4%), Langmuir (2.7%). That shows the importance of plasmonics across many areas of science and technology.

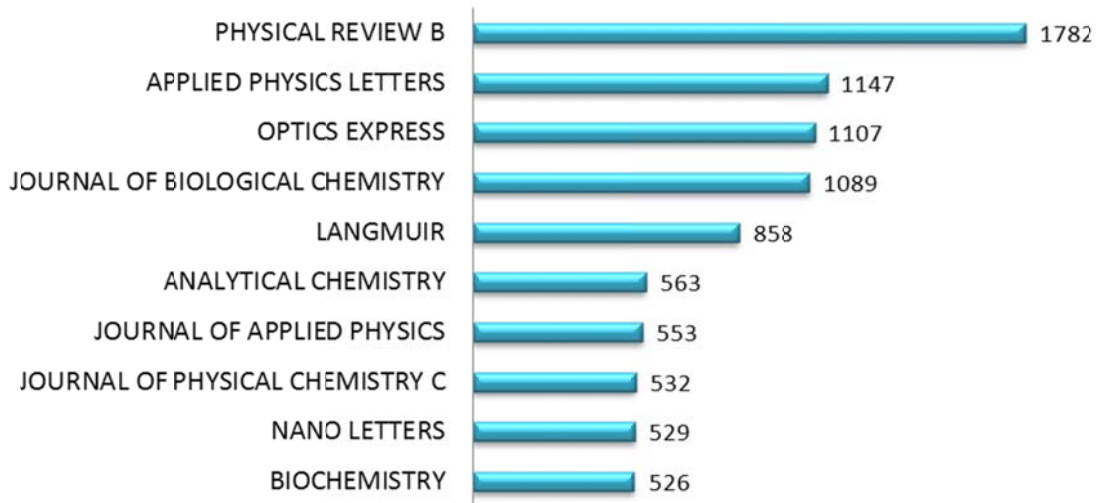


Figure 1-2 The journals that contain plasmonic related topics. (Obtained from Web of Science, Thomson Reuters on June 16, 2011. [7])

Research trends on the topic of plasmonics have been more focused on 1) physics principles of surface plasmons and the impact of surface geometries on the plasmon EM field[3,8,9,10]; 2) minimizing the device sizes, for example, the nanowire plasmonic laser[11] and the plasmon transistor[12,13]; 3) energy harvesting related applications, such as enhancing solar cell efficiency[14]; and 4) nano-particles with LSP effects, which include SERS[15,16] and fluorescent dye emission enhancement [17,18].

Our research interest is on fabricating periodic array nano-structures for surface plasmon excitation and developing novel sensor devices utilizing the unique physical properties of surface plasmon. Large area plasmonic crystal can simplify the optical alignment of devices. The commonly used fabrication method such as FIB milling usually preparing patterns with a

few hundred square micron in size. The cost of making each sample is also high. This research developed a self-assembly method using nanospheres to pattern gold films with low cost, and the area of the plasmonic crystals can reach tens of millimeters.

We are also specifically looking at devices that are enabled by this nano-structure. There is a multidiscipline research trend that applied plasmonic crystals in biology and medical studies. Bio-chemical sensing is an important type of plasmonic applications with lots of devices and methodologies developed. We characterized the sensitivity of the self-assembly gold film and utilized its enhanced EM field near the metal surface to make sensing and light modulation devices. The far field optical properties of the plasmonic crystal were also studied. The angle resolved spectra of the patterned gold films were measured using collimated light with different polarization states. A sun sensor and a wavefront sensor were developed based on the incident angle related momentum matching principle. The work in this dissertation covers the fundamental physics of surface plasmon and also optical devices realization based on those physics principles.

1.2 Dissertation Organization

The structure of the dissertation is as follows. Chapter 2 reviews the physics of surface plasmon and the dielectric model of metal. The dispersion relation of surface plasmon on a metal surface is the key to understand its optical behaviors. The Bloch modes of a 2D array are also discussed, which are related to momentum matching requirement for plasmon excitation.

Chapter 3 gives a brief review of the literatures related to the physical properties and novel applications of surface plasmons. The plasmonic crystal research started with the observation of extraordinary transmission effect. Its dispersion relation was studied by angle resolved spectra, and several novel devices such as plasmonic transistor and plasmon enhanced solar cell were developed.

Chapter 4 provides a description of the fabrication and characterization tools used in this study. A nanosphere self-assembly method was developed to prepare large area hexagonal symmetry plasmonic crystals with low cost. Nano-imprinting was also applied as an

alternative method to fabricate periodic arrays. Their surface geometry and the optical properties were characterized.

Chapter 5 discusses the surface dielectric environment dependency of the plasmonic crystals. Several chemicals were placed on top of the patterned gold film and the shifting in SPR peaks was studied. Temperature sensitive and photon sensitive materials were coated onto the plasmonic crystal surface. By modulating the dielectric constant of these materials, the plasmon resonance peaks of the thin metal films can be controlled.

Chapter 6 discusses the incident angle dependency of the plasmonic crystals. The tilted incident light provided a parallel surface component that changes the momentum matching condition, thus the degenerate plasmon modes were separated. An angle of arrival sensor was developed based on this principle. Applications for this sensor include tracking the movement of the sun or other collimated light sources such as laser beams.

Chapter 7 discusses the design of a wavefront sensor, which was also based on the incident angle dependency of the plasmonic crystals. Comparing to the traditional Shack-Hartmann wavefront sensor, the plasmonic crystal wavefront sensor was 2D in nature so that it had smaller form factor. It was constructed by an array of pixels, where each pixel had the similar structure of the angle of arrival sensor. An op-amp and an ADC were used to convert the photodiode current to a digital signal, and then a least squares algorithm was applied to fit the measurement result to a polynomial function.

Chapter 8 concludes this research by highlighting some of the important results presented and providing some suggestions for future work.

CHAPTER 2

PHYSICS OF SURFACE PLASMONS

This chapter introduces the excitation condition and the electrodynamics of surface plasmons. The physics of surface plasmons can be derived from Maxwell's equations with a suitable set of boundary conditions. The dielectric properties of metal are the key to understand the surface plasmons resonance behaviors. The Drude model is introduced to describe the free electron gas within a metal, thus the metal dielectric constant model can be derived. Excitation of surface plasmons requires special optical configuration due to the wavevector mismatch between photon and surface plasmon polaritons. The traditional prism coupling method and the novel plasmonic crystal coupling method are introduced.

2.1 Maxwell's Equation and Boundary Conditions

The Maxwell's equations are a set of four partial differential equations that form the foundation of classical electrodynamics. It is named after the Scottish physicist James Clerk Maxwell, since in an early form of these equations were published by him between 1861 and 1862. The Maxwell's equations describe how electric charges and currents act as sources for the electric and magnetic fields. It also describes how a time varying electric field interacts with a time varying magnetic field and vice versa. Under SI units, the Maxwell's equations are given as: [19]

$$\begin{aligned}\nabla \cdot \mathbf{D} &= \rho \\ \nabla \cdot \mathbf{B} &= 0 \\ \nabla \times \mathbf{E} &= -\frac{\partial \mathbf{B}}{\partial t} \\ \nabla \times \mathbf{H} &= \mathbf{J} + \frac{\partial \mathbf{D}}{\partial t}\end{aligned}$$

where the electric field \mathbf{E} (V/m) and magnetic field \mathbf{H} (A/m) are related to the electric displacement \mathbf{D} (C/m²) and the magnetic-flux density \mathbf{B} (Tesla). The relation between field and flux density is:

$$\begin{aligned}\mathbf{D} &= \epsilon\epsilon_0\mathbf{E} \\ \mathbf{B} &= \mu\mu_0\mathbf{H}\end{aligned}$$

where ϵ and ϵ_0 are the material dielectric constant and the electric permittivity of free space (8.854×10^{-12} F/m), μ and μ_0 are the material magnetic permeability and the magnetic permeability of free space ($4\pi \times 10^{-7}$ N/A²), respectively. And the Ohm's law for the relation between the current \mathbf{J} and the electric field \mathbf{E} in microscopic is:

$$\mathbf{J} = \sigma\mathbf{E}$$

If we assume that the medium is isotropy and free of charge, the wave equation for \mathbf{E} and \mathbf{H} can be derived as:

$$\begin{aligned}\nabla^2\mathbf{E} &= \sigma\mu\mu_0\frac{\partial\mathbf{E}}{\partial t} + \mu\mu_0\epsilon\epsilon_0\frac{\partial^2\mathbf{E}}{\partial t^2} \\ \nabla^2\mathbf{H} &= \sigma\mu\mu_0\frac{\partial\mathbf{H}}{\partial t} + \mu\mu_0\epsilon\epsilon_0\frac{\partial^2\mathbf{H}}{\partial t^2}\end{aligned}$$

In the case that the electric field has a plane wave form

$$\mathbf{E} = \mathbf{E}_0 \exp(i(\mathbf{k}\cdot\mathbf{r} - \omega t))$$

where \mathbf{k} is the direction of the wave propagation and its magnitude is:

$$k^2 = i\sigma\mu\mu_0\omega + \mu\mu_0\epsilon\epsilon_0\omega^2$$

In vacuum, $\epsilon=1, \mu=1, \sigma=0$, and $k = \omega/c$ then

$$c = \frac{1}{\sqrt{\mu_0\epsilon_0}}$$

The complex optical index \tilde{n} is

$$\begin{aligned}k &= \frac{2\pi}{\lambda} = \frac{\tilde{n}\omega}{c} \\ \tilde{n}^2 &= k^2 c^2 / \omega^2 = \mu\epsilon + i\frac{\sigma\mu}{\epsilon_0\omega}\end{aligned}$$

The optical index can be expressed as $\tilde{n} = n + i\kappa$, where n and κ are the real and imaginary part of the complex optical index, respectively. And the complex dielectric constant of a material is defined as:

$$\tilde{\epsilon} = \tilde{n}^2 = \epsilon_1 + i\epsilon_2$$

$$\text{with } \epsilon_1 = n^2 - \kappa^2, \epsilon_2 = 2n\kappa$$

The boundary condition between two medium 1 and 2 is given as:

$$\begin{aligned} \mathbf{n} \cdot [\mathbf{D}_1 - \mathbf{D}_2] &= \sigma_{12} \\ \mathbf{n} \cdot [\mathbf{B}_1 - \mathbf{B}_2] &= 0 \\ \mathbf{t} \cdot [\mathbf{E}_1 - \mathbf{E}_2] &= 0 \\ \mathbf{t} \cdot [\mathbf{H}_1 - \mathbf{H}_2] &= \mathbf{J}_s \end{aligned}$$

Solving the reflection and transmission field intensity at the interface between two mediums 1 and 2, we get the Fresnel equations of **the amplitude reflection coefficient** r and **amplitude transmission coefficient** t for s-polarized wave:

$$\begin{aligned} r_s &= \frac{n_1 \cos \theta_i - n_2 \cos \theta_t}{n_1 \cos \theta_i + n_2 \cos \theta_t} \\ t_s &= \frac{2n_1 \cos \theta_i}{n_1 \cos \theta_i + n_2 \cos \theta_t} \end{aligned}$$

and for p-polarized waves:

$$\begin{aligned} r_p &= \frac{-n_1 \cos \theta_t + n_2 \cos \theta_i}{n_1 \cos \theta_i + n_2 \cos \theta_t} \\ t_p &= \frac{2n_1 \cos \theta_i}{n_1 \cos \theta_i + n_2 \cos \theta_t} \end{aligned}$$

These four coefficients describe the intensity ratio of the electric field at the two sides of the interface. The fraction of power that has been reflection and transmission depends on the ratio of the squares of the amplitudes, which can be expressed as:

$$\begin{aligned} R &= r^2 \\ T &= \frac{n_2}{n_1} t^2 \end{aligned}$$

The four Fresnel equations describe the reflection/transmission properties of a two layer model. For a three layers dielectric (n_0)/metal (n_1)/dielectric (n_2) structure, the power reflection ratio is expressed as [20]

$$R(\theta) = \left| \frac{r_{01} + r_{12} \exp(2ik_{z1}d)}{1 + r_{01}r_{12} \exp(2ik_{z1}d)} \right|^2$$

where the reflectance coefficients r_{01} and r_{12} are calculated from the Fresnel equations above,

d is the thickness of the metal layer, and $k_{z1} = \frac{\omega}{c} \sqrt{n_1^2 - (n_0 \sin \theta_i)^2}$ is the normal component of

the wavevector of the light propagating in the metal. Simulation result of the reflectance at a silver covered glass surface ($n_{\text{glass}}=1.52$, $n_{\text{silver}}=-18+0.47i$, $n_{\text{air}}=1$, $d=40$ nm) is shown in Figure 2-1, while the light is incident from the glass side. The reflectance is around 80% for most incident angles, but it has a great dip at 41° . This dip is caused by the excitation of surface plasmon at the metal/air interface. This research will focus on the physical properties of the plasmonic effect, and its dispersion relation will be discussed later in this chapter.

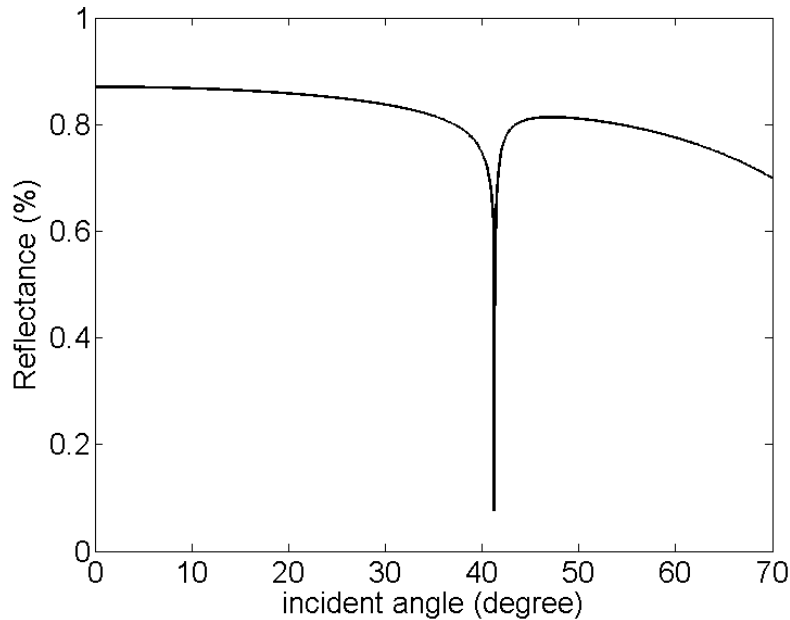


Figure 2-1 Reflectance of a glass/silver/air interface for different incident angles. The curve was calculated using the three layers reflection model. The position of the dip is sensitive to the local surface dielectric constant and is often used for sensing applications.

2.2 Dielectric Constant of Metal

During 1900s, Drude developed a model based on classical theory to describe the complex dielectric constant of materials, as well as their variations with the frequency of light.[19] The model is based on treating electrons as damped harmonically bound particles subject to external electric fields. This model explains the phenomena of normal and anomalous dispersion and their relation to the absorption of radiation. The classical parameters of the theory transform simply to their quantum analogs, so that the results remain valid in modern theories of materials science.

The restoration force of a bound charge can be expressed as:

$$F = -e\mathbf{E}(\omega) = m\ddot{\mathbf{r}}(\omega) + im\Gamma\dot{\mathbf{r}}(\omega) + m\omega_0^2\mathbf{r}(\omega)$$

where ω_0 is the natural frequency of the oscillator and Γ is the damping constant. For an incident electromagnetic field of frequency ω , the field at point \mathbf{r} can be represented by a complex exponential $\mathbf{E}_0 e^{-i\omega t}$. The steady-state solution is given by

$$\mathbf{r} = \frac{-e\mathbf{E}_0}{m} \frac{1}{\omega_0^2 - \omega^2 - i\Gamma\omega}$$

The macroscopic relation of the polarizability $\mathbf{P} = \epsilon_0\chi(\omega)\mathbf{E}$ is the summation of the electric dipole moment of the electron $\mathbf{p} = -e\mathbf{r}$, thus the complex electric susceptibility can be derived as

$$\chi(\omega) = \frac{Ne^2}{\epsilon_0 m} \frac{1}{\omega_0^2 - \omega^2 - i\Gamma\omega}$$

where N being the number of polarizable electrons per unit volume. The dielectric constant is $\epsilon = \epsilon_r\epsilon_0$ with

$$\epsilon_r(\omega) = 1 + \chi_1(\omega) = 1 + \frac{Ne^2}{\epsilon_0 m} \frac{1}{\omega_0^2 - \omega^2 - i\Gamma\omega}$$

We define the plasma frequency as $\omega_p = \sqrt{\frac{Ne^2}{\epsilon_0 m}}$, and the conduction band electrons in metal are not bound to atom so that $\omega_0 = 0$, then the Drude model for metal dispersion is

$$\epsilon_r(\omega) = 1 - \frac{\omega_p^2}{\omega^2 + i\Gamma\omega}$$

In metals, the damping effect is due to electron collisions at a rate of $\tau = 1/\Gamma$, so that the real and imaginary parts of the dielectric constant can be expressed as

$$\begin{aligned} \text{Re}(\epsilon_r(\omega)) &= 1 - \frac{\omega_p^2 \tau^2}{1 + \omega^2 \tau^2} \\ \text{Im}(\epsilon_r(\omega)) &= \frac{\omega_p^2 \tau}{\omega(1 + \omega^2 \tau^2)} \end{aligned}$$

Collision time in metals is $\sim 10^{-14}$ s, so that at optical frequencies $\omega^2 \tau^2 \gg 1$. In this high frequency limit,

$$\begin{aligned} \text{Re}(\epsilon_r(\omega)) &= 1 - \frac{\omega_p^2}{\omega^2} \\ \text{Im}(\epsilon_r(\omega)) &= \frac{\omega_p^2}{\omega^3 \tau^2} \end{aligned}$$

The real part of ϵ_r is negative and decreases with lower frequency (long wavelength), the imaginary part increases with lower frequency.

In the limit of low frequency region, the conductivity of metal can be derived from Drude model. Considering some fraction f_0 of the electrons per molecule is un-bounded at low frequency, the dielectric constant can be expressed as [19]

$$\epsilon(\omega) = \epsilon_b(\omega) + i \frac{Ne^2 f_0}{m\omega(\gamma_0 - i\omega)}$$

And insert $\mathbf{J} = \sigma \mathbf{E}$ into the Maxwell equation $\nabla \times \mathbf{H} = \mathbf{J} + \frac{d\mathbf{D}}{dt}$, it gives

$$\nabla \times \mathbf{H} = -i\omega \left(\epsilon_b + i \frac{\sigma}{\omega} \right) \mathbf{E}$$

Comparing this expression with the dielectric constant expression above yields an expression for the conductivity

$$\sigma = \frac{f_0 Ne^2}{m(\gamma_0 - i\omega)}$$

The conductivity is real and frequency independent from the DC to the microwave region ($\omega < 10^{11}$ 1/s) since γ_0 is usually $\sim 10^{13}$ 1/s. The skip depth is related to the conductivity, and

can be expressed as $\delta = \sqrt{\frac{2}{\mu\sigma\omega}}$. Beyond the infrared wavelength, the conductivity is

complex and varies with frequency. In optical wavelength, the dielectric constant of metal is more commonly used to describe the properties of the material.

In addition, the Lorentz-Drude (LD) model is a more general model for describing the optical properties of metals.[21,22,23] It is developed from the Drude mode, where some Lorentz terms are added to reflect the inter-band effects. The complex dielectric function $\epsilon_r(\omega)$ can be expressed as [24]

$$\epsilon_r(\omega) = \epsilon_r^{(f)}(\omega) + \epsilon_r^{(b)}(\omega)$$

where $\epsilon_r^{(f)}(\omega)$ represents the intra-band effects that is usually referred to as free-electron effects (Drude model), and $\epsilon_r^{(b)}(\omega)$ represents the inter-band effects that is usually referred to as bound-electron effects. These two parts have the form of:

$$\begin{aligned}\epsilon_r^{(f)}(\omega) &= 1 - \frac{\omega_p^2}{\omega^2 + i\Gamma\omega} \\ \epsilon_r^{(b)}(\omega) &= \sum_{j=1}^k \frac{f_j\omega_p^2}{(\omega_j^2 - \omega^2) + i\omega\Gamma_j}\end{aligned}$$

where ω_p is the plasma frequency, k is the number of oscillators with frequency ω_j , strength f_j and lifetime $1/\Gamma_f$. This model is widely used in FDTD simulation, and sometimes a constant term ϵ_∞ is added to describe the background dielectric.[21,25]

Johnson and Christy measured the complex index of refraction $\tilde{n} = n + ik$ for copper, silver and gold by collecting the reflection and transmission of light on vacuum evaporated thin films at room temperature.[26] The film thickness was 343 Å and the wavelength was measured from 193 nm to 2520 nm. The real and imaginary parts of gold dielectric were calculated from the measurement, as shown in Figure 2-2.

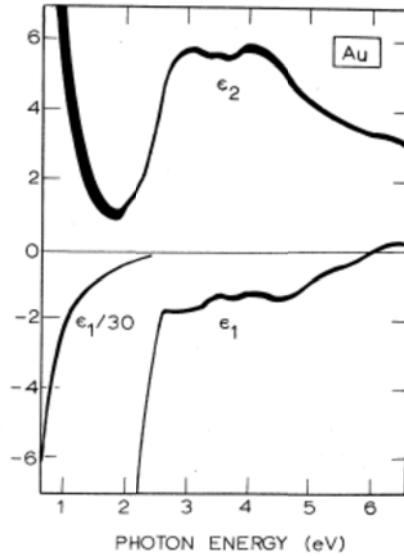


Figure 2-2 Dielectric constant for gold as a function of photon energy. ϵ_1 is the real part and ϵ_2 is the imaginary part of the gold dielectric ϵ_r . The width of the curves is representative of the instrumental error. [26]

The complex dielectric constant of metal leads to many sophisticated optical behaviors. One of the effects was demonstrated in the previous section when applying the Fresnel equations in the reflectance calculation. Qualitative analysis of gold dielectric constant ϵ_r indicates that the transmission rate of a gold film is larger between 400-600 nm wavelengths. The gold film fabricated in this research shows a transmission peak located at 500 nm and the peak position varies with film thickness and environment materials. This peak is caused by the D-band electron transition that can be described with one Lorentz term in the LD dielectric model.

Table 2-1 Plasmon frequency of several commonly used metals. [24]

Metal	Au	Ag	Cu	Al
$\hbar\omega_{SP}$ (eV)	9.03	9.01	10.83	14.98

Several metals can be used for plasmonic study. Gold is inert to most chemicals and do not have an oxidized layer on its surface, thus is widely chose for biology and chemical sensing applications where solvent and biology cells may be put on the metal surface. Other than this, silver, copper and aluminum are also commonly used in plasmon applications. Their plasmon frequencies are listed in Table 2-1. All these metals can be described with the LD model with different parameter values.[24] Gold and silver have relatively long plasmon decay length, so that surface plasmons can cover a larger area. On the other hand, aluminum and copper have large absorptivity thus the plasmon on them are more localized, which can be used to improve resolution in near field imaging.[27] The chemical stability is another consideration when choosing the metal for device fabrication. Silver is good for plasmon excitation and it does not have any inter-band transition frequency overlapped with the visible light wavelength, but it becomes oxidized in air and this oxidized layer may change the plasmon properties. Aluminum experiences the similar issue as silver. Considering all these factors, gold is adopted in this work for surface plasmon excitation.

2.3 Surface Plasmon Excitation

Plasmon is the quantum of the collective excitation of free electrons in solids. Surface plasmons are electron oscillations near a metal surface that stems from the broken translational invariance in the direction perpendicular to the surface. The charge oscillations are orthogonal to the surface plane and induce an evanescent electromagnetic field at the surface which is transverse magnetic. The coupling of surface plasmon with photon generates the propagating surface waves called surface plasmons polariton (SPP).

A schematic of a SPP propagating at the metal–dielectric interface is shown in Figure 2-3.[1] The field in the direction perpendicular to the surface is evanescent, reflecting the non-radiative nature of SPPs that prevents energy from propagating away from the surface. In the dielectric medium above the metal, typically air or glass, the decay length of the field is on the order of half the wavelength of the light, whereas the decay length into the metal is given by the skin depth. The dispersion relation of the SPPs shows that, if the SPPs are chosen to be the signal carrier, the strong sensitivity of their resonances to the surface structure and

environmental parameters could bring a possible solution to several near surface sensing and imaging applications. In this scheme, small changes induced in the refractive index of the dielectric material placed on top of the metal surface would significantly influence the surface plasmon resonance condition.

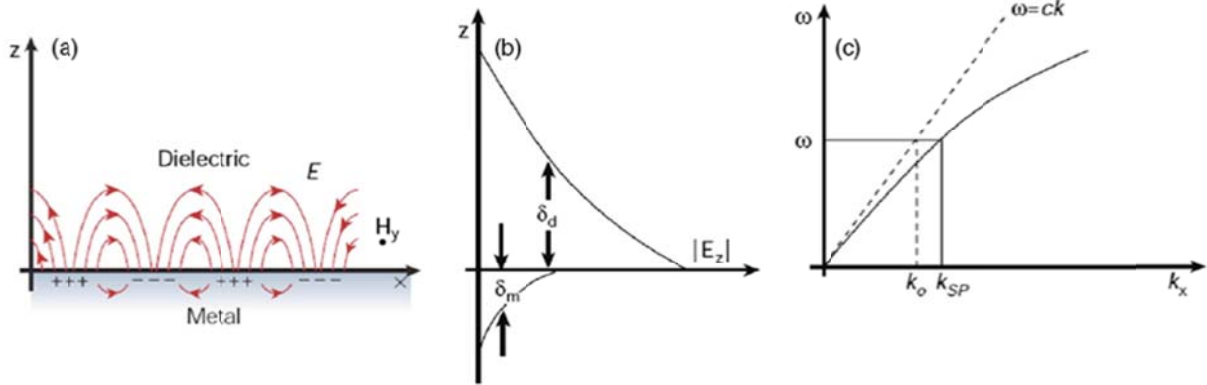


Figure 2-3 Physics principles of surface plasmon. (a) The surface plasmons polariton scheme; (b) the E_z field extension length on the two sides of the surface; (c) the dispersion relations of surface plasmons and free space photon, which show that the wavevector of SPP is always larger than a photon with the same frequency.[1]

2.3.1 Dispersion Relation

We consider a metal (medium 1) / air (medium 2) surface where the p-polarized electric fields are coupled on both sides of the interface. The dispersion relation of surface plasmons can be derived from the Maxwell equations with proper boundary conditions, and it can provide much understood about the coupling between photon and surface plasmons.

In medium 2 (air, $z > 0$), it has a pure imaginary k_{z2} so that the electric and magnetic field can be given by

$$\mathbf{E}_2 = \begin{pmatrix} \mathbf{E}_{x2} \\ 0 \\ \mathbf{E}_{z2} \end{pmatrix} e^{i(k_{x2}x + k_{z2}z - \omega t)}$$

$$\mathbf{H}_2 = \begin{pmatrix} 0 \\ \mathbf{H}_{y2} \\ 0 \end{pmatrix} e^{i(k_{x2}x + k_{z2}z - \omega t)}$$

Using a pure imaginary k_{z1} , the electric and magnetic field in medium 1 (metal, $z < 0$) can be given by

$$\mathbf{E}_1 = \begin{pmatrix} \mathbf{E}_{x1} \\ 0 \\ \mathbf{E}_{z1} \end{pmatrix} e^{i(k_{x1}x - k_{z1}z - \omega t)}$$

$$\mathbf{H}_1 = \begin{pmatrix} 0 \\ \mathbf{H}_{y1} \\ 0 \end{pmatrix} e^{i(k_{x1}x - k_{z1}z - \omega t)}$$

From $\mathbf{t} \cdot [\mathbf{E}_1 - \mathbf{E}_2] = 0$, we can get

$$k_{x1} = k_{x2} = k_x$$

$$E_{x1} = E_{x2}$$

$$E_{z1} = E_{z2}$$

From $\mathbf{t} \cdot [\mathbf{H}_1 - \mathbf{H}_2] = \mathbf{J}_s$ and assume $J_{s,y} \approx 0$

$$H_{y1} = H_{y2}$$

From $\mathbf{n} \cdot [\mathbf{D}_1 - \mathbf{D}_2] = \sigma_{12}$ and assume $\sigma_{12}(k_x, \omega) \ll D_{1z}, D_{2z}$

$$\tilde{\epsilon}_1 \epsilon_0 E_{z1} = \tilde{\epsilon}_2 \epsilon_0 E_{z2}$$

From $\nabla \times \mathbf{H} = \mathbf{J} + \frac{\partial \mathbf{D}}{\partial t}$ and $\mathbf{J} \approx 0$

$$\nabla \times \mathbf{H} = -i \frac{\partial}{\partial z} H_{yi} + k \frac{\partial}{\partial x} H_{yi} = \frac{\partial \mathbf{D}}{\partial t} \quad i=1, 2$$

For medium 1 and 2, we can get

$$ik_{z1} H_{y1} = -i\omega \epsilon_0 \tilde{\epsilon}_1 E_{x1}$$

$$-ik_{z2} H_{y2} = -i\omega \epsilon_0 \tilde{\epsilon}_2 E_{x2}$$

Because $E_{x1} = E_{x2}$ then

$$\frac{k_{z1}}{\omega \epsilon_0 \tilde{\epsilon}_1} H_{y1} + \frac{k_{z2}}{\omega \epsilon_0 \tilde{\epsilon}_2} H_{y2} = 0$$

Because $H_{y1} = H_{y2}$

$$\frac{k_{z1}}{\tilde{\epsilon}_1} + \frac{k_{z2}}{\tilde{\epsilon}_2} = 0$$

From the dispersion relations $k^2 = k_x^2 + k_{zi}^2 = \tilde{\epsilon}_i \left(\frac{\omega}{c} \right)^2$, $i=1,2$, k_x in the two mediums are

$$\begin{aligned} k_x^2 &= \tilde{\epsilon}_1 \left(\frac{\omega}{c} \right)^2 - k_{z1}^2 \\ k_x^2 &= \tilde{\epsilon}_2 \left(\frac{\omega}{c} \right)^2 - k_{z2}^2 \\ &= \tilde{\epsilon}_2 \left(\frac{\omega}{c} \right)^2 - \left(-\frac{\tilde{\epsilon}_2}{\tilde{\epsilon}_1} k_{z1} \right)^2 \end{aligned}$$

Using the above two equations and solve for k_x , we can get

$$k_x = \frac{\omega}{c} \sqrt{\frac{\tilde{\epsilon}_1 \tilde{\epsilon}_2}{\tilde{\epsilon}_1 + \tilde{\epsilon}_2}}$$

Since medium 1 is metal and medium 2 is air, $\tilde{\epsilon}_1 = \epsilon_1' + i\epsilon_1''$, $\tilde{\epsilon}_2 = \epsilon_2$

$$\begin{aligned} k_x &= \frac{\omega}{c} \sqrt{\frac{(\epsilon_1' + i\epsilon_1'')\epsilon_2}{\epsilon_1' + i\epsilon_1'' + \epsilon_2}} \\ &= \frac{\omega}{c} \sqrt{\epsilon_2 \frac{\epsilon_1'(\epsilon_1' + \epsilon_2) + \epsilon_1''^2 + i\epsilon_1''\epsilon_2}{(\epsilon_1' + \epsilon_2)^2 + \epsilon_1''^2}} \end{aligned}$$

If we assume $\epsilon_1'' < |\epsilon_1'|$

$$\begin{aligned} \text{Re}(k_x) &= \frac{\omega}{c} \sqrt{\frac{\epsilon_1' \epsilon_2}{\epsilon_1' + \epsilon_2}} \\ \text{Im}(k_x) &= \frac{\omega}{c} \left(\frac{\epsilon_1' \epsilon_2}{\epsilon_1' + \epsilon_2} \right)^{3/2} \frac{\epsilon_1''}{2 \epsilon_1'^2} \end{aligned}$$

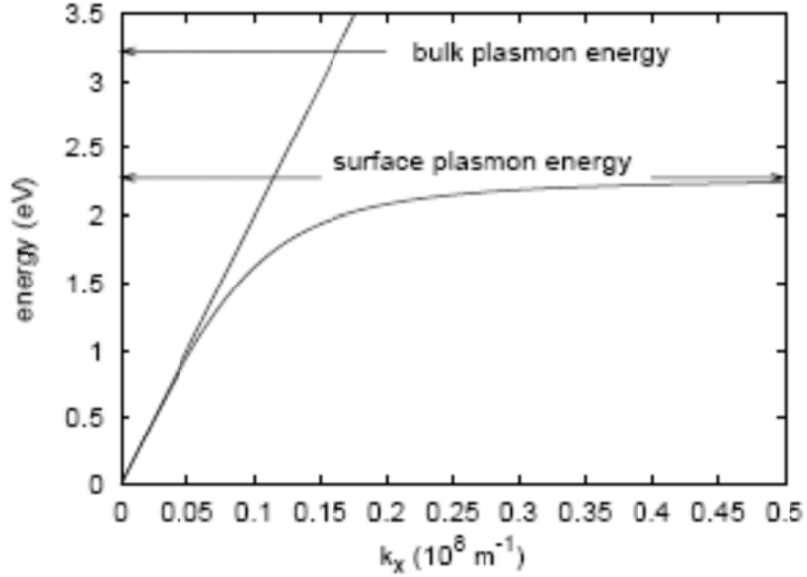


Figure 2-4 Surface plasmon dispersion $\omega(k_x)$ on a gold surface. The straight line shows the light line $k_x = \sqrt{\epsilon_2} \omega / c$. The surface plasmon frequency ω_{sp} is lower than the bulk plasma frequency ω_p .

Usually, the real part of k_x is used in discussing the plasmon dispersion, since it represents the propagation portion of the surface plasmon. The SPP dispersion relation $k_x(\omega)$ is plotted in Figure 2-4. It becomes close to the light line $\sqrt{\epsilon_2} \omega / c$ at small k_x , because at the limit of $\omega \rightarrow 0$, it has $|\epsilon'_1| \gg \epsilon_2$. At high frequency, the denominator $\epsilon'_1 + \epsilon_2$ become zero at some ω_{sp} so that $k_x \rightarrow \infty$. For a simple metal model, the dielectric constant can be described with the Drude model only, so that the real part of the dielectric constant is

$$\epsilon'_1(\omega) = 1 - \frac{\omega_p^2}{\omega^2}$$

Solving for $\epsilon'_1(\omega_{sp}) + \epsilon_2 = 0$, the surface plasmon frequency ω_{sp} can be obtained as

$$\omega_{sp} = \omega_p \frac{1}{\sqrt{1 + \epsilon_2}}$$

This equation gives the maximum frequency for surface plasmon excitation. When the incident photon is close to this frequency from the lower side, coupling the photon into SPP becomes more and more difficult, because the wavevector mismatch is very large. The slope of the dispersion curve $\Delta\omega/\Delta k$ is almost zero when $\omega \rightarrow \omega_{sp}$. Usually, the resonance wavelength is the observable variable in experiments. Thus, at this limit, the resonance wavelength changes will be hard to detect if there is any change in wavevector. In other words, a long operation wavelength should be used in order to improve the sensitivity in normal plasmon applications, and its upper limit is $\Delta\omega/\Delta k = c$ where the point on the curve is close to the origin.

2.3.2 Plasmon Decay Length

The surface plasmon decay in x-direction can be evaluated from $\text{Im}(k_x)$ because the field intensity decreased as $\exp[-2\text{Im}(k_x)x]$. The decay length L_{12} can be obtained as

$$L_{12} = [2\text{Im}(k_x)]^{-1} = \frac{c}{\omega} \left(\frac{\epsilon_1' \epsilon_2}{\epsilon_1' + \epsilon_2} \right)^{-3/2} \frac{\epsilon_1'^2}{\epsilon_1''}$$

The decay length of surface plasmon is wavelength dependent. In the visible and NIR wavelength region, it is around 10-100 μm for silver and gold films.[28,29] Experimental data shows that the decay lengths for surface plasmons on gold and silver film are increasing with wavelength. Silver has longer decay length because its conductivity is relatively large. The results are shown in Figure 2-5.[30] This trend matches the decay length equation above, because the value of the dielectric's real part increases very quick so that the $\epsilon_1'^2 / \epsilon_1''$ term become larger. It is the dominant term in the expression, thus causes a longer the decay length at large wavelength. The decay length for a gold film was calculated. It is $\sim 6 \mu\text{m}$ for water/gold interface and $\sim 16 \mu\text{m}$ for air/gold interface at the red light wavelength.

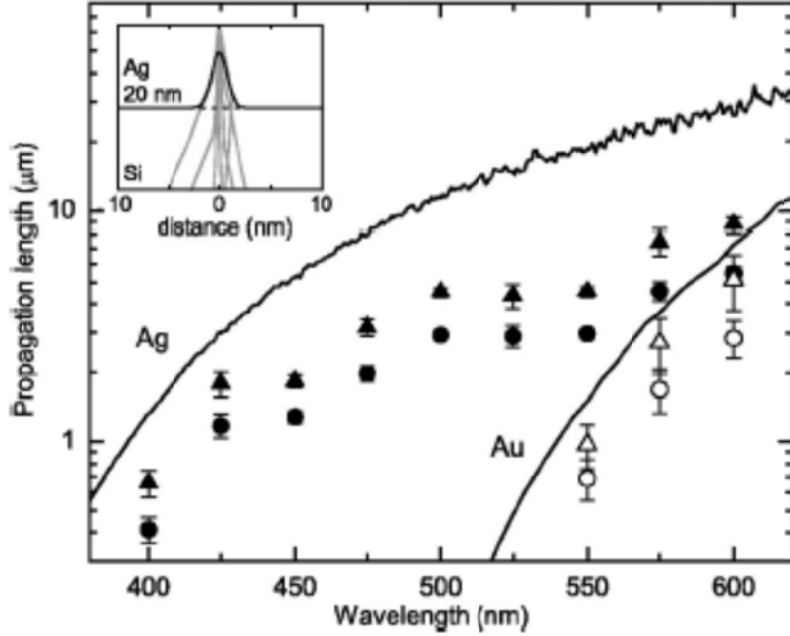


Figure 2-5 SPP propagation length measured by CL imaging spectroscopy for 400 nm thick gold and silver films. The dots were from experimental data, and the drawn lines were calculated using the dielectric constant. [30]

2.3.3 Skin Depth

The skin depth of the EM field at the interface is defined as the penetration distance into the material at which the electric field drops to $1/e$. [31] The field of SPPs decay away from the interface exponentially in both sides. The wavevectors in z direction are given as

$$k_{zi}^2 = \tilde{\epsilon}_i \left(\frac{\omega}{c} \right)^2 - k_{xi}^2, \quad i=1,2$$

Since $k_{x1} = k_{x2} = k_{SP}$, the wavevector for the two interfaces are

$$k_{z1} = \frac{\omega}{c} \sqrt{\frac{\epsilon_1^2}{\epsilon_1 + \epsilon_2}}$$

$$k_{z2} = \frac{\omega}{c} \sqrt{\frac{\epsilon_2^2}{\epsilon_1 + \epsilon_2}}$$

At long wavelength, $|\epsilon_1'| \gg \epsilon_1'', \epsilon_2$, so that

$$k_{z1} = \frac{\omega}{c} \sqrt{\epsilon'_1}$$

$$k_{z2} = \frac{\omega}{c} \frac{\epsilon_2}{\sqrt{\epsilon'_1}}$$

Because $\epsilon'_1 < 0$, both of the wavevectors above are purely imaginary. The skin depth is related to the attenuation of the field, which is

$$\delta_1 = \frac{1}{\text{Im}(k_{z1})} = \frac{c}{\omega} \frac{1}{\sqrt{|\epsilon'_1|}}$$

$$\delta_2 = \frac{1}{\text{Im}(k_{z2})} = \frac{c}{\omega} \frac{\sqrt{|\epsilon'_1|}}{\epsilon_2}$$

The metal side skin depth δ_1 is small because its denominator is large in the equation above. The second equation shows that the skin depth at the dielectric side is relatively large. For a gold/air interface, $\delta_1 \sim 30 \text{ nm}$ and $\delta_2 \sim 200 \text{ nm}$ at 600-700 nm wavelength, thus the field is concentrated at the dielectric side of the interface.

Metal thin films are used for surface plasmons excitation, which has two interfaces that are a few tens of nanometers apart from each other. For example, the Kretschmann configuration uses a glass/gold/air three layer structure for surface plasmons excitation at the gold/air interface. If the device is used for chemical sensing, air is replaced by water or some other chemicals. Another widely used structure is the symmetrical dielectric/metal/dielectric structure, where the dielectric material can be SiO_2 or some other optical transparent materials. A plasmonic waveguide was built with this $\text{SiO}_2/\text{Au}/\text{SiO}_2$ structure.[32] The surface plasmons dispersion relations at the two interfaces of this structure are the same, so that the surface plasmons excited on one interface can be easily coupled to the other side. If the gold layer thickness is smaller than twice of the surface plasmons skin depth in the metal, the electric field on the two interfaces will couple together. For a symmetry dielectric configuration, the modes on the two interfaces are degenerate thus will split into a symmetry low frequency mode and an anti-symmetry high frequency mode. [6]

2.4 Periodic Array for Surface Plasmon Coupling

In order to excite SPP by light incident on a metal surface, the frequency of the incident light must equal to the frequency of the SPP, and the parallel surface component of the wavevector k_x must be the same for the incident light and the SPP. The first condition can be easily satisfied. However, the dispersion curve of the SPP always lies to the right of the light line, which means that the SPP has greater momentum than a free space photon of the same frequency. Because of this momentum mismatch, the SPP cannot be directly coupled with the incident plane-wave light. Special optical arrangements have been designed to provide the necessary wavevector conservation. Two main wavevector matching methods are used to couple photons into the SPP modes. The first method consists of increasing the momentum of the photon by using high refractive index materials and a specific optical configuration. The second technique breaks the translational invariance of a smooth metallic surface through corrugated or roughened structures.

With a flat metal surface, SPP on the front side of a metallic film can be excited by light from the rear side using the Kretschmann configuration[6], as shown in Figure 2-6. The refractive index of the material on the rear side is higher than the one on the front side, thus the in-plane wavevector of the incoming light $k_{\parallel} = n_g k_0 \sin \theta_0$ matches the SPP dispersion relation. The surface plasmon resonance occurs at the minimum of the reflection intensity. This effect can be calculated with the Fresnel equation, which was demonstrated in the previous section.

Patterning the metallic surface with a periodic wavelength scale corrugation provides an alternative solution to the momentum matching issue between the SPP modes and the incoming light. In 1998, Ebbesen *et al* discovered the extraordinary optical transmission effect for a silver film with nano-holes array patterns and this effect was explained by the excitation of surface plasmons on the periodic surface structure.[5] Breaking the translational invariance of the thin film allows one to relax the momentum conservation restriction.

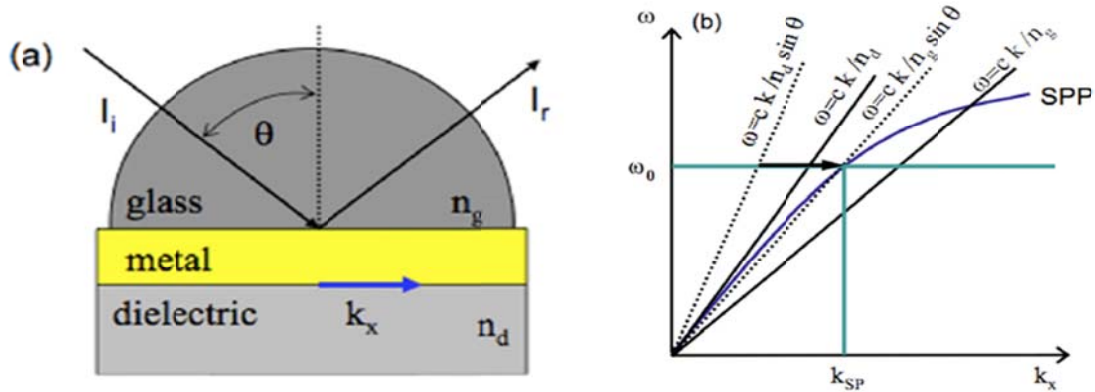


Figure 2-6 The Kretschmann configuration (left) and its surface momentum matching mechanism (right) for exciting SPR on a flat metal film.

2.4.1 Metal Grating

Grating structures on a metal thin film provide momentum matching between the SPP and the incoming photon, thus the SPP modes can be excited with normal incident light at certain frequencies. This greatly simplifies the optical configuration for SPP coupling. Both 1D and 2D gratings are studied by several groups for SPP excitation.[33,34,35] Near surface SPP field and the zero-order transmission spectra are the major techniques used to characterize the devices. The surface plasmon was excited with an infrared laser, thus it has a longer propagation length comparing to the visible light frequency surface plasmon. The plasmon field distribution was studied, as shown in Figure 2-7.



Figure 2-7 Near field image of surface plasmon on a 1D gold grating. (a) Optical microscope picture of the SPP grating. SPP is excited at the launch pad at the left with a 1500 nm wavelength pulsed laser and propagated via an entrance guide to the 55 μm long Bragg grating with 750 nm period. (b) Experimentally measured SPP field amplitude. [33]

These grating structures provide a momentum that can be added to the parallel surface component of the incoming photon, thus the total momentum is the same for photon and SPP, thus the momentum matching condition is satisfied. For a 1D grating of period a , the periodic structure provides a momentum $G_B = 2\pi / a$ which is the Bragg wavevector of the grating. The momentum conservation is now given by $k_{SP} = k_{\parallel, photon} + nG_B$ where the integer n labels the order of the reciprocal lattice. All the momentum is lies in the plane of the metal surface and perpendicular to the grating slits.

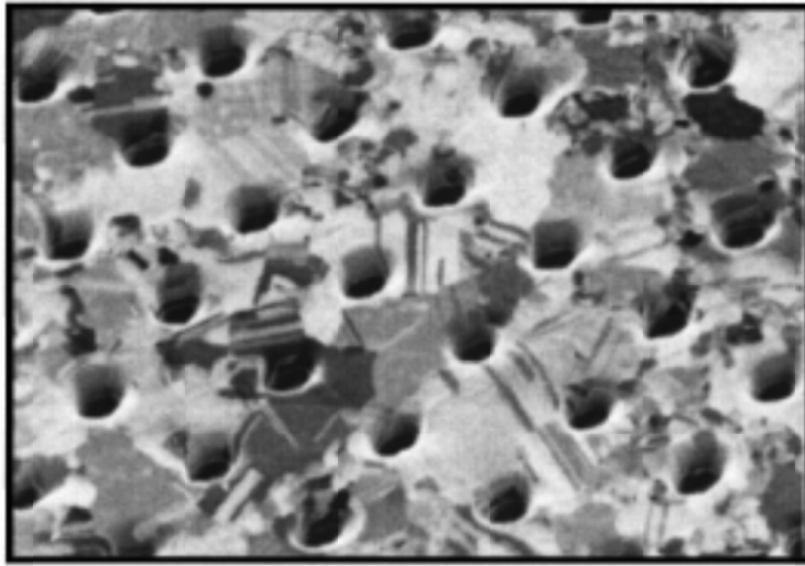


Figure 2-8 SEM image of a Focused Ion Beam prepared 2D holes array in a polycrystalline silver film. The film thickness $t=200$ nm, hole diameter $d=150$ nm and period $a=900$ nm.[36]

For a 2D rectangular lattice (Figure 2-8), the conservation of momentum is given as

$$\mathbf{k}_{SP} = \mathbf{k}_{\parallel, photon} + i\mathbf{G}_x + j\mathbf{G}_y$$

where \mathbf{G}_x , \mathbf{G}_y are the reciprocal lattice vectors and i and j are integers which label the order of the reciprocal lattices. This momentum matching equation is a vector equation where \mathbf{G}_x , \mathbf{G}_y are perpendicular to each other for a rectangular lattice. For a square lattice with

$|\mathbf{G}_x| = |\mathbf{G}_y| = 2\pi/a_0$ and the incoming light is normally incident ($\theta=0$), the momentum matching condition can be written as

$$k_{SP} = \frac{\omega}{c} \sqrt{\frac{\epsilon'_1 \epsilon_2}{\epsilon'_1 + \epsilon_2}} = \frac{2\pi}{a_0} \sqrt{i^2 + j^2}$$

Thus the surface plasmon resonance wavelength is given as

$$\lambda_{SP} = \frac{a_0}{\sqrt{i^2 + j^2}} \sqrt{\frac{\epsilon'_1 \epsilon_2}{\epsilon'_1 + \epsilon_2}}$$

The peak position corresponding to selected value sets of (i, j) and are different for the surface plasmons on the two interfaces of a metal thin film. The material dielectric constant is $\epsilon_2 = 1.5$ for the SPP at the glass substrate side and is $\epsilon_2 = 1$ for the top side where air is above the surface. The first few orders of the SPP modes $(\pm 1, 0)$ $(0, \pm 1)$ $(\pm 1, \pm 1)$ has stronger intensity and their dispersion relation is studied by changing the incident light angle.[36] The periodicity a_0 determines the wavelength of the first order SPP resonance. Usually, it is set to 500-700 nm for gold film nano-arrays that operates at visible light region, so that the SPP peaks are not overlapped with the gold bulk plasma peak at 500 nm.

Rectangular and hexagonal lattice are the most commonly used periodic pattern for wavevector matching.[3] Hexagonal symmetry lattices can be fabricated by self-assembly technique or imprinting technique, and they have similar momentum matching mechanism for exciting SPP on their surface. With e-beam lithography technique, special surface geometries, such as non-symmetry rectangular lattices and point defect structures, have been studied and their optical transmission spectra show directional dependency with the surface geometry.[37]

2.4.2 Dielectric Grating

Other than patterning a metal thin film with grating structures to provide the additional momentum for SPP excitation, fabricating a periodic dielectric layer on top of a flat metal film can also generate surface plasmon enhanced transmission effect. PMMA films with

periodic nano-structures were covered on gold and ITO films to demonstrate this effect.[38,39] These experiments indicate that the excitation of surface plasmons is associated with the periodicity changing in dielectric constant at the interface between a metal and an insulator. Dielectric grating provides an alternative way to exciting SPPs without patterning the metal film, which may simplify the process and reduce fabrication cost. Dielectric patterns are usually easy to fabricated, for example, the PMMA grating can be made by nano-imprint or e-beam writing.

In an argument for the physical reason of the enhanced transmission, Igor I. Smolyaninov *et al* prepared a device constructed by a PMMA(100 nm)/Gold(50 nm)/glass structure and the PMMA layer was patterned by square grating using e-beam lithography, as shown in Figure 2-9a.[38] The grating period is 500 nm. The gold film under the PMMA layer was intact after the grating was developed. With 532 nm laser light illumination, the area of the gold film above which the PMMA grating has been formed exhibited the effect of extraordinary optical transmission. In comparison, a gold film with 200 nm diameter nanoholes array of the same periodicity was illuminated at normal direction with the same laser power. The two samples were similar in brightness at the patterned areas, as shown in Figure 2-9b,c.

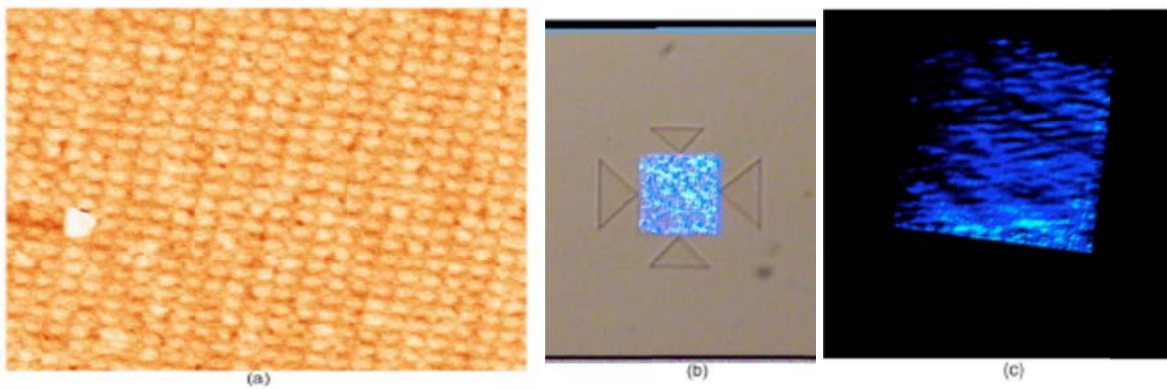


Figure 2-9 Enhanced transmission effect on a 2D dielectric grating. (a) An AFM image of the PMMA square grating on a flat gold film (50 nm); (b) Enhanced transmission for a PMMA pattern illuminated by a 532 nm normal incident laser; (c) enhanced transmission for a nanoholes patterned gold film.[38]

Another work from Yu-Ju Hung *et al* demonstrated that PMMA 1D-grating on both ITO and gold flat film can increase R6D fluorescence emission by enhancing the near surface EM field with surface plasmons.[37] The R6D dye was spin-coated onto the 500 nm periodicity PMMA gratings that were patterned by e-beam lithography, the devices schematic were shown in Figure 2-10. Two kinds of substrates were used: an ITO/glass and a gold/glass substrates. The PMMA layer was 40 nm thick and the gold layer was 50 nm thick. The R6D dye on the patterned PMMA layer showed enhanced fluorescence emission for both substrates and the emission was 10 times stronger for gold/glass substrate comparing to ITO/glass substrate. For the flat PMMA region surrounding the patterns, dye emission was just barely detectable, as shown in Figure 2-11. This result shows that a patterned dielectric layer on top of a conductive film can also excite SPP on its surface.

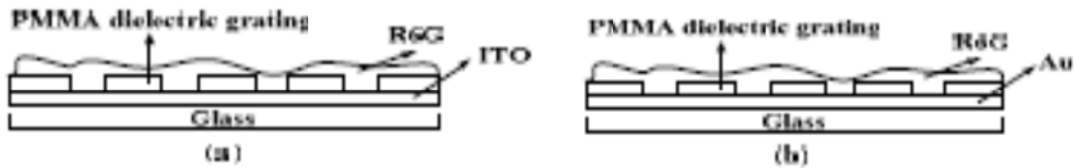


Figure 2-10 Devices structures for R6D /PMMA grating on (a) ITO/glass; (b) Au/glass.[37]

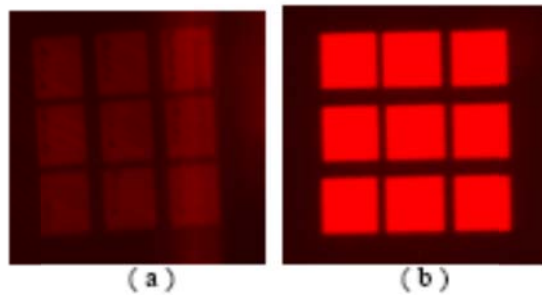


Figure 2-11 The intensity comparison of R6D/PMMA gratings on (a) ITO/glass substrate; (b) Au/glass substrate.[37]

2.5 Localized Surface Plasmon

Different from the surface plasmon polaritons at a planar dielectric–metal interface, localized surface electromagnetic excitations can exist in nanometer size conductive structures, such as metallic particles or voids of various topologies. Such surface excitations in bounded geometries are called localized surface plasmons (LSP).[6,40,41,42] The frequency of a LSP can be determined by the non-retarded (electrostatic) approximation. The electrostatic approximation is valid if the characteristic size a of a system is small compared to the photon wavelength λ corresponding to the LSP frequency ($a \ll \lambda$). For small metal particles, only the dipole-active excitation is important. As the size of the particle increases, the contributions from higher multipoles become more and more significant. In the limit of very large particles ($R \rightarrow \infty$), the LSP frequency become the same as the surface plasmons at a planar dielectric-metal interface. Multiple LSP modes may exist for an irregular shape metal particle, for example, an ellipsoidal particle has three sets of LSP frequencies related to the three axes of the ellipsoid. The range of frequencies where LSP modes exist is bounded from above by the flat film surface plasmons frequency of the metal.

Localized surface plasmons are a different type of excitation than the surface plasmon polaritons discussed before. A surface plasmon polariton is a propagating surface mode with the dispersion relation $\omega_{sp} = \omega(k_{sp})$. In contrast, LSP are confined to curved metal objects. They are characterized by discrete frequencies that depend on the size and shape of the object to which the surface plasmon is confined and also the environment dielectric function. Localized surface plasmons can be resonantly excited with light of appropriate frequency irrespective of the wavevector of the exciting light. In contrast, an SPP mode can be excited only if both the frequency and wavevector of the exciting light and the SPP mode are matched. LSP can be excited within the features on a metal surface, nano-holes and nano-bumps for example. The LSP and SPP interact when their frequency are close. LSP can decay into SPP and, in turn, can be excited by SPP. This results in a significant enhancement of SPP scattering by surface defects if the frequency of SPP and the resonant frequency of

LSP are close to each other.[43] On the other hand, SPP excitation is an efficient channel of LSP decay on a metal surface. [44]

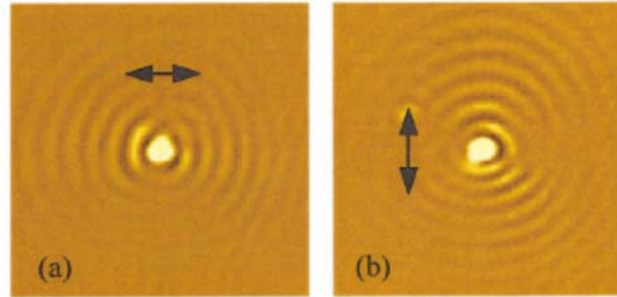


Figure 2-12 Near-field optical images with normal incident light on an isolated nano-hole in a gold film: (a) horizontal and (b) vertical polarization.[45]

The coupling between SPP and LSP for a single nano-hole in a gold film was reported by L. Yin *et al.*[45] The near-field scanning optical microscopy (NSOM) image of an isolated 200 nm diameter nano-hole in a 100 nm thick gold film was collected to demonstrate the excitation of SPP from LSP, as shown in Figure 2-12. The nano-hole was illuminated by a 532 nm laser beam with two perpendicular polarization, and the near field intensity was measured using Al-coated fiber probes with 50-80 nm apertures operating ~5 nm above the sample. The maximum field intensity was over the hole where the LSP was excited. At the edge of the hole, the LSP is radiated as a dipole and excited SPP within the direction of the polarization. Lobes of enhanced intensity extend over several microns with the period around 475 nm, which is significantly shorter than the incident wavelength. This period matches the SPP wavelength at a flat air/gold interface, $\lambda_{SP} = \lambda_i \sqrt{(\epsilon'_m + 1) / \epsilon'_m} = 471 \text{ nm}$ for incident light $\lambda_i = 532 \text{ nm}$ and gold dielectric constant is $\epsilon_m = 4.67 + i2.42$.

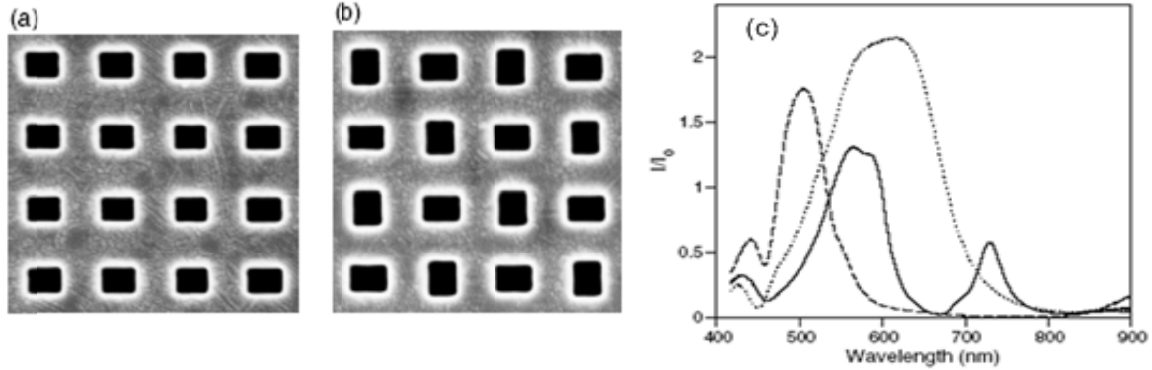


Figure 2-13 Impact of the LSP on the metallic 2D arrays transmission spectra. (a) SEM micrograph images for rectangular holes (a) all in one direction; (b) with alternating directions. (c) Spectra for (solid) alternating holes, (dashed) input polarization perpendicular to the short edge, (dotted) input polarization perpendicular to the long edge.[37]

The spectrum of LSP associated with an ensemble of metallic particles is determined by the interaction between the individual LSP resonances. The resulting spectrum and the magnitude of the electromagnetic field enhancement depend significantly on the shape and the size of the individual particles and on the distance between them. Degiron *et al.* fabricated rectangular nano-holes array with different arrangements to demonstrate the role of LSP in the enhanced optical transmission effect.[37] The nano-holes are 260 nm x 200 nm with a period of 400 nm and are fabricated on a 400 nm silver film, as shown in Figure 2-13a,b. The transmission spectra for two perpendicular polarizations were collected. By changing the surface periodicity, it was observed that the LSP peak was only visible when its frequency significantly overlapped with an SPP frequency, thus the LSP can couple into SPP and generate enhanced transmission effect.

Nanosphere arrays were used as mask to fabricate triangular and circular silver nanoparticles with different size. Amanda J. Haes *et al* measured the optical properties of these nano-particles that were related to LSP excitation.[46] The transmission spectrum were recorded with an un-polarized light over the visible wavelength region, as shown in Figure 2-14. From the spectra we can find that the LSP wavelengths were increased with larger

particle width for the same shape, and the height of the particle slightly change the resonance wavelength. By tuning the geometry parameter of the particle, its LSP resonance wavelength can cover the whole visible light region.

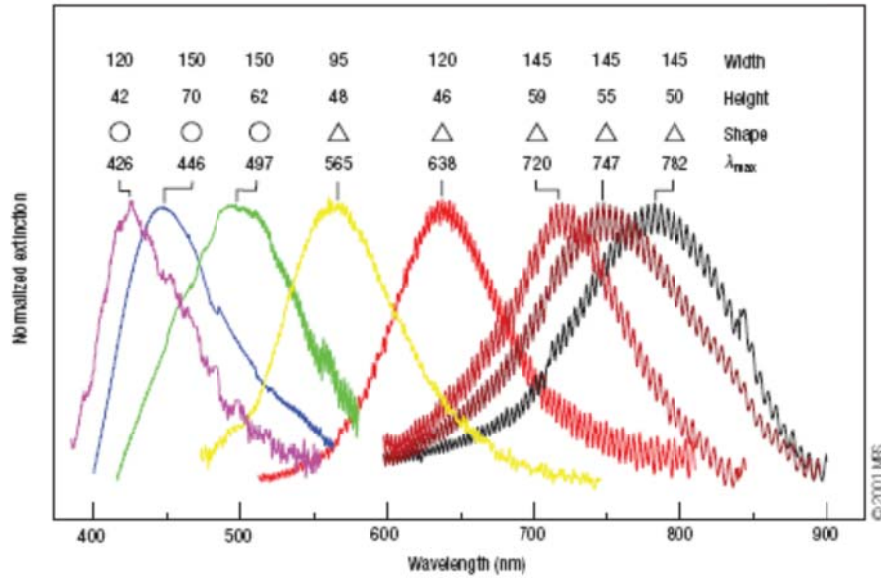


Figure 2-14 Effect of size and shape on LSP excitation for silver nano-particles formed by nanosphere lithography.[18]

CHAPTER 3

REVIEW OF RECENT PLASMONIC CRYSTAL RESEARCH

This chapter reviews the history and recent developments in surface plasmon research, where periodic nano-holes or other nano-structures are used. While there has been significant work concerning surface plasmons since the 1950's, the observation of extraordinary transmission on nanohole arrays patterned metal films in 1998 started the decade long research efforts on plasmonic crystal theory and applications. The primary difference between earlier research and recent work is the understanding that structuring the metal films on length scales similar to the wavelength of the surface plasmon and of the incident light wave enables one to manipulate light and plasmons in sub-wavelength scale. Many metal thin film structures have been tested and most of their applications were focused on sensing and imaging applications. Surface plasmon enhanced fluorescence is one of the important fields which can provide sub-wavelength resolution and selective labeling. The dispersion relation of the devices is explored by angular resolved spectra studies and FDTD field simulation. Novel surface plasmon application such as plasmonic switch for computation, plasmonic laser, plasmon enhanced solar energy harvesting, and plasmon color filter are demonstrated.

In 1902, Wood observed the presence of unexpected narrow bright and dark bands in the spectrum of an optical reflection grating illuminated by a light source with smoothly varying spectral intensity distribution.[47] Since this effect cannot be explained by ordinary grating theory, it was called Wood's Anomalies on optical gratings. The first theoretical explanation of this effect was given by Rayleigh in 1907. His theory correctly predicted the major features in the spectra, however, it was based on a "scattered EM field" assumption and has some limitation. For years, new theoretical approaches were given, but they failed to solve the problem until research on surface plasmons gives new insight into the issues.

The phenomenon of surface plasmons was systematically studied by Raether in the 1980s.[48] The excitation and propagation condition of surface plasmons on a flat metal film

were well understood. Kretschmann and Otto geometry were the commonly used methods to excite surface plasmon, as shown in Figure 3-1.[6] In the early 90s, new tools and methods were developed including near-field optical scanning microscopy[49,50], metallic nanoparticles with SPR effect[51,52,53], and surface enhanced Raman scattering[54]. Plasmonic crystal research was started around 1998, when the enhanced transmission effect was observed and explained by coupling between surface plasmon and the incident photon.

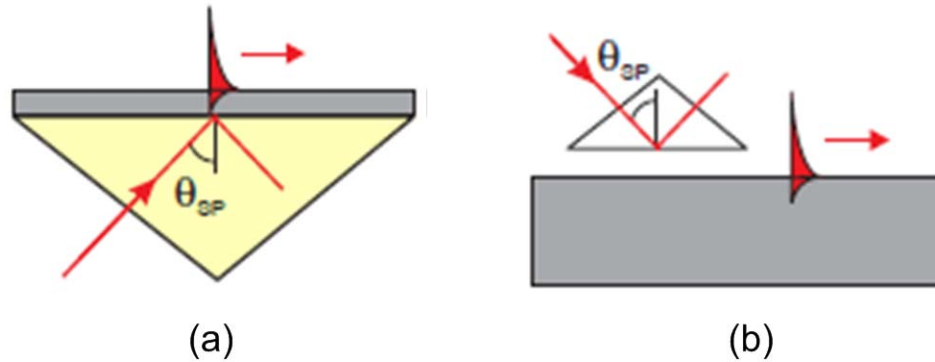


Figure 3-1 Traditional optical configurations to excite SPR on a flat metal film. (a) Kretschmann configuration with glass/gold/air structure; (b) Otto configuration with glass/air/gold configuration.

3.1 Extraordinary Transmission

3.1.1 Metallic Nanohole Array Enhanced Transmission

Research on surface plasmon was focused on the excitation and propagation of surface plasmons on a flat metal surface before T. W. Ebbeson *et al* published their observation of enhanced transmission of light through sub-wavelength hole arrays on a silver film.[5] They prepared several 2D arrays of 150-1000 nm diameter cylindrical holes with 600-1800 nm periodicity. Focused Ion Beam (FIB) milling was used to make the patterns on 200 nm thick silver films. Zero-order transmission spectra for the arrays were collected and a number of distinct features can be observed, as shown in Figure 3-2. The narrow peak at 326 nm wavelength is the bulk plasma peak of silver that becomes insignificant for thicker films. The set of peaks right to the bulk plasmon peak is different from normal transmission of a grating. These peaks become gradually stronger at longer wavelengths and increasing beyond the

periodicity of the array. The maximum transmitted intensity occurs at 1370 nm, which is almost ten times the diameter of an individual hole. The total transmission efficiency is calculated by dividing the fraction of light transmitted by the fraction of surface area occupied by the nanoholes, and it is bigger than 2 at the maxima. This means more than twice amount of light is transmitted as impinges directly on the holes. Although it is sometimes called extraordinary transmission effect, the amount of light transmitted through the nanohole array is a very small portion of the total incident light. Considering that the transmission efficiency of a single hole is scaled as $(r/\lambda)^4$ based on Bethe's calculation [55,56], where r is the hole's radius. For a hole of 150 nm diameter the transmission efficiency is on the order of 10^{-3} . The transmission intensity is also expected to decrease at larger wavelength. Therefore the experiment result indicated that the nanohole arrays itself is an active elements, not just a passive geometrical object that block the incident lights on its path.

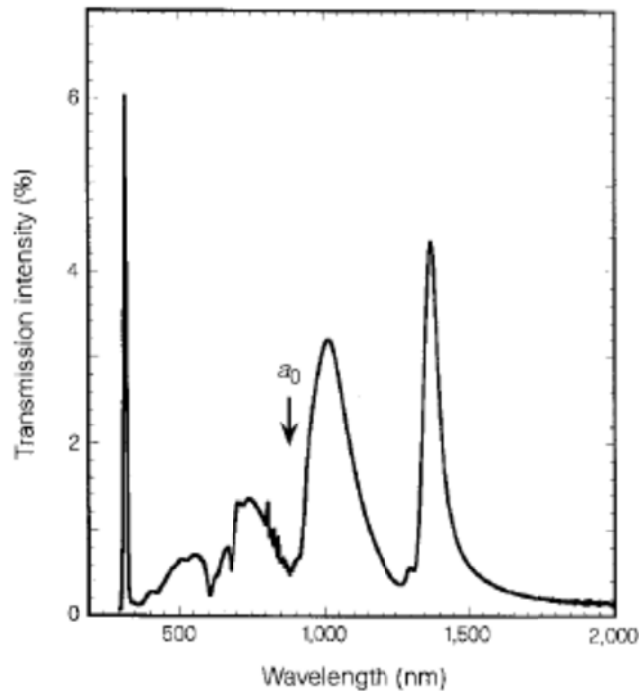


Figure 3-2 Zero-order transmission of a 2D array patterned silver film (period=900 nm, diameter=150 nm, thickness=200 nm). [5]

The geometry and material dependence of this enhanced transmission effect was tested by varying the periodicity, hole diameter and film thickness and by using Ag, Cr, Au, Ge films. Two important facts indicate that the phenomenon is related to surface plasmons. One is the absence of enhanced transmission in hole arrays made in Ge films. This indicates the importance of the metallic nature of the film. The other is the angular dependence of the spectra in metallic samples. The zero-order transmission spectra change even at very small incident angle, and an angle resolve spectra are shown in Figure 3-3. This has the same behavior as light coupling with surface plasmons in reflection gratings.

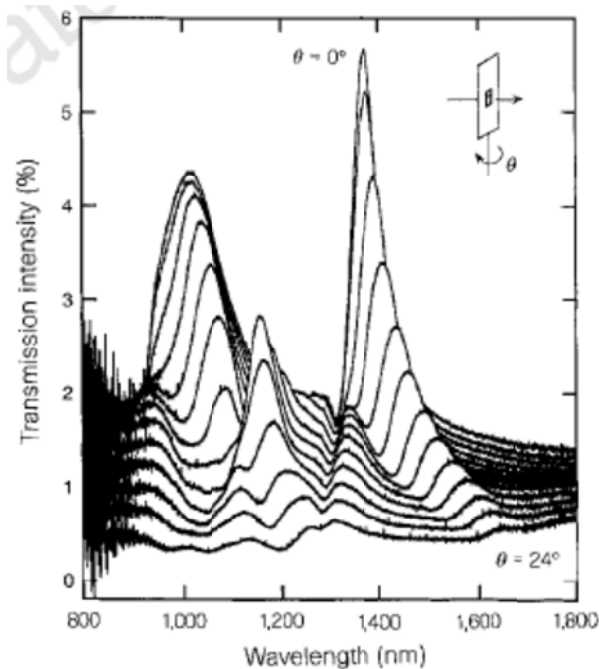


Figure 3-3 Zero-order transmission spectra as a function of incident angle for a square Ag array with 900 nm periodicity, 150 nm hole diameter and 200 nm thickness. The incident angle is changing from 0° to 24° . [5]

Surface plasmons are oscillations of surface charges at the metal/dielectric interface when momentum matching requirements are satisfied. When the incident angle increases from zero, the incoming photon's parallel surface component grows larger. The momentum of surface plasmon equals to the parallel surface component of the incident light shifted by the

nanoholes array lattice momentum. From the dispersion relation, shifting in peak position in the angular resolved spectra can be understood. Ebbesen's report is the first time of observing the coupling of light with surface plasmons in transmission rather than reflection. The result demonstrated strong enhancement of the transmitted light due to photon-SPs coupling on a 2D nano-structure array. Comparing to photonic bandgap array which uses passive material and is translucent at all wavelength except at the energies within the gap, the metallic sub-wavelength array plays an active role and it is opaque at all wavelengths except those for which coupling occurs.

The dispersion relation of the nanohole arrays were under detailed studied in a later paper by analyzing the zero-order transmission spectra in a significant fraction of the Brillouin zone.[36] The spectra were obtained with an incoherent light source at the wavelength from 0.2 μm to 3.3 μm . The sample was rotated around its y axis by 1 degree increments up to 50 degrees that allows a study of the dispersion relation in the k_x direction. The transmitted intensity was plotted in the (E, k_x) plane as shown in Figure 3-4. The maxima appear as bright bands with fairly broad widths and the minima are dark bands with narrow lines. Only p-polarized light show this angular dependent dispersion and the spectra for s light did not change with incident angle. Using the surface plasmon dispersion relation and the momentum matching condition, the surface plasmon excitation condition on square nanohole arrays can be derived as:

$$(i^2 + j^2)^{1/2} \lambda = a_0 \left(\frac{\epsilon_1 \epsilon_2}{\epsilon_1 + \epsilon_2} \right)^{1/2}$$

The peak positions are corresponding to (i,j) combinations, which are called surface plasmon resonance modes. The dielectric material above the metal film are distinguishable since $\epsilon_1 = 1$ for air and $\epsilon_1 = 2.16$ for the quartz substrate, thus resonant modes have different energies on the two sides and there are two sets of peaks corresponding to the two surfaces. At normal incident, the peak at $E=1.3$ eV is associated with Ag-quartz interface with $i^2 + j^2 = 1$, which is four-fold degenerate. As the incident angle increasing, the $(-1,0)$ and $(1,0)$ modes separate and move to opposite directions. At small θ the $(0,\pm 1)$ modes remain at the same λ since

the sample is rotated about the y axis and only the momentum matching in the x direction is affected. Other resonant modes are the $i^2 + j^2 = 2$ mode for Ag-quartz interface locating at $E=1.8$ eV and the $i^2 + j^2 = 1$ mode for Ag-air interface locating at $E=2$ eV. The resonance wavelengths for higher order modes change slower when incident angle increasing, comparing to those low order modes, (1,0) for example. It is because the surface plasmon dispersion curve almost follows the light line when photon energy is low, and becoming flat when energy approaches the materials bulk plasma frequency.

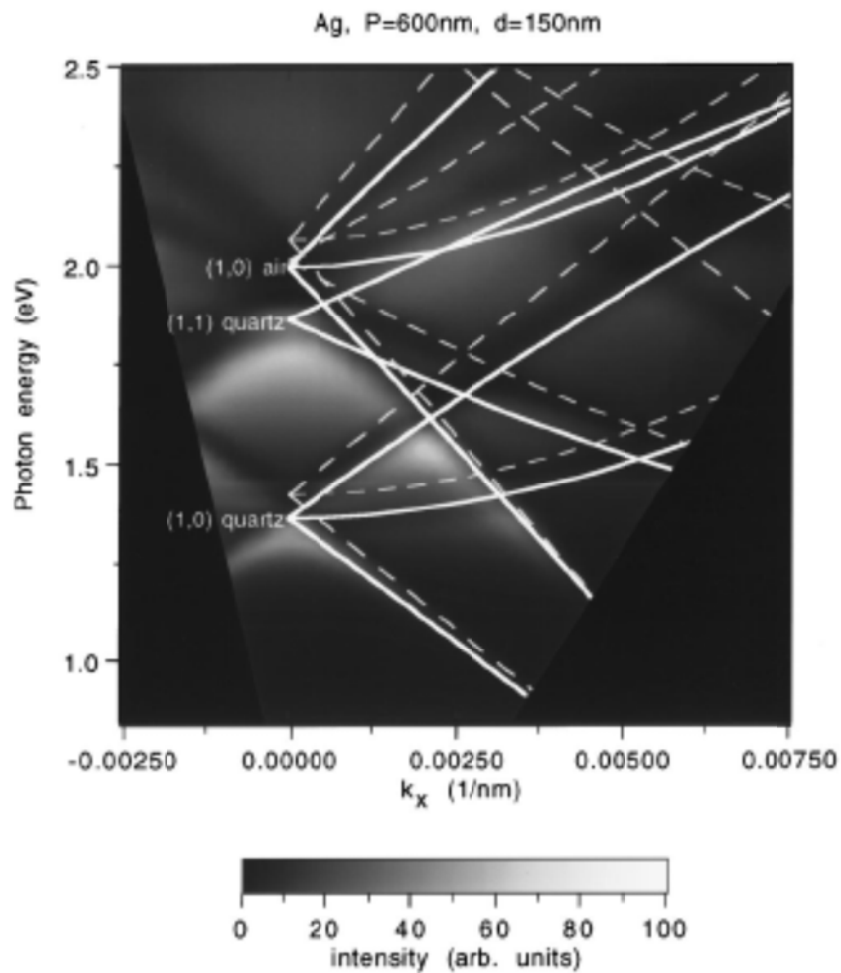


Figure 3-4 Energy dispersion of surface plasmons (solid lines) and loci of Wood's anomaly (dashed lines).[36]

3.1.2 Enhanced Transmission with Different Structures

In addition to 2D square nanohole arrays, the optical properties of several different 2D geometries such as hexagonal self-assembly array, square nano-post array and Fresnel ring structure have been reported. 1D metal grating has simple structure and its spectra illustrate the band structure more intuitively. Christ. A. *et al* reported the observation of strong photon-electron resonant coupling in gold gratings on top of an ITO waveguide layer.[57] E-beam lithography was used to prepare the gold gratings, the structure of the sample is shown in Figure 3-5 with all the spacing labeled. The grating extension was $100 \times 100 \mu\text{m}^2$. Transmission spectra with collimated white light beam were collected for the samples with grating periodicity and incident angle variations. The measured spectra showed pronounced peaks with their maxima indicate strong electromagnetic field resonance near the gold wires. Two light polarizations were applied, the surface plasmon resonance peak showed shifting with reducing grating periodicity (Figure 3-6a) and also split with increasing incident angle (Figure 3-6b,c).

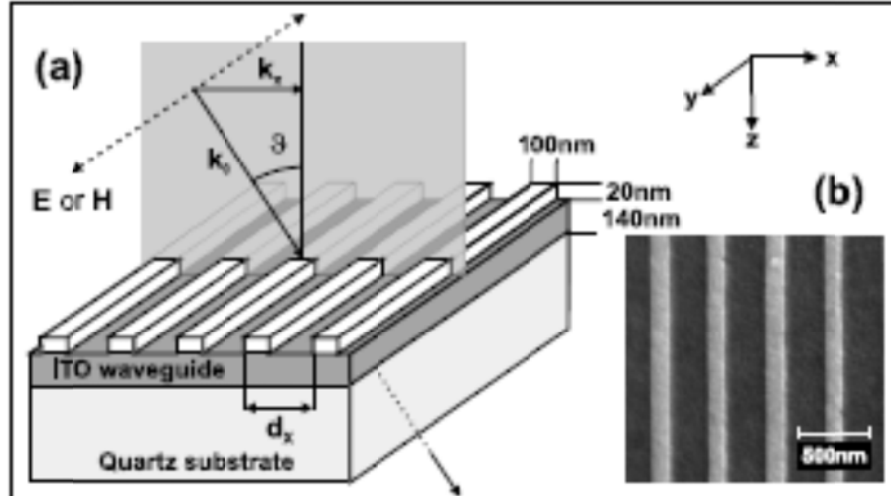


Figure 3-5 Device structure of a 1D grating plasmonic structure. (a) Schematic view of the 1D grating device structure and incoming optical field. The 20 nm thick, 100 nm width gold wire array is on top of a 140 nm thick ITO waveguide. The periodicity of the wires is varied from 375 nm to 575 nm. (b) Electron micrograph of the gold wire array.[57]

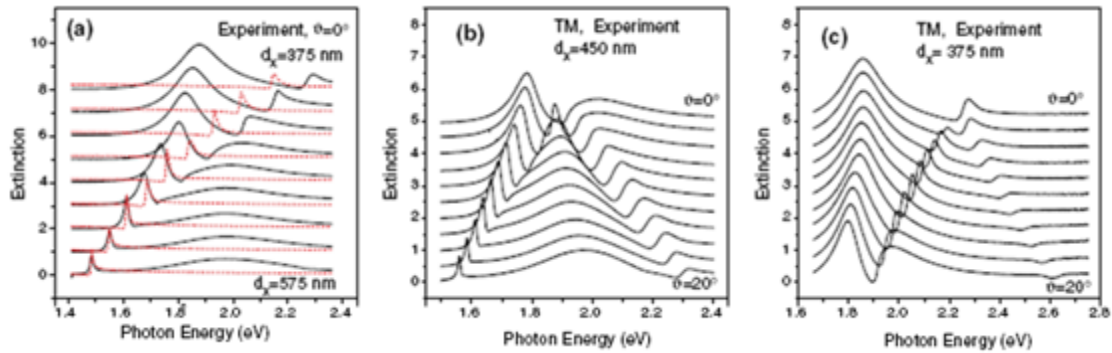


Figure 3-6 Transmission spectra of the 1D grating structure on a ITO waveguide. (a) Spectra with normal incident light. The grating periodicity changes from 375 nm to 575 nm. The red line is TE polarization and the black line is TM polarization. (b) TM light incident angle changes from 0 to 20 degree for a 450 nm periodicity grating. (c) TM light incident angle changes from 0 to 20 degree for a 375 nm period grating.[57]

Spectra from 1D grating pattern is good for illustrating the relation between the surface pattern periodicity and the plasmon resonance frequency, since there is no degeneration of wavevector modes in different direction. The transmission spectra for a normal incident light were collected with two polarizations. The TE polarization light only showed a narrow peak contributed by ITO layer quasi-guided mode, and this peak does not appear in thin ITO layer structure. In TM polarization, a broader peak appeared around 1.6 – 1.8 eV in addition to the narrow peak due to TM quasi-guided mode. This broader peak was due to the photon-plasmon coupling at the gold grating thus generated the enhanced transmission effect. The surface plasmon resonance wavelength increased with grating periodicity, indicating that the excited surface electron oscillation is a propagating wave. For a certain grating periodicity, the enhanced transmission peak split into two when the incident angle increased from normal incident. This peak splitting effect can be understood from the dispersion relation of the surface plasmons on this 1D grating structure. The surface plasmon propagates on two opposite directions perpendicular to the grating slit, and their momentums equal to the vector sum of the lattice momentum and the photon's parallel surface momentum. When the TM

light comes in an angle, it provides a momentum vector which has a specific direction so that now the plasmon momentums for the two directions are not equal. Two plasmon resonance modes were excited and their resonant wavelength moved away from the central.

While the periodic of the grating determines the SPR frequency, groove widths and height also strongly affect plasmon resonance frequency.[58,59,15] Thomas Sondergaard *et al* showed that when the height of the ridge increases, the long-wavelength plasmon mode shifts to longer wavelength.[59] Deep ridges generates strong LSP modes, thus complicated the plasmon enhanced transmission peaks in the spectrum. Detail simulation result of this effect will be discussed later in this chapter.

Another type of pattern studied for surface plasmon enhanced transmission is a single-aperture surrounded by circular surface corrugation, as shown in Figure 3-7a.[60] The concentric rings and the central aperture were fabricated in a nickel film with FIB milling, and a thin layer (30-50 nm) of silver was coated onto the pattern in order to activate the surface plasmon resonance. The periodic of the ring structure was 750 nm. Nickel was used as the patterning substrate because it has much finer grain structure than silver thus resulting in better surface pattern accuracy. The transmission spectra for various aperture diameters were collected and compared between having circular corrugation and having only a bare aperture (Figure 3-7b). The spectra for circular corrugation showed a very broad enhancement peak around 750-820 nm, which is constructing by two distinct resonances. All the samples with ring structure showed plasmon resonance peak at almost the same location and the same intensity disregarding of the aperture diameter, and the resonance wavelengths were close to the surface periodicity. This indicates that they were contributed by surface plasmons propagating on the ring structure, but not the localized plasmon around the aperture. When the aperture size reduced to 200 nm, the direct transmission for a bare hole was pretty low. However, the transmission showed 10-50 times enhancement at the plasmon peaks. It is interesting to know how the plasmon field distributed at near field. Two possible cases are 1) the photon excites LSP at the aperture and then it couples to the corrugation, so that the plasmon wave is radiating out from the center; 2) each ring acts as a waveguide, and the

plasmon field forms a standing wave on the ring when the its circumference equals to n times of the plasmon wavelength. This may possibly happens at outside rings.

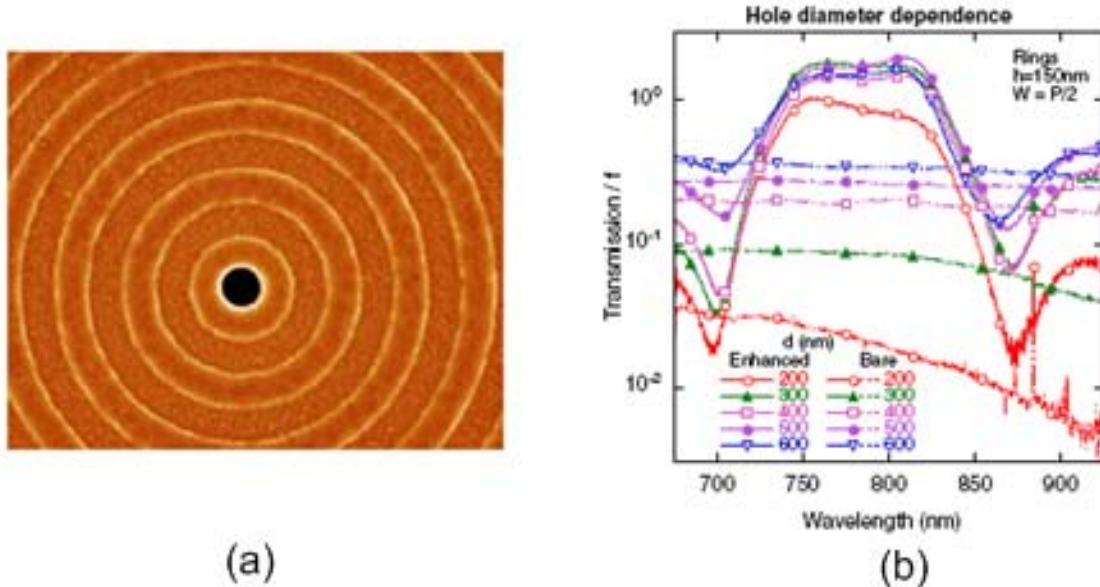


Figure 3-7 Enhanced transmission effect on a concentric circle structure. (a) Electron micrographs of single aperture surrounded by circular surface corrugation; (b) Transmission spectra for both a bare aperture and an aperture with ring corrugation. The ring periodicity is 750 nm, line width is 375 nm and height is 150 nm. The aperture diameter varies from 200 to 600 nm.[60]

3.2 Plasmonic Crystal Dispersion Relation

The enhanced transmission effect in patterned metal films is caused by the resonant coupling of surface plasmons with the incident photon. These surface plasmons propagate in the form of surface charge density waves which are known as surface plasmon polaritons (SPP). The periodic modulated metal structures that generate SPP using free-space light are usually referred to as plasmonic crystals. The dispersion curve for SPP on a flat metal surface sits right to the free-space light line as shown in Figure 3-8a, which means that its momentum is larger than the photon at the same frequency. Plasmonic crystals provide the

additional momentum to compensate for this mismatch so that SPP-Bloch wave modes can be generated on its surface. The momentum matching follows the Bragg coupling equation

$$k_{\parallel} + iG_x + jG_y = k_{SPP}$$

where G_x and G_y are the reciprocal lattice vectors in the two directions. Analogous to photonic crystals, plasmonic crystals can exhibit band structures that depict how the frequency of plasmon resonances evolves with momentum (Figure 3-8b).[3]

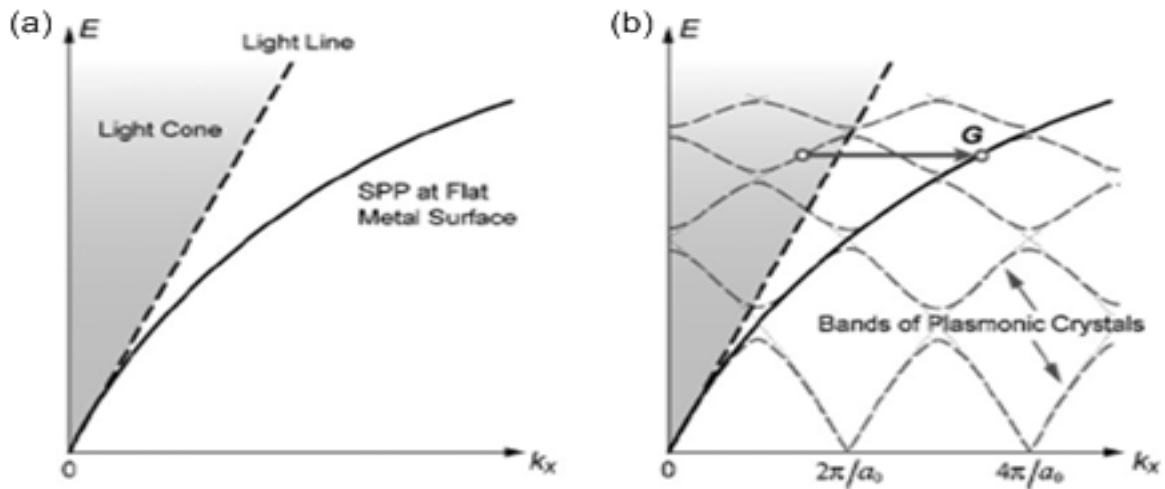


Figure 3-8 Dispersion diagram of a 2D plasmonic crystal. (a) The dispersion relations of free-space photon and SPP show a momentum gap at a certain frequency. (b) SPP dispersion diagrams of 1D gratings are depicted as periodic band structure.[3]

Teri Odom's group developed a high throughput soft interference lithography method to fabricate 2D square array of nano-pyramidal pits in a metal thin film.[61,62,63,64] A SEM image of the nano-pyramidal surface is shown in Figure 3-9a. The zero order reflection spectra of these plasmonic crystals were collected with changing incident angle, where the incident light is a p-polarized white-light source, as shown in Figure 3-9b,c.

The square array has a square reciprocal lattice. The wavevector model of this lattice is shown in Figure 3-10a. The SPP dispersion diagrams along two high-symmetry axes $\Gamma - X$ and $\Gamma - M$ can be obtained by compiling a series of angle-resolved spectra. Figure 3-10b shows the dispersion diagrams of an Ag film with air above the surface, where the black line in the image indicates a low reflectance. Along $\Gamma - X$, a distinct plasmon resonance shifts to lower energies as the wavevector increased. The trend of this mode is in good agreement with the calculated $(-1, 0)$ dispersion curve. When the surface dielectric increases to $n=1.29$, all resonances red-shifts and higher order SPP modes appear. These modes are more condensed because the slopes of the dispersion curves become smaller at higher frequencies.

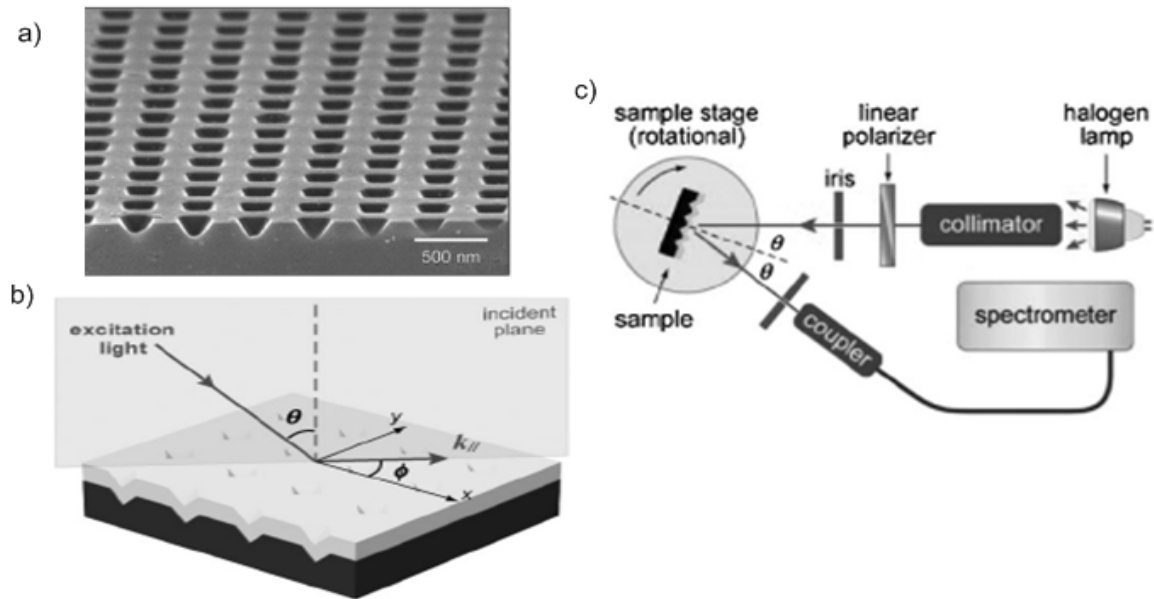


Figure 3-9 The sample geometry and reflection spectra collecting optical setup. (a) SEM image of a pyramidal pits array in an Au film; (b) Scheme showing the geometry relation between the incident plane and the crystal lattice; (c) Optical setup for reflection spectrum collection.[3]

The SPP-BW modes along $\Gamma - M$ direction exhibits different dispersion relation, as shown in the left side of Figure 3-10b,c. The $(-1, -1)$ and the $(-1, +1)$ modes are no longer degenerate and the $(-1,-1)$ mode appears to be the strongest resonance. This indicates that the

most efficient SPP coupling occurs when the in-plan momentum of the incident photon is aligned along the direction where additional momentum is gained from the gratings.[3]

The dispersion relations for a gold nano-pyramidal array at $\Gamma-X$ direction with different surface dielectric are compared in Figure 3-11.[64] The shape of dispersion curves are very similar with the Ag film, where the $(-1,0)$ mode is the strongest resonance mode and red-shifting with larger wavevector. The resonance frequencies for normal incident light are different for Au and Ag film, since their metal dielectric constants are different. The Au film has its lowest order resonance at 2.5 eV, and the Ag film is at 2.7 eV. The width of the resonance peak for Au film is broader because Au has larger grain size.

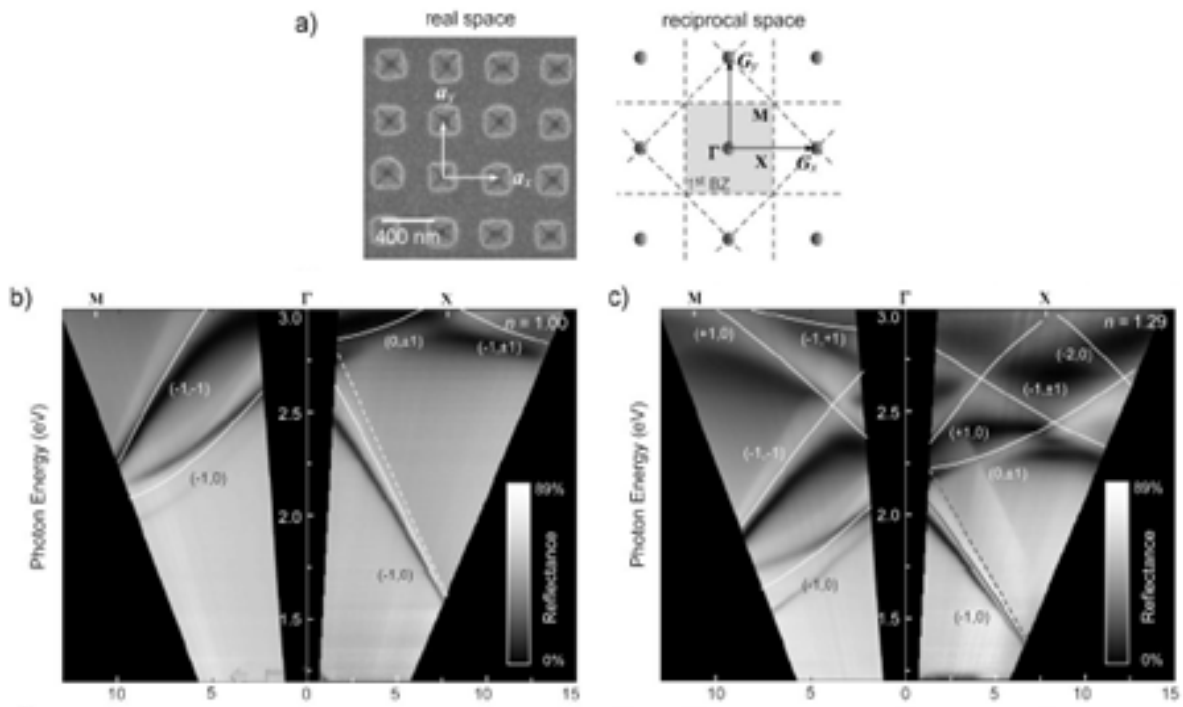


Figure 3-10 The reciprocal lattice of the rectangular 2D array and its dispersion relation measured by optical spectra. (a) Schemes of the Ag square lattice structure in real and reciprocal spaces (b) Dispersion diagrams for $\Gamma-X$ and $\Gamma-M$ directions with surface dielectric $n=1$; (c) dispersion diagrams with surface dielectric $n=1.29$. [3]

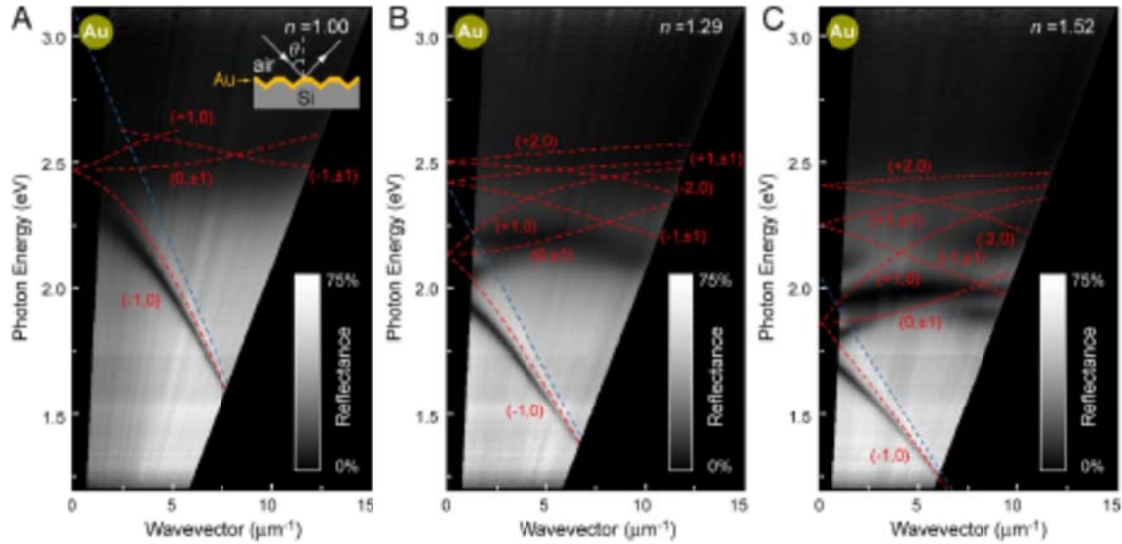


Figure 3-11 Dispersion relation of an Au nano-pyramidal array collected from p-polarized reflection spectra measurement with different dielectric materials above the surface. The surface dielectrics are (a) $n=1$; (b) $n=1.29$; (c) $n=1.52$. [64]

3.3 FDTD EM Field Simulation

The Finite-Difference Time-Domain (FDTD) method, as first proposed by Yee in 1966, is a simple and elegant way to discretize the differential form of Maxwell's equations. Yee's algorithm used an electric-field grid, which was offset both spatially and temporally from a magnetic-field grid, to obtain update equations that yield the present fields throughout the computational domain.[65] The update equations are used in a leapfrog scheme, to incrementally march the E and H fields forward in time. FDTD technique is a direct solution method for Maxwell's curl equations. It does not employ potentials, by just sampling the unknown E and H field within the structure of interest. Usually, 10-20 sample points per wavelength are needed to ensure numerical stability.

With the development of computation technique, many commercial and open source FDTD software are now available. These tools hide the programming detail and help researchers to focus on the physics of the structure under study. MEEP is an open source tool developed by MIT photonic lab, which implements the FDTD method for computational electromagnetism. Metals with complex dielectric constant are described by Drude model in

the program. Since it is hard to model the dielectric response of metal over the whole wavelength, usually we just numerically fit the Drude model to experimental data for the wavelength region under study. In order to correctly simulating plasmonic structures such as gold or silver nanostructures, an ultra-fine mesh is required ($\sim 1\text{nm}$), which causes large memory consumption and very long computation time. Chip multi-processor (CMP) and 64 bits addressed memory provide powerful and low cost solution for this computation intensive application, comparing to build computer cluster or rent computing time on a supercomputer.

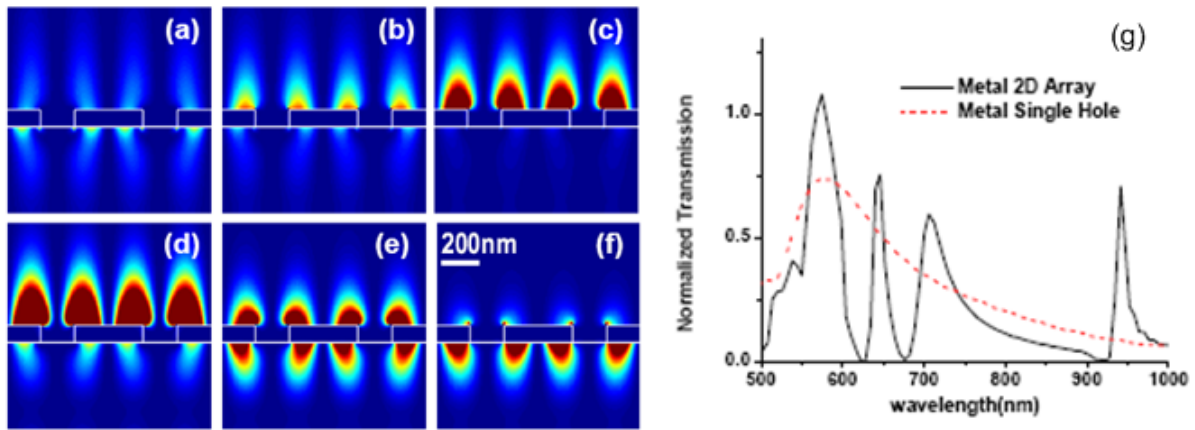


Figure 3-12 FDTD field simulation of a 2D gold array. (a)-(f) The $|E_z|^2$ for a 2D square hole array gold film in x-z plane correspond to $\lambda=610$ to 660 nm; (g) The simulated transmission spectrum for the patterned gold film.[66]

The near surface field distribution and transmission spectrum for a nano-hole array were simulated by Shih-Hui Chang *et al* using the 3D FDTD method.[66] The metal structure under study is a square array of nano-holes with lattice spacing $D=600$ nm and hole diameter $d=200$ nm. The incoming light is a propagating plane wave from the glass side that does not contain $|E_z|$ component. The simulated field distribution near the nano-hole is shown in Figure 3-12a~f, where the light wavelength changes from 610 nm to 660 nm. SPP is excited on the surface and its z component quickly decays when leaving the surface. The maximum

field intensity is happened around $\lambda=640$ nm that indicates a strong surface plasmons resonance. The simulated spectrum also shows that the light has strongly transmission around 640-650 nm region (Figure 3-12g). Comparing to the spectrum of a single hole where the transmission is majorly due to the excitation of localize surface plasmon, the SPP spectrum has discrete enhanced transmission peaks that is corresponding to the SPP-BW modes.

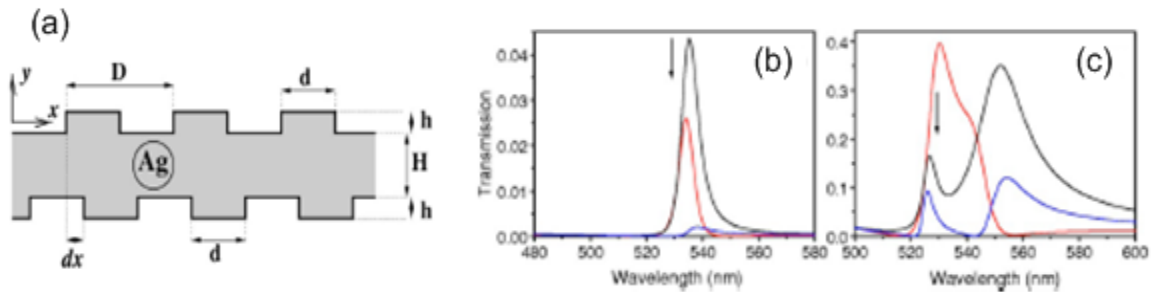


Figure 3-13 FDTD simulation for the ridge-enhanced transmission effect with different film geometries. (a) The metal film geometry with ridges on both interface; (b) Transmission spectra for a silver film ($D=500$, $d=250$) with $H=100$ nm, $h=20$ nm and; (c) $H=40$ nm, $h=20$ nm. The relative position of the gratings are $\Delta\phi = 0$ (black), $\Delta\phi = \pi / 2$ (blue) and $\Delta\phi = \pi$ (red). [67]

Numerical modeling was used to study the ridge-enhanced optical transmission in a continuous film by D Gerard *et al.*[67] A free-standing metal film in air with metal ridges of width $d=D/2$ on both interfaces was modeled, as shown in Figure 3-13a. The periodicity of the ridge was D , and the height of the continuous film was H with the ridge height of h . The phase difference between the ridges at the two interfaces can be expressed as $\Delta\phi = 2\pi \cdot dx / D$. When $\Delta\phi = \pi$, the surface was similar to the nano-pyramidal pits discussed in the previous section. The transmission spectra of different film thickness and phase were simulated and compared in Figure 3-13b,c. For a relatively thick film, the interaction between the SPP modes on the opposite interfaces was weak and only one peak appears in the spectra with its

peak wavelength corresponding to the surface periodicity of the ridge. Variation of the relative position of the ridges did not have significant effect on the peak position but changed the peak intensity a lot. In the case of a thin metal film, the SPP strongly couples between the two interfaces so that the spectrum is more complex. The formation of the film SPP results in splitting of the previous degenerate SPP modes and appearance of the two new modes: a long-wavelength mode with symmetric distribution of the electric field between the two interfaces and a short-wavelength mode with an anti-symmetric field distribution. When the ridges on the two sides have $\Delta\phi = 0$ difference, the symmetric mode peak is stronger in intensity since the ridges on the two sides are in phase. When the two ridges shift by π , the structure can be seen as a locally smooth one, the symmetric mode is suppressed and the anti-symmetric mode is enhanced.

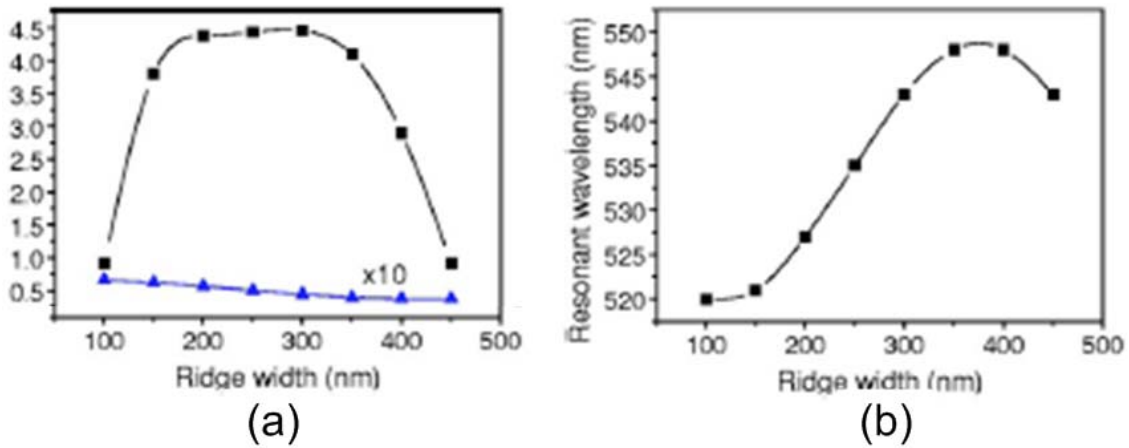


Figure 3-14 Dependencies of (a) the peak transmittance and (b) the resonant wavelength on the width of the ridge. Geometry parameter is $D=500$ nm, $H=100$ nm, $h=20$ nm, and $\Delta\phi = 0$. The blue curve in (a) shows the transmittance of a smooth silver film normalized on the average film thickness at the corresponding resonant wavelength for comparison.[67]

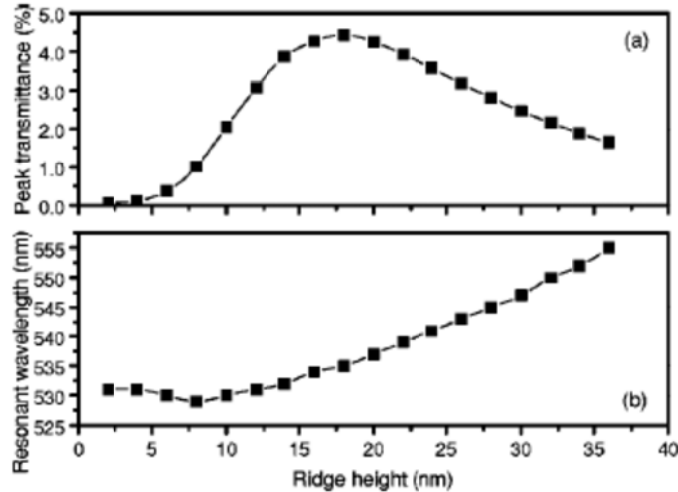


Figure 3-15 Dependencies of (a) the peak transmittance and (b) the resonant wavelength on the height of the ridge. ($D=500$ nm, $d=250$ nm, $H=100$ nm, and $\Delta\phi = 0$).[67]

The dependencies of the transmission on width and height of the ridges were simulated. The optimal ridge width was approximately a half of the grating period, thus the area of the grating covers about 50% of the whole surface, as shown in Figure 3-14. The peak transmittance was at its maximum under this width condition. With the increasing of the ridge height, the resonant wavelength shifted to the longer wavelength. The optimal ridge height was determined by a trade-off between the SPP excitation efficiency, the SPP field overlap, and the SPP radiative losses.[67] For small ridge heights, the coupling of photons to SPP Bloch modes was low. With the increase of the ridge height, the y-direction overlap of the SPP modes decreased since the mode profile roughly follows the topographic profile. The radiative losses due to SPP coupling to photons increased with the ridge height. The competition between these processes leads to the maximum observed in Figure 3-15a, which is located at $h=18$ nm.

3.4 Surface Plasmon Dielectric Sensing

3.4.1 Bio-chemical Sensing

The enhanced EM field on the surface of a plasmonic crystal can be used to sense the changes in refraction index in aqueous solution in the visible wavelength region. Nano-post

square array on gold films were fabricated using soft nano-imprint lithography.[68,69,70] The periodicity of the array was 736 nm and the post diameter was 520 nm. The gold metal film thickness was 35 nm. The geometry of the surface is shown in Figure 3-16a,b. Transmission spectra for the nano-post arrays were measured with normal incident light. Air and water were put onto the plasmonic crystal surfaces and the lowest order plasmon resonance peak wavelengths were at ~ 850 nm and ~ 920 nm for the two cases, as shown in Figure 3-16c,d. Single channel micro-fluidic devices with channel width of 80 μm were used to sequentially inject aqueous solution of poly(ethylene glycol) (PEG) onto the crystal surface. The concentration of PEG was increased from 0 wt% to 5.6 wt%. At 298K, 0 wt% (pure water) has a RI of 1.332 and 5.6 wt% has a RI of 1.340. The transmission spectra collected over time showed changes in peak position and intensities as the refractive index of the solution was increased.

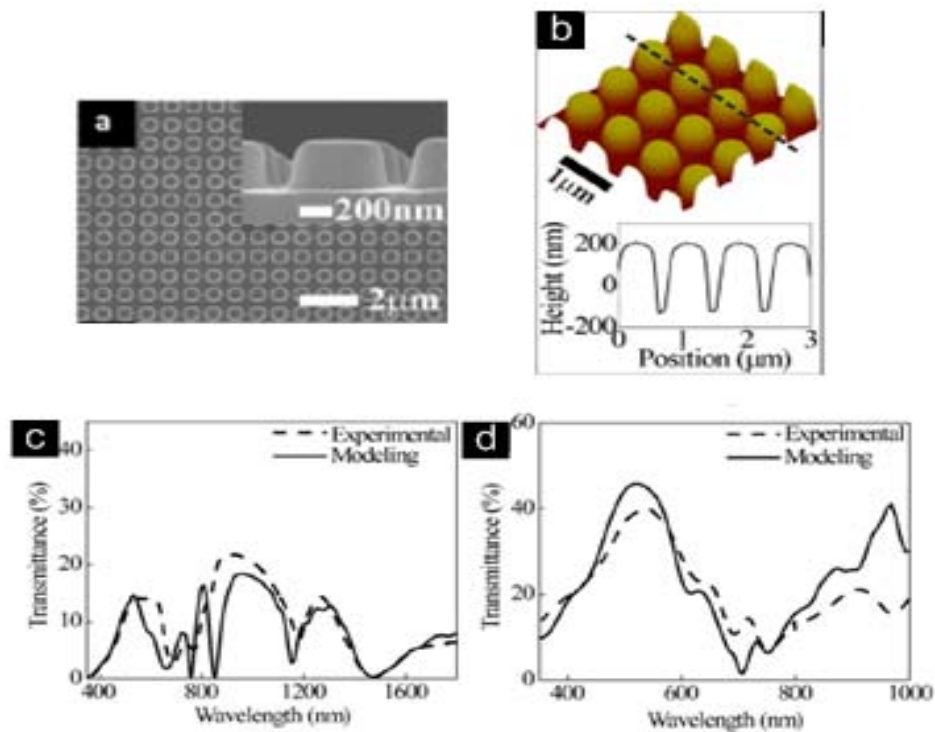


Figure 3-16 Nanopost array for surface plasmon excitation. (a) SEM image and (b) AFM image of the nano-post array pattern in a gold film, and a cross section height profile along the post array; (c) transmission spectra with air on top of the gold surface; (d) with water on top of the surface.[68]

The time sequential spectra were normalized to the reference spectrum at $t=0$ and combined in a series to show the change with different PEC concentration (Figure 3-17a). The spectra intensity increased about 5% at 720 nm when maximum PEC concentration was reached. The integration of full spectrum versus time was shown in Figure 3-17b. This integrated response depended linearly on changes in the refractive index of the PEG solutions, and the sensitivity is 1100 ± 100 nm/RIU. The result suggests that nano-post plasmonic crystals can be used as label-free sensors in bio-sensing and imaging with visible light.

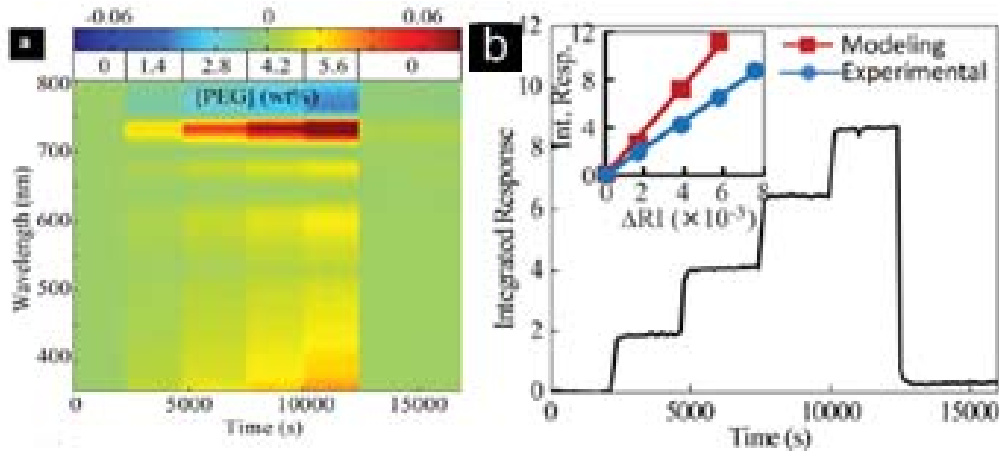


Figure 3-17 PEG solution concentration sensing uses the nanopost array. (a) Spectral response in 355–800 nm wavelength of a nano-post array with sequential injection of increasing concentrations aqueous PEG solution. (b) Integrated response as a function of time over the whole wavelength region.[68]

3.4.2 Microarrays for Bio-sensing

Plasmonic crystal can be patterned in microarray using for real-time multiplex monitoring of binding events. The sensitivity of the SPP to the refractive index adjacent to the metallic surface forms the basic operation principle of the device. Jacson W. Menezes *et al* reported using gold nano-hole microarrays to detect the refractive index changing of the glucose solution above the surface.[71] The transmission spectra of the nano-hole array for glucose solution with $n=1.3320$ to $n=1.3804$ are shown in Figure 3-18a. The SP resonance at

755 nm red-shifted as the refractive index increases, the intensities of the transmission peak also decreased. The resonance peak position shifted almost linearly with the refractive index with the sensitivity of 271 nm/RIU (Figure 3-18b). The nano-hole pattern was used to fabricate microarrays and integration with multichannel fluidic devices for simultaneous detection of bio-molecules from several sensing areas. Figure 3-18c shows a three-channel micro-fluidic device where the arrays contact with different dielectric media. The arrays were illuminated with 633 nm He-Ne laser, and the changes in transmission intensity at this wavelength lead to easily distinguishable difference for the dielectric media under test.

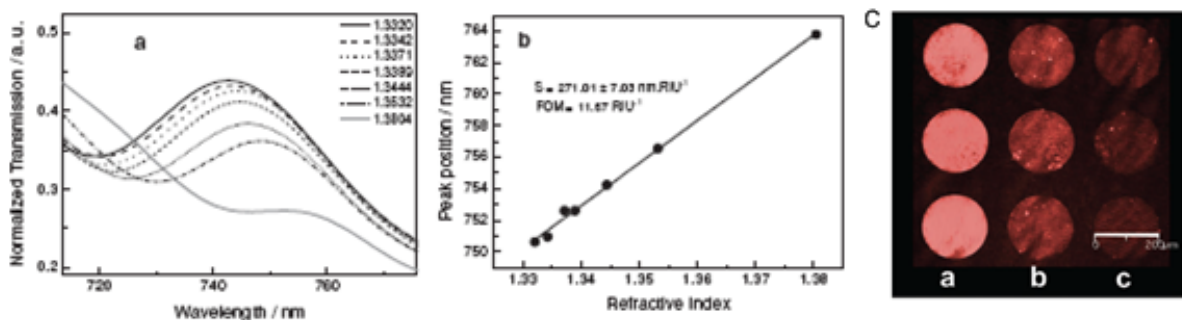


Figure 3-18 Microarray uses in sensing glucose solutions with different refractive indexes. (a) Zero-order transmission from a microarray of PANHs in the presence of glucose solutions with different refractive indexes; (b) Sensitivity plot from 755 nm resonance; (c) SPR image from a microarray with different environmental dielectric (Air $n=1$, water $n=1.33$ and glucose solution $n=1.3804$).[71]

3.5 Surface Plasmon Enhanced Fluorescence

Fluorescent technique is widely used in numerous research and sensing applications.[72,73,74,75] Pushing fluorescence detection to its sensitivity limits is performed by controlling the local electro-magnetic environment of the fluorophore, while the plasmonic crystal could be an option to achieve this goal.[17] In many applications, an instrument such as a fluorescence microscope is used to provide excitation of the fluorophore and detection of the emission of a labeled analyte on a substrate. Sub-wavelength resolution imaging of cells and large-area high throughput microarray detection for DNA and proteins with fluorescent labels are under recent development.[76,77,78] Moreover, the protein

dynamics near a surface can be imaged by selectively exciting the fluorophore closed to the surface using an evanescent field.[79,80] This application can provide novel information about the cell-substrate contact region that could not be emphasized with a normal optical microscope. The evanescent field generated by total internal reflection is used to selectively excite the fluorophore near the surface. However, the sensitivity, which is measured by the signal-to-noise ratio, is low because the number of fluorophore inside the sensing region is limited.

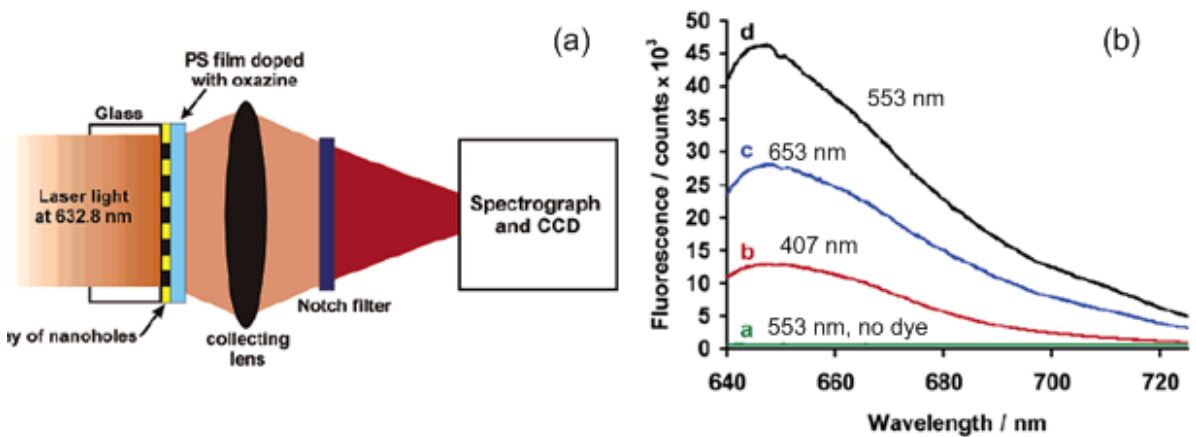


Figure 3-19 Enhancing fluorescence dye emission with 2D nanohole array gold film. (a) Schematic of the experimental setup for enhanced fluorescence measurements in transmission mode. (b) Background fluorescence emission from an array of nano-holes with 407 nm, 553 nm, 653nm periodicity and no dye background intensity. [81]

Recently, the ability to amplify the signal-to-noise ratio of common fluorophore has been developed by replacing the passive glass substrate with a specially designed plasmonic metal surface. A sub-wavelength periodic structure was designed to strongly enhance the electromagnetic field at the excitation wavelength of the fluorophore, resulting in near surface enhanced fluorescence for lower concentration target detection than previously possible.[81] A layer of polystyrene dye was coated on a nano-hole array patterned gold film and its

transmission spectrum was collected (Figure 3-19a). The resonant frequency of the plasmonic crystal surface was tuned to match the excitation frequency of the fluorophore, which involves adjusting the thickness of the film, the periodicity and symmetry of the lattice and the structure of the unit cell. The fluorescence emission from 553 nm periodicity pattern showed the strongest emission comparing to the 653 nm and 407 nm period samples. This result demonstrated that the near surface field of the surface plasmon can strongly enhanced the dye emission close to the surface, when the plasmon resonance frequency, i.e. the near field oscillation frequency, matches the dye absorption frequency.

3.6 Plasmonic Devices for Novel Applications

The emerging field of plasmonic crystals has developed many methods for guiding and localizing the plasmon oscillation at nano-scale structures, and utilizing their unique optical feature to achieve the design goal with tiny device size. Plasmonic switches, plasmonic laser, plasmon enhanced solar energy collection and plasmonic filter for color sensing are among those novel applications that have been introduced recently. This section will briefly summarize the design idea and key achievement of these devices.

3.6.1 Plasmonic Switch

The integrated circuits today use MOSFET as the basic building block to achieve specific functions and the device have continuously scaled according to Moore's law with increasing in both density and bandwidth. However, as gate length approach the single-nanometer scale, interconnects in MOSFET circuits contribute a large part of the circuit delay and device leakage causes higher power dissipation. New technologies are being considered, in particular, special attentions have been given to optical interconnection and devices. Jennifer A. Dlonne *et al* reported an experimental demonstration of a field effect Si modulator based on multimode interferometry in a plasmonic waveguide.[12] The device utilized high optical mode confinement to enhance electro-optical non-linearities in Si and exploited the fast modulation of accumulation conditions in Metal-Oxide-Semiconductor capacitor.

The schematic of the plasmonic MOS modulator device is shown in Figure 3-20a and it was named “plasmistor”. It was four layers structure that had an n-doped Si with a thin layer of SiO₂ on top and they were sandwiched between two Ag layers. A voltage was applied between the two metal layers, which acted as gate and cladding contact of the device. Light was coupled into and out of the device via sub-wavelength slits etched into the metal layer that function as the optical source and drain. When no bias was applied to the gate, the device was fully depleted and light can be guided from the source to the drain through both the Si and SiO₂ layers. The dispersion curve in Figure 3-21b shows that the device supports a variety of TM modes. At $\lambda=1.55 \mu\text{m}$, the unbiased device supports two modes: a photonic mode left to the light line and a plasmonic mode right to the light line. Both modes will be generated at the source and will interfere either constructively or destructively at the drain depending on the source-drain separation. The near flat dispersion of the photonic mode at 1.55 μm suggests that this mode will be extremely sensitive to changes in the Si refractive index.

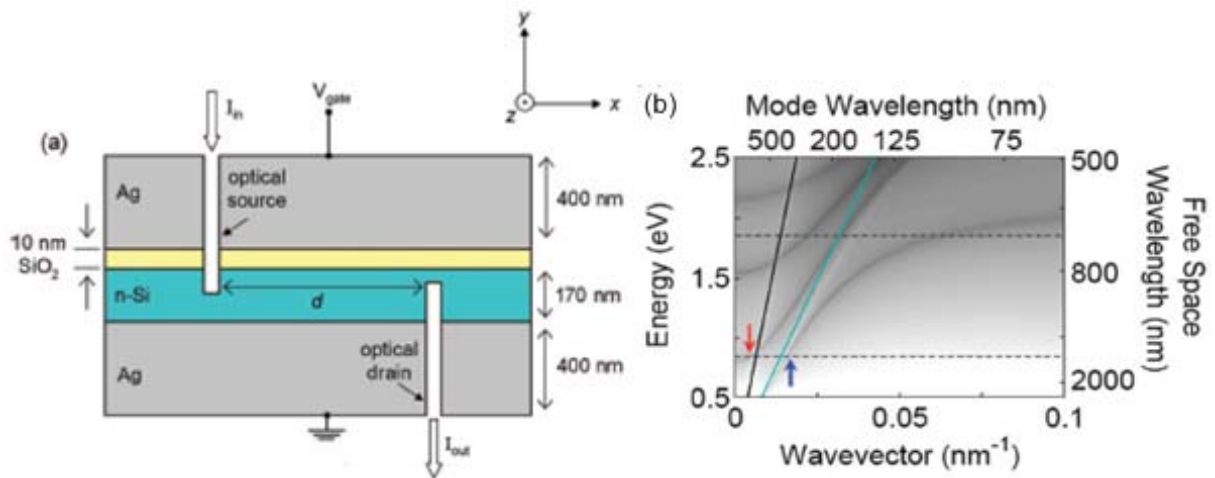


Figure 3-20 Structure and dispersion relation of the plasmon transistor device. (a) Cross-sectional schematic of the Si field effect plasmonic modulator. A 170 nm thick Si layer with 10 nm SiO₂ on top was sandwiched between two 400 nm Ag layers. (b) Dispersion relation for the plasmistor in the voltage-off state. Black line is SiO₂ light line, cyan line is Si light line.[12]

Modulation of the transmitted power was simulated using FDTD method with a device that has 2 μm source-drain separation, which is shown in Figure 3-21. The field was concentrated in Si core during the “off” phase and not much power was coupled to the output. However, with the onset of accumulation, the field transmitted within the Si core was notably decreased and concentrated within the 10 nm SiO_2 layer. The output power at the optical drain has +10dB increasing between the voltage-on/off states. Optical modulator was the critical components for optical circuits, the control signal can either be electrical as the ‘plasmistor’ or optical such as the CdSe quantum dots controlled all-optical modulator.[13] The modulation efficiency, i.e. the signal ratio between on and off states, the device size and maximum operation frequency will be the major considerations for this type of devices.

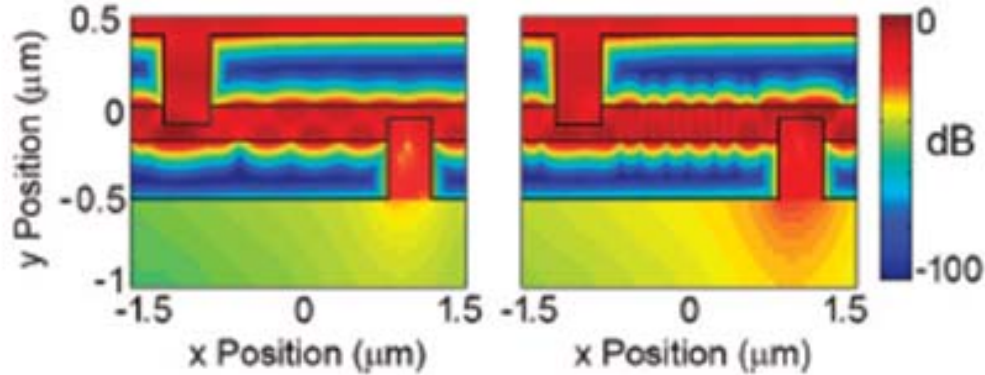


Figure 3-21 FDTD simulation of the plasmistor shows the transmitted power distribution for a 2 μm long optical source-drain separation. The device was illuminated with a Gaussian beam of wavelength $\lambda=1.55 \mu\text{m}$. (Left) Gate bias voltage off; (Right) Bias voltage on.[12]

3.6.2 Plasmonic Laser

Laser has been used as high-powered, narrow spectrum width coherent light source for several decades. Recent advanced in microscopic lasers minimum the device size but still restricted to being larger than half the wavelength of the optical field. Rupert F. Oulton *et al* reported a nanometer-scale plasmonic laser using a hybrid plasmonic waveguide consisting of a high-gain cadmium sulphide semiconductor nanowire lay on a silver surface with a 5 nm insulating MgF_2 gap layer in between.[11] The structure of the device and its SEM micro-image are shown in Figure 3-22a. This semiconductor nanowire sits on top of the Ag surface

with a gap layer, so that the coupling between the plasmonic and waveguide modes across the gap enables energy storage in non-metallic regions. The laser devices were optically pumped at a wavelength of 405 nm and its emission was measured from the dominant I_2 CdS exciton line at 489 nm. Amplified spontaneous emission was observed corresponding to the longitudinal cavity plasmonic modes that resonate between the reflective nanowire end-facets. The stimulated electric field distribution and the field direction of a hybrid plasmonic mode at 489 nm are shown in Figure 3-22b. The physics for the gain mechanism includes exciton dynamics, the modification of spontaneous emission and mode competition. The photo-generated excitons have intrinsic lifetimes of up to 400 ps and diffusion length in bulk CdS around a micron, which is much larger than the nano-wire diameter. The exciton distribution quickly adjusted itself to match the mode profile and generated large spontaneous emission factor within the plasmonic mode region. Comparing to the conventional laser, the plasmonic laser support nanometer scale optical modes and its physical size is much smaller. It maintains strong confinement and its optical gain only depends weakly on nano-wire diameter, which is different from photonic nano-wire laser. This nanometer scale plasmonic laser operating at visible frequency region demonstrated the possibility of making new sources that may produce coherent light far below the diffraction limit.

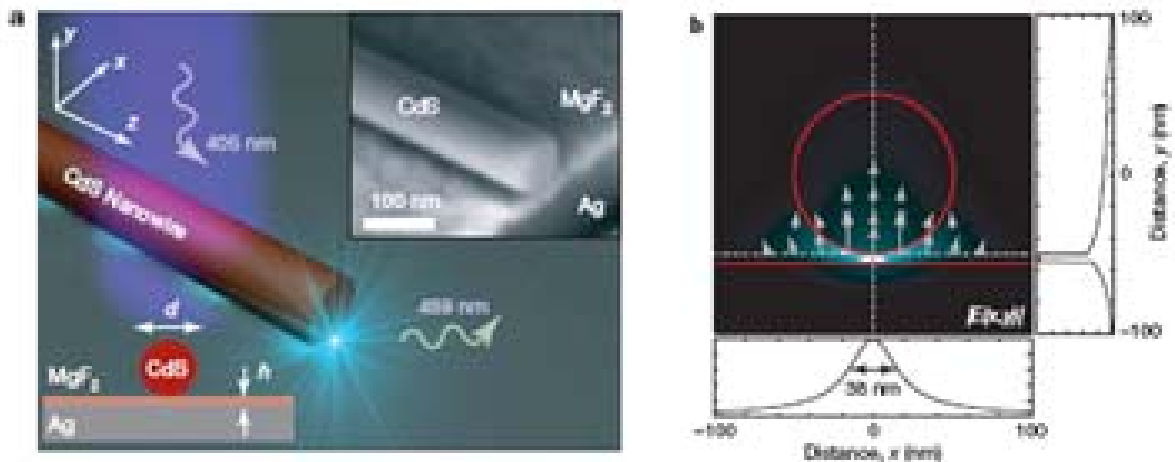


Figure 3-22 Device structure and field distribution of the plasmonic laser. (a) The schematic of the plasmonic laser with a SEM image inserted. A CdS semiconductor nanowire sits on top of a silver substrate, separated by a nanometer thickness MgF_2 layer. (b) The stimulated electric field distribution at a wavelength of 489 nm.[11]

3.6.3 Plasmon Enhanced Solar Energy Harvesting

Photovoltaics is the method of converting sunlight directly into electrical power on a very large scale. It is a promising approach to improve energy security that our society may face in the next generation. Currently, thin-film solar cell attracts much interest because of cost and efficiency consideration. However, a limitation in all thin-film solar cell technologies is that the absorbance of near-bandgap light is small, so that special structures were applied to trap light inside the cell in order to increase the absorbance. The commonly used pyramidal surface texture in conventional thick Si solar cells is not suitable for thin-film cells for geometrical reasons. Plasmonic structures are used as a new method to concentrated light into a thin semiconductor layer, thereby increasing the absorption.[14] These structures can be used as sub-wavelength scattering elements to couple free space light and also generated plasmon modes, which including LSP and SPP, at its corrugated metallic surface. Three methods for light trapping are shown in Figure 3-23, and the third one that uses periodic metal structure for SPP coupling attracts much interest. Light is converted into SPP waves that travel along the interface between the metal back contact and the semiconductor absorber layer. The evanescent electromagnetic SPP field is strong near the interface at the plasmon resonant frequency and it efficiently traps light at the semiconductor layer. Experiments show that light with $\lambda > 800$ nm, which would not be well absorbed by Si, can now be absorbed by conversion into the in-plane SPP and photonic modes.

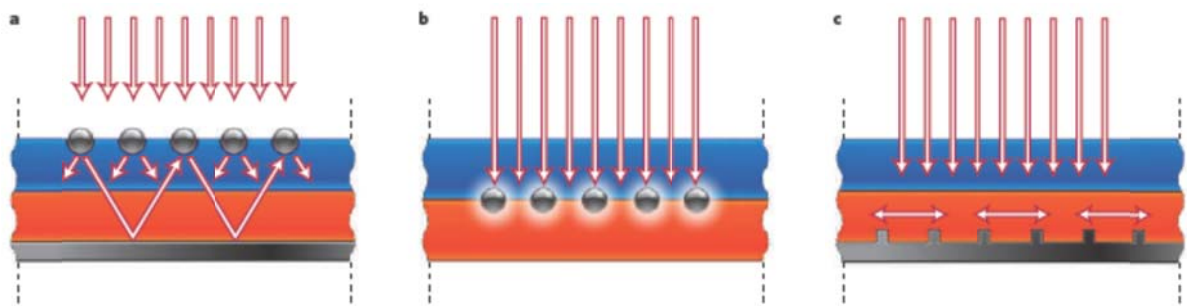


Figure 3-23 Three structures that utilize surface plasmon to enhance solar conversion efficiency. (a) Light trapping by scattering from metal nano-particles; (b) Light trapping by the excitation of localized surface plasmons; (c) Exciting surface plasmon modes on corrugated metal surface to enhance photo-carriers conversion.[14]

3.6.4 Plasmonic Filters for Spectral Imaging

Modern imaging sensing techniques typically use filters or interferometers to subdivide the incoming light spectrally and followed by scanning or sub-sampling to record a color image in spectral image ‘cube’. This leads to inefficient use of the incoming light and may have long recording time. Eric Laux *et al* demonstrated a concentric rings structure that can directly separate the incoming light into spectral image cube with a single exposure.[82] The metal structure for one set of rings on a 300 nm thick Ag film is shown in Figure 3-24a, which includes a single sub-wavelength aperture ($d=170$ nm) surrounded by concentric grooves with adjustable periodicity P . The transmission spectra of various groove periodicity are shown in Figure 3-24b. Surface plasmons were excited on the rings structure and its resonant wavelength can be tuned by controlling the groove periodicity. The transmission peak position can be controlled to cover almost all the visible light wavelength, and the strongest peak intensity happened at 650 nm region. The authors proposed a structure that consisted of overlapping the concentric rings with different periodicity. The concepts is that each structure would collect light over a certain frequency range and be able to redirect it to its central aperture even from the region where it overlaps with other collectors. With photo-detectors placed under the center of each rings, a miniature spectrometer can be made to record the spectrum of light normally incident onto the area.

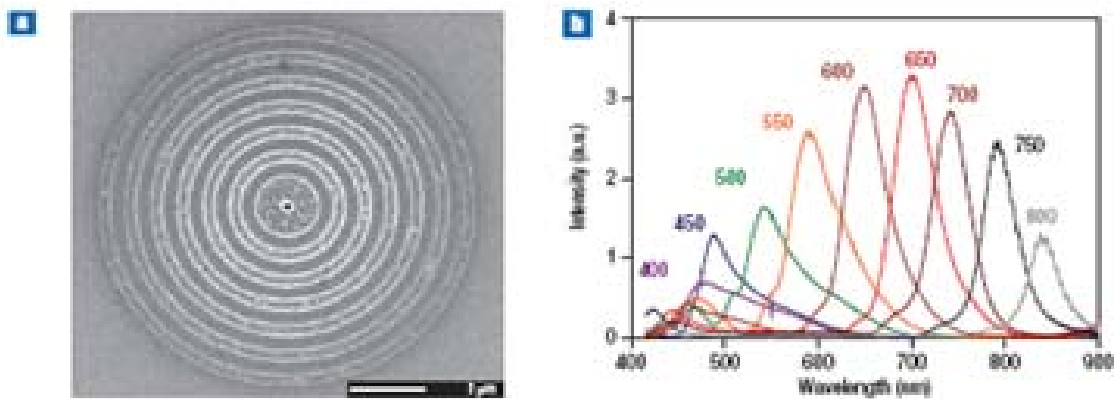


Figure 3-24 A single concentric ring structure that has plasmon enhanced transmission effect depending on its periodicity. (a) The rings structure milled by FIB in a 300 nm thickness Ag film on a glass substrate. Central hole diameter $d=170$ nm with rings periodicity of 800 nm. (b) Transmission spectra for the same structure with 400 – 800 nm ring periodicity. [82]

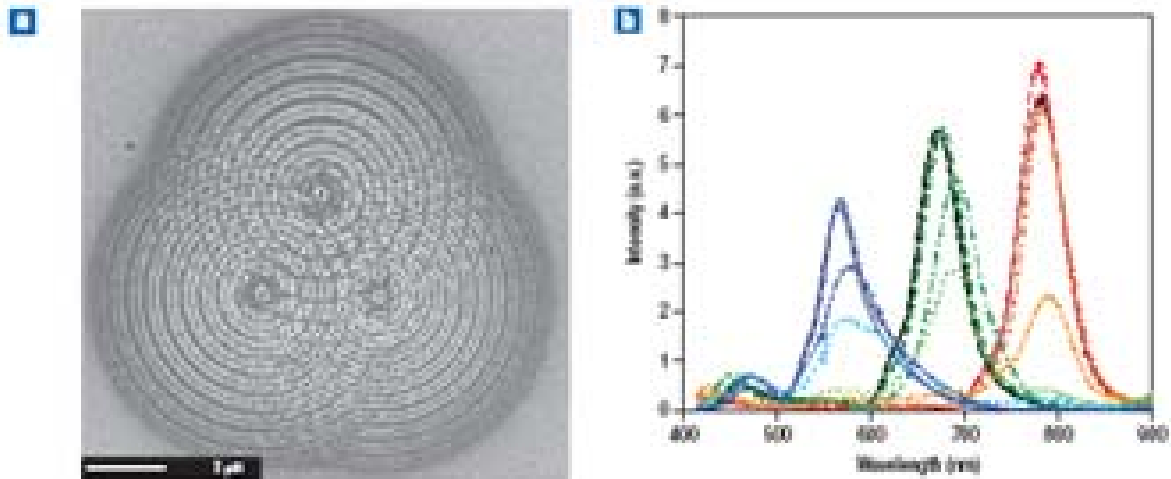


Figure 3-25 Triple rings structure prepared with the same parameter as one ring structure for color separating measurement. (a) Ring periodicities are 730 nm for the top structure, 630 nm for the left structure and 530 nm for the right structure; (b) transmission spectra for different center to center distance.[82]

A triple concentric rings structure was fabricated by FIB milling on an optical thick Ag film, as shown in Figure 3-25a. The periodicities for the three rings were 730 nm, 630 nm and 530 nm, respectively. The distance between the centers of the rings changed for various values, and their spectra are shown in Figure 3-25b. The shape of transmission peak associated with one rings structure was hardly changed by the presence of the others as two sets of rings become closer. Moreover, each ring structure transmitted very little amount of light corresponding to the resonances of the adjoining structures, which means that the SPP on each ring set are independent and does not generate interference effect at far field. This experiment shows that the plasmonic crystal can be used as spectrum band-pass filters with several microns size, and it is possible to minimize the form factor of the device by putting the crystals in a very compact way without affecting the operation of each single structure.

CHAPTER 4

PLASMONIC CRYSTAL FABRICATION AND CHARACTERIZATION

The fabrication of plasmonic crystal requires nanometer scale patterning and precise metal deposition tools. In this chapter, the plasmonic device preparation flow will be described and the instruments used in the research will be introduced. Nanosphere lithography technique is a customized process flow to fabricate large area hexagonal arrays on metal films, which will be used as the plasmonic crystals in this study. The characterization flow of this device will be discussed, which includes SEM, AFM imaging and optical spectrum collection.

4.1 Plasmonic Crystal Fabrication

Plasmonic crystal is the analogue of atomic crystal, however, naturally occurring materials that exhibit plasmonic effects are rare. The periodicity of the plasmonic crystals functioning in visible to NIR wavelength region should have the same scale as the optical wavelength, which is several hundred nanometer to a few micron in length. Therefore, plasmonic crystals must be “synthesized” using micro/nano scale assembly or machining technology. The most common methods to make sub-micron structures are photo lithography[83], e-beam lithography[84,85] and Focused Ion Beam milling[86]. Nano-imprint[87] with interference lithography generated stamps and nanosphere self-assembly masking are also becoming popular fabrication techniques in recent studies.

4.1.1 Nanosphere Self-Assembly

Nanosphere lithography is based on the self-assembly process of colloidal spheres driven by capillary-bridge forces.[88,89] Recent advances in colloidal science have enabled synthesis of highly uniform colloidal particles with good stability.[90,91] Such colloidal particles can be arranged into a 2D array through self-organization and have been used as templates for plasmonic crystal fabrication. Solution containing these uniform size spheres is

deposited on a hydrophilic substrate by drop-coating or tip-directed deposition methods. As water evaporates at the liquid meniscus, the capillary force between the spheres drives them to form a close-packed hexagonal array. This colloidal sphere array will be used as shadow mask in later process.

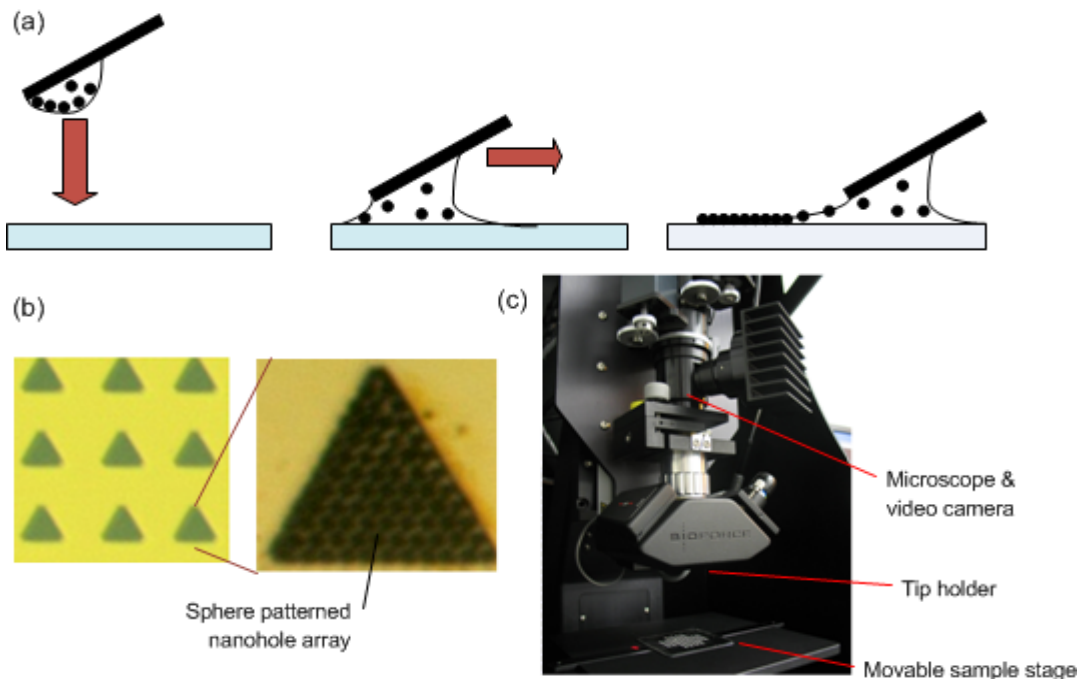


Figure 4-1 The process flow and tools for nanosphere directed self-assembly. (a) The tip directed sphere deposition steps: a droplet of sphere solution is dragged by the tip, and spheres are assembly at the meniscus; (b) A concave box made by gold film with single layer sphere array made pattern inside; (c) the BioForce tip controlling tool.

The polystyrene spheres used in this study were obtained from Duke Scientific in aqueous form, with the sphere diameters vary from 500 nm to 10 μm . For the tip directed deposition method, a Nano Enabler surface patterning platform from BioForce NanoSciences was used to precisely control the tip position for sphere deposition, as shown in Figure 4-1. After placing a droplet of the sphere solution on a flat-end silicon nitride tip, its edge is then lowered to the substrate by a computer controlled motor and dragged along the surface in a step-wise fashion. As water evaporates at the liquid meniscus, the capillary force between the

spheres results in a colloidal crystal. The step rate is adjusted by visually confirming the assembly of single layer periodic structures, and it is approximately 2~5 μm per second. Some pre-defined surface structure can be used to improve the quality of the sphere array. Figure 4-1b shows a triangle shape concave with single layer sphere array made pattern inside. These surface structures are usually 10-20 time of the nanosphere diameter and have a step at their edge. The tip directed method allows crystals to be placed where desired on a substrate and can be used to produce crystals on the size scale of 500 μm^2 .

Inspired by the visual observation of the sphere self-assembly process at liquid meniscus, a drop-coating method was developed for preparing large area hexagonal array patterns. The glass substrates were cleaned with acetone then treated in piranha solution (3:1 concentrated $\text{H}_2\text{SO}_4:\text{H}_2\text{O}_2$) for one hour to make a hydrophilic surface. Piranha solution is used to remove any organic residues from substrates. Then, a droplet of polystyrene spheres was drop-coated onto the surface. The solvent (H_2O) was allowed to slowly evaporate in a home-made humidity controlled chamber with 70%-75% humidity. During evaporation, the spheres self-assembled into hexagonal close-packed arrays on the glass surface. The area of single layer well organized patterns can achieve 20~30 mm^2 . A hydrophilic surface is critical in this process, because it can extend the length of the meniscus and give the spheres more time to self-organize themselves. The environment humidity determines the water evaporation speed thus the meniscus moving speed, which is equivalent to control the tip dragging speed in the tip-directed deposition method. The 70% humidity is good for generating a continuous single layer patter. If the humidity is low, water evaporates quickly and the pattern will have lots of defects; if the humidity is too high, multiple layer patterns will be generated. Substrate material also affects the self-organization process. The arrays self-assembled on glass cover-slip substrates can be very large area well-organized patterns, but the arrays on sapphire substrates do not organize well even if the surfaces are hydrophilic.

The home-made humidity controlled chamber and the arrays patterned by 600 nm spheres are shown in Figure 4-2. A humidifier was used to generate water vapor in the sealed chamber and a hygrometer was used to monitor the humidity. It took about 10-20 minutes to start the system and reach a stable humidity level. After that, the cleaned glass cover slips

were put into the chamber, and a few drops of colloidal sphere solution (1-2 drops) were put onto the slips and spread out to cover the whole substrate. The glass slides were left in the chamber for about 12 hours, and the self-assembly patterns were formed on the slides. The patterns generated from nanosphere self-assembly have hexagonal symmetry with their periodicity defined by the sphere diameter.

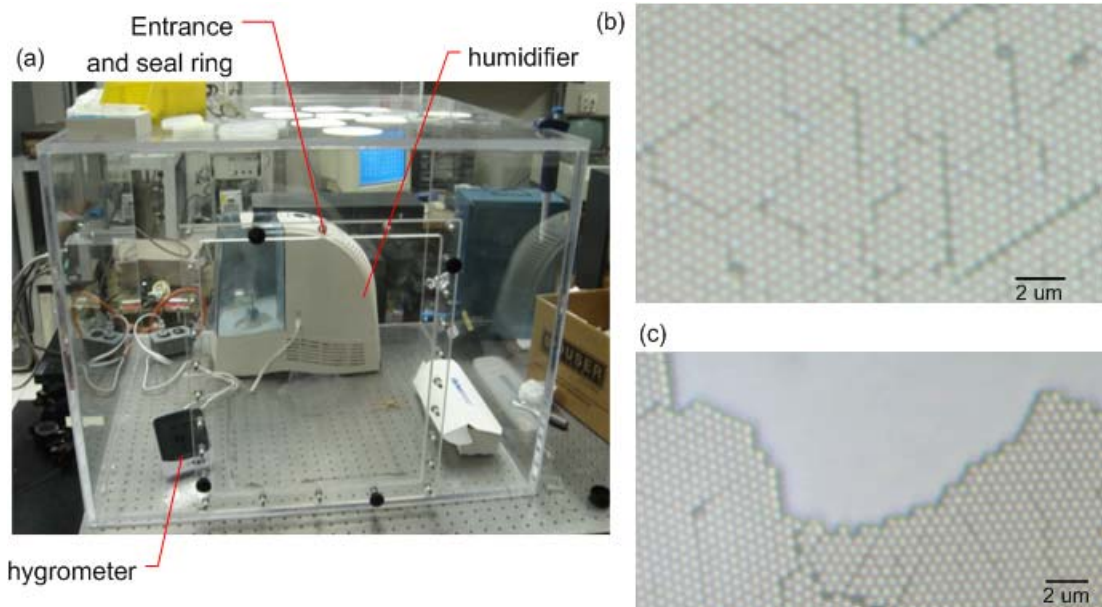


Figure 4-2 The tools for patterning large area nanosphere array on a glass substrate. (a) The humidity controlled box: a humidifier pumps water vapor into the sealed box, and a hygrometer is used to monitor the humidity; (b) Microscope image of the colloidal sphere arrays generated by self-assembly method. The pattern is hexagonal 2D arrays with some line mismatches; (c) A nanosphere array pattern with a boundary between the sphere array and the blank substrate region.

As in natural crystals, nanosphere patterns include a variety of defects that arise as a result of sphere size variation, point defects and line mismatch (slip dislocations). Typical defect-free domain sizes are 15-20 times of the sphere diameter. The environmental humidity

strongly influences the defect density. The speed of evaporation controls the time window the spheres can use to adjust themselves during the self-assembly process. The capillary force drives the spheres to move around and find the lowest energy state of the system. This process need to finish before the water thin film evaporates. On the other hand, the organized region cannot have too much water residue, because the spheres may change their location due to surrounding environment change thus causing a defect. The humidity range of 70-75% was found to be optimal.

4.1.2 Reactive Ion Etching (RIE)

After the arrays were patterned on the substrate, they were processed by Reactive Ion Etching (RIE) with oxygen plasma to reduce the size of each sphere. Both the lateral size and the height of the spheres were reduced by etching, and a non-close-packed hexagonal nanopillar array was formed. Generally speaking, there are three types of etching: 1) Reactive Ion Etching (RIE); 2) physical etching and 3) wet chemical etching, which is a combination of the previous two methods. The tool used in this work is Oxford Plasmalab 80Plus (Figure 4-3a) that has both RIE and PECVD systems. The RIE process is performed in a plasma chamber with computer controlling of the gas flow and RF power input. In RIE, reactive gases dissociate by the RF field impacts then transport to the underlying polystyrene sphere and react with it to form volatile products. Etching in a plasma environment combines the selectivity of purely chemical etching and the anisotropy of physical etching. Generally the physical etching is related to the ion flux and the chemical etching is related to the radical flux, and in some cases the ion energy is required to stimulate the chemical reaction.

The polymer sphere etching speed can be controlled by choosing gas component, chamber pressure, gas flow speed and input RF power. Oxygen is used as the only gas for polymer sphere etching, because it reacts with the spheres at a moderate speed and does not destroy the internal structure of the residual sphere. The oxygen plasma also does not react with the glass substrate and leaves the space between spheres flat. This flat surface has less scattering for the SPP, thus the periodicity of nanospheres is the dominant parameter to determine the surface plasmon resonance frequency. In experiment, fine tuning of the etching

thickness for spheres smaller than 1 μm is achieved by controlling the etching time. The input RF power is fixed at 150 W, the gas flow is 50 sccm and chamber pressure is 0.4 mTorr. The etching rate is 8~10 nm/s with the above parameters. Usually, the 600 nm diameter spheres is etched for 40 seconds and the residual particles are around 250~300 nm. For larger sphere (~10 μm), the chamber pressure is increased and a mixture of oxygen and CF_4 is used to accelerate the etching speed.

4.1.3 E-beam Deposition

Gold and silver are the commonly used metals for plasmonic devices, although copper and aluminum thin films also demonstrate plasmonic effects.[3,24] The propagation length of the SPP is the major consideration when choosing the metal, some other factors including the bulk plasma frequency and surface oxidation are also important. The surface plasmon enhanced transmission was firstly observed on a 200 nm thick silver film. The silver bulk plasma wavelength is in ultraviolet so that a silver film does not have any transmission peak in the visible light region. Its surface plasmon propagation length is about 40 μm thus the resonance coupling is very strong among the nanoholes in the array. Gold is another widely used metal for plasmon devices due to its passive chemical properties. Its SPP propagation length is around 16 μm which leads to shorter plasmon coupling length, and gold thin film has a bulk plasma peak at 500 nm due to d-band electron transition.

In this study, gold is used as the metal for plasmonic crystals. The gold film is fabricated by e-beam deposition method using the Edwards Auto Magnetron Sputtering System, as shown in Figure 4-3b. E-Beam Physical Vapor Deposition (EBPVD) is a physical vapor deposition method in which a metal target anode is bombarded with an electron beam under high vacuum. Atoms from the target sputter out and transform into the gaseous phase. These atoms travel through the vacuumed chamber and coating everything within line of sight, thus a thin layer of the anode material is coated onto the substrate. The vacuum chamber in this experiment was 3×10^{-5} Torr. A 2 nm layer of Cr was coated onto the substrate as adhesion layer with 0.02 nm/sec deposition speed, then 90~180 nm of gold was deposited at a speed of 0.08 nm/sec.

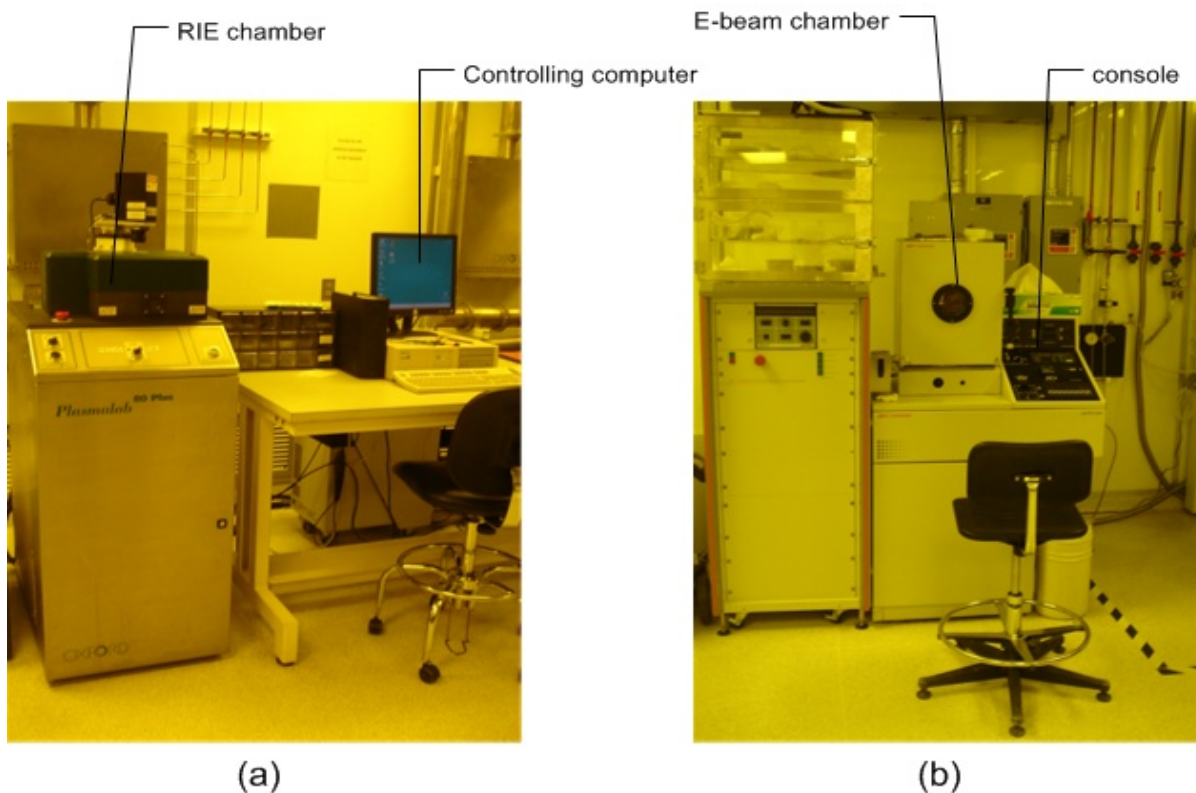


Figure 4-3 RIE and metal deposition tools in the lab. (a) The Plasmalab 80Plus RIE system; (b) The Edwards E-beam deposition system.

4.1.4 Annealing

The gold film deposited by e-beam method is in polycrystalline form. Its surface smoothness can be improved by annealing. At high temperature, the gold atoms move around and re-organize themselves such that dislocations in metal are removed. The RIE etched nanospheres also have rough surfaces due to non-uniform etching. SEM micrographs of a 5 μm polymer sphere after 40 minutes RIE etching and a 600 nm polymer sphere after 1 minute RIE etching are shown in Figure 4-4. These micrographs show that etching is stronger at the top of the spheres, and the side wall of spheres is not uniformly etched. Non-

uniform side wall etching is related to the internal structure of the spheres. Comparing the two micrographs, it shows that longer etching time leads to rougher side wall. The nano-array surface smoothness can be improved by annealing. By using suitable time and temperature, only the surface of the polymer spheres is melted, while the spheres keep their original shape. After cool down to room temperature, the surface of the spheres becomes smooth so that they have a round profile from the top view. The SEM micro-images for a nanobump patterned gold film before and after annealing at 300 °C for 60 seconds are compared in Figure 4-5. The nano-bumps before annealing are coarse while those after annealing are noticeably smoother. After annealing, the low frequency components are reduced in the Fourier transform plot. The reduction of low frequency components in the reciprocal lattice indicates that the long wavelength noise in the transmission spectrum will be reduced, which make the lowest order surface plasmon mode more distinguishable.

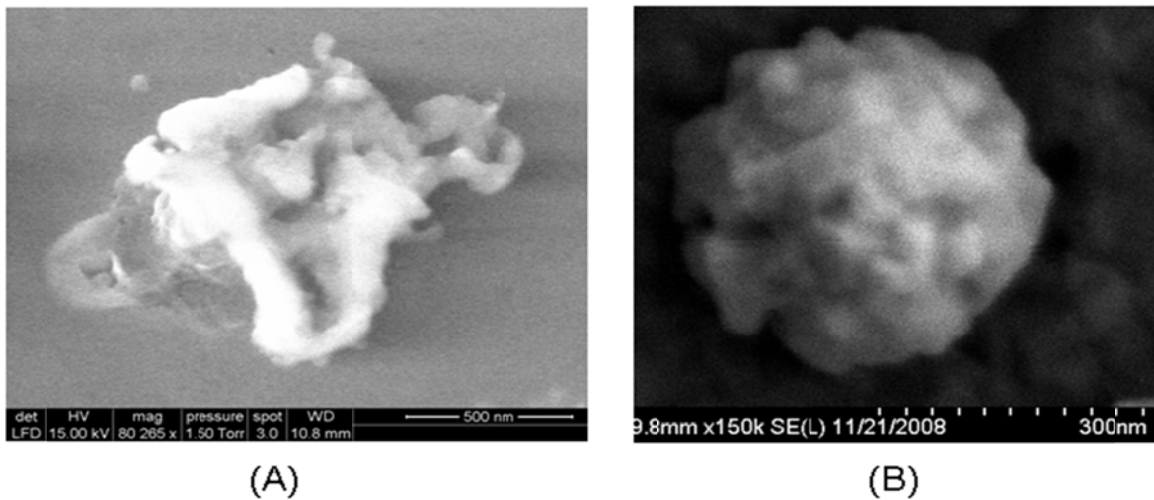


Figure 4-4 SEM images of RIE etched nanospheres. (A) A 5 μm diameter polymer spheres after 40 minutes RIE etching; (B) A 600 nm diameter polymer spheres after 1 minute RIE etching.

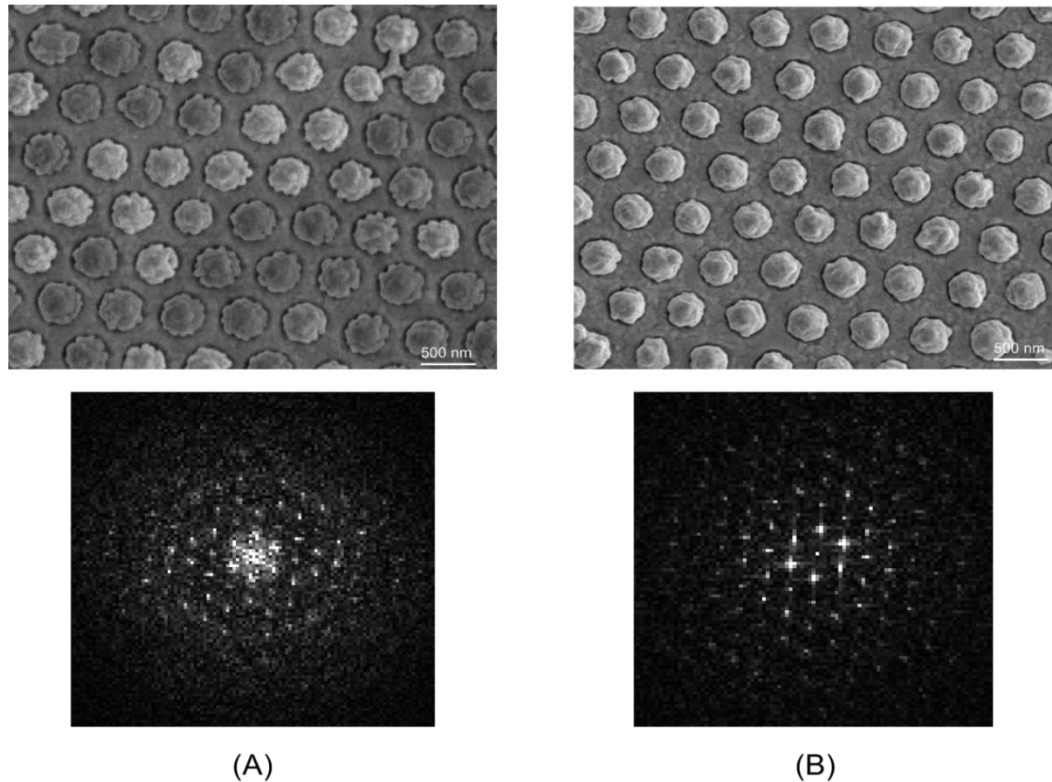


Figure 4-5 Annealing the gold film improves surface smoothness. (A) Before annealing, nano-bumps are coarse and there are a lot of low frequency components in the Fourier transform plot; (B) After annealing, the nano-bumps become smooth and those low frequency components are reduced.

4.1.5 Photolithography

Lithography techniques are the most commonly used step in micro-scale structure fabrication. E-beam lithography and photo lithography are the two major methods used. Their basic concept is to expose a photon/electron sensitive material that called photo resist with a defined pattern then followed by a develop process. The desired patterns will transfer to opening in the photo resist where the substrate is exposed and other parts of the substrate are protected by the photo resist. The basic operation steps employed in the lab are: 1) the photo resist is spin-coated on top of the substrate and soft baked to dehydrate the film; 2) the photo resist is exposed to a UV light source through a Cr mask; 3) the exposed photo resist is

submerged in a developer to define the patterns by selectively removing photo resist; 4) post processing steps is applied to the regions without photo resist.

Both positive and negative photo lithography can be done by controlling the exposure time and the baking time. Photo resist are polymers that consist of three major components: resin, a photoactive component (PAC), and solvent. The type of PAC and the operation to it determine the photo resist type: negative or positive. The major difference lies in the solubility difference between the exposed and the unexposed portions of the resist. In a positive photo resist, the photoactive component decomposes when exposes to UV light, thus these areas become soluble in developer. In a negative photo resist, the photoactive component cross links when exposed to UV light and hence areas exposed to UV light become insoluble in developer.[92]

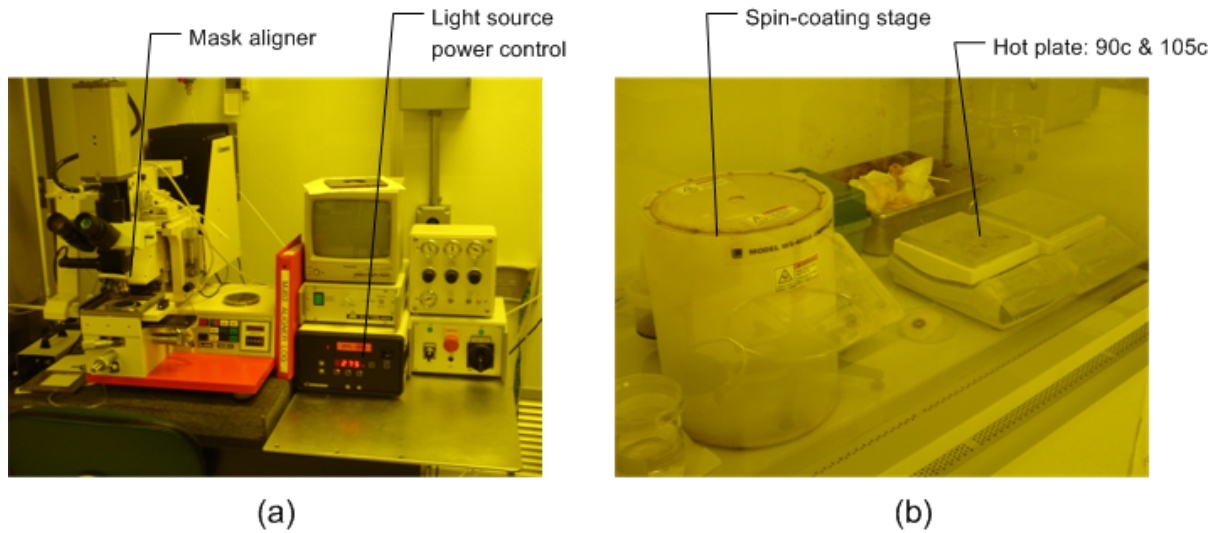


Figure 4-6 Photolithography tools in the lab. (a) The mask aligner and the UV light source for photolithography; (b) the spin-coating stage and the hot plates.

The photo lithography tool used in this study is a MJB 3360 mask aligner with a 365 nm (i-line) UV light source that has exposure energy of 275 mJ/cm^2 , as shown in Figure 4-6. AZ5124E photo resist was used as both positive and negative photo resist. The positive mode

uses 12 seconds exposure time followed by 60-75 seconds of developing time. The negative mode uses 3 seconds exposure time then baked the samples at 115 °C for 90 seconds. After that, 90 seconds of flood exposure without any mask is applied then the photo resist are developed. Photo lithography is used for defining concave boxes for nanosphere self-assembly, and for preparing gold pads for FIB milling.

4.1.6 Focused Ion Beam (FIB) Milling

The FIB has been a powerful tool in the semiconductor industry mainly for mask repairing, device modifying, failure analysis and integrated circuit debugging. It operates similarly to the principle of a Scanning Electron Microscope (SEM) except that it uses a finely focused beam of ions rather than electron beam. It can be operated at low beam current for imaging or at high beam current for site specific writing. The ion beam writing process, also known as FIB milling, is the process of transferring patterns by direct impingement of the ion beam on the substrate.

The principle of FIB direct write or milling is to operate a FIB with a proper beam size, shape, current and energy to remove a required amount of material from a pre-defined location in a controllable manner.[86] In this way, high-precision and complex structures can be sculpted. The ion beam has many advantages over other high-energy particle beams. For example, as compared to photons or electrons, ions are much heavier and can strike with much greater energy density on the target to directly write patterns on hard materials, such as semiconductor, metal or ceramic.

The basic components of a FIB system are normally an ion source, an ion optics column, a beam deflector and a substrate stage. The whole setup is usually placed in a low-pressure chamber evacuated to the 10^{-7} Torr regime. This is done so that the mean free paths of the ions are increased and the strength of the beam is not reduced due to the interference of the particles in the chamber. This system usually produces ion energies from 50 to 250 keV with the minimum full width at half-maximum (FWHM) beam diameter down to 50 nm and it can be used for both sputtering and implantation. The ion intensity is highly non-uniformly distributed, and its intensity is close to a Gaussian profile. Several ion sources can be used in

this type of system to produce different types of ion sources. We used gallium ion source to make patterns on gold film, the SEM image of two FIB prepared patterns are shown in Figure 4-7. The process usually takes a few minutes to make a 20 μm by 20 μm size pattern depending on the film thickness. The FIB milling is limited in pattern size and also has beam drifting issue during long time processing. Moreover, it has to work with conductive material since surface charging will be a serious issue for non-conductive material and the ion beam will be scatter by charges accumulated on the surface.

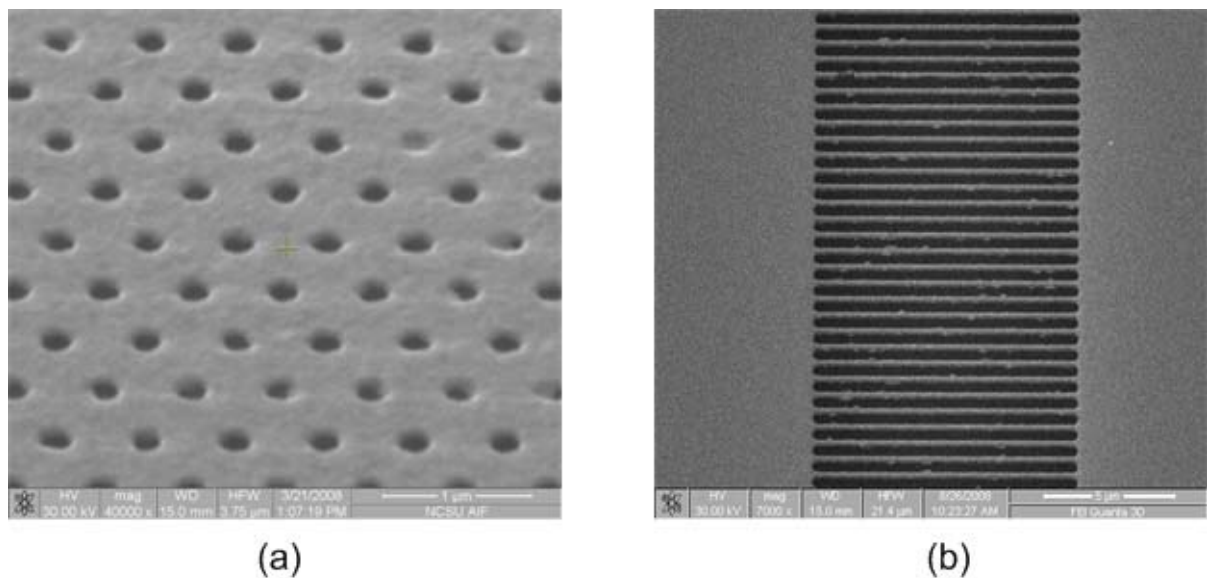


Figure 4-7 1D and 2D arrays fabricated by FIB milling. (a) A 2D hexagonal array and (b) an 1D grating structure fabricated by FEI Quanta 200 3D FIB system.

4.1.7 Nano-stamp Imprint

Alternate methods have been developed to prepare the nanohole/bump arrays. Nano-imprint was widely used as a relatively low cost method to fabricate large size nano-structures with feature size around 100 nm.[93] It has the ability to make very small feature (~ 10 nm) with advanced tools and special surface treatment.[94] Nano-imprint lithography was first developed by Prof. Stephen Chou and his students around 1996.[95] It is a relatively

simple and low cost process, as shown in Figure 4-8a. The principle of nano-imprint lithography is unique to other nano-scale lithography techniques. The pattern is generated by duplicating the protrusion of the imprinting stamp onto a resin layer on the substrate. Reversed stamp pattern is formed on the substrate. From the nature of imprint method, it is a one-step large area patterning process without serious alignment issue [3].

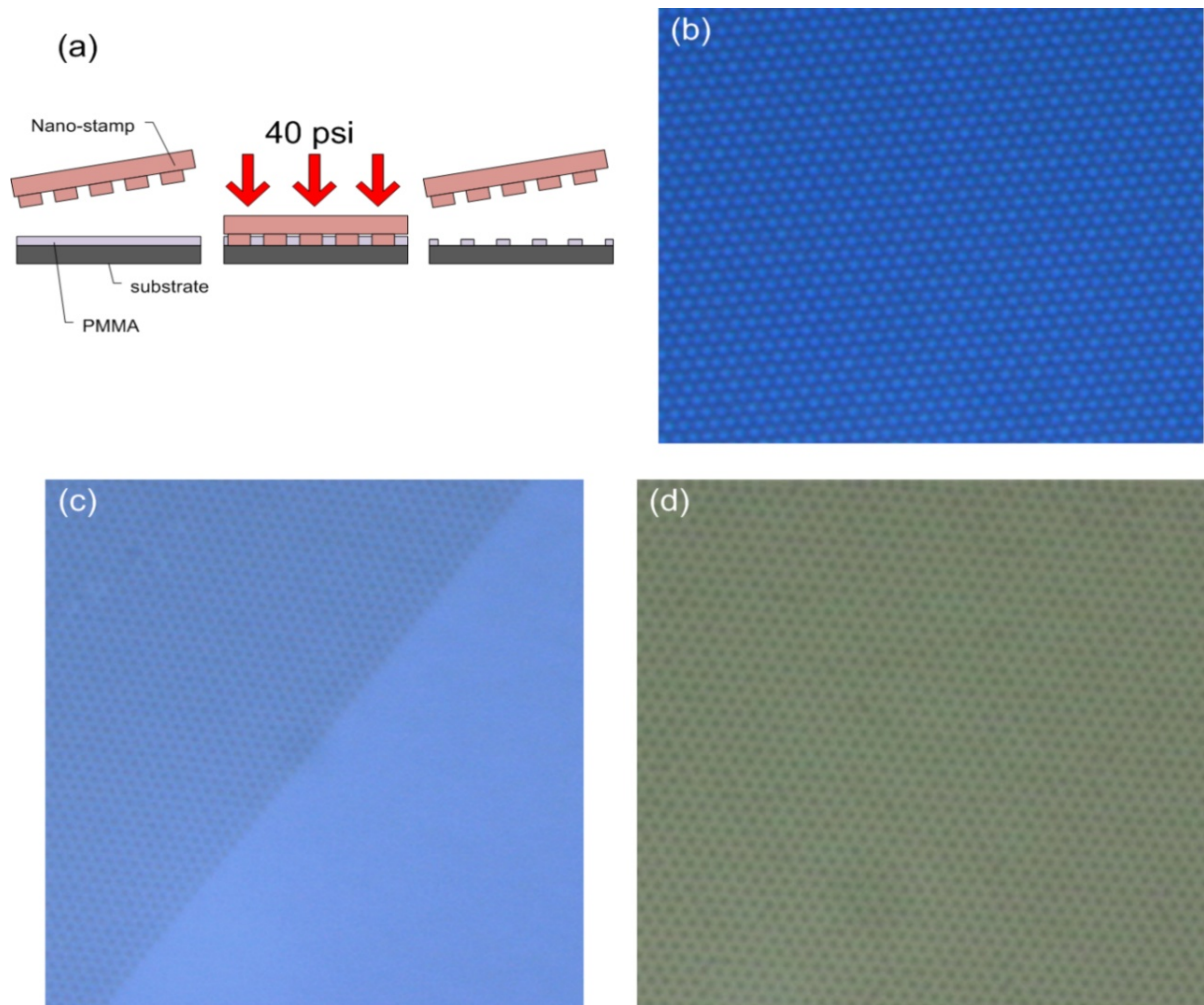


Figure 4-8 Hexagonal arrays fabricated by the nano-imprint technique. (a) Process flow of the nano-imprint method; (b) The optical microscope image of a 600 nm period nano-bump silicon stamp; (c) the PMMA layer with and without imprinted nanohole array patterns; (d) The gold/PMMA/Glass structure with the nanohole array pattern.

The stamp used in nano-imprint can be created with optical lithography or interference lithography methods. There were many research works using interference lithography to make rectangular or hexagonal patterns.[96,97,98,99] The basic principle of this method is the same as interferometry or holography. An interference pattern between two or more coherent light waves is set up and recorded in a recording layer, which usually uses photo resist. This interference pattern consists of a periodic series of fringes representing intensity minima and maxima of light. Upon post-exposure processing, a photo resistor pattern corresponding to the periodic intensity pattern emerges. 2-beam interference method is the most basic way to make parallel lines, while the fringe spacing is determined by the wavelength of light and also the incident angle.[100] Rectangular dots array can be made by rotating the substrate by 90 degrees and then exposing once more. 3-beam interference is also developed to make hexagonal patterns with one exposure.[96] The drawback for interference lithography is the inflexibility to change the pattern design, and it cannot generate complex features or controllable defect points/lines in a periodic structure.

The nano-stamps used in this study are from LightSmyth Technology. Hexagonal and rectangular nano-hole/bump array patterns are fabricated on silicon using photon lithography method. The period of the stamp patterns vary from 500 nm to 700 nm, and the diameters of each bump/hole vary from 165 nm to 240 nm. The optical microscope image of a 600 nm period nanobump stamp is shown in Figure 4-8b. The imprint process transfers the stamp patterns onto a PMMA layer coating on a glass substrate. This is operated at 40 psi and 140 °C. After the imprint process, a layer of gold was deposit onto the patterned PMMA layer to make a nanohole array plasmonic crystal, as shown in Figure 4-8c and 4-8d.

4.1.8 Summary of the Fabrication Methods

Nanosphere lithography is the primary fabrication method to prepare the plasmonic crystals in this study. Its process flow is summarized in Figure 4-9. The close-packed nanosphere arrays were patterned on glass substrates with tip-directed coating and drop-coating methods. Oxygen plasma was used to etch the spheres and a layer of gold with 90-180 nm thickness was deposited by e-beam deposition. The resulting surface was a

hexagonal array nanobump pattern. The spheres can be removed with acetone merged sonic-cleaning and left a nanohole array in the gold film. The nanosphere lithography method has a few advantages over the other lithography techniques: First, it is a cost-effective process to fabricate nano-scale patterns with plasmonic properties. Nanosphere lithography uses a small amount of colloidal to generate regular colloid arrays, and the colloidal is commercially available at a relatively low cost. No complex equipment is required to create patterns with features size around tens of nanometers. Second, it is a simple process. Templates formed by self-assembly can be achieved by tip-directed coating or drop-coating methods. Third, the feature scales are controlled simply by changing the size of the colloidal particles, together with some following processes such as RIE or tilted deposition. The drawback for nanosphere lithography is that the patterns are limit to several simple geometries with high-level symmetry. Defect is another big problem in the self-assembly process. Two sources contribute to the defects formation in the patterns, one is the derivation in nanosphere size that causes point defect, and the other is the environmental variation that causes line defects. In fact, the self-assembly pattern can be viewed as polycrystalline assembly of small blocks of plasmonic crystals, where each block is about 10-20 times of the sphere diameter.

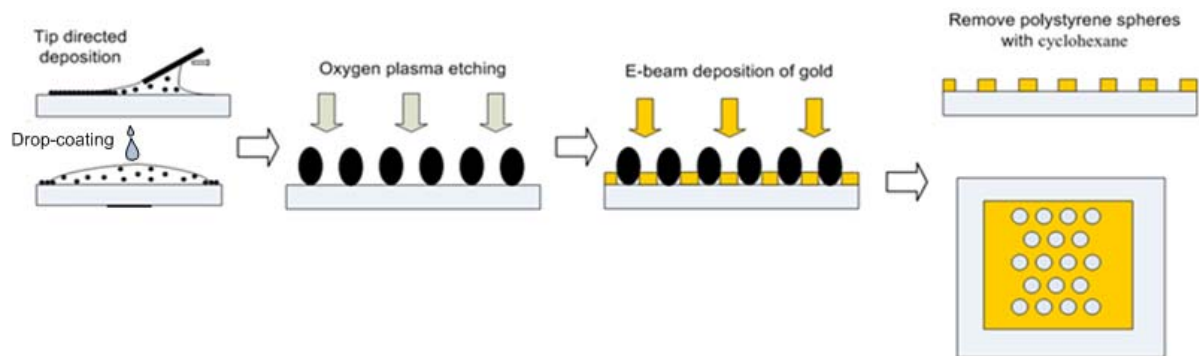


Figure 4-9 Summary of the nanosphere lithography process flow.

The nano-imprint method is used as an alternative to the self-assembly method. It can also fabricate large area hexagonal patterns, but this process may suffer from pattern depth variation. The nanohole depth changes among different locations, because the imprint process is not uniform when the pressure is applied. This causes the transmission spectra change for different spots on an array. The nanosphere lithography method does not suffer from this effect, since the RIE process is uniform. Both of the methods are relatively simple comparing to those lithography methods, and they are good at making periodic patterns for plasmonic crystal study.

4.2 Device Characterization

4.2.1 Scanning Electron Microscope (SEM) Imaging

The smallest feature size on a plasmonic crystal is around 50~200 nm, which is smaller than the resolution of an optical microscope. Scanning electron microscopy was applied to image the gold surface with nanobump and nanohole arrays. The SEM is a type of electron microscope that uses high-energy beam of electrons to scan the sample under test and collect secondary electrons and/or back scattered electrons for image generation. The electrons interact with the atoms on the sample surface and produce signals that contain information about the sample's surface topography, composition, and other properties. The SEM produces very high-resolution images because of the short wavelength of the high energy electron. It can reveal details less than 1 nm in size. Due to the very narrow electron beam, SEM micrographs have a large depth of field that can show a three-dimensional objects shape which is useful for understanding the surface structure of a sample.

The surface geometry of a nanobump patterned gold surface is shown in Figure 4-10. The top one is a SEM micro-picture for an $18\ \mu\text{m} \times 18\ \mu\text{m}$ nanobump arrays, with the insert shows the hexagonal lattice structure. The bottom one is a cross section AFM plot showing that the roughness of the surface is about 150 nm. The 600 nm diameter spheres were RIE etched for 75 seconds with oxygen plasma, reducing their diameter to ~150 nm. A gold layer of 90 nm was deposited. The nanobump diameter was about 300 nm, which included the

sphere core size and the side wall thickness. By varying the RIE time, the nanobump diameter could be varied from 200 to 600 nm with their periodicity determined by the initial size of the spheres.

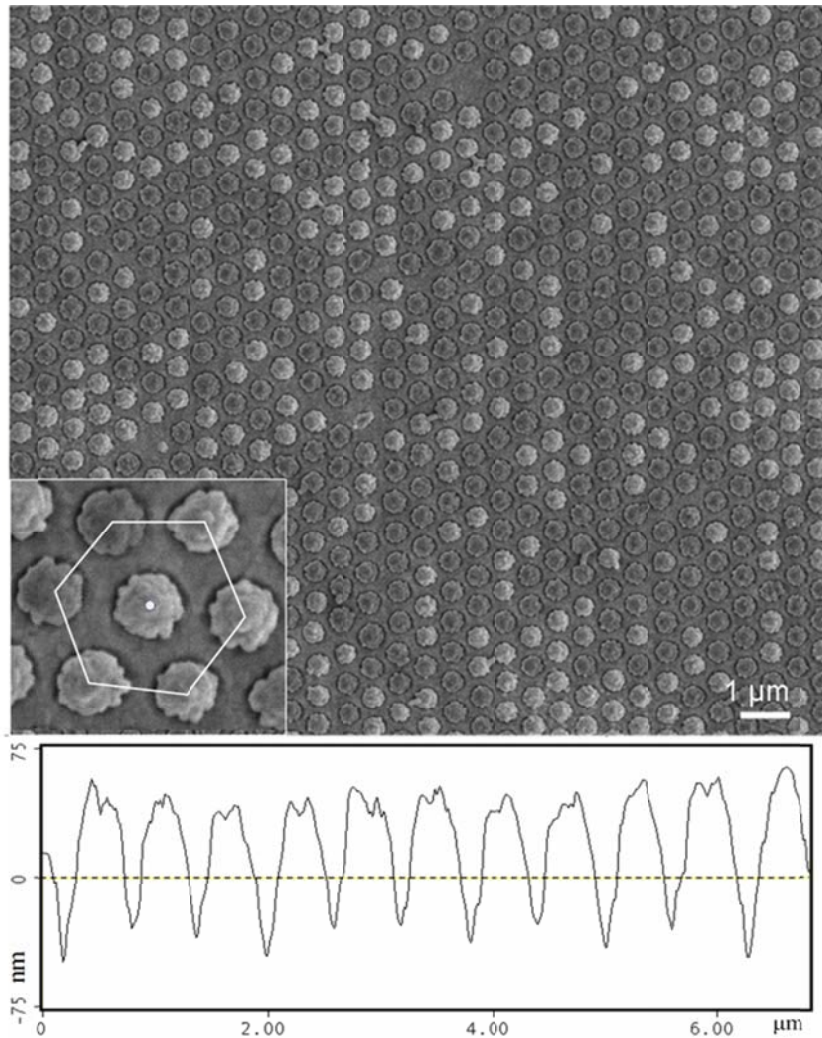


Figure 4-10 SEM picture for a 600 nm periodicity nanobump array plasmonic crystal. The insert shows the hexagonal symmetry of the pattern. The nanobump diameter is around 300 nm. The AFM cross section profile shows the height of the nanobumps.

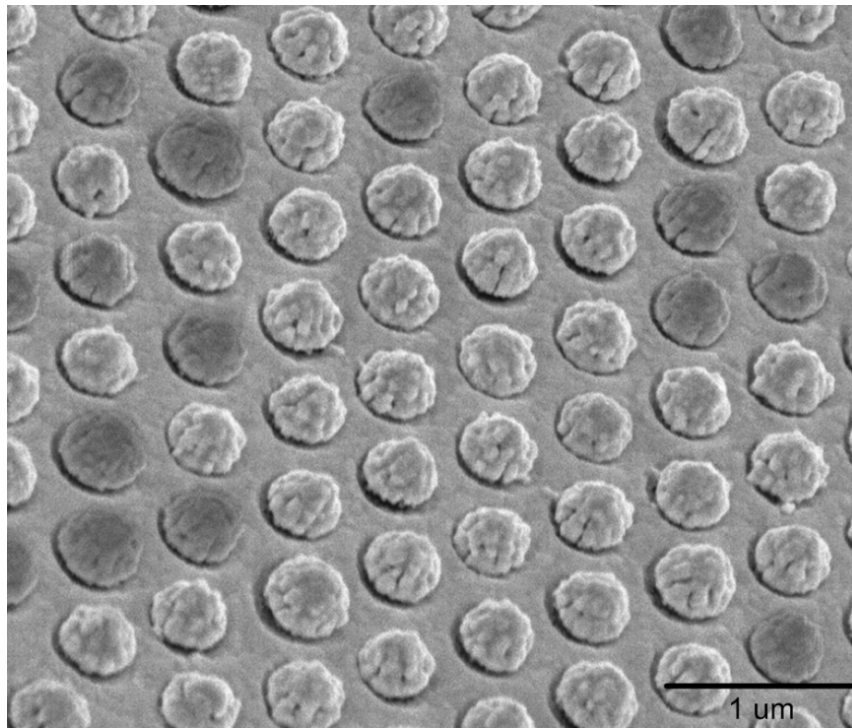


Figure 4-11 SEM micro-image of a 600 nm period nanobump array. The viewing angle is 30 degree from the surface normal. A gap can be seen between the root of a sphere and the gold thin film.

The brightness of the nanobumps is different in the SEM pictures (Figure 4-10). Some of the nanobumps are the same color as the flat gold film region and other bumps are brighter in color. This is caused by the voltage contrast effect. In SEM imaging, a region will charge up if there is no good path connecting it to ground, which usually happens with insulating materials. The charged up region scatters more electrons to the detector than a grounded region, thus it shows brighter color. This effect is applied in IC defect inspection at sub-micron scale, where bad via cause part of the circuit becoming floating. The cross section view of a nanobump is shown in Figure 4-12. The gold film is thicker at the top of the bump, and it is thinner at the root. From a tilted viewing angle shown in Figure 4-11, we find that there is a gap between the cap of the nanobump and the flat film region, thus the cap may not connect to the grounded film region. If the nanobump is electrically floating, it shows brighter color. Other grounded bumps are darker in color.

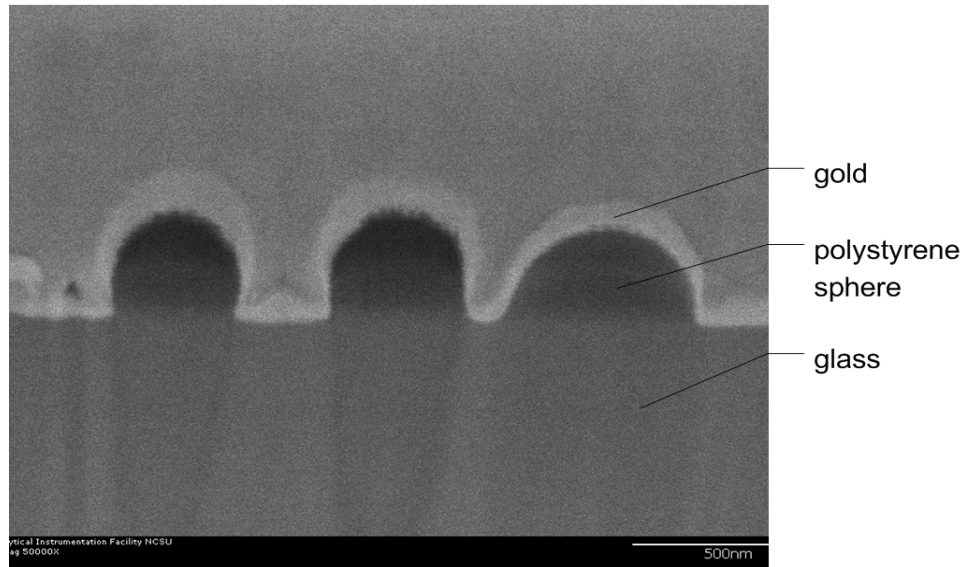


Figure 4-12 A cross section SEM image of the nanobump array surface. The nanobumps were cut by FIB milling after the surface was coated by a platinum protection layer. The gold layer on top of the sphere is greatly thicker than at the side wall. Breaks can be found at the root of the side wall.

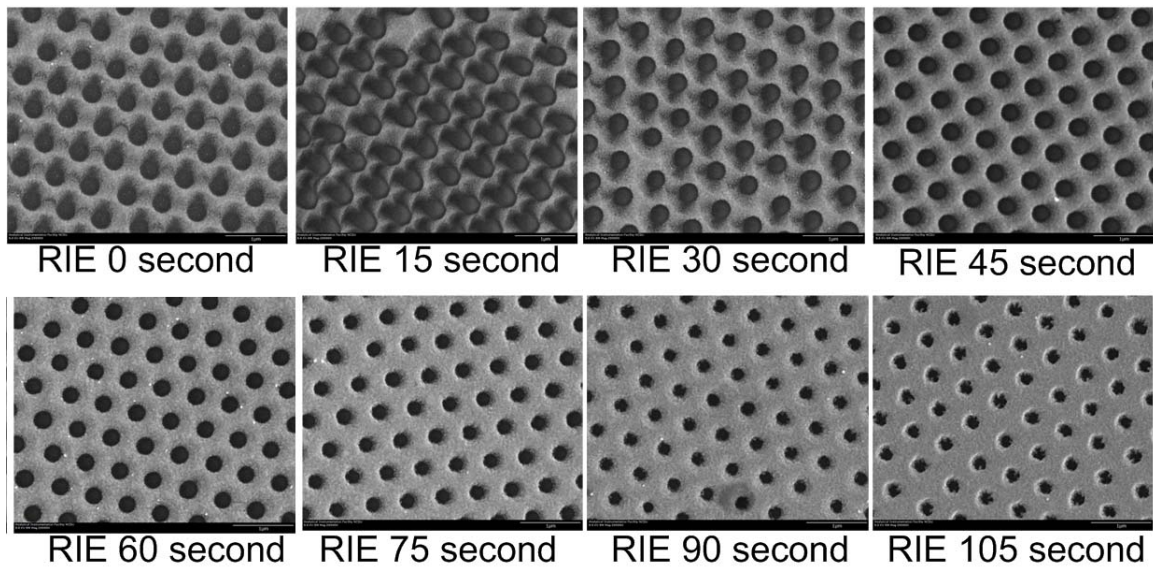


Figure 4-13 Nanohole arrays with different RIE time. The diameter of the nanoholes was reduced when longer etching time was applied. The smallest nanohole that can be achieved was around 100-150 nm in diameter.

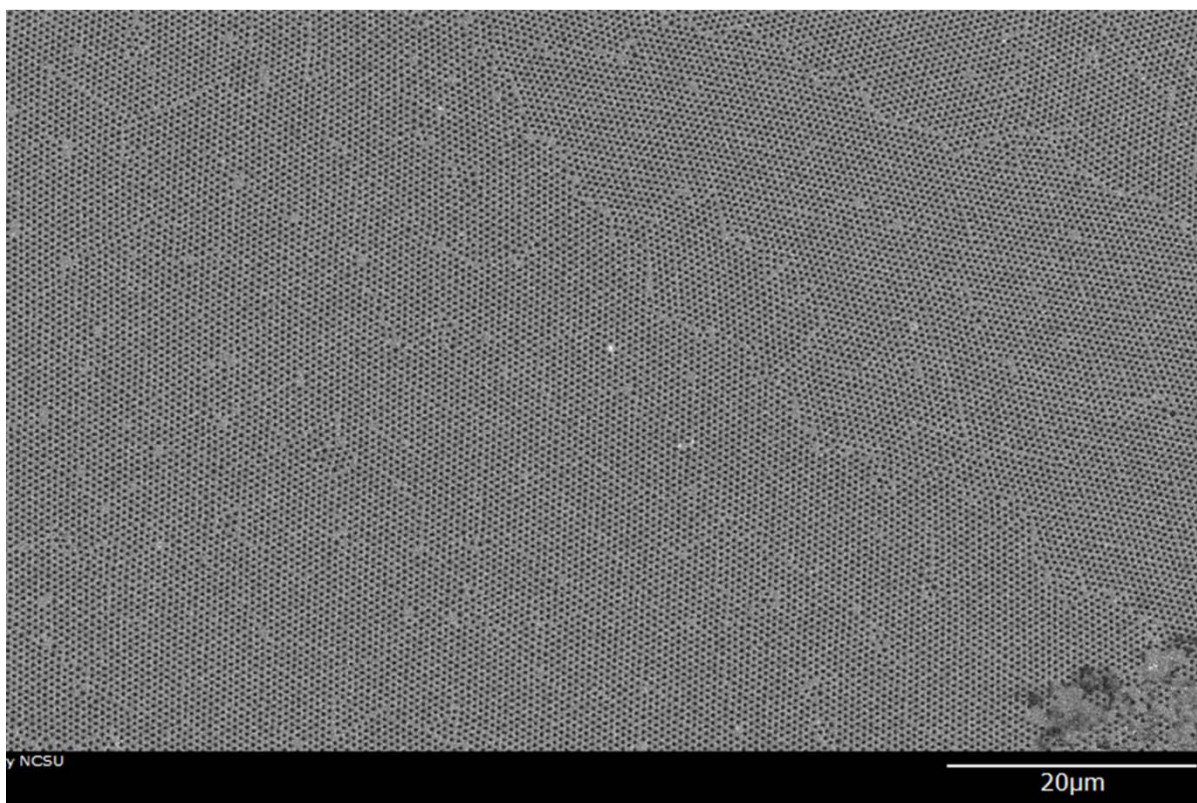


Figure 4-14 A large area ($\sim 80 \mu\text{m} \times 50 \mu\text{m}$) hexagonal nanohole plasmonic crystal with a 90 nm gold layer. The full size of the well-organized pattern is $\sim 10 \text{ mm}^2$ size.

4.2.2 Atomic Force Microscopy and Optical Microscope

Atomic Force Microscopy (AFM) is a type of scanning probe microscopy that has very high resolution which is on the order of fractions of a nanometer. It uses a silicon nitride cantilever with a sharp tip at the end to scan the sample surface. The cantilever is oscillated at a frequency slightly above its resonant frequency with the amplitude of a few nanometers. When the tip is brought into proximity of the surface, forces between the tip and the surface changes the frequency and phase of the oscillating tip. By collecting the above information and processing by software, the topographic image of the sample surface can be constructed.

The AFM surface profiles of the nanobump (Figure 4-15) and nanohole (Figure 4-16) arrays were collected. The AFM image can provide information about the spheres height, which is not available in the SEM micro-image. The nanobump height for the 600 nm

periodicity spheres are around 150~300 nm, depending on their RIE time. Because of the shape of the AFM tip, it cannot measure concave with large aspect ratio. The root of the nanobump connecting to the metal surface is an almost 90 degree right-angle corner, which can be seen in the SEM image. This feature is smoothed in the AFM images, so that the bumps looks like pyramids. In the nanohole image (Figure 4-16), the edge of the holes is sharper because the gold film thickness is less than 100 nm, which is not a large step for the AFM tip. General speaking, the AFM tool can be used to measure the height of the surface features, and it works better with small surface steps or concaves with small aspect ratio.

Optical microscope is also an important tool to image the plasmonic crystal surface pattern. This study uses an OLYMPUS BX60 microscope with both bright field and dark field imaging methods. It has a CCD camera connected, which can capture pictures for the surface pattern under inspect. An image for the 600 nm periodicity surface pattern is shown in Figure 4-16, which is collected using the 100X objective lens.

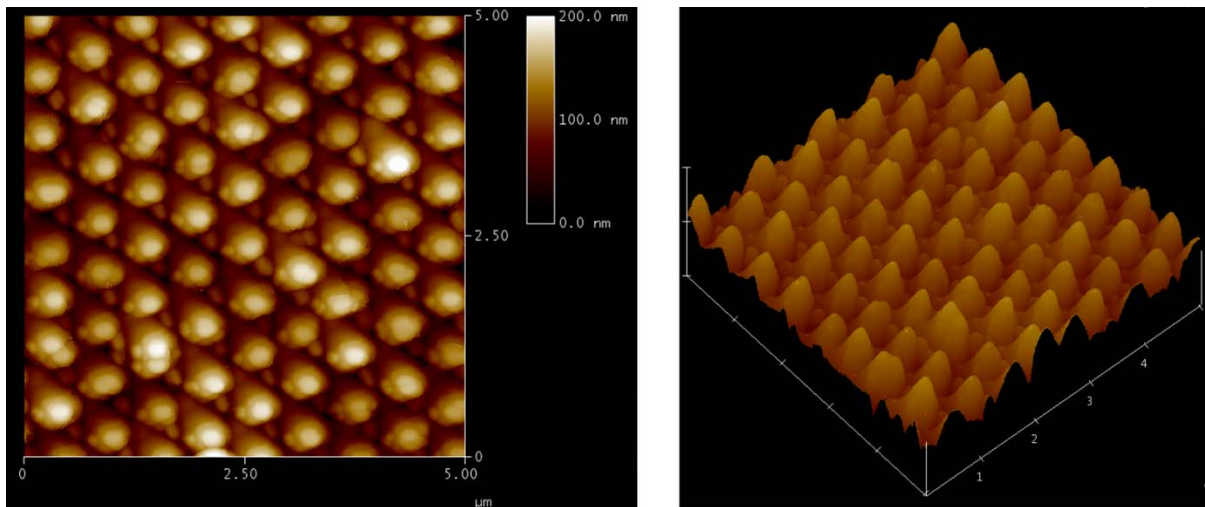


Figure 4-15 AFM images of a 600 nm period nanobump array patterned gold film with (a) top view and (b) 3D side view.

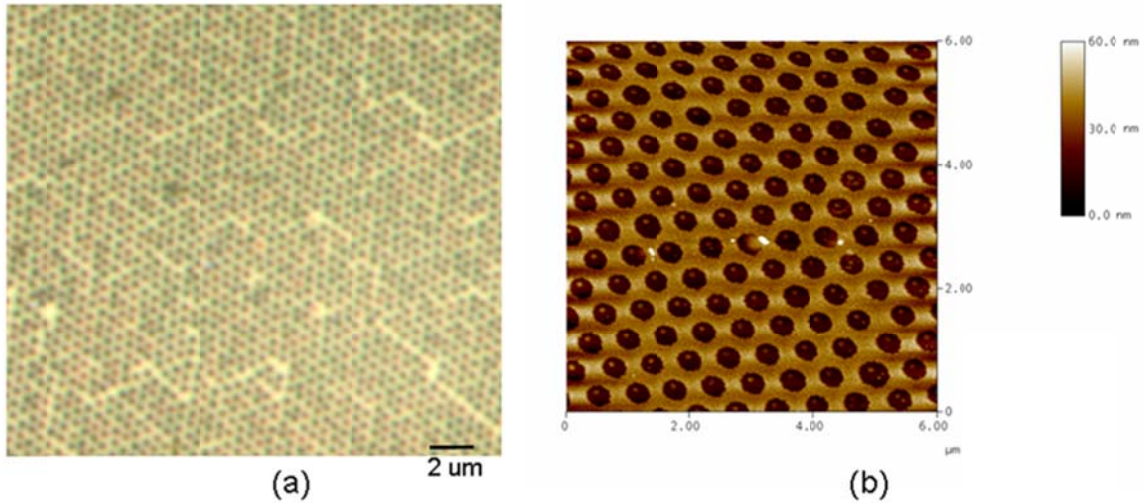


Figure 4-16 Surface geometry of a nanohole array. (a) Optical microscope image and (b) AFM image of a 600 nm periodicity nanohole array plasmonic crystal with 30 second RIE.

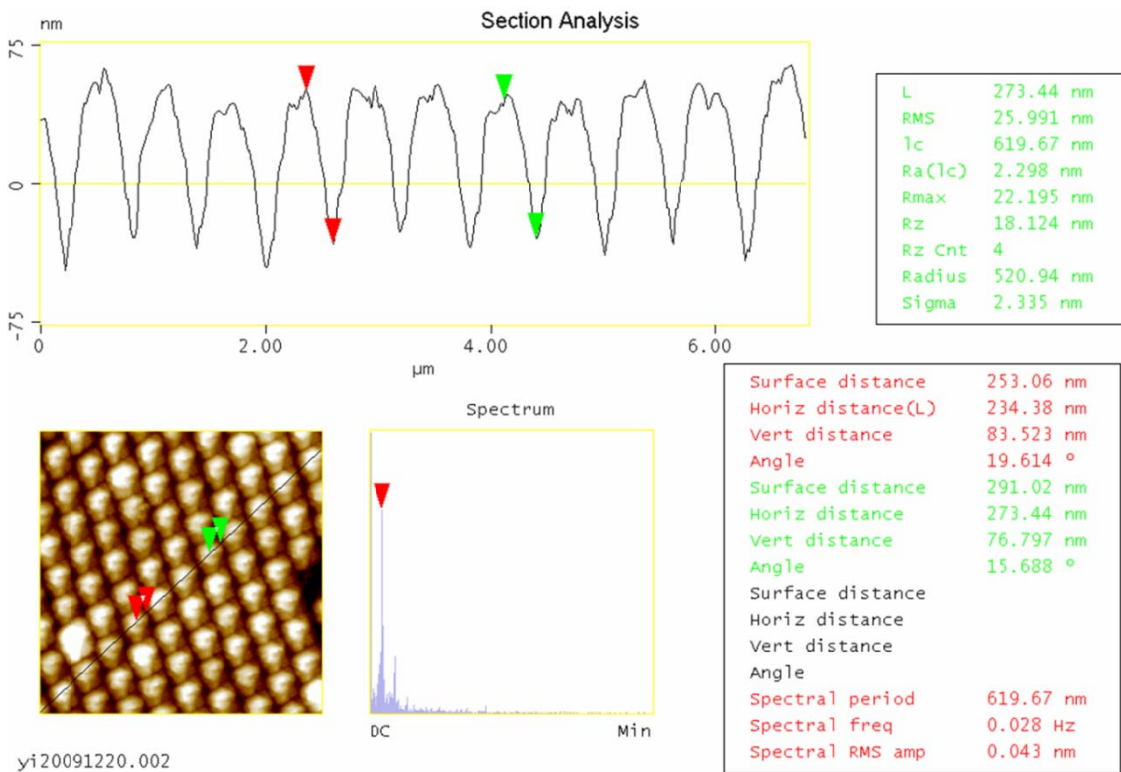


Figure 4-17 Height profile analysis for the AFM image of a nanobump array. The cross section peak distance and the 2D frequency information can be extracted from it.

4.2.3 Optical Spectrum

Optical spectrum is the major technique to characterize the dispersion properties of the plasmonic crystals. The transmission spectra of the patterned metal surfaces were collected by an optical configuration shown in Figure 4-18. A tungsten filament bulb that emits light ranging from 400 to 900 nm was used and an aperture was placed in front of it to limit the size of the light source. The light was focused to a very small area ($\sim 20 \mu\text{m}$ diameter) on the surface by an 80X objective lens. At the focus point, the light beam was almost collimated and its propagation direction was perpendicular to the metal surface. The transmitted light through the sample was collected by another objective lens (20X) and coupled into a fiber detector. OceanOptics USB 4000 spectrometer was used to collect the spectra, as shown in Figure 4-19. The integration time for collecting the spectra varies from 10 ms to a few seconds, depending on the gold film thickness. This integration time was adjusted to let the peak spectrum intensity reach the spectrometer's upper detection limit, which is $\sim 60,000$ (arbitrary unit). This protocol was applied to avoid any non-linear response of the spectrometer with different input intensities.

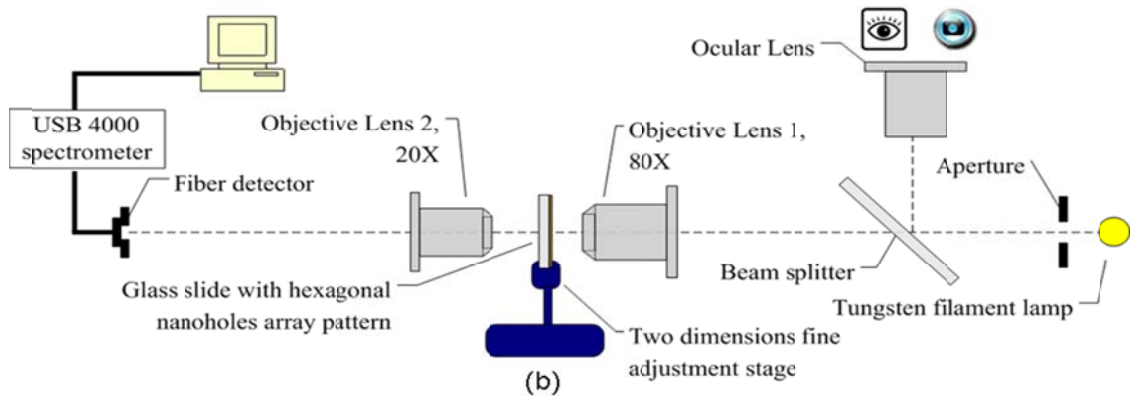


Figure 4-18 The optical configuration to collect the transmission spectra of a $20 \mu\text{m}$ diameter spot on the sample.

Angle resolved spectra for large area plasmonic crystals were also collected. The two objective lenses were replaced by two plano-convex lenses with focus length $\sim 10 \text{ mm}$. The light from the lamp passed through the first convex lens and incident on the sample as a

collimated light beam. The sample stage was driven by a step motor, which had a resolution of 1/32 degree, as shown in Figure 4-20. The travel distance of the stage was about 15 degrees. Large angle range spectra (± 60 degree) can be generated by connecting data from several sweeps. The second convex lens collected the transmitted light and coupled it into a fiber aperture.



Figure 4-19 OceanOptics USB 4000 spectrometer.

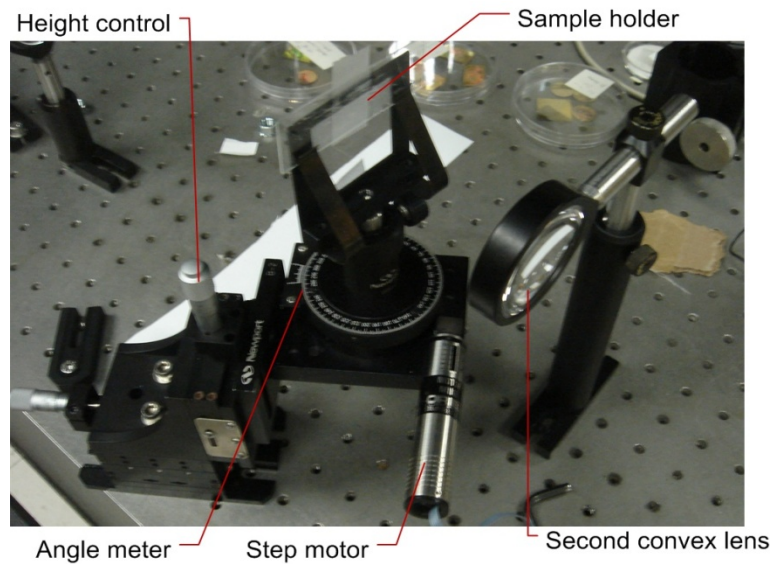


Figure 4-20 The rotation stage for collecting the angle resolved transmission spectra of a large area plasmonic crystal.

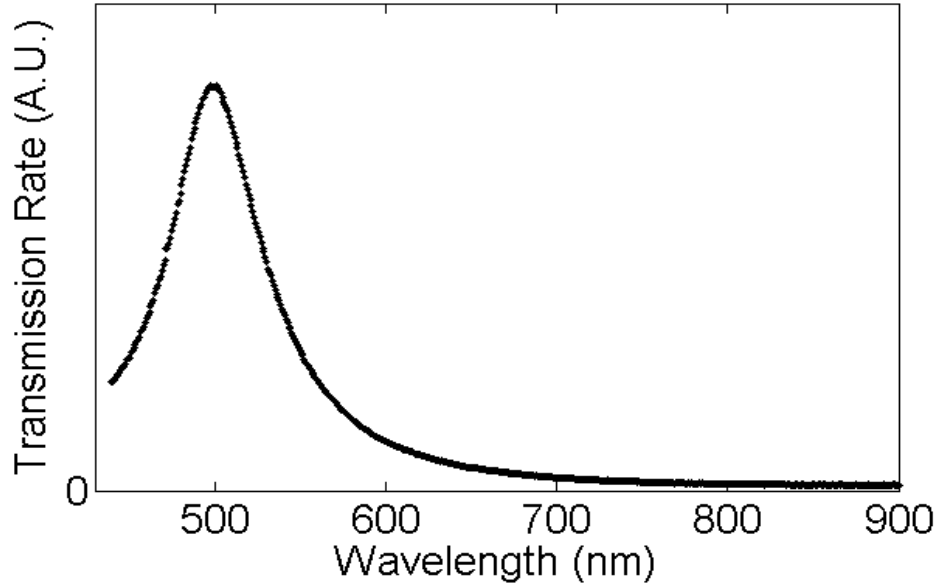


Figure 4-21 Transmission spectrum of a 90 nm flat gold film.

The USB4000 spectrometer from OceanOptics was used to collect the optical spectra at 400 - 950 nm wavelengths. It uses a 3648 element Toshiba linear CCD array for high signal-to-noise spectrum sensing, and can communicate with PC using the USB port. Its portability makes it very convenient for outdoor spectra measurement. The transmission spectra for a 90 nm flat gold film collected by this spectrometer is shown in Figure 4-21. It has a single peak around 500 nm, which is related to the electron transitions between the d-bands in metal and the Fermi level in the conduction band. The intensity of this peak can be used to compare the gold film thickness among different plasmonic crystals with similar patterns.

The transmission spectra of the hexagonal nanoholes array plasmonic crystals with different film thickness are shown in Figure 4-22. The spectrum on the left was collected from a sample with 100 nm thickness gold film, and the right one was collected from a sample with 200 nm thickness film. The spacing between the nanoholes was 600 nm for both samples. The two spectra show a common transmission peak at 500 nm, which is a characteristic of the gold film and is not dependent on the surface geometry or the environment. Both of the spectra show a strong transmission enhancement between 600 nm and 750 nm, and they show a similar profile at the enhanced transmission region. The

difference between the two spectra is the ratio between the 500 nm peak and the enhanced transmission peak. The absorption increases with the film thickness, thus the transmission at 500 nm is reduced. However, the enhanced transmission generated by the excitation of SPPs does not decreased as quickly as the 500 nm peak. The 200 nm thickness nanosphere patterned gold film shows a strong enhanced transmission in the red and NIR region.

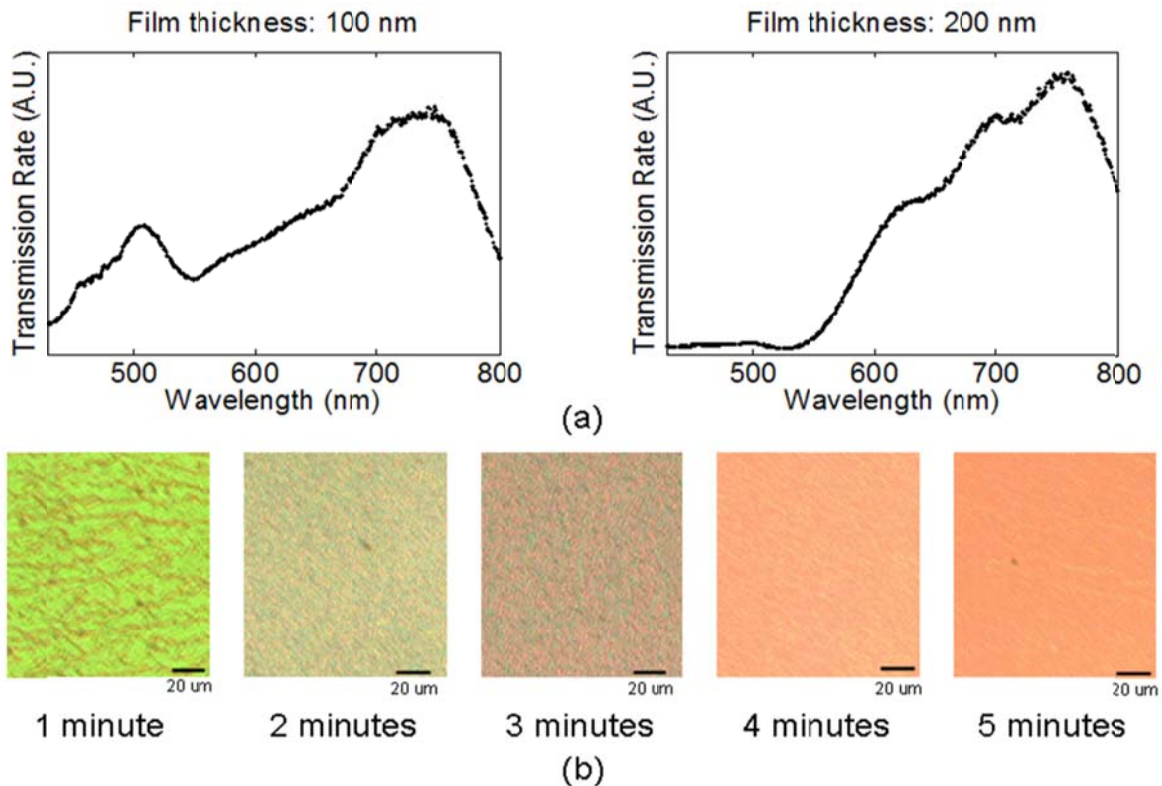


Figure 4-22 Spectra of a collimated white light beam for several patterned film structures. (a) Transmission spectra for the nanoholes array with different film thickness; (b) Micro-image (reflection mode) for 600 nm spacing nanoholes with different RIE etching time (1-5 minutes)

The nanoholes diameter can be modified by changing the RIE time. Increasing the etching time reduced the sphere's diameter, thus smaller holes were made. Samples with different RIE time (1-5 minutes) were prepared and observed under optical microscope in

reflection mode, as shown in Figure 4-22. The reflected light of the nanohole array patterned surface showed green color when 1 minute of RIE etching was applied to the spheres. With a longer etching time, the holes diameter shrank and the surface showed strong reflection for the red light. The reflected light changed to pink color when 5 minutes of RIE etching was applied. This change is caused by the shifting in localized surface plasmon frequency, which is determines by the nanohole diameter. The periodic for the nanoholes were 600 nm for all these plasmonic crystals, thus it showed that the size of the unit cell in the surface patterns will strongly influence the film's transmission and reflection properties.

CHAPTER 5

PLASMONIC CRYSTALS WITH DIFFERENT SURFACE DIELECTRIC MATERIALS

Based on manuscripts:

Fabrication of Nanoshell Arrays Using Directed Assembly of Nanosphere

Yi Lou, Leda M. Lunardi, John F. Muth

IEEE Sensors Journal Vol. 10 No. 3, March 2010 (617)

Thermochromic Effect of the Gold Plasmonic Crystal Tuned Vanadium Dioxide Metal–Semiconductor Transition in the Visible Light Wavelength

Yi Lou, Yan Wang, John F. Muth

(To be submitted to Applied Physics Letters)

Optically Controlled Optical Modulator using a Self-Assembled 2D Plasmonic Crystal

Yi Lou, John F. Muth

MRS 2010 Spring Conference (poster and to be published in MRS proceeding 1248E)

Patterned Hybrid Nanohole Array Surfaces for Cell Adhesion and Migration

Nathan P. Westcott, Yi Lou, John F. Muth, and Muhammad N. Yousaf

Langmuir 2009, 25(19), 11236–11238

The resonant modes of a plasmonic crystal are sensitive to the surface dielectric environment, which can be utilized to design chemical sensors and optical modulation devices. The spectra response of a hexagonal symmetry plasmonic crystal with water and some other chemicals on top of its surface were collected and analyzed. Vanadium dioxide is a semiconductor material that changes its optical dielectric constant during the crystallographic transformation. A temperature sensitive device was made by stacking the VO₂ film on top of a plasmonic crystal, and its optical properties in the visible light wavelength were studied. P3HT is a photon sensitive material that is commonly used in organic solar cells. An all optical modulator was designed utilizing the optical properties of both the P3HT and the plasmonic crystal. Large periodicity nanohole arrays have been used in biology cell study. It was chemically modified to render the gold regions inert to cell attachment in order to let the adhesive interaction only happens in the nanoholes. Swiss Albino 3T3 cell migration rate on this surface was studied.

5.1 Introduction

The enhanced optical transmission through periodic arrays of nano-holes/bumps in a metal film is related to the excitation of surface plasmon polaritons. These structures support plasmonic excitations of the SPP Bloch modes caused by the periodic modulation of the metal-dielectric interface. Satisfying the momentum matching conditions, some of these Bloch modes are optically activated and can be coupled with the incoming photon. When light normally incident upon the crystal under certain wavelengths, photon exchanges energy with plasmonic modes when diffraction from the periodic structure provides momentum matching that satisfies the surface plasmon dispersion relation:

$$k_{SP} = \frac{\omega}{c} \sqrt{\frac{\epsilon_d \epsilon_m}{\epsilon_d + \epsilon_m}}$$

where ϵ_d and ϵ_m are the dielectric constant of the surface dielectric material and the metal, respectively. Usually ϵ_d is a constant at the optical frequency, however, ϵ_m has real and imaginary parts and both of them are functions of frequency. When the incoming light is normally incident on a metal surface, it does not have any parallel surface momentum component. Thus the resonant coupling happens when k_{SP} equals to the Bloch mode wavevectors, which can be expressed as:

$$k_{SP} = k_{Bloch} = i\bar{a}_1 + j\bar{a}_2$$

where a_1 and a_2 are the reciprocal lattice vectors. The right hand side of the above equation only depends on the geometry of a plasmonic crystal, thus the Bloch modes are defined when the plasmonic crystal is fabricated.

The above equations show that the surface plasmon resonance frequency is related to the dielectric environment above the metal surface. Each Bloch mode of a plasmonic crystal generates one enhanced transmission peak under normal incidence light, and its peak wavelength is determined by the dispersion relation. By increasing the environment dielectric constant ϵ_d , and considering that the real part of the metal dielectric constant ϵ_m is negative, the resonant frequency decreases so that the resonant peak shifts to longer wavelength. The shifting behavior is opposite when the surface dielectric constant is decreased. It is necessary

to notice that when solving for the resonance frequency, $\epsilon_m(\omega)$ is a frequency dependent variable so that we cannot simply move ω to the left hand side in the dispersion equation and get the result. In this chapter, several devices were designed and fabricated utilizing this surface dielectric dependent plasmon peak shifting property to achieve chemical sensing and light modulation.

5.2 Chemical Sensing using Plasmonic Crystals

The surface plasmon resonance effect can be used to sense the environmental dielectric changes on the plasmonic crystal's metal surface. The hexagonal symmetry nanobump array patterned gold film were used in this study, which were fabricated by the nanosphere self-assembly method. The periodicity of the pattern was determined by the sphere diameter, and the size of each bump was controlled by RIE time. The SEM image of a 600 nm periodicity nanobump array was collected (Figure 5-1), with the insert showed a magnified image of a single bump. The diameters of the nanobumps were around 230 nm. They were neither round in shape nor uniform in size, because the etching process was not isotropic in the chamber and the internal structure of the polystyrene spheres also influenced the RIE etching process. A relatively long etching time was applied (5 minutes), and the spheres were reduced to smaller than 150 nm. The thickness of the gold film (180 nm) was comparable with the nanosphere core, thus the shape of the nanobumps was highly dependent on the metal deposition process.

The transmission spectra for a nanobump arrays patterned gold film and a flat gold film are compared in Figure 5-2a. The transmission rate curves are normalized by dividing the transmission intensity with the light source intensity at each wavelength. The two curves show a common peak around 500 nm, which is caused by the gold d-band transition. The intensities of this bulk plasma peak are set to unity for both curves, since it is the property of the metal itself and is not related to any surface plasmon effect. The transmission rate of the flat gold film reduces to a very low value at longer wavelengths, because of the real part of the gold dielectric decreases very quick thus the reflection rate is high. The spectrum of the nanobump array pattern shows strong surface plasmon enhanced transmission in the red and

NIR region with its peak centered around 658 nm. The FWHM of this peak is 160 nm. This peak is attributed to the (1,0) SPP mode at the gold/air interface. The surface plasmon wavelength corresponding to this mode is 600 nm, and the photon coupled with it has longer wavelength because of the existence of the square root term in the dispersion relation.

The surface plasmon dispersion relation shows that its resonance frequency is sensitive to the dielectric material on the surface. By changing the surface chemical environment, the SPP modes related transmission peaks shift to longer wavelength. Three chemicals were individually placed above the hexagonal arrays plasmonic crystal to demonstrate this effect. Acetone ($n = 1.359$), methanol ($n = 1.329$) and ethanol ($n = 1.359$) were used in the experiment and the transmission spectra for these cases were collected with a normally incident white light source. In the experiment, a cover slip was put on top of the liquid to prevent the chemical from evaporated, and it also removes the curving liquid surface which could refract the incident light.

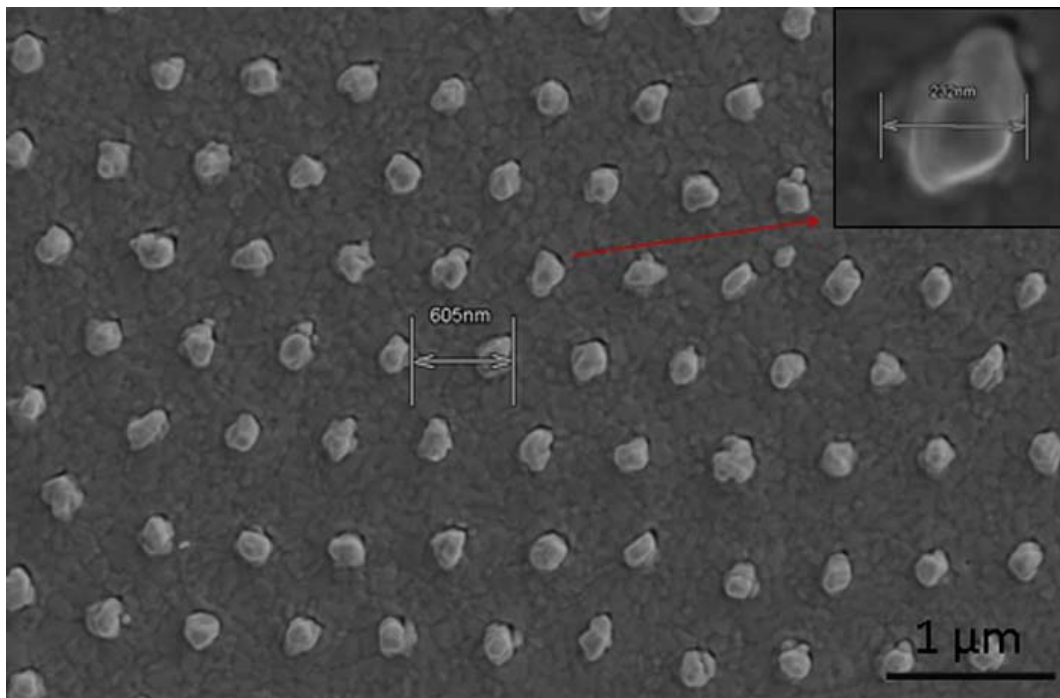


Figure 5-1 The SEM image of a 600 nm periodicity nanobump array patterned gold surface.

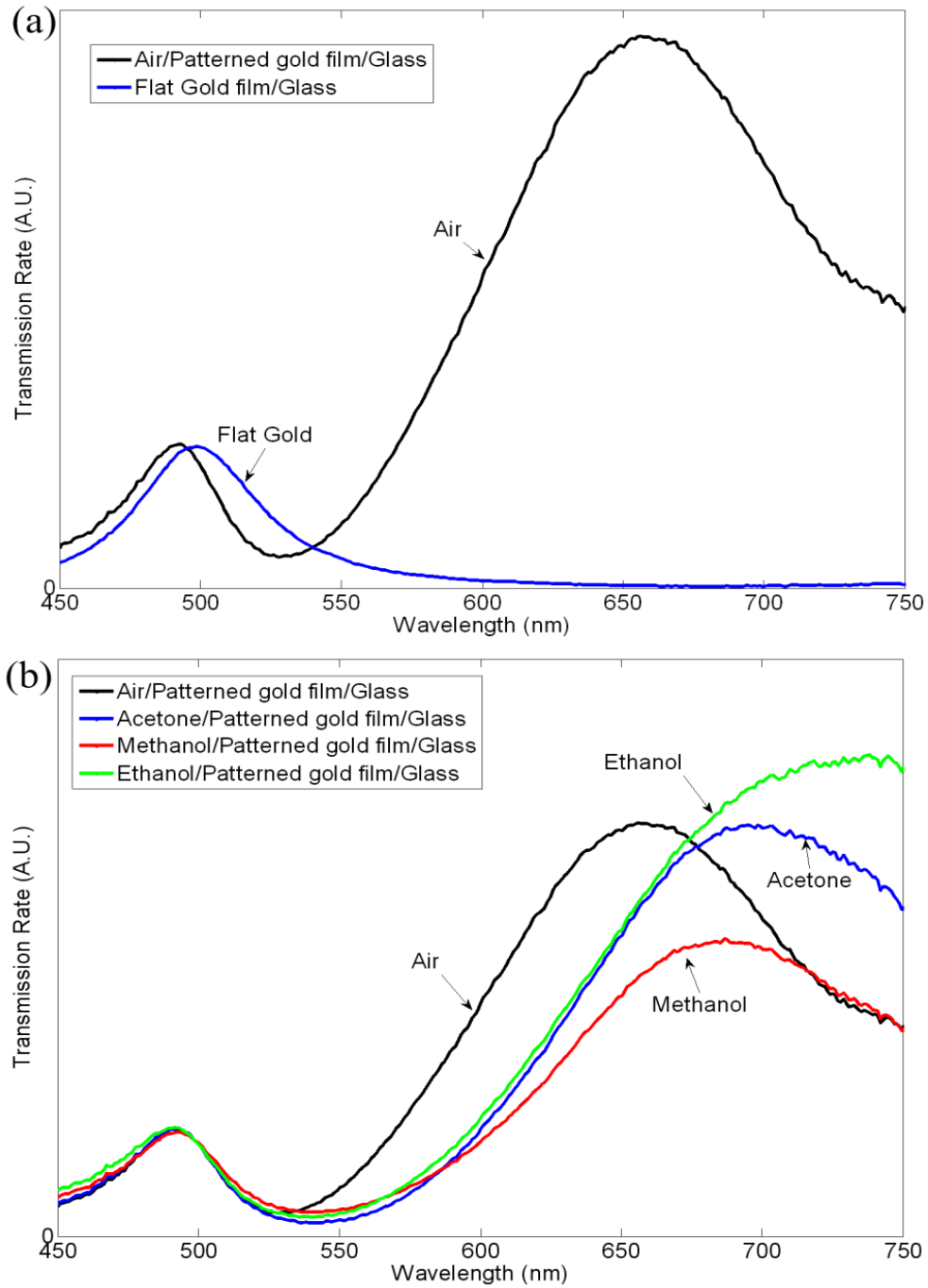


Figure 5-2 Spectra response of a plasmonic crystal with several kinds of chemicals on its surface. (a) Transmission spectra of a flat gold film and a 600 nm periodic hexagonal array nanobump plasmonic crystal. (b) The surface plasmon enhanced transmission peak at 658 nm for air/gold interface shifts when acetone/methanol/ethanol were coated onto the surface.

The transmission spectra for the four cases are compared in Figure 5-2b. All four spectra are scaled to keep the same transmission rate at 500 nm, which locates the peak generated by the gold bulk plasma. The chemicals used in these experiments have a dielectric constant around 1.3, which is larger than the dielectric of air ($n=1.0$). Correspondingly, the enhanced transmission peaks for these chemical environments shift to longer wavelengths. The enhanced transmission effect is attributed to the excitation of the surface plasmon polaritons modes, and its peak positions are very sensitive to the properties of the chemical above the surface, including the dielectric constant, molecular weight and structure. The enhanced transmission peak of methanol shifts to 686 nm, which is smaller than the shift of acetone (695 nm) and ethanol (732 nm) because its dielectric constant is relatively small. Acetone and methanol have almost the same dielectric constant, but their enhanced transmission wavelengths are different due to their different molecular weight and structure. The intensity and FWHM of the enhanced transmission peaks are determined by the geometry of the plasmonic crystal. The FWHM of each SPP resonance peaks in Figure 5-2b are almost the same, which are around 110-120 nm. The sensitivity of this 600 nm period plasmonic crystal is $\Delta\lambda/\Delta n = 100 \text{ nm/RIU}$. The change in spectra peak wavelengths for different surface dielectric materials demonstrate the potential of designing label free chemical sensor with the nanobump array patterned gold film.

The influence of surface dielectric constant was also studied by putting water above the plasmonic crystal. The transmission spectra for air and water above the surface were compared in Figure 5-3. The plasmonic crystal was constructed by 500 nm periodicity nanobumps array with 45 seconds RIE processing time. The SEM image of the patterned gold surface was showed in the insert of Figure 5-3. When there was just air above the surface, the surface plasmon resonance generated a strong resonant peak at 610 nm, which was correspondent to the (0,1) mode of the SPP at the gold/air interface. Then a droplet of DI water ($RI=1.333$) was put onto the surface, and the resonant peak shifted to 655 nm. The intensity of the surface plasmon enhanced transmission peak was reduced, because impurities in water caused it to attenuate the propagating SPP waves. After water was removed from the surface, the transmission spectrum was collected again and the resonant peak moved back to

its original position. Acetone (RI = 1.358) was used as another test chemical, and we found that the resonant peak was again red shift to 660 nm position. The resonant wavelength difference for water and air shows a sensitivity of approximately $\Delta\lambda/\Delta n = 135 \text{ nm/RIU}$ for this plasmonic crystal chemical sensor.

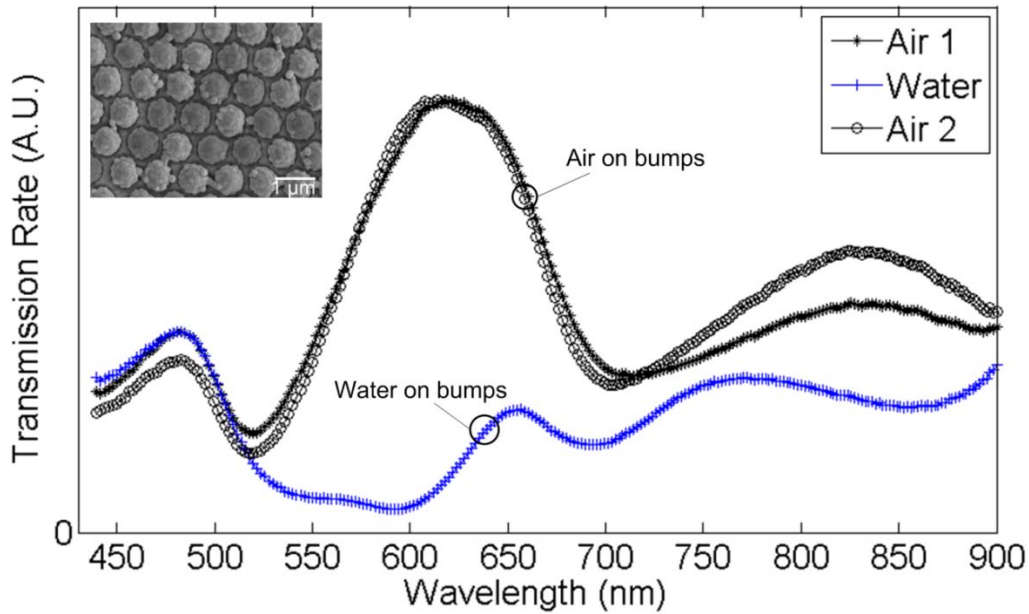


Figure 5-3 Transmission spectra response of a 500 nm periodicity plasmonic crystal with air and water on top of its surface. The lowest order mode on air/gold surface shifts from 610 nm to 655 nm when water is put onto the surface. (insert) SEM image of the nanobumps array.

The surface dielectric material changes cause the plasmon modes on the corresponding interface shift, thus changes the wavelength of the incoming photon that can couple with the SPR modes. This property can be used to detect chemical compounds change, which is demonstrated by the experiments above. The limitation of this method is that it can only sense the existence of one specified chemical in a single experiment. For example, if three chemicals with similar dielectric constant may exist in a solution, it cannot tell which component is existed by only measuring the wavelength shifting of a single plasmon peak.

Many different combinations can cause the same peak shifting, because this method is purely based on sensing the dielectric constant. The sensitivity of the device is depending on the pattern geometry, which includes its periodicity and the bump diameter, and also the operation wavelength. The commonly achieved sensitivity is around 100~150 nm/RIU among different experiments.

5.3 Vanadium Oxide Reflectivity Modulation

Vanadium Oxides shows a crystallographic transformation that accompanies a reversible semiconductor-to-metal transition at its critical temperature. Its optical and electrical properties change greatly during this transition. Vanadium dioxide (VO_2) thin film undergoes this transition near 68 °C. It transforms from a monoclinic structure to a tetragonal structure, and the film color changes from semi-transparent to dark red. [101,102,103,104,105,106] This type of materials is well known as thermochromic material. Thermochromic thin films whose reflectivity depends on temperature can be used as coating materials for smart windows and switchable glass. The use of smart windows can save power for heating, air-conditioning and lighting by controlling the heat and light passing through. VO_2 is one of the most interesting thermochromic materials because of its high infrared transmission in the semiconducting phase and high infrared reflectivity in the metallic phase. Thermochromics in infrared region have been observed from single VO_2 films or VO_2 films coated with oxides.[107,108,109] In addition, this research observes that VO_2 coated with a metal film shows optical properties changing in the visible light wavelength, the magnitude of change can be controlled by changing the type of metal and the thickness of the metal. This effect indicates that the dielectric constant of the VO_2 on the metal surface is changing with the device temperature. Surface plasmon resonance condition of the plasmonic crystals is sensitive to the surface dielectric constant change as discussed before, which indicates that VO_2 can be used as a temperature or electric field sensitivity plasmon modulation material. We studied the optical properties of VO_2 films and showed that in the near infrared, the magnitude of the reflectivity increased for metal coated VO_2 films, but decreased for uncoated VO_2 films. This was explained by the equivalent conductivity change of a

multilayer film structure. When surface plasmon was excited on the metal film, the resonance peak shifting effect was superimposed on the VO₂ thermochromic effect. We studied the color change of a VO₂ covered plasmonic crystal devices and plotted the color changing trace on the CIE plots.

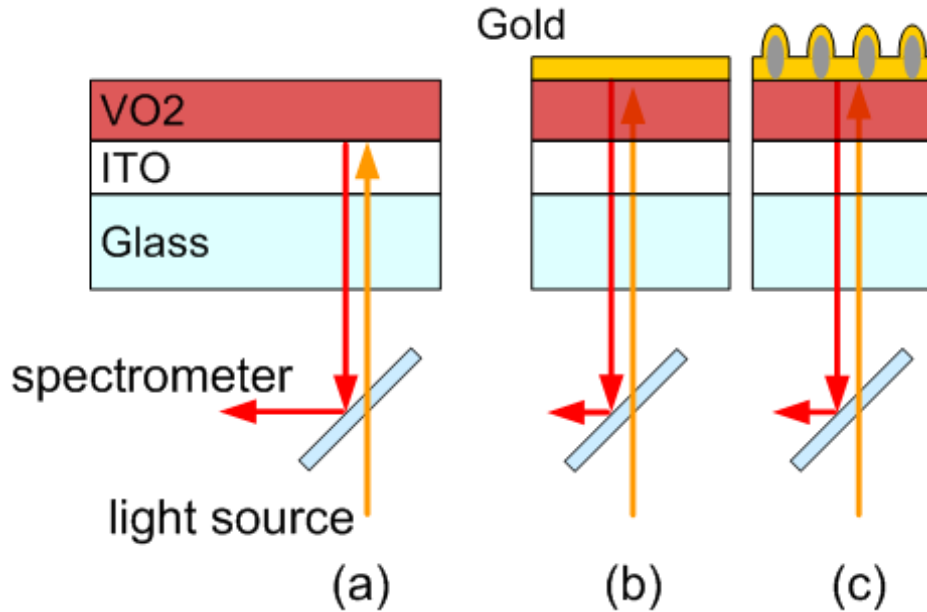


Figure 5-4 Schematic and optical configurations of three devices for VO₂ thermochromic study. (a) VO₂/ITO/Glass structure. The incoming white light was reflected at the VO₂/ITO interface and collected by a spectrometer. (b) Gold/VO₂/ITO/Glass structure. Light was majorly reflected at the Gold/VO₂ interface. (c) The gold film was patterned with a hexagonal symmetry nanobump array in addition to case (b).

Pulsed Laser Deposition (PLD) was used to deposit the VO₂ films on an ITO covered glass substrate. A KrF excimer laser at a wavelength of 248 nm was focused on a homemade vanadium oxides target. The repetition rate and energy level of the laser pulses were kept at 10 Hz and 200 mJ during deposition. The base pressure of the deposition chamber was pumped to 10⁻⁷ Torr. The depositions were performed in an ambient of 20 mTorr oxygen and the substrate temperature was maintained at 800 °C. After the film deposition, the samples

were cooled down at the deposition oxygen pressure to room temperature. Three devices were fabricated for comparison, as shown in Figure 5-4. The first device was simply a VO₂/ITO/Glass structure. The second device had a layer of e-beam deposited gold (180 nm) on the VO₂ layer that forms a Gold/VO₂/ITO/Glass structure. The third device was fabricated by patterning the gold layer with hexagonal array nanobump patterns for surface plasmon excitation. The periodic nanobump arrays were fabricated by nanosphere lithography method. In this process, 600 nm diameter polystyrene nanospheres were self-assembled onto a VO₂ film in a humidified chamber. The VO₂ film surface is hydrophilic thus does not need to be processed by piranha solution. The spheres were processed with RIE using oxygen plasma for 45 seconds, and the etched spheres were used as a template for subsequent gold deposition. The thickness of the gold film was 90 nm. The diameter of these gold nanobumps was 400 nm, and their height was 200-300 nm.

The optical properties of these devices were measured at the temperatures when changes between the semiconducting and metallic phases happen. A tungsten light source with 430-900 nm wavelength range was used to generate a collimated light beam and normally incident onto the VO₂ film. The transmission and reflection light were collected by an Ocean Optics USB 4000 spectrometer, when the temperature of the VO₂ film were 30 °C and 80 °C, as shown in Figure 5-5. The device active area was around 1 mm² for optical response collection, and the spectra show little variation for different spots on the same film. A Peltier cooler was used to adjust and monitor the temperature of the VO₂ film. The device was placed face down on the cooler, and its VO₂ film was in direct contact with the cooler surface in order to guarantee accurate temperature controlling. There was a small hole in the center of the cooler, which allowed collecting the transmission spectrum when the temperature changes. For reflection spectrum collection, the device responses were measured from the glass substrate side, as shown in Figure 5-4. The device with gold layer on top of the VO₂ film had two interfaces that contribute to the reflection. The reflection at the VO₂/ITO interface was weaker comparing to the reflection at the Gold/VO₂ interface. Thus we consider the observed optical effects were mainly caused by the physical properties at the Gold/VO₂ interface.

With only a VO₂ layer on top of the ITO glass, the optical reflectivity was higher at low temperature semiconducting phase in the infrared region. The reflectivity around 630 nm did not change when the VO₂ film temperature increased from 30 °C to 80 °C. This stable point had also been observed after the gold layer was coated, which will be demonstrated later. The transmission spectra at the two phases are shown in Figure 5-5b. The transmission kept almost unchanged in the visible wavelength (400 nm to 700 nm), and decreased when the temperature increased for wavelength beyond 700 nm. The change of transmission in the visible region was very small, and there was no change in color when examined by eyes.

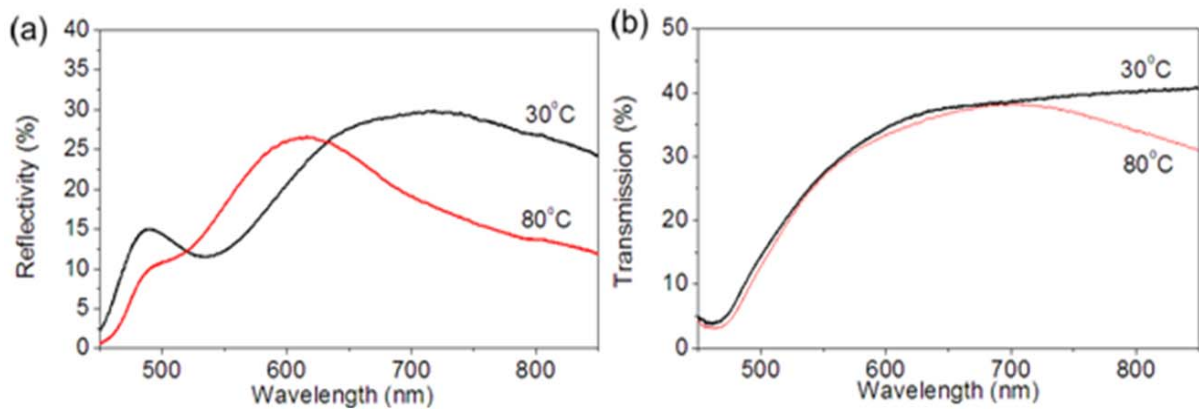


Figure 5-5 Spectra of the VO₂/ITO/Glass structure at different temperature. (a) Reflection and (b) Transmission spectra of the VO₂ (120 nm)/ITO (130 nm)/glass device measured at 30 °C and 80 °C.

A layer of gold was deposited onto the VO₂ film, and the reflection properties at the gold/VO₂ interface were studied. Because of the gold layer was relatively thick (180 nm), the transmission intensity was low and the changes between the two phases were undetectable. Thus only the reflectivity curve was collected for this device, as shown in Figure 5-6. With a gold layer coated on the VO₂ film, the magnitude of the reflectivity at high temperature increased to as much as two times of the reflectivity at low temperature at the wavelength longer than 630nm. The trend of the spectrum curve shifting was different from what we observed without the gold layer, where the reflection rate was decreasing at infrared

wavelength. Moreover, the stable point where the reflectivity intensity kept unchanged for different temperatures was still around 630 nm. We also tested a flat gold film under 30 °C and 80 °C, but did not see any reflection rate change. All these effects indicated that the spectrum curve changes were caused by the crystallographic transformation of the VO₂ film. Its dielectric constant at long wavelength decreased when switched from the semiconducting to the insulating phase.

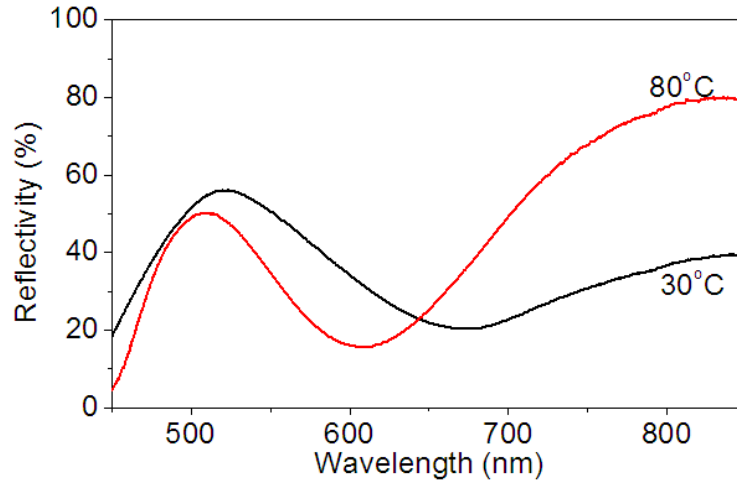


Figure 5-6 Reflection spectra at 30 °C and 80 °C for a flat gold (180 nm) /VO₂ (120 nm)/ITO (130 nm)/glass structure.

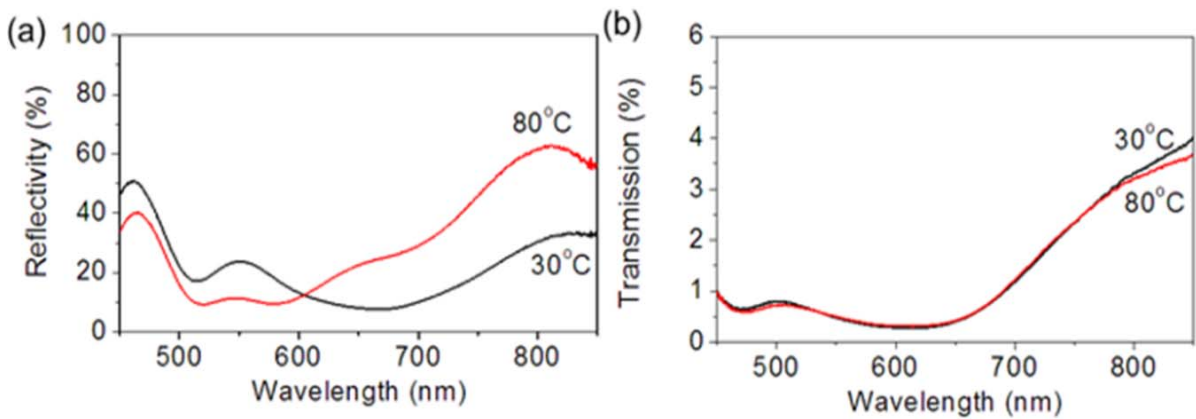


Figure 5-7 Spectra of the gold nanobump array/VO₂/ITO/Glass structure at different temperatures. (a) Reflection and (b) Transmission spectra of the nanobump array patterned gold (90 nm)/VO₂ (120 nm)/ITO (130 nm)/glass device measured at 30 °C and 80 °C.

In the third device, the gold film was patterned with nanobump arrays using nanosphere self-assembly method, and the other layers were the same as the previous devices. Its optical responses under different temperatures are shown in Figure 5-7. Surface plasmon modes were excited on the gold film. Enhanced transmission effect was observed in the infrared wavelength. The plasmon peak was pretty wide because the two lowest order modes on the gold/air and gold/VO₂ interfaces were overlapped. There is no Cr adhesion layer between the gold and the VO₂ layer, thus the plasmon mode on this interface was stronger comparing to the other plasmonic crystals discussed previously in this chapter.

This device had similar spectra shifting trend as the flat gold film device, but the magnitude of changing was larger. When the film temperature increased from 30 °C to 80 °C, the reflection rate at high temperature metallic state increased to nearly 4 times of the rate at low temperature for wavelength around 675 nm. This maximum changing happened in the visible light range which means human eyes is more sensitive to the change. The stable point moved to 610 nm for this device. Figure 5-7b shows the transmission spectra at 30 °C and 80°C, where no significant temperature dependence was observed. The transmission rate in the visible range was low (0.5%~1.5%) because the gold layer blocked most of the incoming photon. However, the spectra changing behavior in the infrared region was worth to notice. The transmission rate kept almost unchanged in the 700-800 nm regions, which was caused by the VO₂/gold interface SPR peak shifting. The peak shifting model for this observation is illustrated in Figure 5-8. Dielectric constant of the VO₂ film decreased during the low to high temperature transition, and the corresponding plasmon peak shifted to shorter wavelength. This effect compensates the VO₂ film transmission rate dropping around 700 nm, thus the total rate kept unchanged at this region. This is different from the VO₂/ITO/Glass structure that the transmission rate dropped between 700-800 nm, as shown in Figure 5-5b. This device demonstrates that the plasmonic crystal can be used to turn the color changing process during crystallographic transformation of the VO₂ film. By adjusting the periodic and diameter of the nanobumps, the trend of lower transmission for metallic phase VO₂ film at infrared wavelength can be compensated of even reversed.

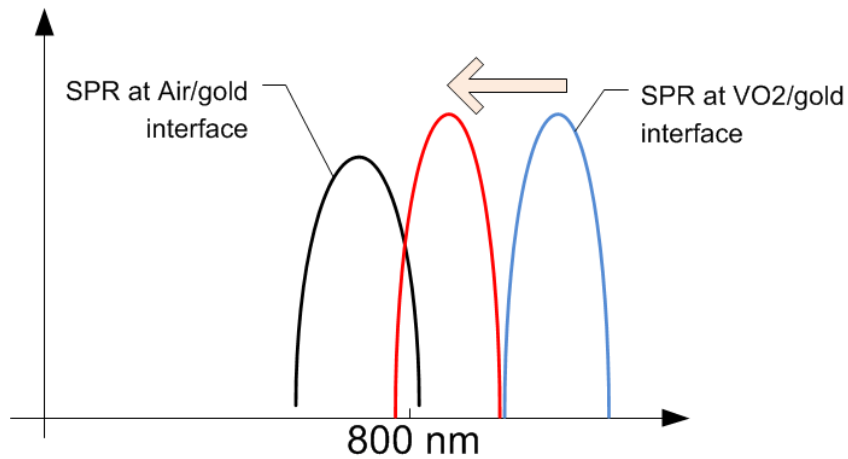


Figure 5-8 The SPR peak shifting scheme for the air/plasmonic crystal/ VO_2 /ITO structure. The SPR peak at the VO_2 /gold interface blue shifted when the VO_2 changes from semiconducting to metallic phase, thus compensates the VO_2 film IR transmission intensity drops around 700-800 nm wavelength regions.

The reflection color of the VO_2 films was labeled on the CIE 1931 plot. They were shown as traces when the films experienced crystallographic transformation. Photoreceptors in the human eye, which is called cone cells, has three sensitivity peaks in short (S, 420–440 nm), middle (M, 530–540 nm), and long (L, 560–580 nm) wavelengths. Thus, three parameters can describe a color sensation. The CIE color space denotes the amounts of these three primary colors in a three-component set called X, Y, and Z, which are roughly red, green and blue. Two light sources with different mixtures of various wavelengths may appear to be the same color. Their corresponding points on the CIE plot have the same location, no matter what spectral distributions of light were used to produce them. The CIE 1931 Standard Observer is defined by the chromatic response of an average human viewing through a 2° angle. The color changing trace for the three devices discussed above is shown in Figure 5-9. The reflected color was observed with a tungsten light source. The VO_2 /ITO device and the flat gold/ VO_2 /ITO device shows small changes in color, and the nanobump array gold film/ VO_2 /ITO shows relatively large changes. For each curve, the low temperature color spot is located at bottom end with small Y value, and the high temperature spot is located at the top end with large Y value.

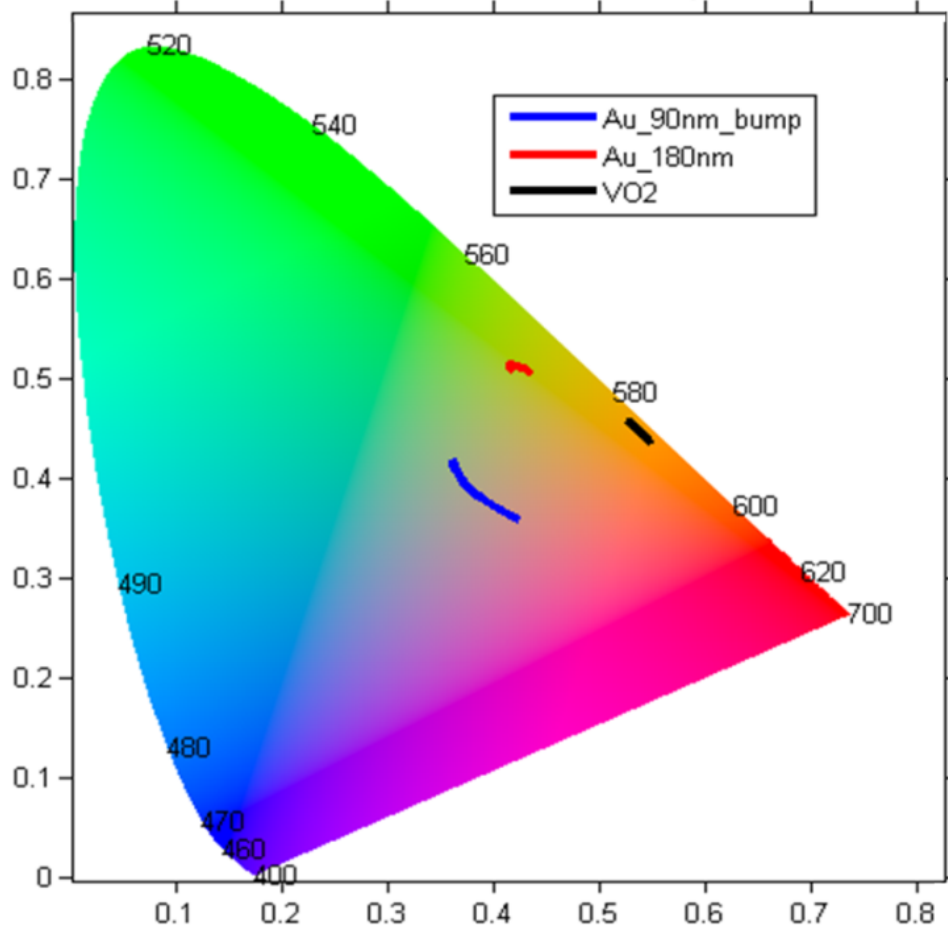


Figure 5-9 Color changing traces on CIE 1931 color space during the VO₂ phase transition. (blue) the nanobump array patterned gold film on VO₂; (red) flat gold film on VO₂; (black) flat VO₂ film on ITO glass substrate. Upper end of the trace is at the metallic phase and lower end is at the semiconducting phase.

The traces for heating up and cooling down processes were overlapped on the CIE plot, but the correspondent color points for each temperature were not at the same location. These devices showed a hysteresis effect that is commonly seen for VO₂ film during the phase transition. The reflected light intensity for the flat gold/VO₂ device was plotted for the two phase changing directions at 675 nm wavelength, as shown in Figure 5-10. For the semiconducting to metallic transition, the transition temperature (medium) was at 75 °C and

the intensity changing slope was 7.9% per degree. The transition temperature for metallic to semiconducting transition was at 60 °C with a slope of 6.3% per degree. The average transition temperature was 67.5 °C with a 15 °C hysteresis width.

The reflection color changing traces at Gold/VO₂ and Aluminum/VO₂ interfaces during the VO₂ phase transition are plotted in the CIE 1931 color space, as shown in Figure 5-10. Gold and Aluminum were deposited onto a flat VO₂ film, respectively. The trace for Gold/VO₂ film was at the middle of the color space, while the trace for Aluminum/VO₂ film located right to the edge of the color space. Both films showed a yellow color at low temperature when the VO₂ was in the semiconducting phase, the reflection color moved to blue-green side with an increasing in temperature.

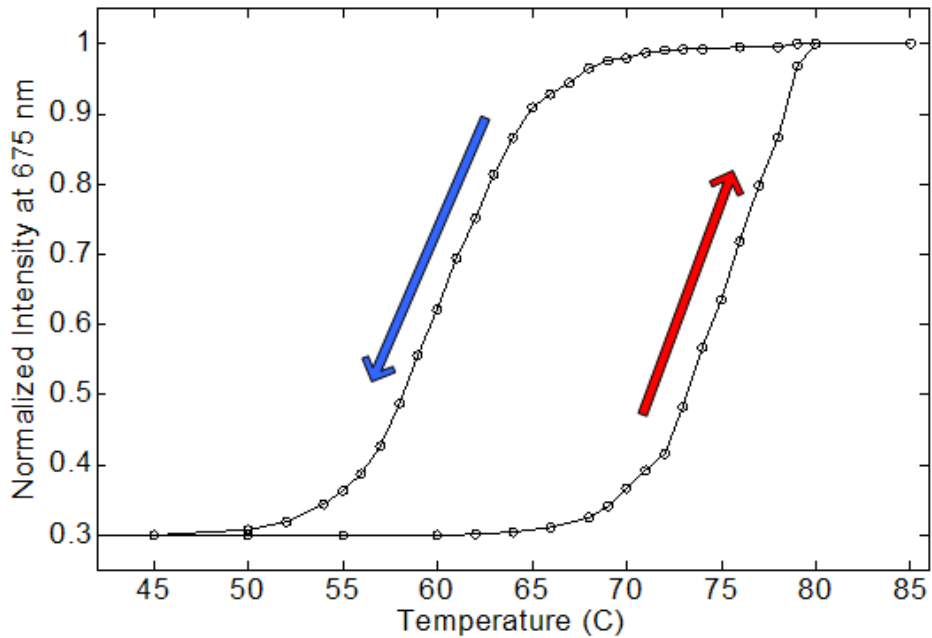


Figure 5-10 Light intensity traces at 675 nm wavelength showed hysteresis effect during the phase transition. The transition from semiconducting to metallic transition happened at 60 °C and the reversed transition happened at 75 °C.

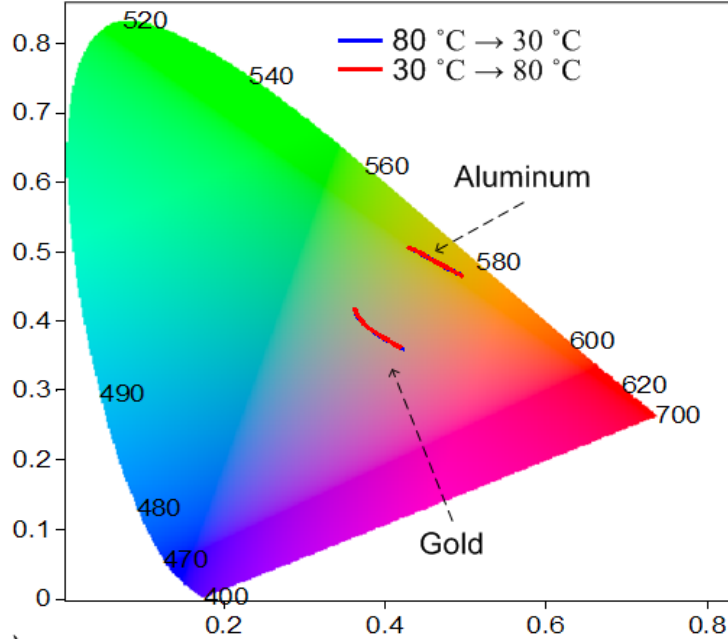


Figure 5-11 Color changing traces for the Gold/VO₂ and Al/VO₂ devices during the semiconducting-metallic phase transition.

The observed reflection spectra shifts can be explained by the equivalent conductivity changes of a multilayer film structure during the semiconducting-metallic phase transition. The reflection coefficient of a thin film structure sandwiched between two dielectric materials with the refractive indices of \tilde{n}_1 and \tilde{n}_2 can be expressed as: [110]

$$r_{12} = \frac{E_r}{E_i} = \frac{\tilde{n}_1 \cos(\theta_i) - \tilde{n}_2 \cos(\theta_t) - y}{\tilde{n}_1 \cos(\theta_i) + \tilde{n}_2 \cos(\theta_t) + y}$$

with $y(\omega) = \sigma(\omega)d / \epsilon_0 c$, and $\sigma(\omega)$ is the frequency dependent equivalent conductivity of the multilayer thin film with the total thickness of d . We are interested in the optical properties at red to infrared wavelength region since its large change in reflectivity may be used for modulator devices. The devices are made on ITO glass substrate ($n_{ITO} = 2-3$ [57,111]) with air on above, so that $n_1 = 3, n_2 = 1$ in the above equation when light are incident from the glass side. And we consider the normal incident case so that $\theta_i = \theta_t = 0$. The reflectivity $R = r_{12} \cdot r_{12}^*$ is plotted as a function of “ y ”, as shown in Figure 5-12.

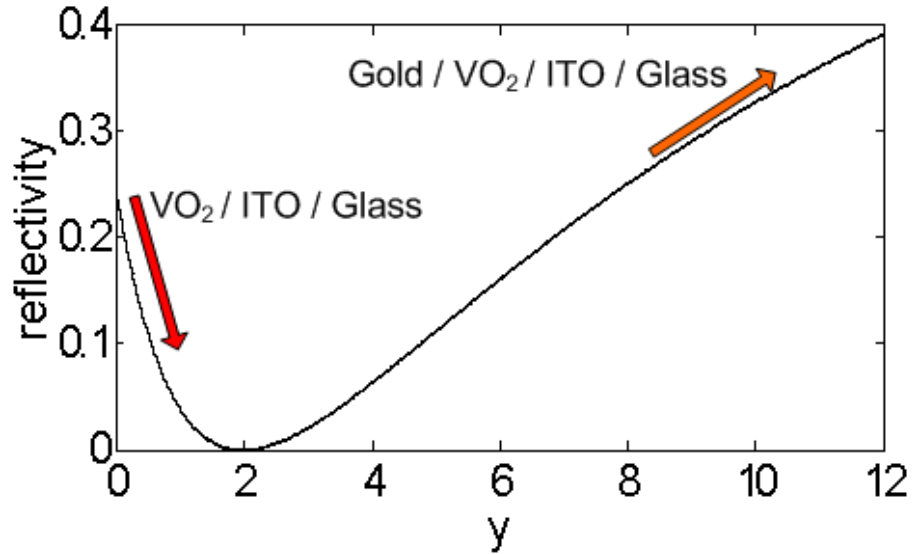


Figure 5-12 Reflectivity for a multilayer thin film structure with different conductivities. ($R = [(2 - y)/(4 + y)]^2$) The phase changing region of 'y' corresponding to the VO₂/ITO/glass structure is labeled on the left side (red arrow) and the section for Gold/VO₂/ITO film is on the right side (orange arrow).

For the VO₂ on ITO structure, the reflectance was reduced at 650-750 nm regions because the conductivity σ of the VO₂ film increased from insulating to conductive during the phase transition. Y was increased with σ , thus the reflectivity moved away from the left end of the curve in Figure 5-12. The slope of the curve was negative in this region, and the reflectivity was reduced during the phase transition. On the other hand, the Gold/VO₂/ITO film had a relatively large equivalent conductivity due to the existence of the gold layer, so that the point of $y(\omega)$ corresponding to this structure was on the right hand side of the curve with a positive slope. When the VO₂ changes from insulating to conductive, the equivalent conductivity σ increased and the reflectivity also increased. This explains the different shifting behaviors in the infrared wavelength for the two devices with and without the gold layer.

In summary, the reflection spectra of several Gold/VO₂ thin film structures were studied. The devices showed optical modulation effect when the VO₂ experienced semiconducting-metallic phase transition. The trend of change was opposite with and without the existence of the gold layer. Reflectivity of the nano-bump array patterned gold film/VO₂/ITO structure showed a larger modulation effect at red and NIR wavelength due to the SPR wavelength shifts. This effect can be utilized to design temperature sensors with optical output signal and electrically controlled light modulators.

5.4 All Optical Modulation Device with Organic Photovoltaic Material

In this study, we demonstrated that surface plasmon resonance effect imposed by periodicity of the nanobump arrays can be utilized to control the transmission rate of a normally incident light. The resonant condition of SPR is sensitive to the dielectric constant of the material just above the metal surface. Poly(3-hexylthiophene) (P3HT) was used as the dielectric material and transmission light modulation was demonstrated using hexagonal lattice plasmonic crystals formed by nanosphere lithography. P3HT is a high mobility polymer that is widely used in organic solar cells [112,113,114]. It can be pumped with light at 400-500 nm wavelength and generating electron/hole pairs that modify the local dielectric constant. A 670 nm red laser was used as signal light, and the transmission rate of this normally incident signal light was modulated by a 475 nm blue laser that pumped the P3HT at the same incident spot of the signal light. We expect that this approach is general in nature and that the use of photo refractive polymers, or other nonlinear materials, should provide similar and potentially larger effects.[2,115,116,117,118]

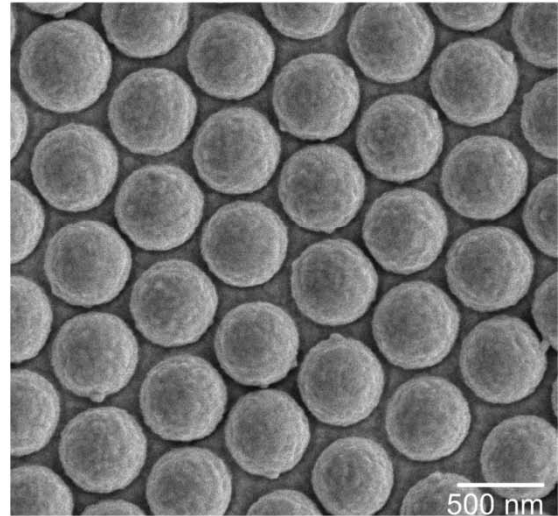
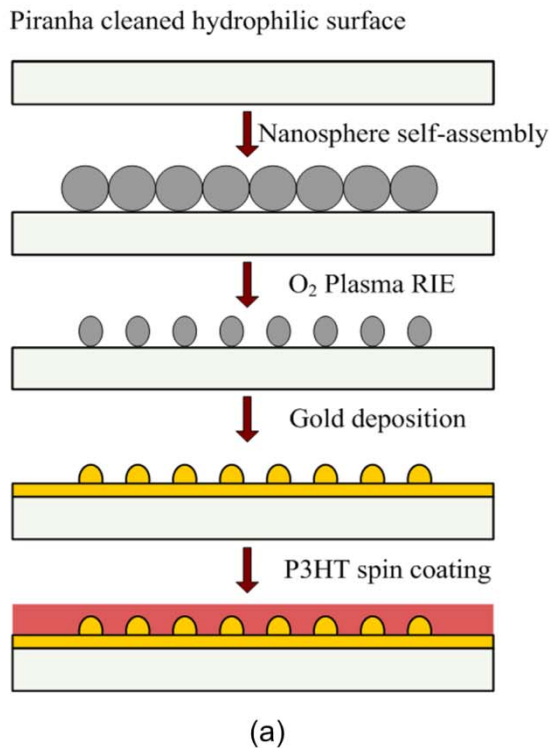


Figure 5-13 The P3HT coated plasmonic crystal structure for light modulation applications. (a) Process flow for fabricating the plasmonic all optical modulator. (b) SEM image of the 600 nm periodicity nanobump array before P3HT coating.

The nanosphere self-assembly method was used to fabricate the close-packed hexagonal lattice plasmonic crystals. The strategy is outlined in Figure 5-13. The periodicity of the array was 600 nm, nanosphere RIE processing time was 45 second, and the gold layer thickness was 160 nm. After the gold plasmonic crystals were fabricated, a layer of P3HT was spin coated onto the gold surface. The thickness of the P3HT layer was determined by the spin rotation speed, and usually it was between 500-800 nm. The P3HT was purchased from American Dye Source in dry form, and was dissolved in chlorobenzene at a concentration of 10 mg/mL.

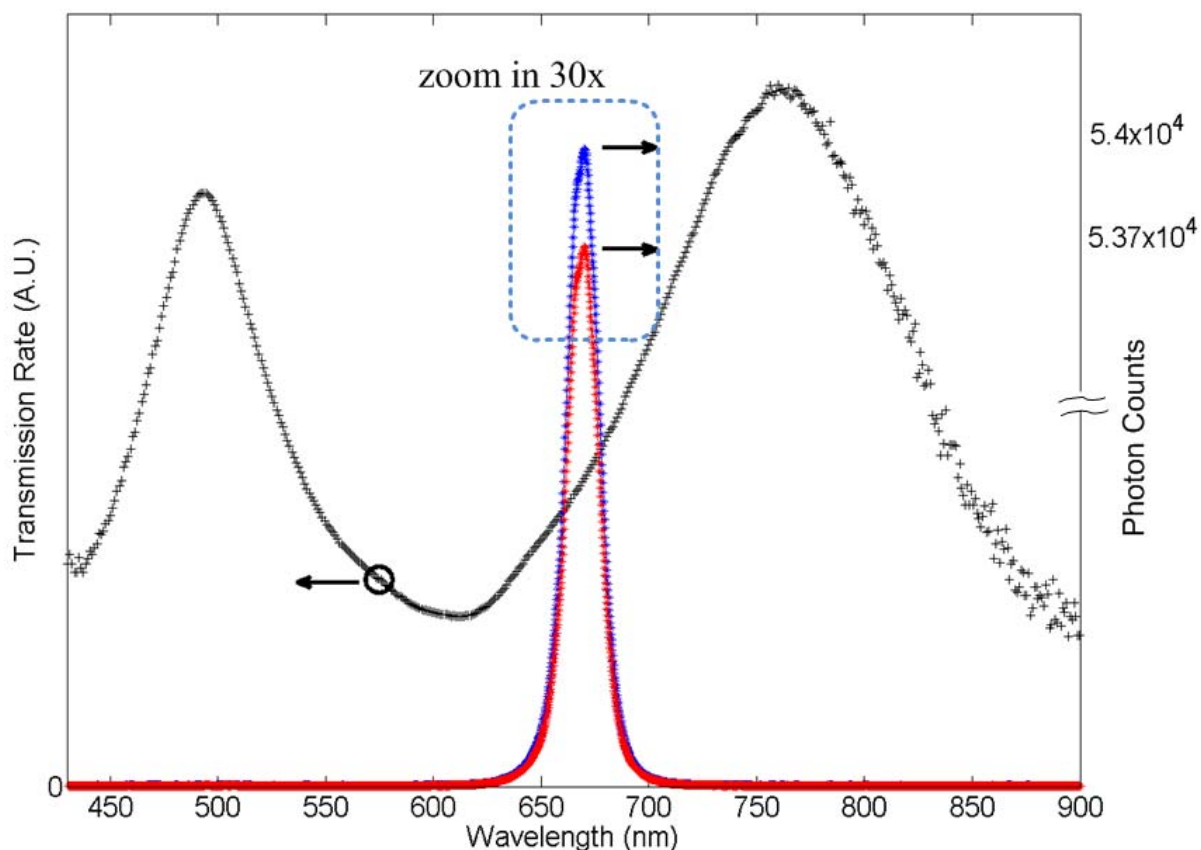


Figure 5-14 Spectra response of the light modulation device and the input light source. (left axis) The transmission spectrum of the P3HT coated plasmonic crystal. The periodicity of the nanobump array is 600 nm and the gold layer thickness is 160 nm. (right axis) The spectra of the signal light. Its intensity is stronger when the control light is on.

The surface plasmon resonance frequency was measured by collecting the transmission spectrum of a normally incident tungsten light, as shown in Figure 5-14. The gold bulk plasma peak located at 495 nm, and the gold/air interface (0,1) plasmon mode located at 760 nm. The dielectric constant of the P3HT film was an important parameter to determine the resonance wavelength. Changes in it will shift the plasmon peak and also influence the transmission rate at the shoulder of the peak. P3HT is a polymer used in organic solar cells. It can generate free charge carrier when pumped by light, the material becomes more conductive and its dielectric constant decreases. The optical configuration for modulating the

device is shown in Figure 5-15. A 670 nm laser was used as signal light, which was generated by a laser diode driven at 40 mA current. The signal light was normally incident on the nanobump patterned gold area, and the transmission light was collected by a fiber and sent to the USB4000 spectrometer. The spectrum of the signal light was at the left shoulder of the plasmonic crystal's 760 nm resonance peak. Another 475 nm blue laser was used as the control light. It incidents at the same spot of the signal light on the device surface in order to pump the P3HT material on the signal light propagation path.

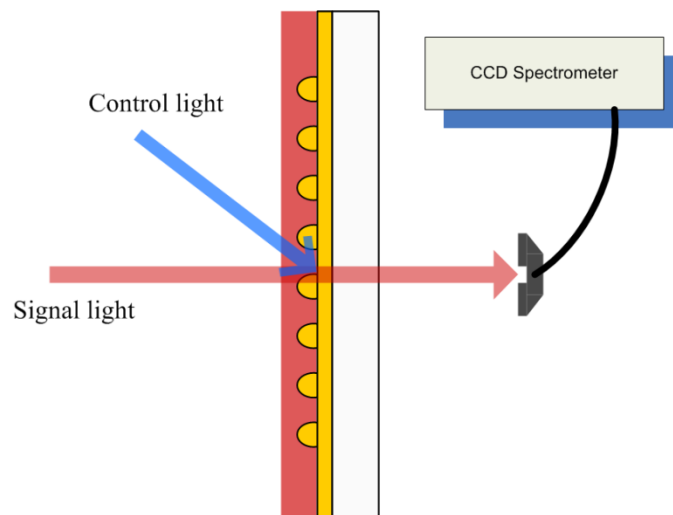


Figure 5-15 The schematic of the all optical modulation device. The control light is from a 475 nm blue laser, and the signal light is from a 670 nm collimated red laser. The transmission light is collected by a fiber aperture at the back side of the device and sent to the USB4000 spectrometer.

The control light excited electron/hole pairs that decreased the dielectric constant of the P3HT layer. The surface plasmon enhanced transmission peak shifted to shorter wavelength and this shifting increased the transmission intensity of the signal light, because its wavelength was located at the left shoulder of the plasmon peak. The P3HT also emitted a small amount of red light when pumped. This emission was subtracted, and the transmission light intensities at both on and off states of the control light were shown in Figure 5-16. The

intensities showed about 0.6% change between on and off states. The real part of the gold dielectric is around $-5 \sim -10$ at the signal light wavelength (670 nm), thus the changes in P3HT dielectric constant can be estimated from the SP dispersion relation, which was decreased by -0.002 RIU when the control light switching from “off” to “on”. Due to the small change in intensity and the low transmission rate of the gold film, it was necessary to use an integration time of 200 ms to measure the changes in spectrum. While the response time of this modulation was expected to be on the time scale of the surface plasmon creation and decay, the experiment was limited in time resolution. The thickness of the P3HT layer was also critical for the device response. The polymer film should be thin in order to make the dielectric change happened close to the gold surface. However, the patterned gold surface was rough, so that at least 500 nm thick of P3HT was necessary to fully cover the gold surface. The patterned gold surface was also not hydrophilic, so that it is challenging to use a high rotation speed during the spin coating process.

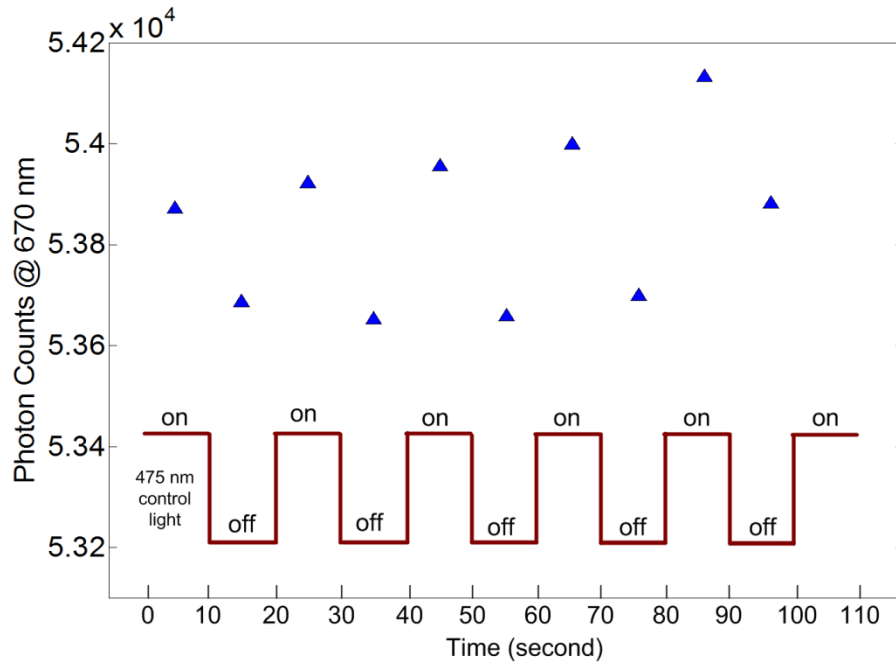


Figure 5-16 Transmission intensities of the signal light respond to a switching input. The waveform of the control light is showed as red lines, and the peak spectrum intensities of the signal light are showed in blue triangles.

5.5 Cell Migration on Large Periodicity Nanohole Array

The ability for cells to correctly adhere and to migrate based on internal and external inputs is essential for a number of fundamental cell biological processes, including development, inflammation, cancer metastasis, and wound healing.[119] To ensure survival, cells are able to decipher, respond, and adapt to complex spatial and temporal environmental cues.[120] In order to study cell behavior in vitro, many model substrate platforms have been developed. One of the most promising substrates to study bio-interfacial phenomena is based on tailoring gold surfaces with self-assembled monolayers (SAMs).[121] SAMs are molecularly well-defined, synthetically flexible, and, when terminated with oligo (ethylene glycol) groups, are inert to nonspecific protein adsorption.[122] Furthermore, many analytical techniques can be used to characterize associations on these thin films. To study ligand-receptor interactions during cell adhesion and motility, many SAM patterning techniques have been developed ranging from dip pen nanolithography[123], micro-contact printing[122], self-assembly[124], and microfluidic lithography[121]. In particular, self-assembly has been used to generate ligand spot sizes as small as 50 nm with ligand spacing in the hundreds of nanometers. The small ligand size is important to study focal adhesions, but the small inter-ligand distance means the cells can only experience a substrate with high ligand density. Although there has been much progress in generating patterned surfaces, there have been few inexpensive methods that can control both the size of the adhesive area (at the nanometer scale) and the spacing between adhesive islands (at the micrometer scale) to study cell behavior.

Herein, we report a flexible fabrication strategy to generate various hybrid gold/glass nanohole surfaces for studies of cell adhesion and cell migration.[125] The surfaces were fabricated with 500 nm ligand spot sizes and separated by 3 or 5 μm and characterized with scanning electron microscopy (SEM) and optical microscopy. For cell adhesion studies, cells were seeded to these substrates to study the effect of ligand spacing on cell spreading, stress fiber formation, and focal adhesion structure and size. Finally, cell migration rates were determined and compared on the various nanohole surfaces with the use of time-lapse microscopy.

The hybrid substrate fabrication flow was based on the nanosphere self-assembly process. A glass slide was sonicated in acetone followed by cleansing in piranha for 1 hour. Next, a solution of polystyrene spheres in water was drop-coated to the surface and allowed to dry in a humidity-controlled environment (~70% humidity). The 5 μm spheres were etched with O_2 plasma for 30 min to generate 500 nm holes with 5 μm spacing. The 3 μm beads were etched with O_2 plasma for 20 min to generate 500 nm holes with 3 μm spacing. Afterward, the glass slide was coated with chromium (2 nm) then gold (15 nm). Finally, the spheres were removed by sonication with acetone.

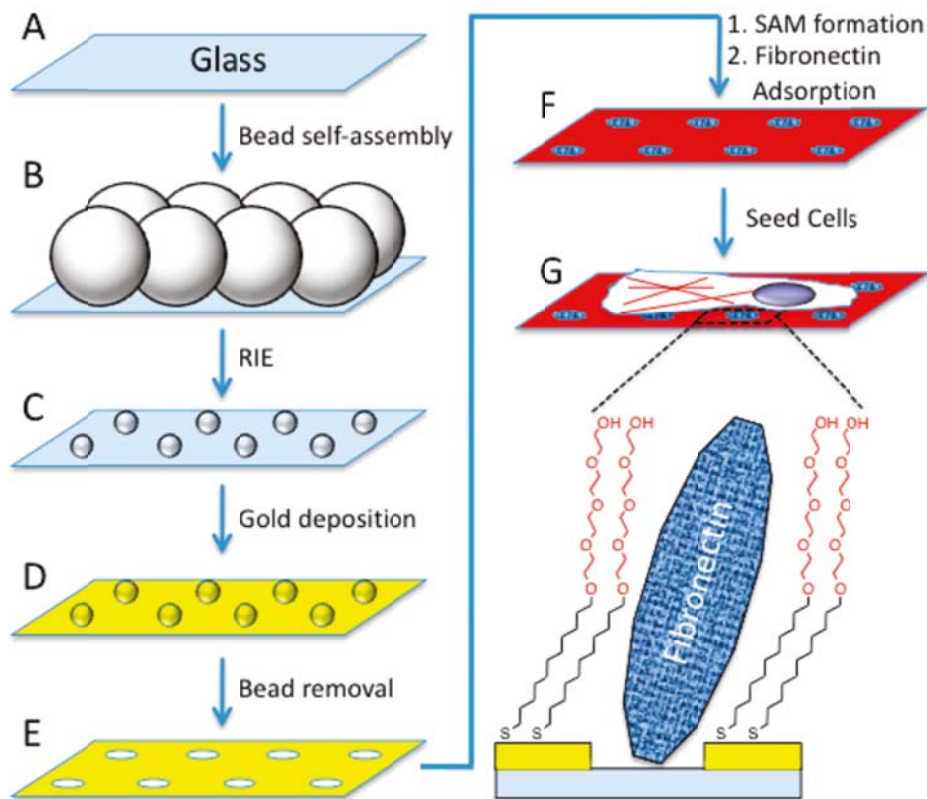


Figure 5-17 Strategy to generate patterned hybrid nanohole SAM surfaces for studies of cell adhesion and cell migration. (A) glass slide cleaning; (B) nanosphere self-assembly; (C) RIE using O_2 plasma; (D) Gold deposition; (E) Remove the nanospheres; (F) The bare gold was exposed to a tetra(ethylene glycol) alkanethiol to form an inert SAM. The extracellular matrix protein fibronectin was then added and adsorbed only to the glass regions; (G) Cells were seeded to the surface.

The fibronectin absorption and cell culture steps are describe as follow. The substrates were then immersed in a 1 mM solution of tetra(ethylene glycol) undecane thiol for 12 h. For fibronectin adsorption, the surfaces were placed in a 30 μL of 0.1 $\mu\text{g}/\mu\text{L}$ fibronectin solution for 3 h before cell seeding. Swiss Albino 3T3 fibroblasts (ATCC) were cultured in Dulbecco's modified Eagle medium (Gibco) containing 10% calf bovine serum and 1% penicillin/streptomycin at 37 °C and 5% CO_2 .

The 3T3 Swiss Albino mouse fibroblasts were seeded on the patterned substrates, incubated for 20 h in Dulbecco's modified Eagle's medium (Sigma) with 10% bovine calf serum and 1% penicillin/streptomycin, and then fixed with 3.2% formaldehyde in Dulbecco's phosphate-buffered saline (PBS; Sigma). The cells were then permeated with PBS containing 0.1% Triton X-100 and stained with three fluorescent dyes and one antibody, 40,6-diamidino-2-phenylindole dihydrochloride (DAPI; Sigma), antipaxillin (BD Biosciences, San Jose, CA), phalloidin-tetramethylrhodamine B isothiocyanate (Sigma), and a secondary fluorescently labeled antibody (Cy-2 conjugated goat antimouse IgG, Jackson ImmunoResearch Laboratories, Inc., West Grove, PA). The sample preparation process is summarized in Figure 5-17.

The cells were observed by fluorescent and bright-field microscopy using a Nikon TE2000E inverted microscope. For time lapse microscopy, bright-field images were obtained at 10 min intervals over a period of 24 h. A FEI Quanta 200 FEG was used for ESEM. The imaging was done at 0.5 Torr water pressure and 12 kV accelerating voltage.

The nanohole array surfaces were characterized with ESEM, as shown in Figure 5-18. The first ESEM image shows the spheres after RIE; the spacing was measured to be 5 ± 0.75 μm between the spheres, and the sphere diameter was 500 ± 18 nm. After metal deposition and sphere removal, ESEM of the surface shows the nanohole surface with roughly the same hole size and spacing. For the surfaces made with 3 μm spheres, the spacing measured 3 ± 0.3 μm and the hole size was 500 ± 23 nm. The ESEMs show that our nanohole surfaces have consistent spacing over cell dimensions to serve as substrates for cell studies.

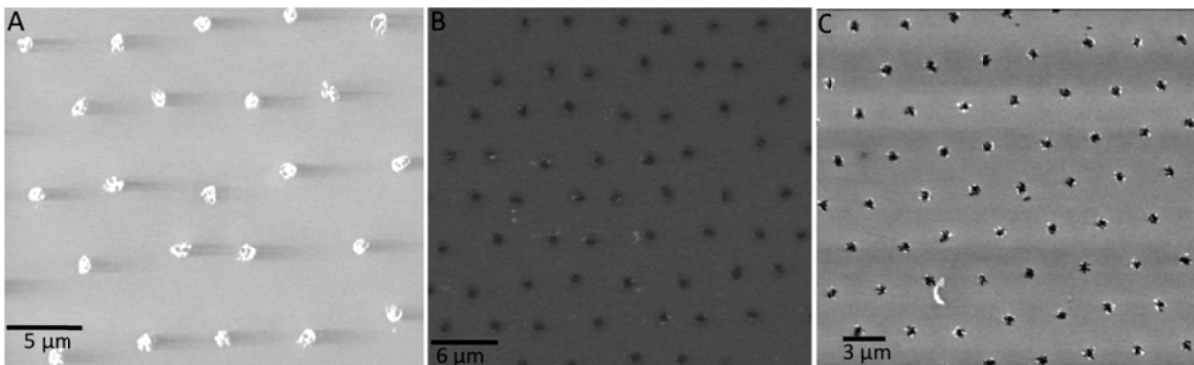


Figure 5-18 ESEM images of the hybrid nanohole surfaces. (A) ESEM image of nanospheres after O₂ plasma etching. Hybrid surfaces made with (B) 5 μm and (C) 3 μm beads after gold evaporation and sphere removal.

To study the role of ligand spacing on cell spreading, stress fiber formation and focal adhesion structure and size, Swiss 3T3 fibroblasts were seeded to the hybrid nanohole surfaces then fixed to observe internal structures after 24 hours (Figure 5-19a). Cells were visualized by fluorescent microscopy and were stained with markers for the nucleus (blue), actin (red), and focal adhesions (green). Figure 5-19b shows a table summarizing the cell characteristics on the various surfaces. Cells spread well on all the surfaces, but focal adhesion structures were only found on surfaces with adsorbed fibronectin irrespective of nanohole spacing. Unlike the fibronectin-coated glass surface, cells on the nano-patterns did not have actin stress fibers throughout the cell length. Larger and more focal adhesion structures were found on the 3 μm spacing of the 500 nm holes along with some actin stress fibers compared to the 5 μm spacing 500 nm holes. This observation is most likely due to the greater density of adhesive sites on the 3 μm nanohole array.

For cell migration studies on the nanohole array surfaces, we used time-lapse microscopy. After cell seeding, bright-field images were taken every 10 min for 24 h, and the migration rates were determined with Metamorph software for 10 cells. For fibronectin adsorbed on glass, the migration rate was 1.34 μm/h, and, for cells migrating on the nanoholes (no fibronectin) with 5 μm spacing, the migration rate was 1.20 μm/h (nanohole size is 500 nm

for all cell migration experiments). Once fibronectin was adsorbed to the glass nanoholes, the rate roughly doubled for the 5 μm spacing (2.88 $\mu\text{m}/\text{h}$). When the cells were seeded to a surface with 3 μm spacing with fibronectin, the migration rate quadrupled to 11.32 $\mu\text{m}/\text{h}$.

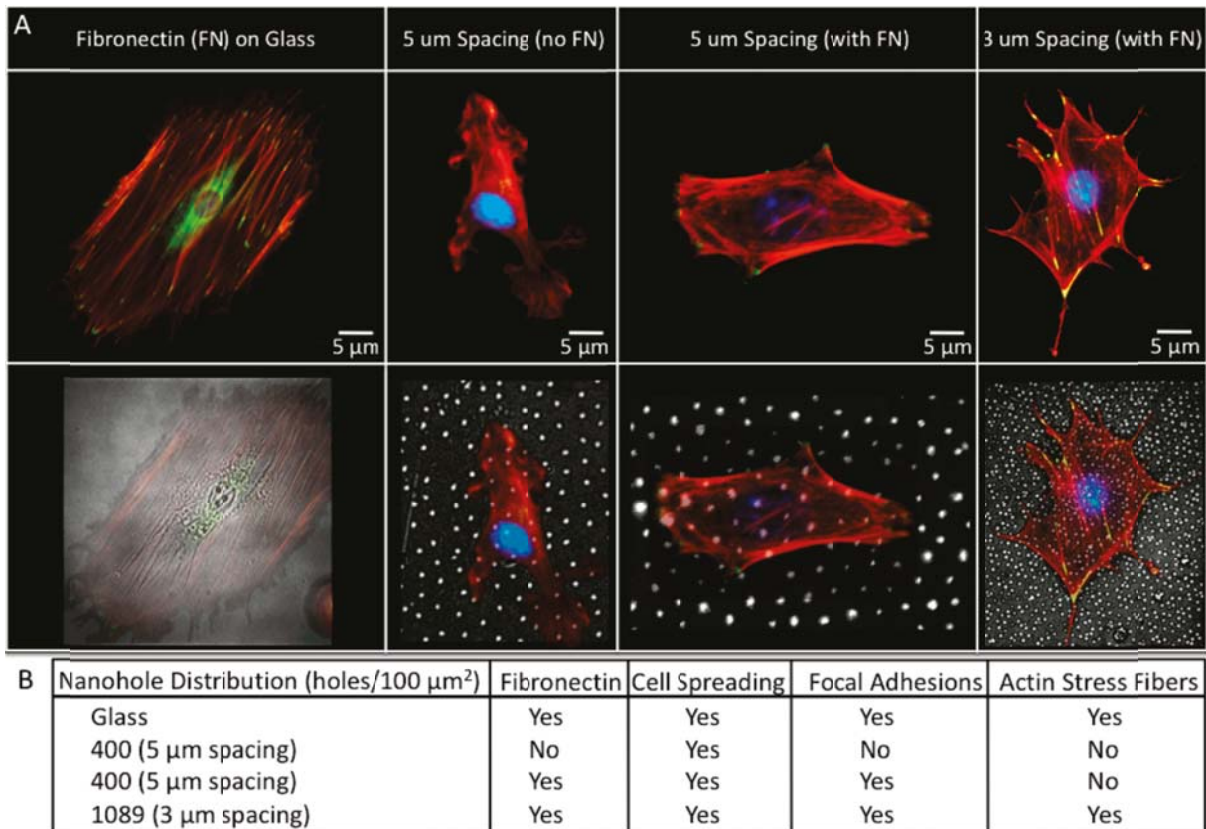


Figure 5-19 Representative micrographs of fibroblast cells adhered to various hybrid nanohole surfaces. Cells were fixed and stained for nucleus (blue), actin (red), and focal adhesions (green). (a) Top row: Fluorescent micrographs of cells immobilized on the different nanohole (500 nm) surfaces including fibronectin on glass, 5 μm spacing with and without fibronectin, and 3 μm spacing with fibronectin. Bottom row: The corresponding bright-field images with the fluorescent micrographs superimposed to aid in the visibility of the cells and nanohole spacing. (b) Comparison of cell adhesion characteristics on the various surfaces.

Cells on the 3 and 5 μm array show characteristics of a motile cell with the lack of stress fibers but well-formed focal adhesions. The increase in ligand density on the 3 μm array resulted in a significant increase in migration rates. We observed on the series of fibronectin nanohole arrays that the cells had much greater lamellapodia and filopodia protrusions compared to the glass/fibronectin surface. Furthermore, we observed more focal adhesions on the 3 μm arrays than on the 5 μm arrays, which is most likely due to the higher ligand density on the surface. We believe that there is a complex interplay between ligand density and spacing that contributes to the overall ability for the cell to make focal adhesions, which then allows for subsequent lamellapodia and filopodia protrusions for motility.

In conclusion, we have developed a novel hybrid nanohole array substrate to study cell adhesion and migration. The fabrication methodology relies on a straightforward nanosphere self-assembly/RIE method to generate gold/glass hybrids with control over nanometer size holes and spacing between holes. These substrates were used to study cell adhesion characteristics by antibody staining. Cells spread on the different nanohole surfaces, but did not form long actin stress fibers. However, on fibronectin containing holes, the cells formed focal adhesions. Finally, cell migration rates were studied on the substrates with time-lapse microscopy. Migration rates increased on higher density surfaces containing fibronectin with increasing protrusions and focal adhesion. The fabrication strategy is simple and inexpensive, and does not require multi-step photolithography, baking, and cleaning methods, and will allow for the production of various nanohole array surfaces on a variety of materials. We believe that this fabrication strategy combined with tailored surfaces and microfluidic lithography techniques will allow for the generation of straightforward model systems to study a variety of fundamental cell behaviors ranging from growth and differentiation to apoptosis.

CHAPTER 6

PLASMONIC CRYSTAL SUN SENSOR

Based on manuscript:

A 2D Plasmonic Crystal Incident Angle Sensor to Track the Motion of the Sun

Yi Lou, John F. Muth
(to be submitted)

This chapter introduces a sun sensor design based on the light incident angle dependency of the plasmonic crystals. A self-assembled hexagonal array of sub-wavelength pillars with the pitch of 600 nm in a gold metal film is used in conjunction with a photodetector to form a plasmonic crystal device that is sensitive to the incident angle of nearly collimated light sources such as laser beams or the sun. This principle of operation is distinctly different than the three dimensional angle of incidence sensors and wavefront sensors that rely on imaging the position of a focused spot or a measuring a change in intensity due to a shadow changing with incident angle. The two dimensional nature of the plasmonic crystal allows it to be placed directly on a photodetector or conformally on a photosensitive surface to make a very compact device. Its utility is demonstrated by tracking the motion of the sun. This potentially simplifies the control systems of satellites, heliostats and photovoltaic systems where efficiency of operation is directly related to pointing the system accurately at the light source.

6.1 Introduction

The design concept of this plasmonic crystal sun sensor is that the coherent relationship between the incident lightwave and the surface plasmon allows one to design devices that utilize the sensitivity of the surface plasmon to the angle of incident light to construct angle of incidence or wavefront sensors. Since its sensitivity is inherent in the fundamental physics of the light-surface plasmon interaction, this allows these sensors to be constructed in a very low cost, simple manner resulting in an essentially two dimensional device that requires no

lenses or other three dimensional elements. The sensor is constructed by stacking a plasmonic crystal on a silicon photodiode to measure the transmitted light intensity, while the plasmonic crystal is fabricated by patterning a hexagonal nanobump array in a gold film. The active surface area of the device can be as small as a few tens of microns in length, and its thickness is majorly contributed by the silicon photodiode underneath the gold film.

This sensor design relies on the nanofabrication of structured metallic thin films to allow the manipulation and excitation of the collective oscillations of electrons known as surface plasmons. This has previously resulted in surprising experimental observations such as the extraordinary transmission of light through subwavelength apertures and control of light emission from plasmonic structures. Understanding how to design these nano metallic structures is resulting in a new design paradigm for engineering photonic devices. Due to the sensitivity of surface plasmon resonances to the local dielectric environment and the ability to concentrate electric fields as well as demonstrations that plasmon and lightwave can be confined and manipulated at subwavelength dimensions, many of the devices thus far designed have focused on engineering biological sensors, the construction of plasmonic waveguides, increasing the efficiency of optical emission or devices that otherwise utilizing advantages that near field optical effects can provide.

The ability to construct a sensor that directly converts the incident angle of collimated light sources to photocurrent signals should be useful for systems that track the sun or need to determine the angle of incidence from bright collimated light sources like lasers. Considering the sun example, the compact form factor of the sun sensor can reduce the size, weight, power and computation required for control systems on satellites, especially nano-satellites that use the sun for navigation and attitude control.[126] On earth, conventional photovoltaic systems have shown efficiency improvements of ~40 percent when solar tracking is used.[127] Precision tracking is required for systems that use lenses to concentrate sunlight on triple junction solar cells. Solar concentrating power plants with fields of heliostats require precision tracking of ~1 mrad to obtain the high temperatures required.[128] In adaptive optics system, for example astronomical telescopes and laser communication systems, wavefront sensors are used to remove the effects of atmospheric distortion.[129,130]

Reduce the sensor sizes and simplify the device structures in these system can reduce both the design complicity and maintenance cost.

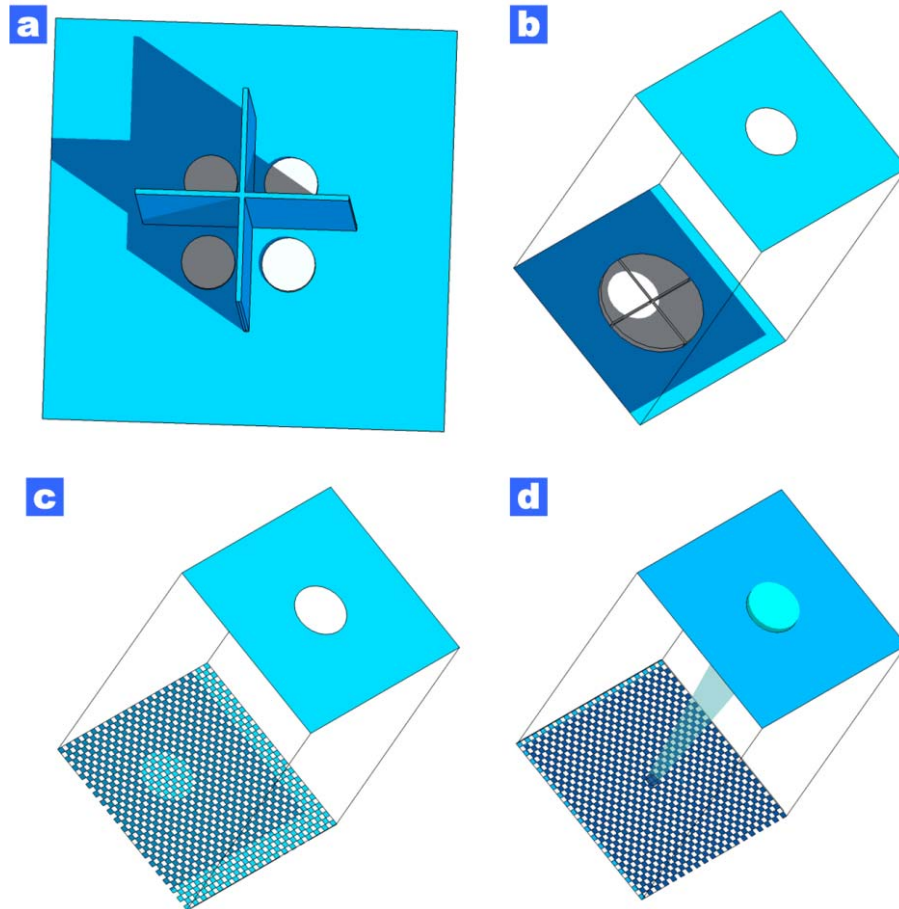


Figure 6-1 Conventional methods of sensing the incident angle of light that rely on shadowing a sensor or measuring the position of a spot determined by an aperture or lens. a) When all sensors are un-shadowed the axis of the cross is pointed at the sun b) A quadrant photodiode used to determine the position of the disk defined by the aperture. c) An imaging array used to determine the spot defined by an aperture. d) A lens used to focus the spot position on an imaging sensor. When used in an array format to measure a wavefront as a function of position, c) and d) are known as Hartmann and Shack-Hartmann wavefront sensors.

In general, the apparent position of the sun can be computed if time and geographic location are known, or directly measured. Often a combination of approaches is used. While the celestial mechanics are well understood, the computational approach is complicated since the apparent position of the sun is a function of latitude, time of day, time of year.[131] For precision systems the refraction of the atmosphere when the sun appears low on the horizon needs to be taken into account. Directly sensing the position of the sun usually requires measuring the position of a bright spot, or shadow using a quadrant or lateral photodiode, or imaging sensor as shown in Figure 6-1a, 6-1b and 6-1c.[132,133,134,135] Recently there has been an emphasis on miniaturizing sun sensors using micro-fabrication and MEMS techniques.[136,137] When multiple micro apertures or arrays of micro-lenses are used, the tilt of the incident wavefront as a function of position can be obtained resulting in a Hartman, or Shack-Hartmann wavefront sensor.[138,139,140] These types of wavefront sensors have been widely used for metrology purposes and in adaptive optics systems where wavefront correction can be used to improve imaging resolution, as can be seen in Figure 6-1d. All these sensors require separation between the photodetector and shield or aperture. In the case of imaging sensors determining the centroid of the spot location require computation.[141,142] In contrast, the plasmonic crystal sun sensor described here requires no computation of the location of a spot and the form factor of the sensor is essentially two dimensional.

6.2 Device Structure and Optical Properties

The plasmonic crystal used in this sensor was prepared by Nanosphere Lithography technique that fabricated hexagonal symmetry nanobump arrays in a gold film. The polystyrene spheres used in the self-assembly process were 600 nm in diameter. The glass substrates were cleaned then treated in piranha solution for one hour to make a hydrophilic surface. A droplet of solution containing polystyrene spheres was drop coated and then dried in a humidified chamber (75% humidity). Spheres self-assembled into hexagonal arrays pattern that can achieve tens of square millimeters in area. The nanospheres were processed by RIE using O₂ plasma (150 W power and 0.04 Torr pressure). The size of the particle could

be controlled by varying the etching time, where 40 seconds etching time was applied in this study. After etching, a layer of chromium (8 nm) and gold (90 nm) was deposited by e-beam to form a continuous film with hexagonal nanobump array. The sun sensor device was prepared by stacking the previous plasmonic crystal on a silicon photodiode, which was Hamamatsu S2386-5K in this experiment. The active area of the photodiode was aligned with the defect free region of the plasmonic crystal, and kept away from boundaries of the nanobump array to avoid light scattering from any irregular structures. The schematic of the sensor device is shown in Figure 6-2.

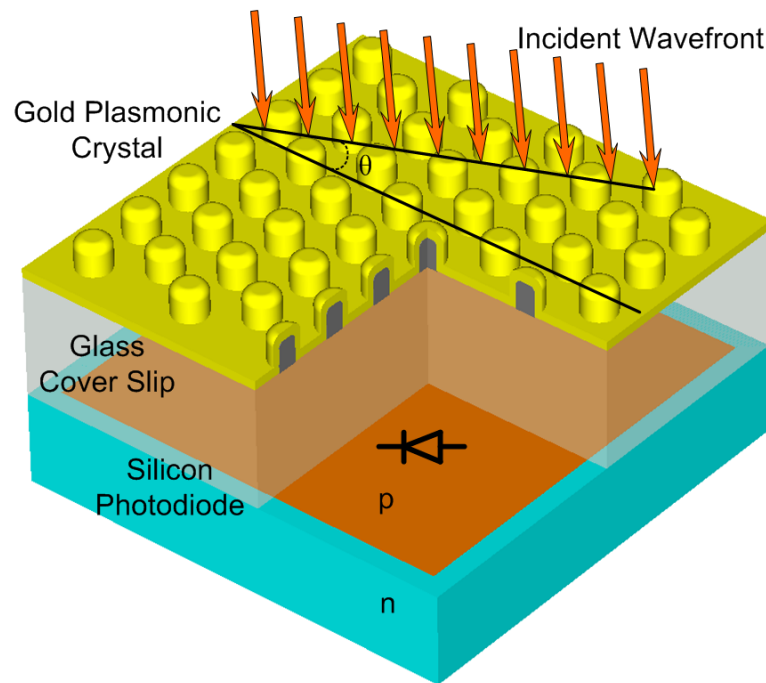


Figure 6-2 The schematic shows the hexagonal nano-bump array used in conjunction with a silicon photodiode, with the angle θ determining the angle of incidence of the wavefront.

The SEM images of a patterned gold film and the cross section of a single nanobump are shown in Figure 6-3. The gold layer was 90 nm thick with an 8 nm chromium layer underneath. The nanobump had a semi-sphere head and the gold layer was thinned at its root. The height of the bumps was 400 nm, which includes the gold header part. The bumps occupied about 60% of the surface area from the top-down view, however, the actual flat

gold region was larger since the bump diameter was reduced at its root. The actual flat gold film was estimated to be 50%-60% of the total surface area. Thickness of the gold film was not uniform. It was thicker between the spheres and was thinner at the root of the spheres. The hexagonal lattice structure was pretty well organized with a few void defects and line mismatch appeared. These defects caused surface plasmon resonance peaks broadening, but did not change the resonant frequencies.

In our device the thickness, the size and the periodicity of the nanobumps in the nanostructure patterned gold film serve multiple purposes. Since the sun is a very bright light source, the thickness of the gold and size of the bumps determine the attenuation of the incident light that reaches the photodiode. It acts as an attenuation filter. The periodicity of the nanobumps is used to determine the wavelength of operation. Although the sun is often considered a broad band, blackbody light source, the solar spectrum has sharp dips due to Fraunhofer absorption and by atmospheric absorption. Thus the surface plasmon resonance wavelength was chosen to avoid absorption dips in the solar spectrum.

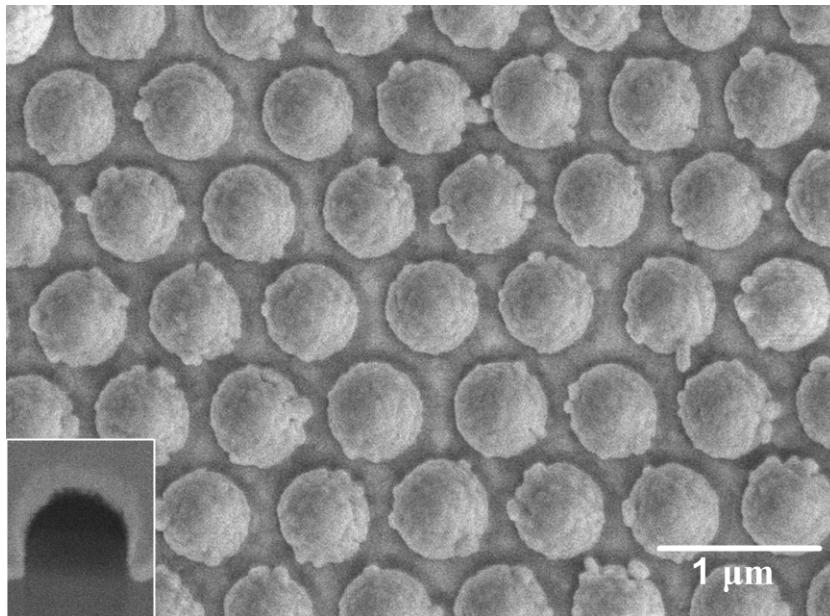


Figure 6-3 An SEM image of the 600 nm periodic self-assembled gold nanobump array with the inset showing the cross section of one nanobump. The outside diameter of the bump is 480 nm and inside diameter is 350 nm. Its height is 400 nm.

The periodic nanostructure couples incident photon into surface plasmons by providing momentum matching and generating enhanced transmission effect at the resonant frequencies. The dispersion relation of surface plasmons can be expressed as [3,6]:

$$\frac{\omega}{c} \sqrt{\frac{\epsilon_m \epsilon_d}{\epsilon_m + \epsilon_d}} = |\vec{K}_{sp}| = |\vec{k}_{lattice} + \vec{k}_{\parallel, photon}|$$

where ϵ_m and ϵ_d are the dielectric constant of metal and environment, \vec{K}_{sp} is the surface plasmon wavevector, respectively. For incident photon with zero incident angle, its parallel surface momentum $\vec{k}_{\parallel, photo}$ is equal to zero, so that the periodic surface structure provides all the momentum $\vec{k}_{lattice}$ for surface plasmon excitation. The lattice momentum of a hexagonal symmetry array is $|\vec{k}_{lattice}| = a\sqrt{x^2 + xy + y^2}$. The derivation is given below.

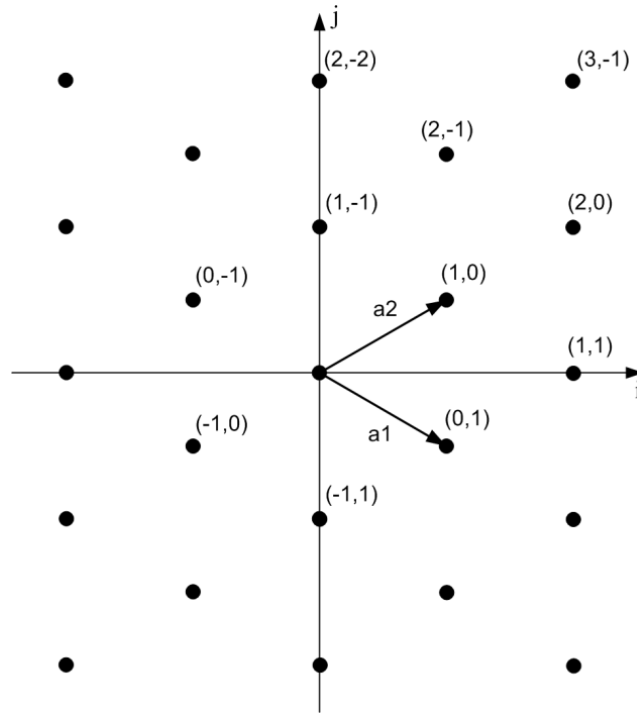


Figure 6-4 The reciprocal lattice of a hexagonal array. a_1 and a_2 are the two primitive vectors corresponding to the (0,1) and (1,0) modes. The other modes are also labeled in the plot.

The primitive vectors a_1, a_2 of the reciprocal lattice of a hexagonal array is shown in Figure 6-4, which is labeled as (0,1) and (1,0) modes. The other lattice vectors can be expressed in terms of the primitive vectors as $x\vec{a}_1 + y\vec{a}_2$, where (x, y) are the index of the corresponding mode. Taking the length of the primitive vector $a = |\vec{a}_1| = |\vec{a}_2|$, they can be expressed in the i-j axes as below:

$$\vec{a}_1 = \left(\frac{\sqrt{3}}{2}\vec{i} + \frac{1}{2}\vec{j}\right) \cdot a$$

$$\vec{a}_2 = \left(\frac{\sqrt{3}}{2}\vec{i} - \frac{1}{2}\vec{j}\right) \cdot a$$

where \vec{i}, \vec{j} are the unit vectors for the two axes. The length for any lattice vector labeled by (x,y) can be calculated as:

$$G = x\vec{a}_1 + y\vec{a}_2$$

$$= \left(\frac{\sqrt{3}}{2}x + \frac{\sqrt{3}}{2}y\right) \cdot a\vec{i} + \left(\frac{1}{2}x - \frac{1}{2}y\right) \cdot a\vec{j}$$

and

$$|G| = \sqrt{a^2 \left(\frac{\sqrt{3}}{2}x + \frac{\sqrt{3}}{2}y\right)^2 + a^2 \left(\frac{1}{2}x - \frac{1}{2}y\right)^2}$$

$$= a\sqrt{x^2 + xy + y^2}$$

where $x, y = 0, 1, 2 \dots$ and $|x| + |y| \geq 1$. Usually, the lowest order ($G = a$) and the second order ($G = \sqrt{3}a$) vectors are the major contributor for surface plasmon coupling, and the corresponding modes are six order degenerate.

Transmission spectra of a 600 nm periodic plasmonic crystal were collected with an increasing incident angle from 0 to 10 degrees as shown in Figure 6-5. The enhanced transmission peaks at normal incident match the surface plasmon resonance wavelength calculated from the dispersion equation, and they are assigned to the correspondent lattice momentum wavevectors. The peak at 773 nm is from the lowest order surface wavevector, and the peak at 603 nm is contributed by the second order surface wavevectors. Both of the

peaks are generated by surface plasmon coupling at the air/gold interface. An absorption layer (8 nm Chromium) was deposited at the gold/glass interface, thus the lowest order peak (around 915nm) at this back side interface is greatly reduced. This absorption layer also broadens the air/gold interface surface plasmon resonance peak, thus the FWHM of the 773 nm peak is 111 nm.

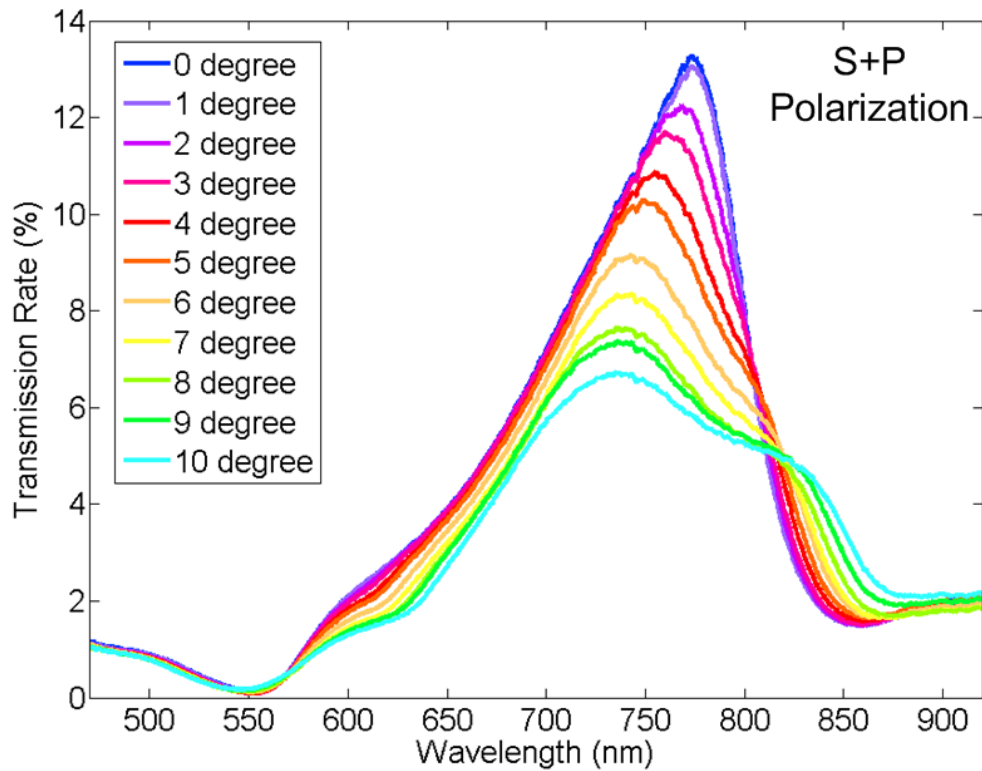


Figure 6-5 The angle resolved transmission spectra of the sensor in response to an unpolarized light from a collimated tungsten white light source. The incident angle is from 0 to 10 degrees.

When the incident angle θ increases from zero degree, the incoming photon provides a momentum term that can be expressed as $\vec{k}_{\parallel, photon} = (\omega/c)\vec{n}\sin\theta$, where \vec{n} is a unit vector

within the incident plane and parallel to the plasmonic crystal surface. This momentum changes the surface plasmon resonant frequencies depending on the incident light's polarization and the direction of the lattice momentums. The degenerate lowest order surface plasmon resonance mode split into two with less intensity and shifting away from their original position when the incident angle increases. Surface plasmon coupling efficiency also decreases with tilted incident light, thus the intensities of the resonance peaks drop with increasing incident angle.

6.3 Device Response for the Sun Light

Based on the angle dependent spectrum changing, a sun sensor was designed by stacking the plasmonic crystal with a silicon photodiode. Sunlight passing through the plasmonic crystal was filtered by the metal thin film, and the transmitted light generated photocurrent with its strength depending on the incident angle. The device testing setup included an optical mount that aligns the normal of the plasmonic crystal surface with the sunlight and a photocurrent measurement instrument, as shown in Figure 6-6. A laser diode controller was used to measure the photocurrent from the diode, and it was connected to a laptop using the GPIB port. A homemade program in LabView CVI was used to record data every one second and plot the response curve.

The steps for acquiring the sunlight response data was as follow: 1) move all the data collection setup to outdoor and connect the power supply; 2) align the normal of the plasmonic crystal surface with the incoming sunlight; 3) start the data collection program and wait 20 minutes for the collection process. The sun moves at a speed of 15 degrees per hour, thus it takes 20 minutes to collect the device response from 0 to 5 degrees. During this period, the optical mount should not be moved and the sunlight should not be blocked by cloud. All the sensor response curves were measured between 11am and 3 pm at the latitude of 35 degrees. The weather was clear and did not have wind.

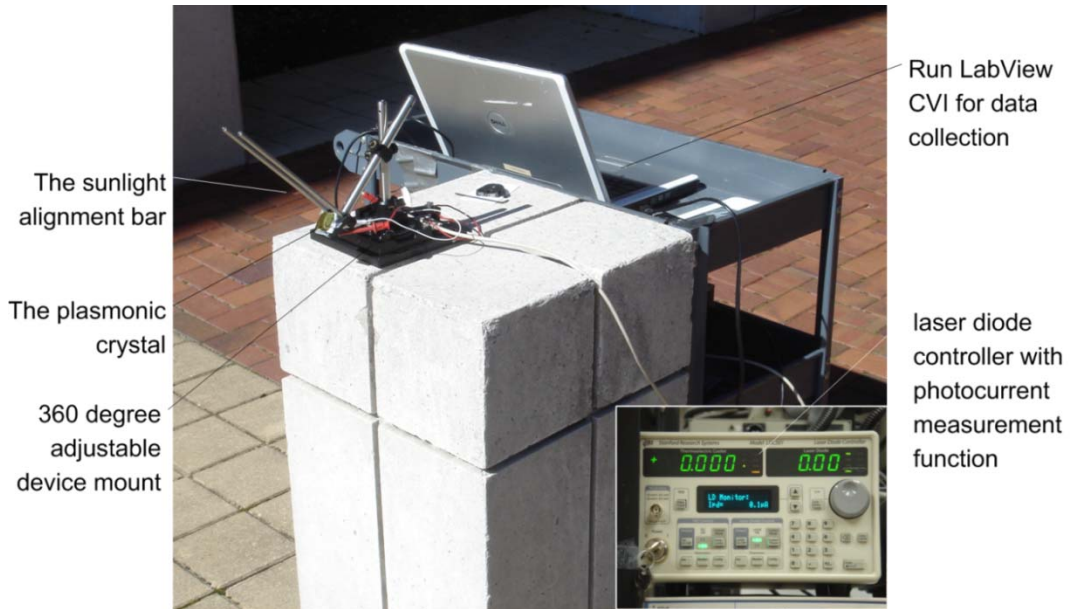


Figure 6-6 The optical setup for outdoor data collection.

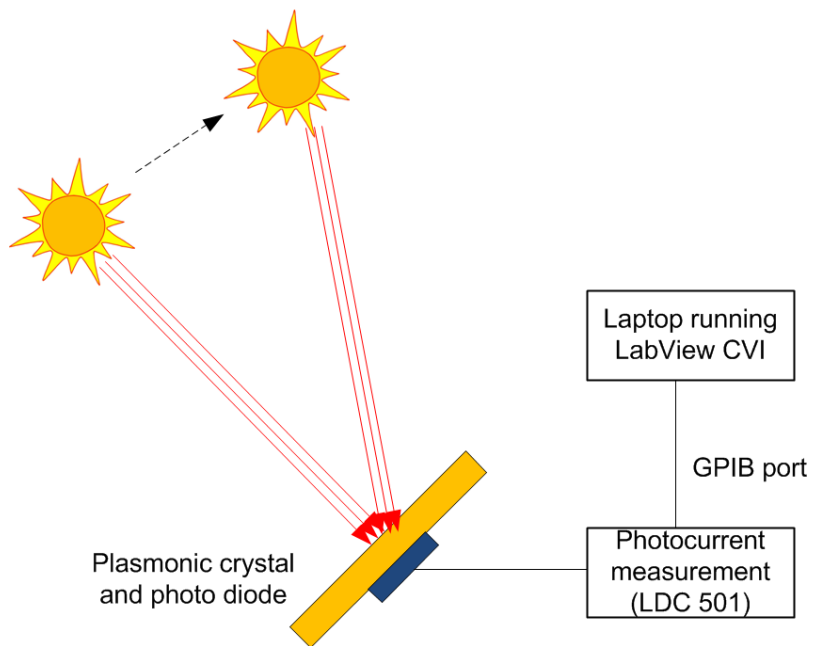


Figure 6-7 The schematic for the device response testing setup under the sunlight.

The sunlight response curve is shown in Figure 6-8. It is normalized to the maximum value, which happens at normal incident. The absolute photocurrent is determined by the active area of the device, which can be adjusted during the design stage to fit the photocurrent measuring circuit. The photodiode output current can be express as:

$$I = \int A_{active} T_{SP}(\omega, \theta) P_{Sun}(\omega) R_{diode}(\omega) d\omega$$

where A_{active} is the active area of the device, T_{SP} is the transmission ratio of the plasmonic crystal, P_{Sun} is the radiation power of the sun at the location of the sensor, and R_{diode} is the photocurrent response rate of the photodiode, respectively. R_{diode} is a function of the wavelength, and it is around 500 mA/W at 700-800 nm wavelength.

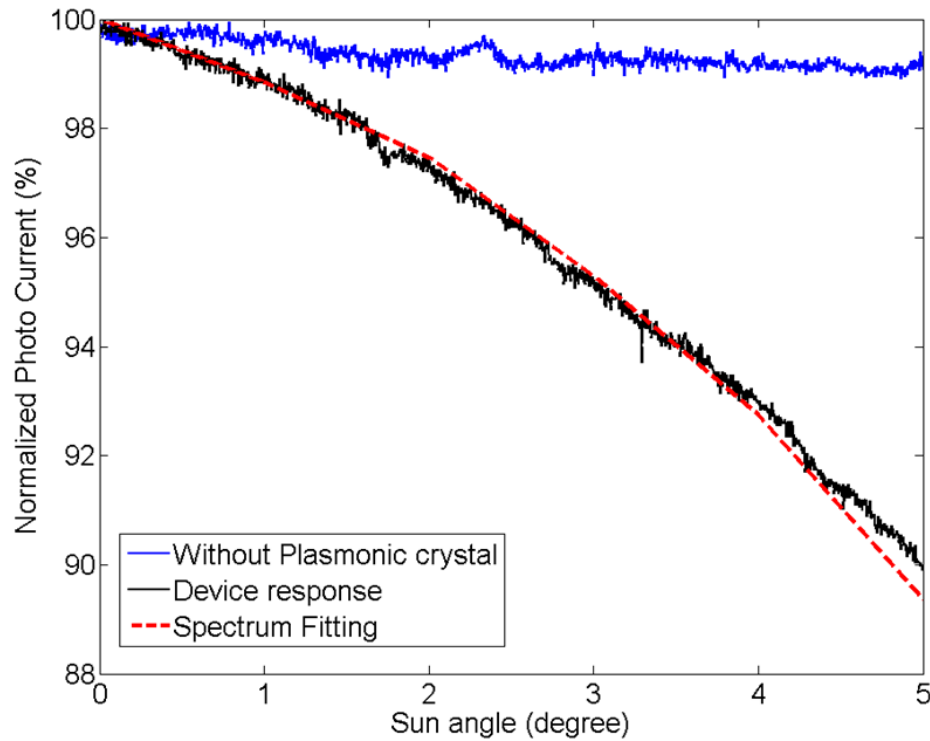


Figure 6-8 Experimental data for the device response to the sunlight shows strong angular dependence when the nanobump array is installed. In contrast, there is little change in the photocurrent response curve without the plasmonic crystal.

Without the plasmonic crystal, the photocurrent was kept within 99% of its maximum. It decreased because the cross section of the device active area and incident sunlight was reduced in a tilted incident case. It followed a $\cos(\theta)$ relation where θ was the incident angle, and $\cos(5^\circ)$ was approximately 99.6%. This can be used as a reference signal. After the plasmonic crystal was installed, the sensor output dropped at a speed of 1.8%~2% per degree with increasing incident angle. At 5 degrees, the output dropped to 90% of its maximum, as shown in Figure 6-8. Two mechanisms contributed to this change: 1) power distribution of the sunlight and the photodiode response rate were not constant around the enhanced transmission wavelength, thus shifting in surface plasmon resonant frequency changed the amount of power received by the photodiode; 2) the plasmon coupling efficiency was sensitive to the incident angle and decreased from its maximum that happens at normal incident.

6.4 Angle Resolved Spectrum for Polarized Light

Polarization state of the incoming photon changes the sensor's response. Angle resolved transmission spectra for p and s polarized light were collected for the 600 nm periodic plasmonic crystals. The spectra were identical for both polarizations at normal incident. For p-polarized light, the lowest order surface plasmon resonance peak at 773 nm splits into two peaks, as shown in Figure 6-9. The blue shifting peak was stronger in intensity and its FWHM was ~120 nm, the red shifting peak was weaker and had a FWHM of ~60 nm. The two peaks move at an average speed of 10-15 nm/degree to opposite directions. The second order plasmon peak at ~600 nm also split, but its intensity was low so that the shifted peak position cannot be viewed clearly. In contrast, the gold plasma peak at 500 nm keeps constant during the incident angle changes.

On the other hand, the resonance peaks of s-polarized light did not split with tilted incident light, and its intensity dropped due to reduction in coupling efficiency, as shown in Figure 6-10. The sunlight does not have a specific polarization, thus the sensor response was the linear combination of the transmission intensities for both s and p polarized light.

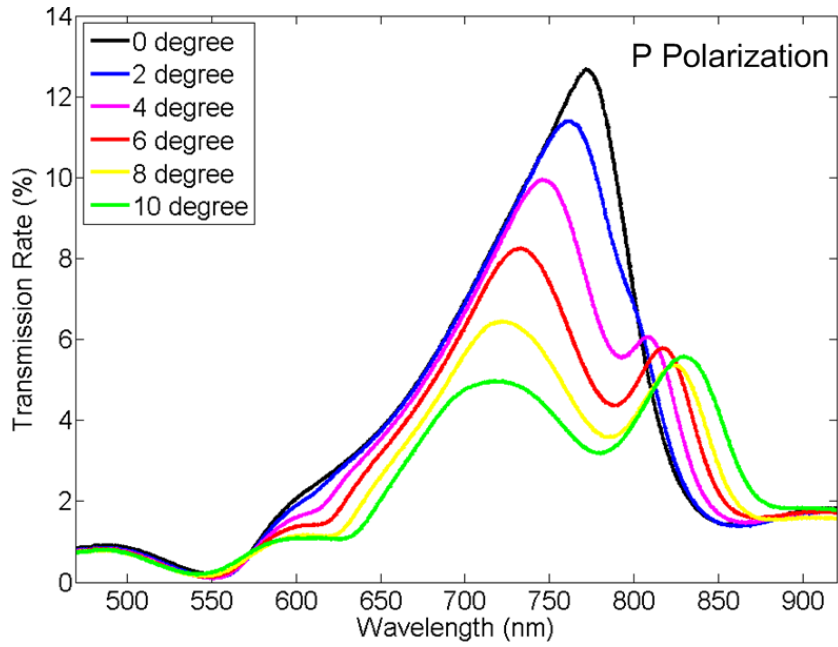


Figure 6-9 The p-polarized light transmission spectra for 0-10 degree incident angles. The surface plasmon peak at 773 nm splits into two peaks with increasing incident angle.

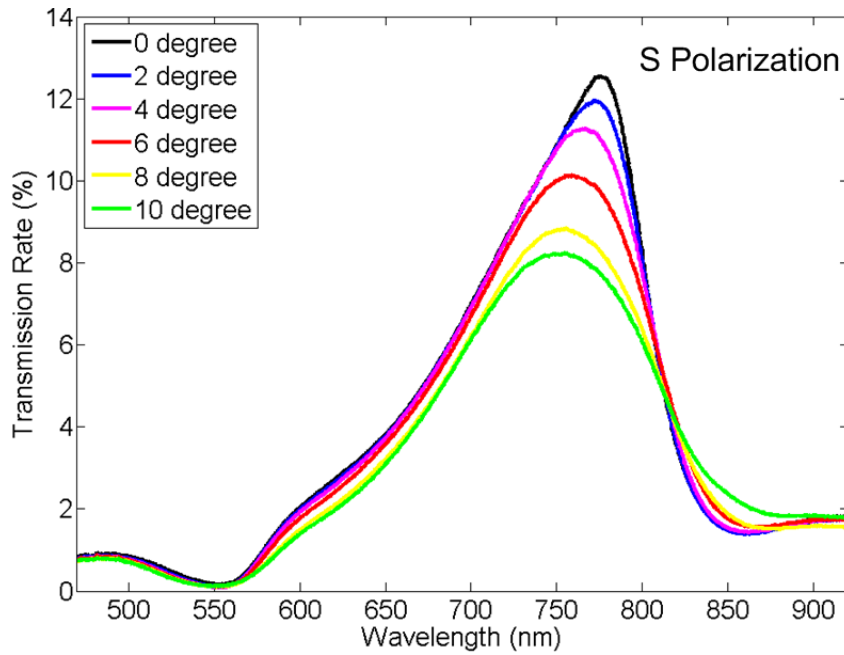


Figure 6-10 The s-polarized light transmission spectra for 0-10 degree incident angles.

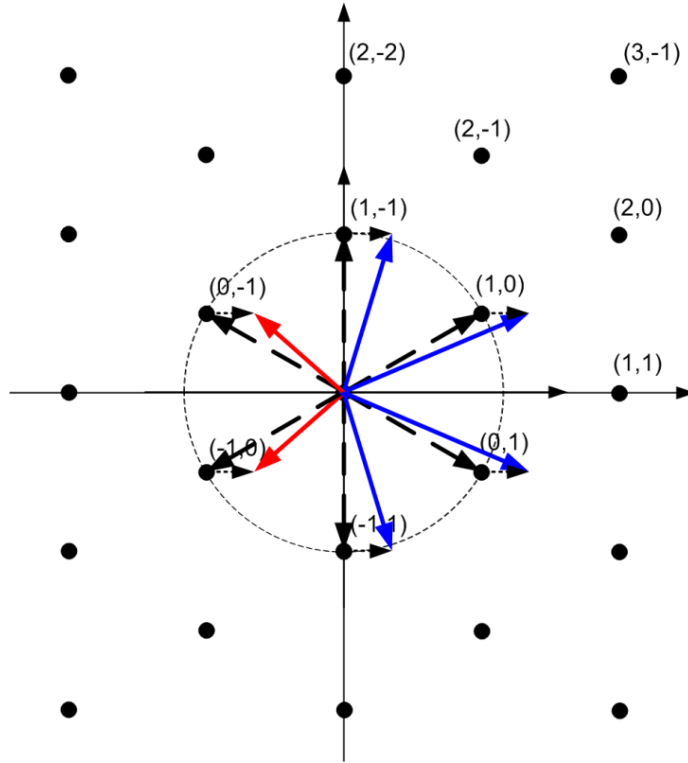


Figure 6-11 The p-polarized light provides additional momentum at the direction parallel to the incident plane. The total momentums are the vector sum of the lattice momentums and the photon momentums, which are labeled by the red and blue vectors.

The polarization state dependent resonance peaks shifting can be explained by the wavevector matching mechanism. The reciprocal lattice for a hexagonal array also has six-fold symmetry, and the lowest order wavevectors have the same magnitude thus the corresponding surface plasmons polariton modes are degenerate in energy at normal incidence, as shown in Figure 6-11.[143] For photon with incident angle $\theta > 0$, the p-polarized light provides a surface momentum along the direction of the incident plane. The total momentum is the vector summation of the lattice momentum and the incident photon parallel surface momentum, which is labeled by the color arrows in Figure 6-11. The blue arrows indicate blue shift, and the red arrows indicate red shift. Magnitude of the (0,-1) and (-1,0) wavevectors are decreased and their surface plasmons resonance peaks shift to longer wavelength. The magnitude for the other four wavevectors (0,1)/(1,0)/(1,-1)/(-1,1) are

increased and their surface plasmons resonance peaks shift to shorter wavelength. The resonance peaks for (0,1)/(1,0) and (1,-1)/(-1,1) modes are overlapped at small incident angle. The total number of the blue shifted modes is greater than the red shifted modes, causing the blue shifted peak has stronger intensity. It is interesting to notice that the p-polarized light transmission rate changes greatly at the surface plasmons resonance at the normally incident case wavelength (around 773 nm), which is caused by modes shifting. There is a 20-30 nm window where the transmission intensity drops to 20% within ten degrees. The 780 nm wavelength is chosen within this window to demonstrate the possibility of performing high sensitivity measurement, which will be discussed in later sections.

On the other hand, the s-polarized transmission light cannot provide any additional momentum, thus the total momentum keeps unchanged during the incident angle increasing process. The spectra of s-polarized light do not show surface plasmons resonance peak splitting, since the degeneracy of the lowest order mode is not removed. Its peak intensity drops much slower than the p-polarized light case, and this can be used to obtain a wide field of view for the sensor design.

6.5 Device Response for Collimated Laser Beam

This sensor can also be used to detect the incident angle change of a collimated laser beam that has the wavelength closed to its surface plasmons resonance wavelengths. A tunable wavelength Ti:sapphire laser was adjusted to 780 nm in CW mode and used as the light source for transmission spectrum collection. The optical configuration is shown in Figure 6-12. The laser light transmitted through the plasmonic crystal and was collected by a photodiode. The plasmonic crystal was mounted on a rotation stage that was driven by a step motor. It rotated at a speed of 1/40 degree per step, and the maximum range of rotation was 20 degrees. Wide range transmission intensity measurement were generated by sweeping the incident angle 20 degree at one run and connecting the response curves for each run. The output beam of the laser was p-polarized for the rotation direction of the sample holder. A quarter waveplate was used to change the polarization direction of the laser light if necessary.

The sensor response for both s and p polarization 780 nm laser were collected, as shown in Figure 6-13. Transmitted intensity for p-polarized light reduced at a speed of 13.5% per degree, and reached 40% of its maximum at 5 degrees incident angle. The curve for s-polarized light dropped at 6.8% per degree and was reduced to about 70% of the maximum at 5 degrees. The curves are symmetrical around zero degree when the incident angle is not too large (< 20 degree), which was expected since the nanobump arrays did not have any orientation preference. At larger incident angle (~ 40 - 50 degree), the two sides of the curve were not perfectly symmetrical because the laser spot moves on the plasmonic crystal surface thus process variation caused the difference. The inserted curve in Figure 6-13 shows that the device can have ± 60 degree field of view when uses s-polarized laser as light source.

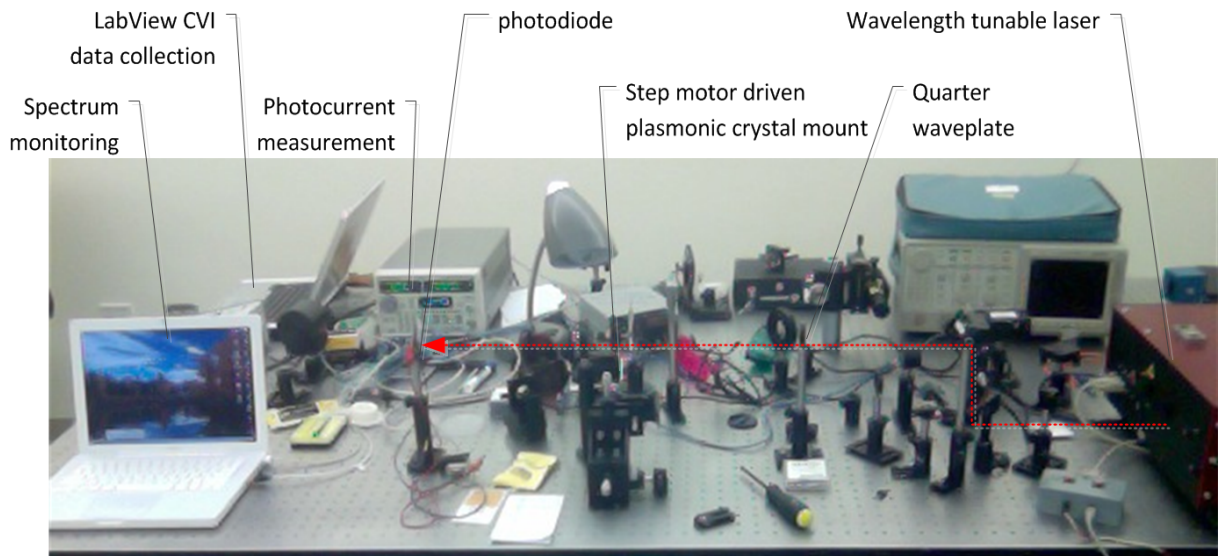


Figure 6-12 Optical setup for collimated laser beam transmission intensity collection. The tunable wavelength laser was tuned to 780 nm output wavelength, and a quarter waveplate was used to change the polarization state of the laser light. The sample mount was driven by a step motor that moved at $1/40$ degree per step.

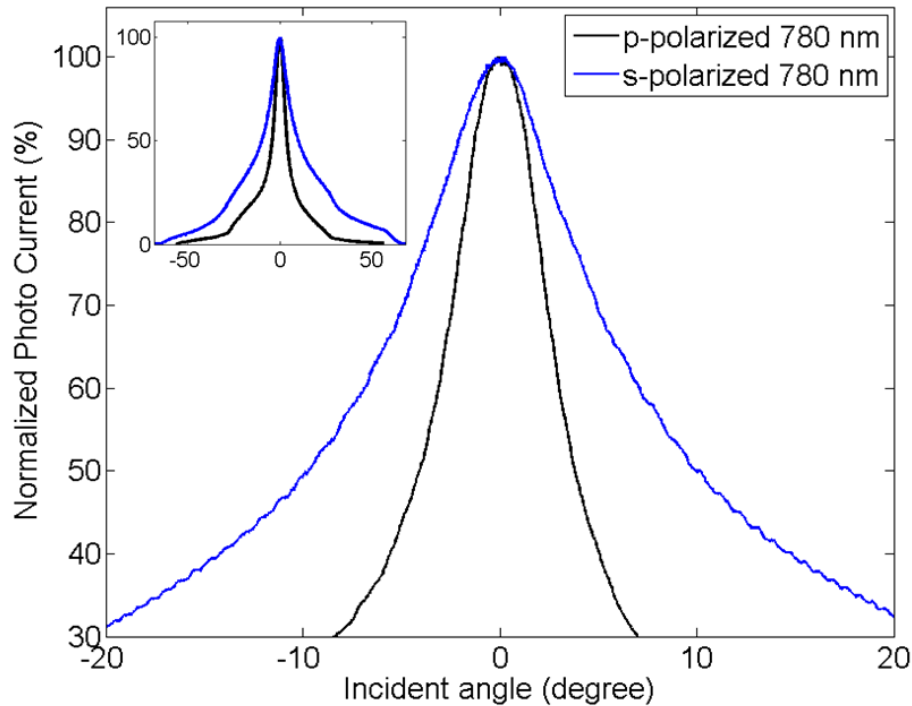


Figure 6-13 Photocurrent response to a 780 nm collimated laser beam with both s and p polarizations. P-polarized light response drops below 30% of its maximum within 10 degrees, while s-polarized light decreases slower. The insert shows a large angle (+/-60 degree) device response to the laser beams.

The device sensitivity for a single frequency laser light was larger comparing to the sunlight curves because the sunlight response integrated over all the sun's spectrum range. The transmission ratio for gold bulk plasma at 500 nm did not change with incident angle and the sun spectrum has its maximum power intensity around 500-550 nm, thus it contributed a constant background power which reduced the device sensitivity. The wavelength of 780 nm was chosen for maximizing the device response because the surface plasmon peak splitting effect with p-polarized light made it possible to reduce the transmission intensity very quick with small incident angle changes. The device response for 775-790 nm wavelength laser light were collected taking advantage of the adjustability of the laser, as shown in Figure 6-14. All the curves were normalized to its maximum value, which happened at normal

incident. The fastest intensity reduction was located around 780 nm, where ± 5 nm in wavelength did not give much difference. In contrast, the curve for 790 nm wavelength keep larger intensity remains at 5 degree and beyond. However, the improvement in device sensitivity for laser light also introduced the issue of process variation. The response curves did not have good symmetry at large incident angles.

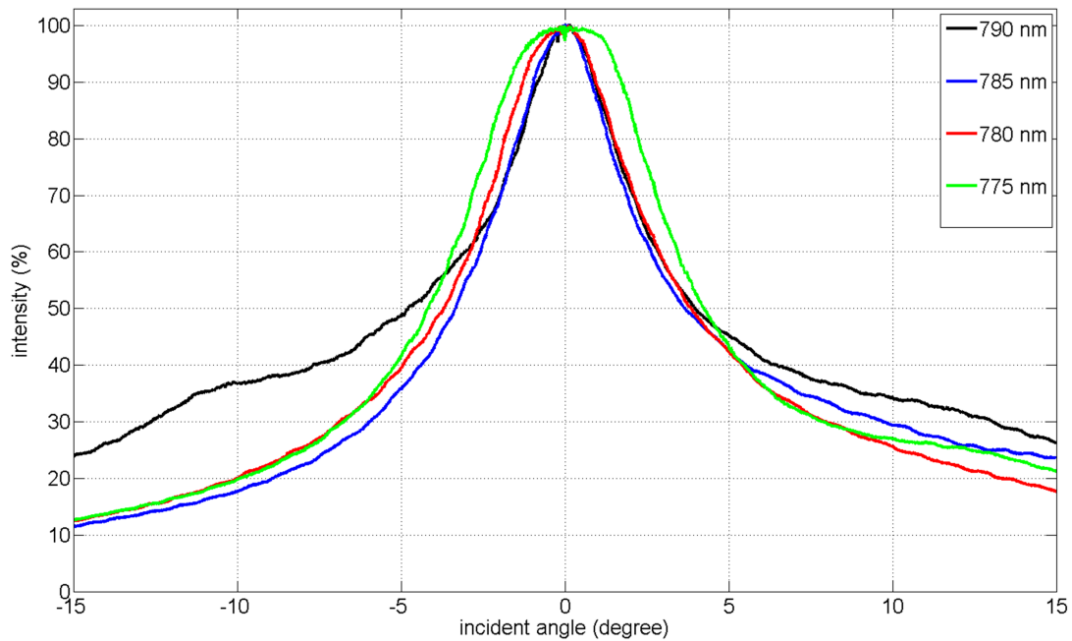


Figure 6-14 Device response for p-polarized laser with different wavelength (775-790 nm).

The sensor response was also collected with a commonly used 633 nm He-Ne laser. Its wavelength was close to the second order surface plasmons peak position, thus changes in incident angle cause transmission spectrum intensities decreasing. The response curve for s and p polarization laser light are shown in Figure 6-15. The p-polarized light dropped at an average speed of 9.3% per degree between 2-8 degrees, which was lower than the 13.5% per

degree at 780 nm wavelength. At small incident angle (< 2 degree), the intensity change was relatively small, which is about 4% per degree. The response curve also saturated when the incident angle was larger than 10 degree, because the blue shifting peak of the lowest order surface plasmon peak overridden the second order peak and dominates the trend of the intensity changes. The curve for p-polarized light become almost flat at large wavelength, and had some small fluctuations. On the other hand, the curve for s-polarized light keeps with 95% of its maximum for small incident angle (< 4 degree). Then it decreased at a speed of 4~5% per degree, which was slower than the p-polarized light but did not saturate at large angle. Comparing the sensor response at the two laser wavelength, the transmission intensities decreasing speed were similar for p-polarized light, and both of them decreased to ~30% at an incident angle of 10 degrees. For s-polarized light, the 780 nm wavelength curve dropped more quickly than the 633 nm wavelength curve.

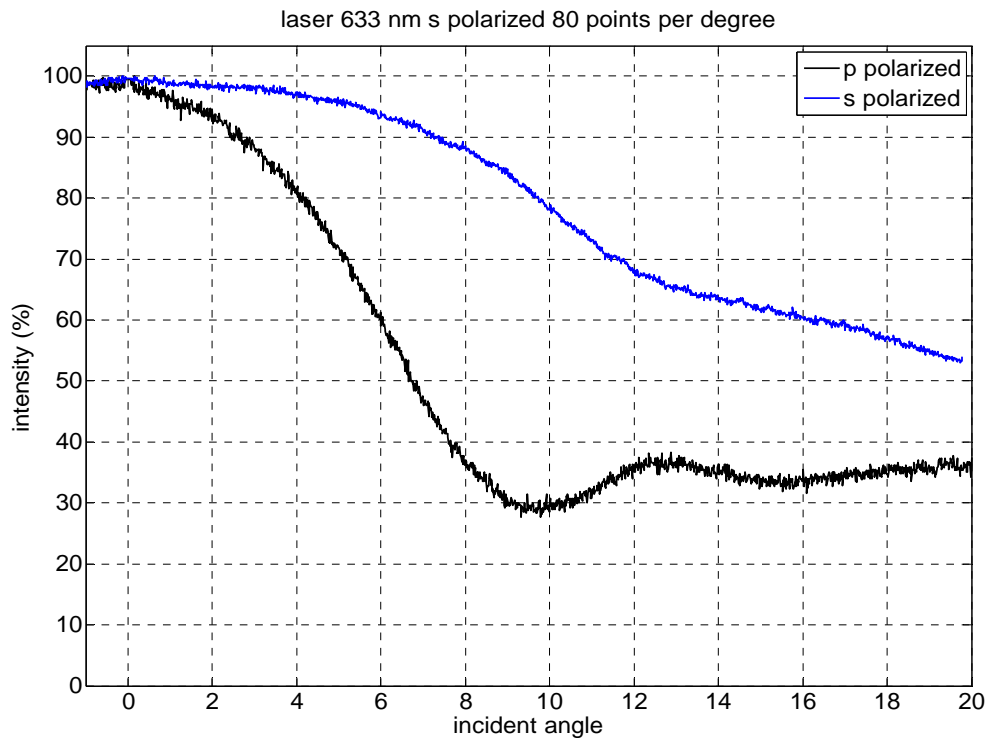


Figure 6-15 Device response curve for a 633 nm He-Ne laser with both s and p polarized light.

6.6 Hexagonal and Rectangular Symmetry

The sensor uses hexagonal symmetry lattice for plasmonic crystal construction, which is better than the commonly used rectangular lattice in previous research.[3,144] The self-assembly process of nanosphere is driven by capillary force between spheres, and it naturally generated a close-packed hexagonal structure. The spacing between the centers of two neighbor spheres is determined by the sphere's diameter, while the RIE processing time controls the size of a single nanopost or nanohole. The primitive cells for the rectangular and hexagonal lattice are shown in Figure 6-16. The primitive vectors for the rectangular lattice are 90 degrees from each other, while the vectors for the hexagonal lattice are 60 degrees apart. Considering the two types of plasmonic crystals that are constructed by nanobump arrays with both rectangular and hexagonal symmetries, the properties of their reciprocal lattices are studied by performing 2D Fourier transform to the lattice.[145] The patterns after Fourier transform have the same symmetry as its original lattice and are transferred from real space to momentum space. Then the strength of each wavevector is calculated, which is determined by the distance between the point and origin in the reciprocal space. The density distributions of the wavevectors are plotted on the right side of Figure 6-16 for the two symmetries.

The first four modes in the momentum space are labeled to their correspondent intensity peaks. Both of the wavevector density spectra are calculated with 600 nm periodicity lattices, i.e. the spacing between any two closest neighboring nanohole centers is 600 nm. The first order wavevector (1,0)/(0,1) for the hexagonal lattice is larger than its correspondent in the rectangular lattice, indicating that a shorter surface plasmon resonance wavelength in optical spectrum can be achieved with the hexagonal lattice of the same pitch. While the cost of making smaller structures is higher and also requiring more complicate tool, choosing the lattice symmetry is an easy way to shift the resonance wavelength to smaller wavelength if it is required for certain application. Moreover, comparing the distance among the peaks, hexagonal lattice has larger distance between the first order (1,0)/(0,1) peak and the second order (1,1) peak. This leads to less overlapping among the low order surface plasmon resonance peaks in the optical spectrum.

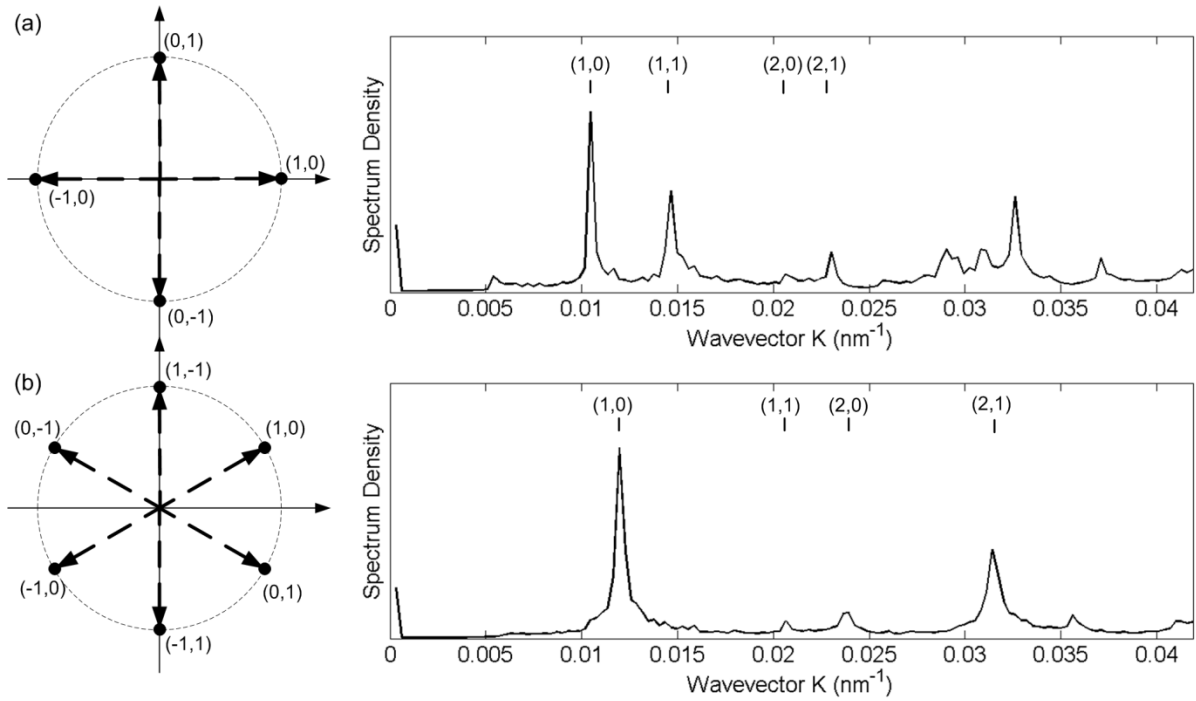


Figure 6-16 The primitive vectors for (a) rectangular and (b) hexagonal arrays. The density distributions of the wavevectors are plotted for each pattern with their first four modes labeled.

Another important factor for the hexagonal lattice is that it has a stronger first order (1,0)/(0,1) peak comparing with the second and third order peaks. In contrast, the first four modes for the rectangular lattice have similar intensities. The strong first order (1,0)/(0,1) peak in the hexagonal lattice is caused by the six fold symmetry of the lattice. Six degenerate wavevectors contribute to this peak, while the rectangular lattice has only four degenerate wavevectors for the first order mode. Other than the periodicity of the lattice, diameter of each individual bumps also affects the relative strength distribution among the wavevector modes, but this is a secondary effect and does not change the position of the modes. All these properties of the hexagonal symmetry lattice show that it a better geometry for narrow frequency surface plasmon resonance with discrete peaks.

In summary, we proposed a novel sun sensor design based on the transmission spectrum changes of a hexagonal lattice plasmonic crystal. This type of sun sensor has the potential to be integrated on a silicon chip by patterning a photodiode surface with nanobump arrays then coating a layer of metal on its surface. Large area arrays with 200-400 nm nanobump diameters can be fabricated in volume by lithography methods with lost cost. The minimum active area for the device is limited by the surface plasmons decay length. However, the device is usually larger than this limit in practice in order to generate enough photocurrent. The sensor does not have any complex 3D structure, and its performance is controlled by turning the surface geometry parameters such as periodicity, nanobump diameter and aspect ratio. The prototype device presented here has its limitation in detection range and sensitivity, but its unique concept of applying plasmonic crystal in angle detection opens a new design path for multiple applications.

CHAPTER 7

PLASMONIC CRYSTAL WAVEFRONT SENSOR

Using the incident angle sensor introduced in the previous chapter, a plasmonic crystal wavefront sensor can be developed. Wavefront sensors are commonly used in adaptive optics systems for controlling the wavefront corrector. Applying the plasmonic crystal in wavefront detection can reduce the form factor of the device because the plasmonic crystal is a 2D structure and does not use any lens that requires a focal length. The physical layout of the sensor and the schematic of the data collection & processing circuit are presented. An algorithm for reconstructing the incident wavefront is discussed. There is some limitation in applying this plasmonic crystal sensor, because the azimuth angle information of the incident wavefront normal vector is not intrinsically obtained. The condition for successfully reconstructing the wavefront is discussed. This chapter will focus on the system level integration of the sensor and the data processing circuit.

7.1 Wavefront Sensor Pixel Array Design

A wavefront sensor is a device to measure the aberrations of an incident wavefront. It is commonly used in adaptive optical systems to reconstruct the wavefront and generate the control signals for wavefront correctors. The Shack-Hartmann (S-H) wavefront sensor is one of the most widely used wavefront sensors. It was developed in the late 1960s at the Optical Sciences Center at University of Arizona to improve the imaging of satellites.[146] Its basic idea was to measure the Optical Transfer Function (OTF) of the atmosphere and remove its effects by dividing the OTF of the image by the OTF of the atmosphere. The difficulty in realizing this idea was how to measure the atmosphere OTF at the same time the image was taken. In addition, the exposure time need to be short so that changes in wavefront were not more than $\lambda/10$ over the measurement, thus requiring an exposure time of about 1/60 second. A beam splitter was inserted in the telescope optical path to redirect part of the light to a wavefront sensor, so that the image and the atmosphere OTF can be captured simultaneously.

However, this method caused a relatively small amount of photon going to the wavefront sensor. Micro-lens array was applied to replace the pin-holes array in the Hartmann sensor, so that it can collect more photons for a stronger signal. This leads to the design of Shack-Hartmann wavefront sensor.

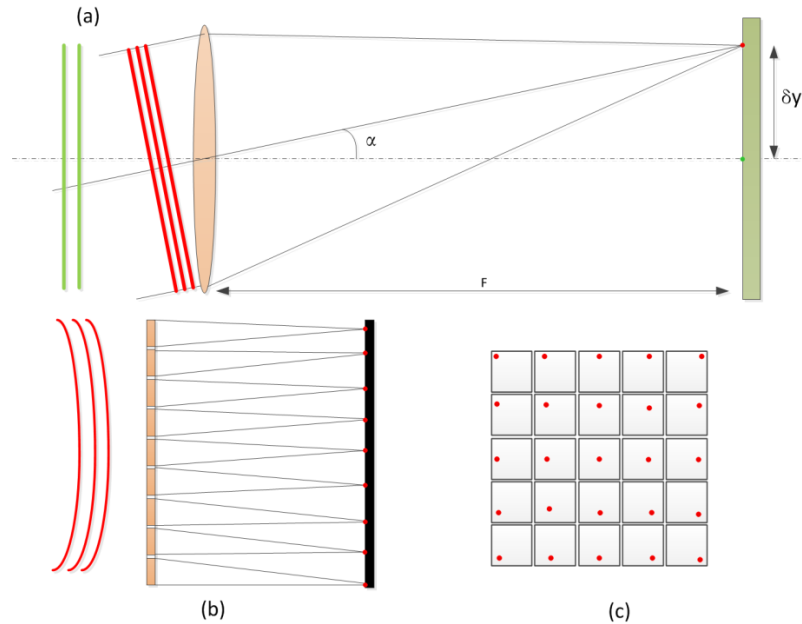


Figure 7-1 The principles of operation of the Shack-Hartmann wavefront sensor. (a) The focus spot of a tilted incident wavefront pass through one micro-lens is shifted from the reference center by δy ; (b) A array of micro-lenses redirect the locally incident wavefront to their correspondent light spots; (c) A CCD array is placed at the focus plane and recorded the position of the light spots for each micro-lens. This will be used to reconstruct the wavefront.

The principle of operation for the S-H wavefront sensor is illustrated in Figure 7-1. It consists of an array of micro-lenses with the same focus length. Each lens focuses the local incident wavefront to a light spot on the CCD detector array. The tilting of the incident wavefront at the position of each lens can be calculated from the shifting of the focal spot comparing to a reference wavefront. To reconstruct the wavefront from the sensor data, several different algorithms have been developed. They can be roughly divided into two classes: iterative methods are fast and often used in real time applications; matrix inversion

methods are slower but more accurate.[147] The matrix inversion method fits the 2D wavefront surface with polynomials, and calculates the coefficients of each term using a pre-defined matrix.[147,148,149,150] This method will be applied to this plasmonic crystal (PC) wavefront sensor design, and the reconstructed surface will be compared with the original wavefront for error analysis.

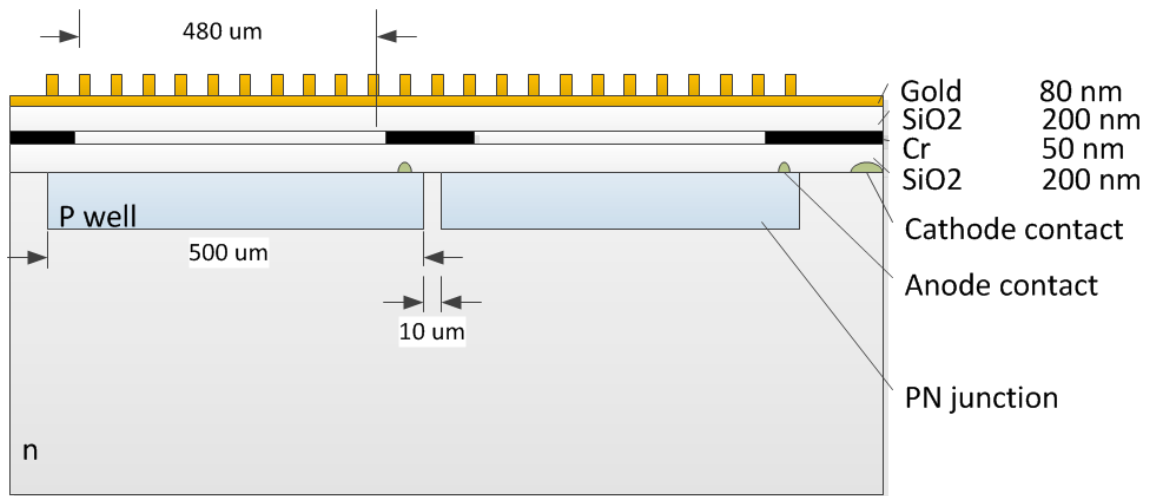


Figure 7-2 The cross section schematic of the plasmonic crystal (PC) wavefront sensor. The p-n junction photodiode collects the light intensity. The plasmonic crystal is placed above the diode to filter the incident light depending on the incident angle.

The fabrication process of the PC wavefront sensor is compatible with the modern CMOS technology. It is a multilayer 2D structure with its cross section view shows in Figure 7-2. The process starts with a N-type bulk silicon that is used as the substrate. P-wells are formed by selective diffusion of boron to a thickness of approximately 1 μm or less. Each block of P-well is a 500 $\mu\text{m} \times 500 \mu\text{m}$ square. This p-n junction forms the photodiode for light intensity sensing. The area of the photodiode is decided by the amount of the photocurrent required to drive the data collection circuit. For the application of sun sensor, the solar radiation at the surface of the earth is about 1000 W/m^2 . In space for satellite

applications, the intensity is about $1400\text{W}/\text{m}^2$. The transmission rate of the plasmonic crystal is around 15% depending on the gold film thickness, and the photo sensitivity of the photodiode has a maximum of $0.6\text{A}/\text{W}$. Considering that all these parameters are wavelength dependent and the atmosphere absorption reduces sun light intensity, an attenuation factor ~ 0.5 is added and the photocurrent generated by the diode is $15\sim 20\ \mu\text{A}$. If the sensor is designed for laser beam wavefront sensing, the photodiode active area for each pixel can be much smaller. For a $5\ \text{mW}$ He-Ne laser with a beam diameter of $2\ \text{mm}$, the radiation power is $1600\ \text{W}/\text{m}^2$. The photo current generates from a sensor with $250\ \mu\text{m} \times 250\ \mu\text{m}$ pixel size can be around $10\ \mu\text{A}$.

Metal wires with contact vias are used to connect the anode and cathode of the silicon photodiodes, which is the same as drain/source connection in CMOS technology. The photodiodes are shadowed by a layer of Cr at its border to reduce the edge effect, so that only the central part of the diode to be illuminated by light. The plasmonic crystal is fabricated on the very top layer of the whole structure. A SiO_2 layer is used to separate the crystal from the Cr layer, and chemical mechanical polishing is required to prepare a flat substrate surface for plasmonic crystal fabrication.

Alternatively, a different device structure could be applied. The gold layer could be directly patterned on the silicon substrate, thus no buffer layer exists in this structure. The advantage of this method is the reduction in fabrication steps lower the cost and improved yield. The downside is that the electron-hole pairs excited by photon may change the dielectric constant of the silicon substrate thus affecting the surface plasmon peaks position. A relatively thick Cr layer ($\sim 10\ \text{nm}$) can be deposited between the gold layer and the silicon body to block the surface plasmon field from extending into the substrate, but this will also reduce the transmission ratio. The wire routing for connecting the diode electrodes to peripheral circuits will be a challenge in this design, if the plasmonic crystal gold layer is a continuous film covering the whole surface. The choice in device structure depends on which specific semiconductor foundry and process is used. Since gold is not allowed in most silicon foundries, it is likely the first method proposed where the gold is deposited on a SiO_2 layer will be preferred.

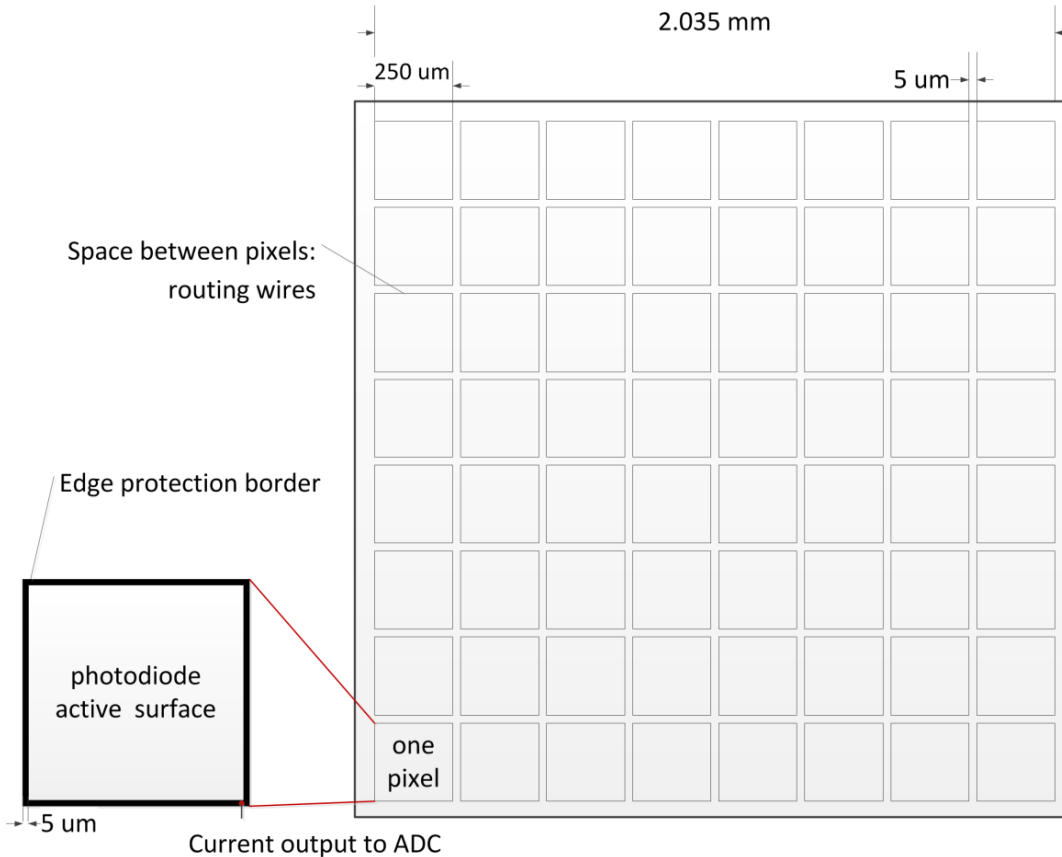


Figure 7-3 Layout of a $\sim 4 \text{ mm}^2$ PC wavefront sensor that is constructed by an array of pixels. Each pixel is an angle of arrival sensor with a protection border. An 8x8 array was chosen in this design.

The layout of the whole sensor is constructed by an array of photodiodes with a continuous plasmonic crystal gold film on top of it. An 8x8 array of photodiodes is applied, as shown in Figure 7-3. Each pixel has a 5 μm protection border made by Cr, which can block the light from reaching the edge of the diode that may have doping density variation. This border also provides space for placing the anode contacts. The spacing between pixels is 5 μm, which is enough for signal wire routing. If the pitch of the signal wire is 500 nm, it requires $8 \times 500 \text{ nm} = 4 \text{ μm}$ width for routing, since each row has eight pixels. All the wires will firstly route to one edge of the array, and then connect to the designated output pins.

The plasmonic crystal can only detect the polar angle of the incident light. The azimuthal angle information is lost during the measurement. In comparison, the S-H wavefront sensor

measures the focused light spot shifting in both x and y direction, so that it knows in which direction the wavefront is tilted. The azimuthal angle can be measured by the plasmonic crystal with two grating structures, however, this requires more complex design and consumes more area. The layout for one pixel is shown in Figure 7-4. It contains four photodiode sensors with different gold patterns on top of them. Each of them is a $400\ \mu\text{m}$ by $400\ \mu\text{m}$ square, and the spacing between them is $10\ \mu\text{m}$ to insure less plasmon field coupling between any two structures. The total length of a pixel is around $800\ \mu\text{m}$ in one side, thus it requires the incoming wavefront should be smooth at millimeter scale. This design is operated under the assumption that the wavefront detected by the four photodiodes within one pixel are almost the same.

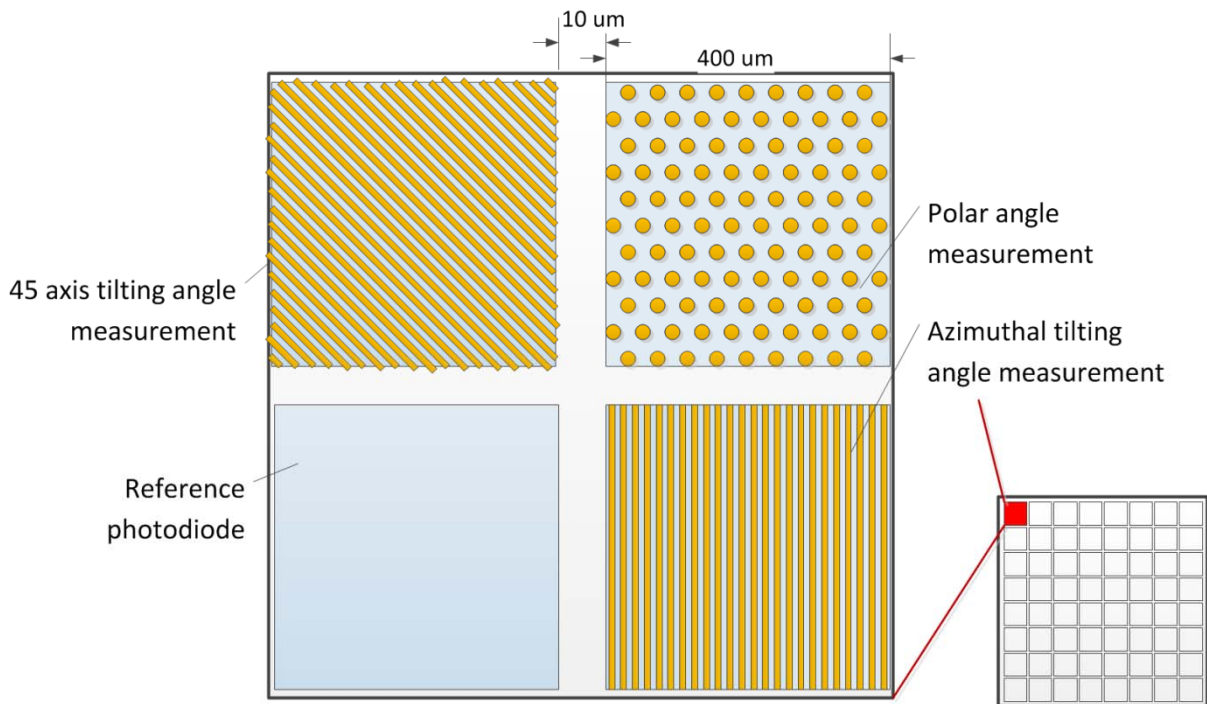


Figure 7-4 The layout for a pixel with multiple PC sensors. One pixel contains two gratings, one reference photodiode and one hexagonal nanobump array. Each block is $400\ \mu\text{m}$ x $400\ \mu\text{m}$ and the spacing between them is $10\ \mu\text{m}$.

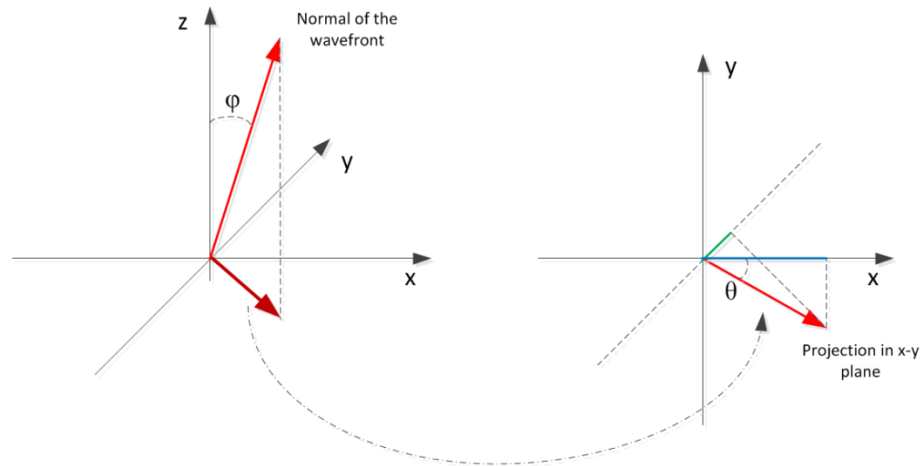


Figure 7-5 The wavevector model for measuring the polar and azimuthal angle of the incident wavefront with the four photodiode in one pixel structure.

The patterns on top of the four photodiodes consist of one hexagonal nanobump array, two grating structures oriented in different direction, and a bare silicon surface. The photodiode with no metal pattern on top is used as a reference signal. Its photocurrent output is related to $A_{max} \cos(\theta)$ where A_{max} is the photocurrent response at normal incident, and θ is the incident angle. When θ is small (< 5 degrees), the photocurrent keeps almost unchanged (within 99% of the maximum), thus it can be used as a constant reference signal. The hexagonal array measures the polar angle of the incident light, and its detail was discussed in the previous chapter. The two grating structures measure the azimuthal angle of the incident light in x-y plane. The vector model for this measurement is illustrated in Figure 7-5. The strength of the parallel surface component can be calculated from the polar angle. The projection of the wavevector on x axes can be measured by the grating in the lower right corner of the pixel. The angle between the parallel surface wavevector and the x axis is calculated using this information. However, there are four vectors satisfy this angle condition. The 45 degree tilted grating at the upper left corner of the pixel can measure the projection of the parallel surface wavevector along its grating normal direction. This result can be used to

choose two vectors from the four possible solutions. Usually, the wavefront are smooth and curving in one direction. This assumption will be added to pick the direction of the parallel surface wavevector for wavefront reconstruction.

7.2 System Model for the Sensor

The photocurrent generated from each pixel of the wavefront sensor need to be converted to digital signals and then calculating the incident angle in spherical coordinates. The system block diagram is shown in Figure 7-6. The 8x8 pixels array was discussed in the previous section. A MUX is used to select 1 of the 64 photodiodes and connecting it to an op-amp. Only one op-amp is used in this design to save area and also can reduce process variation. Since this design is not targeted for high speed operation, it can use multiple cycles to collect the outputs of the pixels one at a time. The ADC compares the op-amp output with a reference voltage to digitalize the signal and save it into the registers of the DSP. The DSP uses a look-up table to convert the measurement result into angle information, and reconstructs the wavefront surface using least squares fitting algorithm.

The photodiode can be modeled as a current source in connection with some parasitical resistance.[151] In short circuit mode, the output current is linear with the intensity of the incoming light. This requires that the output load resistance is small ($< 1 \text{ k}\Omega$). The schematic of the op-amp and the ADC is shown in Figure 7-7. A 64 to 1 MUX is used to choose the current output from one pixel. The “SELECT” signal of the MUX is coming from the DSP unit. An op-amp is configured in negative feedback loop to convert the current signal to a voltage signal. The feedback resistance depends on the VDD voltage and the maximum photocurrent. For 180 nm technology, power supply is 1.8V. Assuming that the maximum photocurrent is $20 \mu\text{A}$, the resistance R should be $90 \text{ k}\Omega$. Usually the on-chip op-amp can reach 40 dB gain, which is $A=100$. The input resistance of the op-amp circuit is $90000/100=0.9 \text{ k}\Omega$, which satisfies the requirement above. The MUX circuit uses the transmission gate structure with large transistor width to achieve a low resistance from any input to the output.

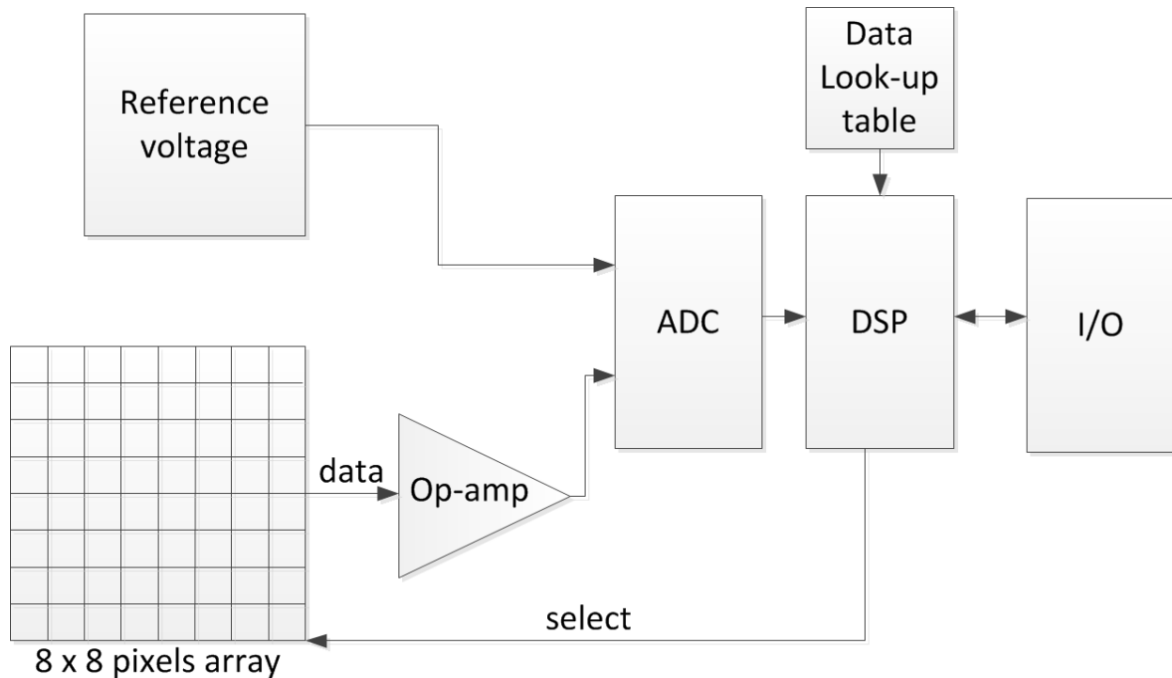


Figure 7-6 Block diagram of the data collection and processing system.

The analog-to-digital converter circuit uses the classical Flash ADC structure. It has a linear voltage ladder with a comparator at each step of the ladder to compare the input voltage with a reference voltage. When the input voltage is smaller than a reference in the voltage ladder, the comparator output zero. Otherwise, the output is one. It generates an array of 16 bits data total. A 16 to 4 encoder is used to convert this data array into a 4 bits binary number. Its function is to find the first “1” in the array, and output the index of this bit. This binary value passes through a de-MUX and saves into the corresponding register.

The analog part of the system uses a MUX and a de-MUX to share the op-amp and the ADC among all the pixels. This can avoid the issue of process variation in the resistance values among different ADCs. The design area is also small comparing to use one ADC per pixel. The design trade-off is that the speed is sacrificed, because it will take 64 cycles to collect all the data from the pixels. The clock frequency can achieve 50-100 MHz for 180 nm ASIC or FPGA design, thus it is will take 1-2 us to capture all the data and save them into

registers. Usually, the wavefront is smooth and do not change quickly in time, so that the sensor data throughput is suitable for most applications.

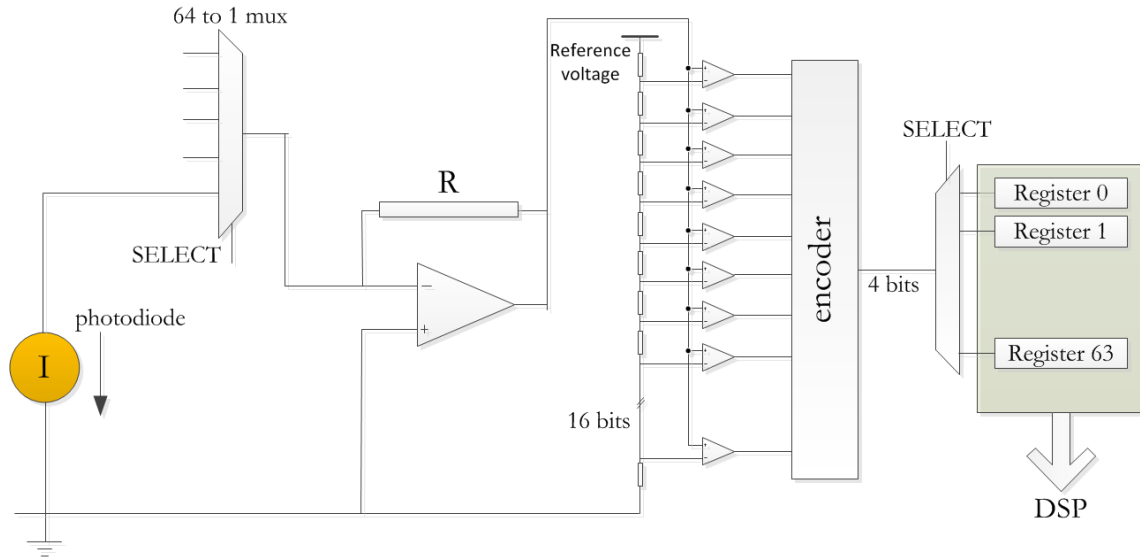


Figure 7-7 Schematic of the analog part of the system, which contains an op-amp and an ADC.

7.3 Imaging Processing Algorithm

The DSP unit processes the light intensity data collected by the pixel array and generates the phase profile of the wavefront. The time-independent electric field of a coherent light beam propagated along the z-axis can be described as $\vec{E}(x, y; z) = \left| \overline{E}(x, y; z) \right| \exp[i\phi(x, y; z)]$, where ϕ is reference to the wavefront phase on the z-axis.[152] The pixel array measures the gradient of the wavefront phase in rectangular coordinates, which is $\frac{\partial \phi}{\partial x}$ and $\frac{\partial \phi}{\partial y}$. An algorithm is need to reconstruction the incident wavefront from the measured information. Its design target can be stated as: Given the magnitude and the direction of the partial derivative

ϕ_x and ϕ_y of the phase function, which is defined on a discretely array indexed by $x,y=1..n$, the algorithm need to generate a function of $\phi(x, y)$ with minimum time complexity.

The phase function $\phi(x, y)$ can be expressed in series expansion, and keep its first N terms that satisfies the accuracy requirement. Expending the phase function with polynomials in rectangular coordinates, we can get:

$$\phi(x, y) = \sum_{i=0}^4 \sum_{j=0}^i c_{ij} x^j y^{i-j}$$

where c_{ij} is the unknown coefficient of each term that needs to be solved. The highest order in this expression is 4, which is enough for describing a relatively smooth 2D surface. There are totally 15 terms in this series expansion. The gradient of the wavefront surface can be expressed as:

$$\begin{aligned} \phi_x(x, y) &= \sum_{i=0}^4 \sum_{j=0}^i c_{ij} j x^{j-1} y^{i-j} \\ &= \sum_{i=0}^4 \sum_{j=0}^i c_{ij} Z_x^{ij}(x, y) \\ \phi_y(x, y) &= \sum_{i=0}^4 \sum_{j=0}^i c_{ij} (i-j) j x^j y^{i-j-1} \\ &= \sum_{i=0}^4 \sum_{j=0}^i c_{ij} Z_y^{ij}(x, y) \end{aligned}$$

where $Z_x^{ij}(x, y) = j x^{j-1} y^{i-j}$ and $Z_y^{ij}(x, y) = (i-j) x^j y^{i-j-1}$ are only related to the position index (x,y) and do not change with the sensor measurement. Re-write the above two equations in matrix form, we can get:

$$\begin{pmatrix} \phi_x(x=0, y=0) \\ \phi_x(x=0, y=1) \\ \vdots \\ \phi_y(x=0, y=0) \\ \phi_y(x=0, y=1) \\ \vdots \end{pmatrix} = \begin{pmatrix} Z_x^{00}(x=0, y=0) & Z_x^{01}(x=0, y=0) & \dots \\ Z_x^{00}(x=0, y=1) & Z_x^{01}(x=0, y=1) & \dots \\ \vdots & \vdots & \vdots \\ Z_y^{00}(x=0, y=0) & Z_y^{01}(x=0, y=0) & \dots \\ Z_y^{00}(x=0, y=1) & Z_y^{01}(x=0, y=1) & \dots \\ \vdots & \vdots & \vdots \end{pmatrix} \begin{pmatrix} c_{00} \\ c_{01} \\ \vdots \end{pmatrix}$$

In a short form, we use

$$\Phi = ZC$$

to represent the matrix multiplication above. Φ contains the partial derivatives from measurement and has $2 \times 64 = 128$ terms. Z is a pre-calculated matrix that is defined at the sensor design stage, and its size is 128×15 . The target is to solve C for each sensor measurement outcome. Using the least-squares method to estimate the unknown vector of coefficients C , the equations are given by

$$\begin{aligned} (Z^T Z)C &= Z^T \Phi \\ C &= (Z^T Z)^{-1} Z^T \Phi \\ C &= A\Phi \end{aligned}$$

with $A = (Z^T Z)^{-1} Z^T$ is also a pre-calculated matrix at the design stage. The time complexity of this algorithm is $O(\log N)$, where N is the number of pixels in the sensors. The length of Φ is $2N$, thus it requires $2N$ “multiply-add” operations to calculate one of the c_{ij} . All the multiplication operations can be done simultaneously, and the addition operation needs $O(\log N)$ steps for a binary tree type adding structure. This algorithm will use a large number of adders and multipliers, thus resource sharing can reduce area consumption but at the expense of longer computation time.

The fitting algorithm was validated using numerical simulation. The input wavefront is a curving surface that can be described as:

$$\phi = 1 - 0.2x - 0.5y + 5 \sin\left(\frac{x}{5} + \frac{y}{7} - \frac{\pi}{2}\right)$$

with $x, y = 1 \dots 8$

The slope of this surface in x and y direction can be calculated from the equation above. The data for $\Phi = \begin{pmatrix} \Phi_x \\ \Phi_y \end{pmatrix}$ can be found in the sensor data look-up table. With the pre-defined matrix A , the coefficients c_{ij} are calculated and the curve for the fitting function

$\phi(x, y) = \sum_{i=0}^4 \sum_{j=0}^i c_{ij} x^j y^{i-j}$ is shown in Figure 7-8. The difference in absolute value is shown in

the right side of the figure also. The maximum relative difference is 23%, and the RMS difference is 7% among all the 64 pixels.

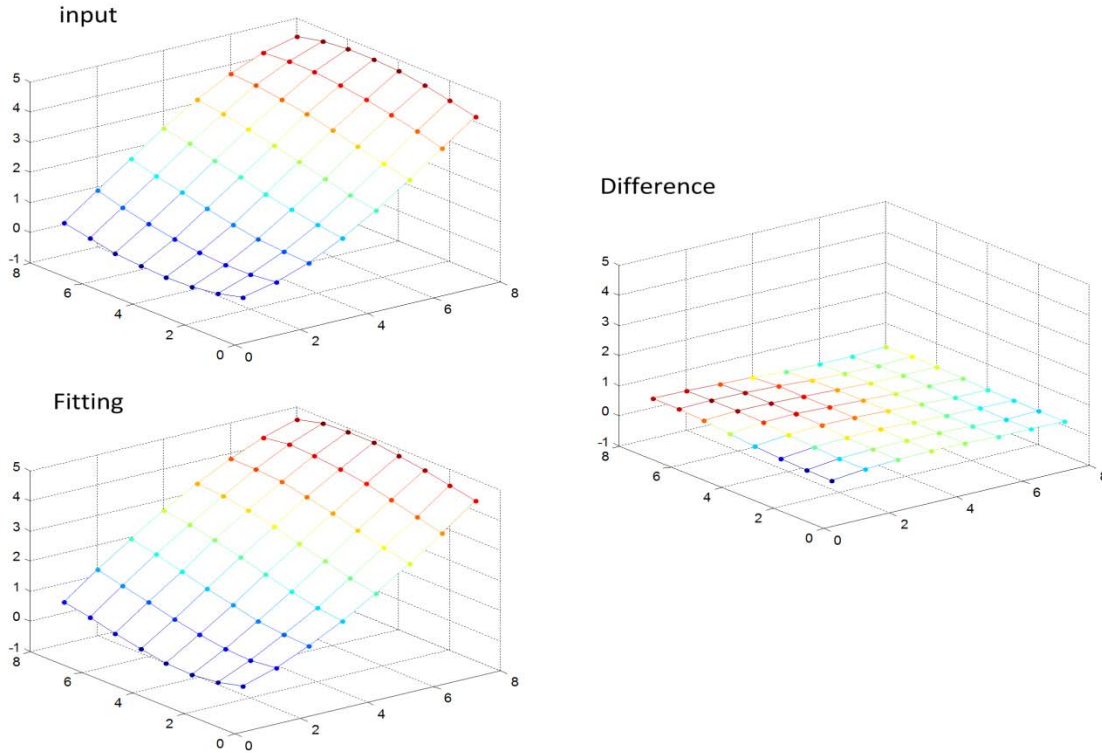


Figure 7-8 The surface fitting result of a curving input wavefront using Matlab simulation.

Table 7-1 Comparison of several wavefront sensors.

	Hartmann	Shack-Hartmann	Plasmonic Crystal
Dimension	3D	3D	2D
Pixel size	Pin-hole spacing	Micro-lens diameter	Photodiode pixel size
Cost	Low	High	Medium
Light source	Laser, sun light	Star, laser, sun light	Laser, sun light
Field of view	Small	Small	Large
Sensitivity	Low	High	Low

In summary, the system configuration of a plasmonic crystal wavefront sensor is discussed in this chapter. The physical layout of the plasmonic crystal/photodiode stacking is presented. It is compatible with modern CMOS fabrication technology, and the plasmonic crystal layout is on the very top of the device, so that it can be fabricated in the last step with customized processing methods. The data collection section of the sensor is constructed by an op-amp and an ADC to generate a 4 bits data that represents the photodiode current value. A least-squares fitting algorithm is used to reconstruct the wavefront surface, and an surface fitting example is performed to demonstrate the validity of this method. The implementation of this system can be done in one piece of silicon. Another option is to use the 3D IC technology, where the photodiode array is on one die and the data processing unit is on another die. TSVs are used to connect different modules between dies. The large capacitance on TSVs will not be a big issue for this design, since it is not targeting for high speed operation.

Comparison of this PC wavefront sensor design with the Hartmann and the Shack-Hartmann wavefront sensor is shown in Table 7.1. The 2D nature of the PC wavefront sensor reduces its size in Z direction. Its pixel size in X-Y dimension is similar to the other two sensors, which is around 150-300 μm . [153] The cost to fabricate a Hartmann sensor is the lowest among the three devices, because it only uses arrays of pin-hole. The Shack-Hartmann sensor uses micro-lens arrays that are complex and expensive. The major cost of the PC wavefront sensor is to make the nanobump array plasmonic crystal, since the photodiode array fabrication is pretty standard and cost less than the CCD array. The Shack-Hartmann sensor can work with low intensity input light, for example the star light. Due to the strong attenuation of the gold layer, PC wavefront sensor requires strong input intensity to generate enough photocurrent. If small pixel size is required for special design, CCD array can be used and the gold thickness can be reduced to increase the transmission ratio. The field of view for Shack-Hartmann sensor is limited by the ratio of the pixel size to the focus length. If the incident angle is too large, the focus light spot will shift out of the design area of that pixel on the CCD array, thus the system cannot differentiate its spot with the pixel next to it. PC wavefront sensor does not have this issue since it is a 2D device, and the plasmonic

crystal can have 60 degrees field of view for s-polarized light, which was demonstrated in chapter 6.

In conclusion, this chapter proposes the construction of a new type of wavefront sensor using the angle of arrival information that is inherent in the physics of the surface plasmon interaction with periodic nano-structures. Although funding and availability of silicon foundry limits this design from being experimentally realized, it points the way for an interesting wavefront sensor that potentially could be built in the future.

CHAPTER 8

CONCLUSIONS AND SUGGESTIONS FOR FUTURE WORK

8.1 Conclusions

In this work, we have studied the use of plasmonics and made the following contributions:

- Developed a low cost nanosphere self-assembly technique that allows hexagonal symmetry nano-bump array plasmonic crystals to be made and studied. The area of the self-assembly pattern is much larger than those made by FIB or E-beam lithography methods. The optical properties of the plasmonic crystal are characterized using transmission spectra with different incident angle.
- Applied this self-assembly plasmonic crystal to sensing and modulation devices. The patterned gold film shows a sensitivity of ~ 100 nm/RIU for dielectric environment changes, which can be used for chemical sensing applications. An all optical modulator device is demonstrated, where the normally transmitted light intensity is modulated by another light that can excites free charge carriers in the organic dielectric material on the surface of the gold nano-structure pattern.
- Pointed out that the plasmonic crystals may extend the tunability of electro-chromic and thermo-chromic thin films. The reflection spectra changing for a VO₂ film stacking on a nanobump array shows different trend comparing with a VO₂ film stacking on a flat gold film.
- Most importantly, developed a novel angle of arrival sensor that can be used to track the sun or other collimated light sources such as laser beam. This design utilizes the far field transmission property of the plasmonic crystal, which is based on the momentum matching mechanism, to derive the incident angle of a collimated light beam. The device response depends on the polarization state of the incident light.

8.2 Suggestions for Future Work

Several aspects of this research work can be pushed further in the future. The potential topics are categorized into two sections:

Fabrication:

1. Make smaller period self-assembly arrays

Current process uses 600 nm diameter spheres with 40-45 seconds RIE time, thus the gold nanobump diameter is around 450 nm for a 90 nm thick gold film. The lowest order plasmon peaks are located around 750-900 nm, which is in the infrared region. Reducing the sphere diameter to 400-450 nm will shift the plasmon peaks to 550-650 nm, so that applications in visible light region can be developed. The major challenge is that multiple layer structures are easy to form when small spheres are used, which will reduce the yield of the self-assembly process. Exploring the RIE time and metal thickness parameters for strong plasmon coupling also requires a lot of effort.

2. Improve the nano-imprint method

Nano-imprint is a promising technique to make large area array with relatively simple steps. Currently the process we applied can prepare $\sim 1 \text{ mm}^2$ nanohole arrays on PMMA. However, the silicon stamp cannot touch the whole surface during imprinting, thus the good area of the pattern is limited. The problem may cause by the thin glass coverslip substrate. It becomes soft when the substrate is heated up to 140 °C. Silicon and thick glass substrates were tried in experiment, but the silicon stamps have lift-off issue after imprint. A good anti-adhesion layer is requires to coat on the stamp for a successful imprint process.

3. Photolithography with 193 nm light source

The AMSL 193 nm Step and Scan system at NCSU NNF facility can be used for fabricating $\sim 100 \text{ nm}$ features on six inch wafers. The cost for preparing a reticle for this system is relatively expensive. This lithography system experience technical difficulty recently, thus I did not explore using it during my study. Photolithography prepared nano-structures can be made after this system comes back online or another

reliable lithography system is available. This will be a convenient way to fabricate a fixed design in large volume. Some interesting patterns that cannot be prepared with nanosphere self-assembly should be tried with this lithography tool, as shown in Figure 8-1. This type of pattern allows the Block modes to be tailored for other applications.

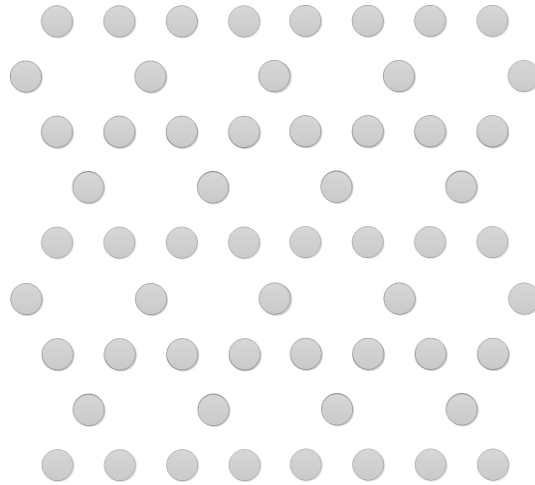


Figure 8-1 Hexagonal array pattern with regular defects for lithography mask design.

Device improvement:

4. Optical modulator with VO₂/Plasmonic crystal structure

The optical modulation effect was demonstrated by controlling the P3HT polymer dielectric above the plasmonic crystal, but its speed is limited because the modulation ratio is small and can only be captured by a CCD spectrometer. VO₂/nanobump array gold film shows large spectrum changes in reflection mode during the phase transition, which can be utilized to develop a novel optical modulator. The major issue in fabricating this device is that the high temperature for growing the VO₂ film may melt and destroy the gold nano-structure. Minimize the device size is important for high speed operation at kHz to MHz frequency, because the VO₂ film is operated

under the principle of temperature induced phase change, thus small device will decrease the amount of energy needed for the heating and cooling process.

5. *1D Grating structure for azimuthal angle sensing*

The 2D-hexagonal array is six-fold symmetrical and can response to the incident photon with any azimuthal angle. This makes it hard to determine the direction of the light source. 1D-grating structures will only response to the photon that has the momentum component parallel to its grating normal direction, so that the azimuthal angle of the incident light can be measured. The periodicity of the grating should be around 450 - 650 nm, and the slit width should be ~ 300 nm for maximum plasmon coupling efficiency (50% area occupation). The pattern can be fabricated by E-beam lithography or FIB milling, and the major challenge is how to make a large area crystal will few defects. The cost of using these tools will also be a consideration.

6. *Improve the sensitivity of the sun sensor*

Several parameters affect the sensitivity of the sun sensor, which include the wavelength, FWHM of the plasmon peak and the response curve of the photodiode. In the dispersion relation, the slope of the $\omega(k)$ curve is larger at small wavevector k . It indicates that operating in longer wavelength will has larger plasmon peak shifting. Currently the plasmon wavelength is at 770 nm, and the FWHM is 120 nm with a 600 nm periodic array. If 650-700 nm array is used, it plasmon peak will move to longer wavelength, and the photodiode response rate is higher. The challenge for this work is to find out a method to reduce the defect rate in the self-assembled pattern in order to achieve a narrow FWHM. The sun light intensity is low at 800 nm and beyond, thus thinner gold film thickness (~ 50 nm) is required to get enough photon transmitted through the plasmonic crystal.

7. *Physical implementation of the wavefront sensor*

The system level design of the wavefront sensor is presented in this research. The physical implementation of this sensor requires cooperation with a CMOS foundry or a nano-fabrication facility. The data processing part of the system can use 0.18 μm or 0.25 μm CMOS technology. The pixel array requires ~ 0.15 μm minimum feature size,

and it needs gold film deposition which is not common in CMOS process. The whole chip will use two metal layers. The challenge for this task is to find the suitable process and also requires knowledge in DSP design and post-silicon test procedures.

REFERENCES

- 1 W. L. Barnes, A. Dereux, and T. W. Ebbesen, "Surface plasmon subwavelength optics," *Nature* **424** (6950), 824-830 (2003).
- 2 G. A. Wurtz and A. V. Zayats, "Nonlinear surface plasmon polaritonic crystals," *Laser & Photonics Reviews* **2** (3), 125-135 (2008).
- 3 H. W. Gao, W. Zhou, and T. W. Odom, "Plasmonic crystals: A platform to catalog resonances from ultraviolet to near-infrared wavelengths in a plasmonic library," *Advanced Functional Materials* **20** (4), 529-539 (2010).
- 4 J. A. Schuller, E. S. Barnard, W. S. Cai, Y. C. Jun, J. S. White, and M. L. Brongersma, "Plasmonics for extreme light concentration and manipulation," *Nature Materials* **9** (3), 193-204 (2010).
- 5 T. W. Ebbesen, H. J. Lezec, H. F. Ghaemi, T. Thio, and P. A. Wolff, "Extraordinary optical transmission through sub-wavelength hole arrays," *Nature* **391** (6668), 667-669 (1998).
- 6 A. V. Zayats, Smolyaninov, II, and A. A. Maradudin, "Nano-optics of surface plasmon polaritons," *Physics Reports-Review Section of Physics Letters* **408** (3-4), 131-314 (2005).
- 7 Thomson Reuters, "Web of Science," www.isiknowledge.com (2011).
- 8 A. L. Baudrion, J. C. Weeber, A. Dereux, G. Lecamp, P. Lalanne, and S. I. Bozhevolnyi, "Influence of the filling factor on the spectral properties of plasmonic crystals," *Physical Review B* **74** (2006).
- 9 S. A. Maier and H. A. Atwater, "Plasmonics: Localization and guiding of electromagnetic energy in metal/dielectric structures," *Journal of Applied Physics* **98** (1) (2005).
- 10 W. C. Tan, T. W. Preist, J. R. Sambles, and N. P. Wanstall, "Flat surface-plasmon-polariton bands and resonant optical absorption on short-pitch metal gratings," *Physical Review B* **59** (19), 12661-12666 (1999).
- 11 R. F. Oulton, V. J. Sorger, T. Zentgraf, R. M. Ma, C. Gladden, L. Dai, G. Bartal, and X. Zhang, "Plasmon lasers at deep subwavelength scale," *Nature* **461** (7264), 629-632 (2009).

- 12 J. A. Dionne, K. Diest, L. A. Sweatlock, and H. A. Atwater, "PlasMOSstor: A metal-oxide-si field effect plasmonic modulator," *Nano Letters* **9** (2), 897-902 (2009).
- 13 D. Pacifici, H. J. Lezec, and H. A. Atwater, "All-optical modulation by plasmonic excitation of CdSe quantum dots," *Nature Photonics* **1** (7), 402-406 (2007).
- 14 H. A. Atwater and A. Polman, "Plasmonics for improved photovoltaic devices," *Nature Materials* **9** (3), 205-213 (2010).
- 15 J. J. Baumberg, T. A. Kelf, Y. Sugawara, S. Cintra, M. E. Abdelsalam, P. N. Bartlett, and A. E. Russell, "Angle-resolved surface-enhanced Raman scattering on metallic nanostructured plasmonic crystals," *Nano Letters* **5** (11), 2262-2267 (2005).
- 16 Z. Q. Tian, B. Ren, and D. Y. Wu, "Surface-enhanced Raman scattering: From noble to transition metals and from rough surfaces to ordered nanostructures," *Journal of Physical Chemistry B* **106** (37), 9463-9483 (2002).
- 17 E. Fort and S. Gresillon, "Surface enhanced fluorescence," *Journal of Physics D-Applied Physics* **41** (1) (2008).
- 18 J. N. Anker, W. P. Hall, O. Lyandres, N. C. Shah, J. Zhao, and R. P. Van Duyne, "Biosensing with plasmonic nanosensors," *Nature Materials* **7** (6), 442-453 (2008).
- 19 J.D. Jackson, *Classical electrodynamics*. (Wiley, 1999).
- 20 K. S. Chang, C. Chou, and C. H. Lin, "Focused-beam attenuated total-reflection technique on absorptive film in Kretschmann configuration," *Applied Optics* **32** (16), 2957-2962 (1993).
- 21 P. G. Etchegoin, E. C. Le Ru, and M. Meyer, "An analytic model for the optical properties of gold," *Journal of Chemical Physics* **125** (16) (2006).
- 22 A. Vial, A. S. Grimault, D. Macias, D. Barchiesi, and M. L. de la Chapelle, "Improved analytical fit of gold dispersion: Application to the modeling of extinction spectra with a finite-difference time-domain method," *Physical Review B* **71** (8) (2005).
- 23 S. A. Maier, P. G. Kik, and H. A. Atwater, "Optical pulse propagation in metal nanoparticle chain waveguides," *Physical Review B* **67** (20) (2003).
- 24 A. D. Rakic, A. B. Djuricic, J. M. Elazar, and M. L. Majewski, "Optical properties of metallic films for vertical-cavity optoelectronic devices," *Applied Optics* **37** (22), 5271-5283 (1998).
- 25 A. Vial and T. Laroche, "Comparison of gold and silver dispersion laws suitable for FDTD simulations," *Applied Physics B-Lasers and Optics* **93** (1), 139-143 (2008).

- 26 P. B. Johnson and R. W. Christy, "Optical-constants of noble-metals," *Physical Review B* **6** (12), 4370-4379 (1972).
- 27 K. F. Giebel, C. Bechinger, S. Herminghaus, M. Riedel, P. Leiderer, U. Weiland, and M. Bastmeyer, "Imaging of cell/substrate contacts of living cells with surface plasmon resonance microscopy," *Biophysical Journal* **76** (1), 509-516 (1999).
- 28 B. Lamprecht, J. R. Krenn, G. Schider, H. Ditlbacher, M. Salerno, N. Felidj, A. Leitner, F. R. Aussenegg, and J. C. Weeber, "Surface plasmon propagation in microscale metal stripes," *Applied Physics Letters* **79** (1), 51-53 (2001).
- 29 J. A. Dionne, L. A. Sweatlock, H. A. Atwater, and A. Polman, "Planar metal plasmon waveguides: Frequency-dependent dispersion, propagation, localization, and loss beyond the free electron model," *Physical Review B* **72** (7) (2005).
- 30 J. T. van Wijngaarden, E. Verhagen, A. Polman, C. E. Ross, H. J. Lezec, and H. A. Atwater, "Direct imaging of propagation and damping of near-resonance surface plasmon polaritons using cathodoluminescence spectroscopy," *Applied Physics Letters* **88** (22) (2006).
- 31 A. K. Azad and W. L. Zhang, "Resonant terahertz transmission in subwavelength metallic hole arrays of sub-skin-depth thickness," *Optics Letters* **30** (21), 2945-2947 (2005).
- 32 B. Steinberger, A. Hohenau, H. Ditlbacher, A. L. Stepanov, A. Drezet, F. R. Aussenegg, A. Leitner, and J. R. Krenn, "Dielectric stripes on gold as surface plasmon waveguides," *Applied Physics Letters* **88** (9) (2006).
- 33 M. Sandtke and L. Kuipers, "Spatial distribution and near-field coupling of surface plasmon polariton Bloch modes," *Physical Review B* **77** (23) (2008).
- 34 J. Y. Chu, T. J. Wang, J. T. Yeh, M. W. Lin, Y. C. Chang, and J. K. Wang, "Near-field observation of plasmon excitation and propagation on ordered elliptical hole arrays," *Applied Physics A-Materials Science & Processing* **89**, 387-390 (2007).
- 35 E. S. Kwak, J. Henzie, S. H. Chang, S. K. Gray, G. C. Schatz, and T. W. Odom, "Surface plasmon standing waves in large-area subwavelength hole arrays," *Nano Letters* **5** (10), 1963-1967 (2005).
- 36 H. F. Ghaemi, T. Thio, D. E. Grupp, T. W. Ebbesen, and H. J. Lezec, "Surface plasmons enhance optical transmission through subwavelength holes," *Physical Review B* **58** (11), 6779-6782 (1998).

- 37 A. Degiron and T. W. Ebbesen, "The role of localized surface plasmon modes in the enhanced transmission of periodic subwavelength apertures," *Journal of Optics A-Pure and Applied Optics* **7** (2), S90-S96 (2005).
- 38 Smolyaninov, I and Y. J. Hung, "Enhanced transmission of light through a gold film due to excitation of standing surface-plasmon Bloch waves," *Physical Review B* **75** (3) (2007).
- 39 Y. J. Hung, Smolyaninov, I, C. C. Davis, and H. C. Wu, "Fluorescence enhancement by surface gratings," *Optics Express* **14** (22), 10825-10830 (2006).
- 40 T. Rindzevicius, Y. Alaverdyan, B. Sepulveda, T. Pakizeh, M. Kall, R. Hillenbrand, J. Aizpurua, and F. J. G. de Abajo, "Nanohole plasmons in optically thin gold films," *Journal of Physical Chemistry C* **111**, 1207-1212 (2007).
- 41 J. Prikulis, P. Hanarp, L. Olofsson, D. Sutherland, and M. Kall, "Optical spectroscopy of nanometric holes in thin gold films," *Nano Letters* **4** (6), 1003-1007 (2004).
- 42 K. H. Su, Q. H. Wei, X. Zhang, J. J. Mock, D. R. Smith, and S. Schultz, "Interparticle coupling effects on plasmon resonances of nanogold particles," *Nano Letters* **3** (8), 1087-1090 (2003).
- 43 A. V. Shchegrov, I. V. Novikov, and A. A. Maradudin, "Scattering of surface plasmon polaritons by a circularly symmetric surface defect," *Physical Review Letters* **78** (22), 4269-4272 (1997).
- 44 V. M. Agranovich, V. E. Kravtsov, and T. A. Leskova, "New type of local resonances in thin rough films," *Solid State Communications* **47** (11), 925-930 (1983).
- 45 L. Yin, V. K. Vlasko-Vlasov, A. Rydh, J. Pearson, U. Welp, S. H. Chang, S. K. Gray, G. C. Schatz, D. B. Brown, and C. W. Kimball, "Surface plasmons at single nanoholes in Au films," *Applied Physics Letters* **85** (3), 467-469 (2004).
- 46 Christy L. Haynes Amanda J. Haes, Richard P. Van Duyne, presented at the Materials Research Society Meetings, 2001 (unpublished).
- 47 A. Hessel and A. A. Oliner, "A new theory of wood's anomalies on optical gratings," *Applied Optics* **4** (10), 24 (1965).
- 48 H. Raether, *Surface plasmons on smooth and rough surfaces and on gratings*. (Springer-Verlag, Berlin ; New York, 1988).

- 49 M. F. Pascual, W. Zierau, T. A. Leskova, and A. A. Maradudin, "Surface electromagnetic waves in near-field optical scanning microscopy," *Optics Communications* **155** (4-6), 351-360 (1998).
- 50 E. M. Yeatman, "Resolution and sensitivity in surface plasmon microscopy and sensing," *Biosensors & Bioelectronics* **11** (6-7), 635-649 (1996).
- 51 M. Perner, P. Bost, U. Lemmer, G. vonPlessen, J. Feldmann, U. Becker, M. Mennig, M. Schmitt, and H. Schmidt, "Optically induced damping of the surface plasmon resonance in gold colloids," *Physical Review Letters* **78** (11), 2192-2195 (1997).
- 52 A. Liebsch, "Surface-plasmon dispersion and size dependence of Mie resonance - silver versus simple metals," *Physical Review B* **48** (15), 11317-11328 (1993).
- 53 P. Mulvaney, "Surface plasmon spectroscopy of nanosized metal particles," *Langmuir* **12** (3), 788-800 (1996).
- 54 A. Otto, I. Mrozek, H. Grabhorn, and W. Akemann, "Surface-enhanced Raman-scattering," *Journal of Physics-Condensed Matter* **4** (5), 1143-1212 (1992).
- 55 H. A. Bethe, "Theory of diffraction by small holes," *Physical Review* **66** (7/8), 163-182 (1944).
- 56 J. D. Joannopoulos, Robert D. Meade, and Joshua N. Winn, *Photonic crystals : Molding the flow of light*. (Princeton University Press, Princeton, N.J., 1995).
- 57 A. Christ, S. G. Tikhodeev, N. A. Gippius, J. Kuhl, and H. Giessen, "Waveguide-plasmon polaritons: Strong coupling of photonic and electronic resonances in a metallic photonic crystal slab," *Physical Review Letters* **91** (18) (2003).
- 58 A. Dhawan, M. Canva, and T. Vo-Dinh, "Narrow groove plasmonic nano-gratings for surface plasmon resonance sensing," *Optics Express* **19** (2), 787-813 (2011).
- 59 T. Sondergaard, S. I. Bozhevolnyi, and A. Boltasseva, "Theoretical analysis of ridge gratings for long-range surface plasmon polaritons," *Physical Review B* **73** (4) (2006).
- 60 T. Thio, H. J. Lezec, T. W. Ebbesen, K. M. Pellerin, G. D. Lewen, A. Nahata, and R. A. Linke, "Giant optical transmission of sub-wavelength apertures: Physics and applications," *Nanotechnology* **13** (3), 429-432 (2002).
- 61 J. Henzie, K. L. Shuford, E. S. Kwak, G. C. Schatz, and T. W. Odom, "Manipulating the optical properties of pyramidal nanoparticle arrays," *Journal of Physical Chemistry B* **110** (29), 14028-14031 (2006).

- 62 J. Henzie, J. Lee, M. H. Lee, W. Hasan, and T. W. Odom, "Nanofabrication of plasmonic structures," *Annual Review of Physical Chemistry* **60**, 147-165 (2009);
- 63 J. Lee, W. Hasan, C. L. Stender, and T. W. Odom, "Pyramids: A platform for designing multifunctional plasmonic particles," *Accounts of Chemical Research* **41** (12), 1762-1771 (2008).
- 64 H. W. Gao, J. Henzie, M. H. Lee, and T. W. Odom, "Screening plasmonic materials using pyramidal gratings," *Proceedings of the National Academy of Sciences of the United States of America* **105** (51), 20146-20151 (2008).
- 65 N. G. Skinner and D. M. Byrne, "Finite-difference time-domain analysis of frequency-selective surfaces in the mid-infrared," *Applied Optics* **45** (9), 1943-1950 (2006).
- 66 S. H. Chang, S. K. Gray, and G. C. Schatz, "Surface plasmon generation and light transmission by isolated nanoholes and arrays of nanoholes in thin metal films," *Optics Express* **13** (8), 3150-3165 (2005).
- 67 D. Gerard, L. Salomon, F. de Fornel, and A. V. Zayats, "Ridge-enhanced optical transmission through a continuous metal film," *Physical Review B* **69** (11) (2004).
- 68 T. T. Truong, J. Maria, J. Yao, M. E. Stewart, T. W. Lee, S. K. Gray, R. G. Nuzzo, and J. A. Rogers, "Nanopost plasmonic crystals," *Nanotechnology* **20** (43) (2009).
- 69 Y. Liu, J. Bishop, L. Williams, S. Blair, and J. Herron, "Biosensing based upon molecular confinement in metallic nanocavity arrays," *Nanotechnology* **15** (9), 1368-1374 (2004).
- 70 M. J. Levene, J. Korlach, S. W. Turner, M. Foquet, H. G. Craighead, and W. W. Webb, "Zero-mode waveguides for single-molecule analysis at high concentrations," *Science* **299** (5607), 682-686 (2003).
- 71 J. W. Menezes, J. Ferreira, M. J. L. Santos, L. Cescato, and A. G. Brolo, "Large-area fabrication of periodic arrays of nanoholes in metal films and their application in biosensing and plasmonic-enhanced photovoltaics," *Advanced Functional Materials* **20** (22), 3918-3924 (2010).
- 72 F. Tam, G. P. Goodrich, B. R. Johnson, and N. J. Halas, "Plasmonic enhancement of molecular fluorescence," *Nano Letters* **7** (2), 496-501 (2007).
- 73 C. Farcau and S. Astilean, "Silver half-shell arrays with controlled plasmonic response for fluorescence enhancement optimization," *Applied Physics Letters* **95** (19) (2009).

- 74 H. Fischer and O. J. F. Martin, "Engineering the optical response of plasmonic nanoantennas," *Optics Express* **16** (12), 9144-9154 (2008).
- 75 O. Stranik, H. M. McEvoy, C. McDonagh, and B. D. MacCraith, "Plasmonic enhancement of fluorescence for sensor applications," *Sensors and Actuators B-Chemical* **107** (1), 148-153 (2005).
- 76 M. A. Cooper, "Label-free screening of bio-molecular interactions," *Analytical and Bioanalytical Chemistry* **377** (5), 834-842 (2003).
- 77 G. L. Liu, Y. D. Yin, S. Kunchakarra, B. Mukherjee, D. Gerion, S. D. Jett, D. G. Bear, J. W. Gray, A. P. Alivisatos, L. P. Lee, and F. Q. F. Chen, "A nanoplasmonic molecular ruler for measuring nuclease activity and DNA footprinting," *Nature Nanotechnology* **1** (1), 47-52 (2006).
- 78 G. J. Nusz, S. M. Marinakos, A. C. Curry, A. Dahlin, F. Hook, A. Wax, and A. Chilkoti, "Label-free plasmonic detection of biomolecular binding by a single gold nanorod," *Analytical Chemistry* **80** (4), 984-989 (2008).
- 79 Y. H. Choi, T. Kang, and L. P. Lee, "Plasmon resonance energy transfer (PRET)-based molecular imaging of cytochrome c in living cells," *Nano Letters* **9** (1), 85-90 (2009).
- 80 V. Silin and A. Plant, "Biotechnological applications of surface plasmon resonance," *Trends in Biotechnology* **15** (9), 353-359 (1997).
- 81 A. G. Brolo, S. C. Kwok, M. G. Moffitt, R. Gordon, J. Riordon, and K. L. Kavanagh, "Enhanced fluorescence from arrays of nanoholes in a gold film," *Journal of the American Chemical Society* **127** (42), 14936-14941 (2005).
- 82 E. Laux, C. Genet, T. Skauli, and T. W. Ebbesen, "Plasmonic photon sorters for spectral and polarimetric imaging," *Nature Photonics* **2** (3), 161-164 (2008).
- 83 James D. Plummer, Michael D. Deal, and Peter B. Griffin, *Silicon VLSI technology :Fundamentals, practice and modeling*. (Prentice Hall, Upper Saddle River, NJ, 2000).
- 84 Y. N. Xia, J. A. Rogers, K. E. Paul, and G. M. Whitesides, "Unconventional methods for fabricating and patterning nanostructures," *Chemical Reviews* **99** (7), 1823-1848 (1999).
- 85 C. Vieu, F. Carcenac, A. Pepin, Y. Chen, M. Mejias, A. Lebib, L. Manin-Ferlazzo, L. Couraud, and H. Launois, "Electron beam lithography: Resolution limits and applications," *Applied Surface Science* **164**, 111-117 (2000).

- 86 N. Stokes, A. M. McDonagh, and M. B. Cortie, "Preparation of nanoscale gold structures by nanolithography," *Gold Bulletin* **40** (4), 310-320 (2007).
- 87 S. Y. Chou, P. R. Krauss, and P. J. Renstrom, "Imprint lithography with 25-nanometer resolution," *Science* **272** (5258), 85-87 (1996).
- 88 P. A. Kralchevsky and N. D. Denkov, "Capillary forces and structuring in layers of colloid particles," *Current Opinion in Colloid & Interface Science* **6** (4), 383-401 (2001).
- 89 B. G. Prevo, E. W. Hon, and O. D. Velev, "Assembly and characterization of colloid-based antireflective coatings on multicrystalline silicon solar cells," *Journal of Materials Chemistry* **17** (8), 791-799 (2007).
- 90 H. Q. Li and N. Q. Wu, "A large-area nanoscale gold hemisphere pattern as a nanoelectrode array," *Nanotechnology* **19** (27) (2008).
- 91 X. Chen, X. Wei, and K. Jiang, "Fabrication of large-area nickel nanobump arrays," *Microelectronic Engineering* **86** (4-6), 871-873 (2009).
- 92 Arun Suresh, Ph D Thesis, North Carolina State University, 2009.
- 93 V. N. Truskett and M. P. C. Watts, "Trends in imprint lithography for biological applications," *Trends in Biotechnology* **24** (7), 312-317 (2006).
- 94 P. R. Krauss and S. Y. Chou, "Nano-compact disks with 400 Gbit/in(2) storage density fabricated using nanoimprint lithography and read with proximal probe," *Applied Physics Letters* **71** (21), 3174-3176 (1997).
- 95 S. Y. Chou, P. R. Krauss, W. Zhang, L. J. Guo, and L. Zhuang, "Sub-10 nm imprint lithography and applications," *Journal of Vacuum Science & Technology B* **15** (6), 2897-2904 (1997).
- 96 J. de Boor, N. Geyer, U. Gosele, and V. Schmidt, "Three-beam interference lithography: Upgrading a Lloyd's interferometer for single-exposure hexagonal patterning," *Optics Letters* **34** (12), 1783-1785 (2009).
- 97 I. Wathuthanthri, W. D. Mao, and C. H. Choi, "Two degrees-of-freedom Lloyd-mirror interferometer for superior pattern coverage area," *Optics Letters* **36** (9), 1593-1595 (2011).
- 98 J. de Boor, D. S. Kim, and V. Schmidt, "Sub-50 nm patterning by immersion interference lithography using a Littrow prism as a Lloyd's interferometer," *Optics Letters* **35** (20), 3450-3452 (2010).

- 99 D. Y. Xia, Z. Y. Ku, S. C. Lee, and S. R. J. Brueck, "Nanostructures and functional materials fabricated by interferometric lithography," *Advanced Materials* **23** (2), 147-179 (2011).
- 100 Michael E. Walsh, Ph D Thesis, Massachusetts Institute of Technology, 2004.
- 101 M. M. Qazilbash, A. A. Schafgans, K. S. Burch, S. J. Yun, B. G. Chae, B. J. Kim, H. T. Kim, and D. N. Basov, "Electrodynamics of the vanadium oxides VO₂ and V₂O₃," *Physical Review B* **77** (11) (2008).
- 102 P. Jin, G. Xu, M. Tazawa, and K. Yoshimura, "Design, formation and characterization of a novel multifunctional window with VO₂ and TiO₂ coatings," *Applied Physics a-Materials Science & Processing* **77** (3-4), 455-459 (2003).
- 103 S. M. Babulanam, T. S. Eriksson, G. A. Niklasson, and C. G. Granqvist, "Thermochromic VO₂ films for energy-efficient windows," *Solar Energy Materials* **16** (5), 347-363 (1987).
- 104 N. R. Mlyuka, G. A. Niklasson, and C. G. Granqvist, "Thermochromic VO₂-based multilayer films with enhanced luminous transmittance and solar modulation," *Physica Status Solidi a-Applications and Materials Science* **206** (9), 2155-2160 (2009).
- 105 E. E. Chain, "Optical-properties of vanadium dioxide and vanadium pentoxide thin-films," *Applied Optics* **30** (19), 2782-2787 (1991).
- 106 C. B. Greenberg, "Optically switchable thin-films : A review," *Thin Solid Films* **251** (2), 81-93 (1994).
- 107 F. Guinneton, J. C. Valmalette, and J. R. Gavarrri, "Nanocrystalline vanadium dioxide: Synthesis and mid-infrared properties," *Optical Materials* **15** (2), 111-114 (2000).
- 108 F. Guinneton, L. Sauques, J. C. Valmalette, F. Cros, and J. R. Gavarrri, "Optimized infrared switching properties in thermochromic vanadium dioxide thin films: Role of deposition process and microstructure," *Thin Solid Films* **446** (2), 287-295 (2004).
- 109 C. G. Granqvist, "Transparent conductors as solar energy materials: A panoramic review," *Solar Energy Materials and Solar Cells* **91** (17), 1529-1598 (2007).
- 110 S. Bauer, "Optical-properties of a metal-film and its application as an infrared absorber and as a beam splitter," *American Journal of Physics* **60** (3), 257-261 (1992).
- 111 G. Xu, Y. Chen, M. Tazawa, and P. Jin, "Influence of dielectric properties of a substrate upon plasmon resonance spectrum of supported Ag nanoparticles," *Applied Physics Letters* **88** (4) (2006).

- 112 H. Hoppe and N. S. Sariciftci, "Organic solar cells: An overview," *Journal of Materials Research* **19** (7), 1924-1945 (2004).
- 113 X. N. Yang, J. Loos, S. C. Veenstra, W. J. H. Verhees, M. M. Wienk, J. M. Kroon, M. A. J. Michels, and R. A. J. Janssen, "Nanoscale morphology of high-performance polymer solar cells," *Nano Letters* **5** (4), 579-583 (2005).
- 114 R. Kroon, M. Lenes, J. C. Hummelen, P. W. M. Blom, and B. De Boer, "Small bandgap polymers for organic solar cells (polymer material development in the last 5 years)," *Polymer Reviews* **48** (3), 531-582 (2008).
- 115 W. Dickson, G. A. Wurtz, P. R. Evans, R. J. Pollard, and A. V. Zayats, "Electronically controlled surface plasmon dispersion and optical transmission through metallic hole arrays using liquid crystal," *Nano Letters* **8** (1), 281-286 (2008).
- 116 E. Hendry, M. J. Lockyear, J. G. Rivas, L. Kuipers, and M. Bonn, "Ultrafast optical switching of the THz transmission through metallic subwavelength hole arrays," *Physical Review B* **75** (2007).
- 117 Smolyaninov, I., A. V. Zayats, A. Stanishevsky, and C. C. Davis, "Optical control of photon tunneling through an array of nanometer-scale cylindrical channels," *Physical Review B* **66** (20) (2002).
- 118 D. Gerard, V. Laude, B. Sadani, A. Khelif, D. Van Labeke, and B. Guizal, "Modulation of the extraordinary optical transmission by surface acoustic waves," *Physical Review B* **76** (23) (2007).
- 119 A. J. Ridley, M. A. Schwartz, K. Burrige, R. A. Firtel, M. H. Ginsberg, G. Borisy, J. T. Parsons, and A. R. Horwitz, "Cell migration: Integrating signals from front to back," *Science* **302** (5651), 1704-1709 (2003).
- 120 C. M. Lo, H. B. Wang, M. Dembo, and Y. L. Wang, "Cell movement is guided by the rigidity of the substrate," *Biophysical Journal* **79** (1), 144-152 (2000).
- 121 E. W. L. Chan and M. N. Yousaf, "Immobilization of ligands with precise control of density to electroactive surfaces," *Journal of the American Chemical Society* **128** (48), 15542-15546 (2006).
- 122 J. C. Love, L. A. Estroff, J. K. Kriebel, R. G. Nuzzo, and G. M. Whitesides, "Self-assembled monolayers of thiolates on metals as a form of nanotechnology," *Chemical Reviews* **105** (4), 1103-1169 (2005).

- 123 D. K. Hoover, E. W. L. Chan, and M. N. Yousaf, "Asymmetric peptide nanoarray surfaces for studies of single cell polarization," *Journal of the American Chemical Society* **130** (11), 3280 (2008).
- 124 M. Arnold, E. A. Cavalcanti-Adam, R. Glass, J. Blummel, W. Eck, M. Kantelehner, H. Kessler, and J. P. Spatz, "Activation of integrin function by nanopatterned adhesive interfaces," *Chemphyschem* **5** (3), 383-388 (2004).
- 125 H. Q. Li, J. Low, K. S. Brown, and N. Q. Wu, "Large-area well-ordered nanodot array pattern fabricated with self-assembled nanosphere template," *IEEE Sensors Journal* **8** (5-6), 880-884 (2008).
- 126 P. Ortega, G. Lopez-Rodriguez, J. Ricart, M. Dominguez, L. M. Castaner, J. M. Quero, C. L. Tarrida, J. Garcia, M. Reina, A. Gras, and M. Angulo, "A Miniaturized Two Axis Sun Sensor for Attitude Control of Nano-Satellites," *IEEE Sensors Journal* **10** (10), 1623-1632 (2010).
- 127 Y. C. Kuo, T. J. Liang, and J. F. Chen, "Novel maximum-power-point-tracking controller for photovoltaic energy conversion system," *IEEE Transactions on Industrial Electronics* **48** (3), 594-601 (2001).
- 128 J. M. Quero, C. Aracil, L. G. Franquelo, J. Ricart, P. R. Ortega, M. Dominguez, L. M. Castaner, and R. Osuna, "Tracking control system using an incident radiation angle microsensor," *IEEE Transactions on Industrial Electronics* **54** (2), 1207-1216 (2007).
- 129 M. E. Furber and D. Jordan, "Optimal design of wavefront sensors for adaptive optical systems .1. Controllability and observability analysis," *Optical Engineering* **36** (7), 1843-1855 (1997).
- 130 K. Richards, T. Rimmele, S. L. Hegwer, R. S. Upton, F. Woeger, J. Marino, S. Gregory, and B. Goodrich, "The adaptive optics and wavefront correction systems for the advanced technology solar telescope", in *Adaptive Optics Systems II*, edited by B. L. Ellerbroek, M. Hart, N. Hubin, and P. L. Wizinowich (2010), Vol. 7736.
- 131 G. J. Capps D. L. Beshears, D. D. Earl, J. K. Jordan, L. C. Maxey, and J. D. Muhs, presented at the International Solar Energy Conference, Kohala Coast, Hawaii Island, Hawaii US 2003 (unpublished).
- 132 F. F. Chen, J. Feng, and Z. W. Hong, "Digital sun sensor based on the optical vernier measuring principle," *Measurement Science & Technology* **17** (9), 2494-2498 (2006).
- 133 C. W. de Boom, J. A. P. Leijtens, L. M. H. von Duivenbode, and N. van der Heiden, *Micro digital sun sensor: System in a package*. (2004).

- 134 P. Bajons, U. Wernhart, and H. Zeiler, "A sensor element for direct radiation measurement," *Solar Energy* **63** (2), 125-134 (1998).
- 135 T. Bohnke, M. Edoff, and L. Stenmark, "Development of a MOEMS sun sensor for space applications," *Sensors and Actuators a-Physical* **130**, 28-36 (2006).
- 136 C. C. Liebe, "Solar compass chip," *IEEE Sensors Journal* **4** (6), 779-786 (2004).
- 137 F. Xing, Z. You, G. F. Zhang, and J. Sun, "A novel active pixels sensor (APS) based sun sensor based on a feature extraction and image correlation (FEIC) technique," *Measurement Science & Technology* **19** (12) (2008).
- 138 L. Seifert, J. Liesener, and H. J. Tiziani, "Adaptive Shack-Hartmann sensor", in *Optical Measurement Systems for Industrial Inspection Iii*, edited by W. Osten, K. Creath, and M. Kujawinska (2003), Vol. 5144, pp. 250-258.
- 139 B. H. Pui, B. Hayes-Gill, M. Clark, M. G. Somekh, C. W. See, S. Morgan, and A. Ng, "Integration of a photodiode array and centroid processing on a single CMOS chip for a real-time Shack-Hartmann wavefront sensor," *IEEE Sensors Journal* **4** (6), 787-794 (2004).
- 140 R. J. Zawadzki, S. M. Jones, S. S. Olivier, M. T. Zhao, B. A. Bower, J. A. Izatt, S. Choi, S. Laut, and J. S. Werner, "Adaptive-optics optical coherence tomography for high-resolution and high-speed 3D retinal in vivo imaging," *Optics Express* **13** (21), 8532-8546 (2005).
- 141 C. Y. Lee, P. C. Chou, C. M. Chiang, and C. F. Lin, "Sun tracking systems: A review," *Sensors* **9** (5), 3875-3890 (2009).
- 142 H. Mousazadeh, A. Keyhani, A. Javadi, H. Mobli, K. Abrinia, and A. Sharifi, "A review of principle and sun-tracking methods for maximizing solar systems output," *Renewable & Sustainable Energy Reviews* **13** (8), 1800-1818 (2009).
- 143 W. Zhou, H. W. Gao, and T. W. Odom, "Toward broadband plasmonics: Tuning dispersion in rhombic plasmonic crystals," *ACS Nano* **4** (2), 1241-1247 (2010).
- 144 H. L. Tam, K. F. Li, K. W. Cheah, J. B. Xia, R. Huber, W. H. Wong, and Y. B. Pun, "Surface plasmon coupling in hexagonal textured metallic microcavity," *Applied Physics Letters* **89** (13) (2006).
- 145 John G. Proakis and Dimitris G. Manolakis, *Digital signal processing*. (Pearson Prentice Hall, Upper Saddle River, N.J., 2007, 4th ed).

- 146 B. C. Platt and R. Shack, "History and principles of Shack-Hartmann wavefront sensing," *Journal of Refractive Surgery* **17** (5), S573-S577 (2001).
- 147 L. Seifert, H. J. Tiziani, and W. Osten, "Wavefront reconstruction algorithms for the adaptive Shack-Hartmann sensor", in *Optical Measurement Systems for Industrial Inspection IV, Pts 1 and 2*, edited by W. Osten, C. Gorecki, and E. Novak (2005), Vol. 5856, pp. 544-553.
- 148 D. M. Topa, "Wavefront reconstruction for the Shack-Hartmann wavefront sensor", in *Optical Design and Analysis Software Ii*, edited by R. C. Juergens (2002), Vol. 4769, pp. 101-115.
- 149 L. Seifert, H. J. Tiziani, and W. Osten, "Wavefront reconstruction with the adaptive Shack-Hartmann sensor," *Optics Communications* **245** (1-6), 255-269 (2005).
- 150 X. Y. Li and W. H. Jiang, "Comparing between zonal reconstruction algorithms and modal reconstruction algorithms in adaptive optics system," *High-Resolution Wavefront Control: Methods, Devices, and Applications IV* **4825**, 121-130 (2002).
- 151 Amnon Yariv and Po-ji Yeh, *Photonics : Optical electronics in modern communications*. (Oxford University Press, New York, 2007, 6th ed).
- 152 D. R. Neal, W. J. Alford, J. K. Gruetzner, and M. E. Warren, "Amplitude and phase beam characterization using a two-dimensional wavefront sensor", in *Lboc - Third International Workshop on Laser Beam and Optics Characterization*, edited by M. Morin and A. Giesen (1996), Vol. 2870, pp. 72-82.
- 153 Thorlabs.com, "Shack-Hartmann wavefront sensor", www.thorlabs.com, (2011).